Emergence through non-local interactions: From mechanical coupling of proteins to long-range signaling in active agents

Alexander Ziepke

Munich 2024

Emergence through non-local interactions: From mechanical coupling of proteins to long-range signaling in active agents

Alexander Ziepke

born in Hennigsdorf, Germany

A dissertation submitted to the Faculty of Physics
at the Ludwig–Maximilians–Universität München for the degree of
Doctor Rerum Naturalium

Munich, December 18, 2024

First referee: Prof. Dr. Erwin Frey
Second referee: Prof. Dr. Igor Aranson
Date of submission: December 18, 2024
Date of oral examination: February 11, 2025

ZUSAMMENFASSUNG

Emergente Muster in biologischen Systemen entstehen aus einfachen Interaktionen zwischen individuellen Komponenten und führen zu komplexen, organisierten Strukturen über mehrere Skalen hinweg. Auf zellulärer Ebene treiben Reaktions-Diffusions-Prozesse von Proteinen wesentliche Funktionen wie Polarisation und Zellteilung an. Auf größeren Skalen organisieren sich Gruppen von Zellen oder Bakterien zu dynamischen, kollektiven Strukturen. In dieser Arbeit untersuchen wir, wie nicht-lokale Interaktionen dieses emergente Verhalten beeinflussen. Insbesondere betrachten wir, wie mechanische Kopplung mit deformierbaren Geometrien die Musterauswahl beeinflusst und wie langreichweitige Kommunikation in Systemen aktiver Materie die Entstehung neuartiger Strukturen und kooperativer Funktionalitäten fördert.

Wir beginnen mit der Untersuchung von Musterbildung in räumlich modulierten, röhrenförmigen Geometrien. Der Fokus liegt hier auf den Auswirkungen geometrischer Deformationen auf die Strukturbildung in Reaktions-Diffusions-Systemen mit reaktiver Kopplung zwischen Spezies im Volumen und auf einer umschließenden Oberfläche. Diese Systeme stellen relevante, paradigmatische Modelle für die zelluläre Musterbildungn dar. Durch eine Dimensionsreduktion leiten wir eine effektive eindimensionale Beschreibung her, die die geometrischen Effekte der Deformationen auf die Reaktions-Diffusions-Dynamik berücksichtigt. Mit einer störungstheoretischen Analyse identifizieren wir das räumlich variierende Verhältnis von Volumen zu Oberfläche als den entscheidenden Faktor, der die Auswahl geometrischer Längenskalen in diesen Systemen bestimmt. Wir zeigen, dass die gebildeten Muster von Proteinsystemen in Wechselwirkung mit den begrenzenden Geometrien stehen. Durch die Analyse der Langzeitdynamik im System, finden wir eine geometrisch kontrollierte Musterstabilisierung und identifizieren die Minimierung von Grenzflächen als treibenden Faktor hinter der geometrisch unterbrochenen Vergröberung und Reifung der Strukturen.

Aufbauend auf diesen Ergebnissen untersuchen wir ein System, in dem eine dynamische geometrische, nicht-lokale Kopplung zu emergenten Phänomenen führt. Wir betrachten die Entmischung von membrangebundenen Proteinen, die durch eine Induzierung einer bevorzugten Krümmung mit der Membran gekoppelt sind. Die resultierenden dynamischen Deformationen der elastischen Membran erzeugen eine effektive Form nicht-lokaler mechanischer Kopplung. Durch thermodynamische Analysen zeigen wir, wie Oberflächendeformationen die Entmischung sowohl induzieren als auch unterdrücken können und durch Selektion einer endlichen Längenskala die Vergröberung und Reifung der Muster stoppen.

Insgesamt stellen wir fest, dass geometrische Effekte, wie statische Deformationen oder dynamische, mechanische Rückkopplungsschleifen, eine bedeutende Rolle bei der Musterbildung und -dynamik in räumlich-zeitlich modulierten Geometrien spielen.

Im zweiten Teil der Arbeit gehen wir über diese unmittelbare nicht-lokale mechanische Kopplung hinaus und betrachten die Rolle von langreichweitiger Kommunikation durch chemische und akustische Signale in beweglicher aktiver Materie. Dazu untersuchen wir ein System von selbstangetriebenen, polaren Agenten, die mit einem zusätzlichen internen Freiheitsgrad ausgestattet sind. Dieser interne Zustand, der nicht direkt mit der Bewegung der Agenten gekoppelt ist, implementiert einen Mechanismus der zur Kommunikation genutzt werden kann. Abhängig von ihrem internen Zustand und der lokalen Konzentration chemischer Signalmoleküle, können Agenten die Weiterleitung der Signale unterstützen. Dieser Weiterleitungsmechanismus ermöglicht langreichweitige Kommunikation, da chemische Signale nicht auf diffusive Ausbreitung beschränkt sind, sondern durch Weiterleitung die Ausbreitung von Erregungswellen ermöglichen. Wir zeigen, dass solche chemische Signalweiterleitung in Kollektiven aktiver Agenten zu einer hierarchischen Selbstorganisation führt. Das System nimmt im Verlauf des Aggregationsprozesses verschiedene kollektive dynamische Zustände ein. Diese Zustände weisen unterschiedliche phänotypische Verhaltensweisen auf und erfüllen je-

weils spezifische Rollen. Durch die Quantifizierung des dynamischen Informationsgehalts, der mit der emergenten Ordnung im System verbunden ist, stellen wir einen qualitativen Zusammenhang zwischen dieser Ordnung und den Signalverarbeitungsvorgängen auf der Ebene der individuellen Einheiten her.

Aufbauend auf dieser Untersuchung der emergenten Selbstorganisation durch nicht-lokale Kommunikation, konzentrieren wir uns auf kooperative Funktionalitäten, die entstehen, wenn Agenten Informationen über entfernte Regionen des Systems durch Signalübertragung erhalten. Zu diesem Zweck stellen wir ein Modell akustisch interagierender aktiver Materie vor, bei dem Agenten interne Oszillatoren besitzen, die kontinuierlich akustische Signale in ihre Umgebung aussenden. Dieses System dient als Analogon zu einem Kollektiv selbstangetriebener Oszillatoren, die durch ein gemeinsames, selbstgeneriertes akustisches Feld wechselwirken und synchronisieren.

Unsere Ergebnisse zeigen, dass Synchronisation es den Agenten ermöglicht, sich selbstorganisiert zu differenzieren und in unterschiedliche phänotypische Zustände zu aggregieren, die durch unterscheidbare akustische Signaturen charakterisiert sind. Über die akustische Kopplung zwischen einzelnen Agenten hinaus ermöglichen die akustischen Signale dass die Kollektive Informationen über ihre internen Zustände durch spezifische Emissionen in die Umgebung senden. Bemerkenswerterweise beobachten wir die Entwicklung kollektiver Funktionalität: Das System passt sich dynamisch an Umweltveränderungen an, indem es auf reflektierte Signale reagiert. Zudem verleiht die selbstorganisierte Differenzierung den Agenten eine Form von phänotypischer Resilienz, die es dem Kollektiv ermöglicht, sich selbst nach erheblichen Störungen wiederherzustellen.

Zusammenfassend untersuchen wir verschiedene Szenarien, in denen nicht-lokale Kopplung zu emergenten Phänomenen führt. Die Arbeit liefert wichtige Erkenntnisse über das Zusammenspiel zwischen geometrischen Deformationen und mechanischer Kopplung in musterbildenden Systemen mit Implikationen für die Bildung zellulärer Strukturen. Darüber hinaus beleuchten wir die Rolle nicht-lokaler Kommunikation in aktiven Materiesystemen, erweitern das Verständnis von emergenter Selbstorganisation und ebnen den Weg für die Entwicklung funktionaler Systeme aktiver Materie.

SUMMARY

Emergent patterns in biological systems arise from simple interactions between individual components, leading to complex, organized structures across multiple scales. At the cellular level, protein reaction-diffusion processes drive essential functions such as polarization and division. On larger scales, groups of cells or bacteria self-organize into dynamic, collective structures. In this thesis, we investigate how non-local interactions shape this emergent behavior. Specifically, we examine how mechanical coupling with deforming geometries affects protein pattern selection and how long-range communication in active matter systems promotes the emergence of novel structures and cooperative functionalities.

We start by investigating pattern formation within spatially modulated tubular geometries. We focus on the impact of geometric deformations in bulk-boundary reaction-diffusion systems which are paradigmatic models for cellular pattern formation. By performing a dimensionality reduction, we derive an effective one-dimensional description that incorporates the geometric effects of deformations on the reaction-diffusion dynamics. Through perturbative analysis, we identify the spatially varying ratio of bulk volume to surface area as the key factor driving geometric length scale selection in these systems. We find that protein systems can collectively form patterns that sense external geometries. By analyzing the long term dynamics in the system, we find geometrically controlled pattern stabilization and identify interface minimization as the driving factor behind geometrically interrupted coarsening.

Building on these findings, we explore a system in which a dynamic geometric non-local coupling gives rise to emergent phenomena. We consider demixing of membrane-embedded protein systems where the species geometrically couple to the membrane by inducing a preferred curvature in the surface. The resulting dynamic deformations of the elastic membrane generate an effective form of non-local mechanical coupling. By analyzing the thermodynamics of the system, we demonstrate how surface deformations can both induce and suppress demixing, enforce the selection of a finite pattern length scale, and arrest coarsening.

Altogether, we find that geometric effects such as static deformations or dynamic mechanical feedback loops play a significant role in shaping pattern formation and dynamics in spatio-temporally modulated domains.

In the second part of the thesis, we go beyond this immediate non-local mechanical coupling and consider the role of long-distance communication by chemical and acoustic signals in self-propelled active matter. Therefore we consider a system of self-propelled active agents with polar alignment that are equipped with an additional internal degree of freedom. This state, which is not directly coupled to the agents' self-propulsion behavior, can be used for a communication machinery. Depending on their intrinsic states and the local concentration of chemical signaling molecules, agents can contribute by relaying the signal. Such a relaying mechanism gives rise to long-range communication as chemical signals are not limited by diffusive spreading but relaying yields trigger wave propagation of the signals. We find that such a chemical signaling in collectives of active agents yields a hierarchical self-organization. The system employs different collective dynamic states at different stages of the aggregation process. Thereby the different states exhibit phenotypical behaviors and fulfill distinct roles. By quantifying the dynamic information content related to the emergent order in the system, we qualitatively link the emergent order to the signal processing events at the level of the individual units.

Building on this study on emergent self-organization enabled by non-local communication, we focus on cooperative functionalities that arise when agents acquire information about distant regions of the system through signaling. To this end, we introduce a model of acoustically interacting active matter, where agents possess internal oscillators that continuously emit acoustic signals into their

environment. This system serves as an analog to a collective of self-propelled oscillators that achieve synchronization through a shared, self-generated acoustic field.

Our findings demonstrate that synchronization enables agents to undergo self-organized differentiation and aggregation into distinct phenotypic states, each characterized by unique acoustic signatures. Beyond individual acoustic coupling, these collectives broadcast information about their internal states into the environment through their specific acoustic emissions. Notably, we observe the emergence of collective functionality: the system adapts dynamically to environmental changes by responding to reflected signals. Moreover, the self-organized differentiation of agents confers a form of phenotypic resilience, allowing the collective to recover robustly even after substantial perturbations.

In summary, we explore various scenarios where non-local coupling gives rise to emergent phenomena. Our work provides insights into the interplay between geometric deformations and mechanical coupling in pattern-forming systems, with implications for cellular structure formation. Additionally, we shed light on the role of non-local communication in active matter systems, advancing the understanding of emergent self-organization and paving the way for the development of functional active matter systems.

List of Publications

Publications directly relevant to this thesis

1. Alexander Ziepke, Michael Reichert, Luca Stadtmüller, and Erwin Frey, Geometric control of protein pattern formation in bulk-boundary systems. *in preparation*.

2. Antonia Winter[*], Yuhao Liu[*], Alexander Ziepke [*], George Dadunashvili, and Erwin Frey, Phase Separation on Deformable Membranes: interplay of mechanical coupling and dynamic surface geometry. Preprint available at arXiv.2409.16049 (2024).

3. Alexander Ziepke, Ivan Maryshev, Igor S. Aranson, and Erwin Frey, Multi-scale organization in communicating active matter. *Nature Communications* **13**, 6727 (2022).

4. Alexander Ziepke, Ivan Maryshev, Igor S. Aranson, and Erwin Frey, Acoustic signaling enables collective perception and control in active matter systems.
   Preprint available at arXiv.2410.02940 (2024).

Other publications

5. Jinghui Liu[*], Tom Burkart[*], Alexander Ziepke, John Reinhard, Yu-Chen Chao, Tzer Han Tan, Zachary Swartz, Erwin Frey, and Nikta Fakhri, Light-induced cortical excitability reveals programmable shape dynamics in starfish oocytes. Preprint available at arXiv.2409.08651 (2024).

[*] These authors contributed equally.

Project Contributions and Associated Publications

Chapter 2 – Geometric control of protein pattern formation in bulk-boundary systems*

Project Contributions

I am the main contributor to this project under the supervision of Prof. Dr. Erwin Frey. I designed and performed most of the presented research and co-supervised sub-parts of this project together with Prof. Dr. Erwin Frey. Michael Reichert worked on the analysis of geometric perturbations on the basis of the perturbative linear stability analysis and Luca Stadtmüller investigated geometrically interrupted coarsening on the basis of the dimensionally reduced equations and the perturbative analysis.

Associated Publications

The contents of Chapter 2 will also be presented in a manuscript, currently in preparation (Ref. [1]) in

Geometric control of protein pattern formation in bulk-boundary systems
by Alexander Ziepke, Michael Reichert, Luca Stadtmüller, and Erwin Frey.
(in preparation)

Parts of the content on the perturbative linear stability analysis have been presented in another form in the Master's thesis of Michael Reichert ("Geometric Pattern Selection in Reaction-Diffusion Systems"). Parts of the section on the deformation-induced interruption of coarsening have been presented in another form in the Master's thesis of Luca Stadtmüller ("Geometric Wavelength Selection in Mass-Conserving Reaction-Diffusion Systems with Bulk-Boundary Coupling").

Chapter 3 – Phase Separation on deformable membranes*

Project Contributions

This was a collaborative project with two intern students Antonia Winter and Yuhao Liu. I co-supervised the internship project as well as the related Master's thesis of Antonia Winter together with Dr. George Dadunashvili and Prof. Dr. Erwin Frey.

Associated Publication

The contents of Chapter 3 are adapted from the article (Ref. [2]) in

Phase Separation on Deformable Membranes: interplay of mechanical coupling and dynamic surface geometry
by Antonia Winter*, Yuhao Liu*, Alexander Ziepke*, George Dadunashvili and Erwin Frey.

Preprint available at arXiv.2409.16049.

* These authors contributed equally

A preliminary version of this text was also used as part of the Master's thesis of Antonia Winter ("Mechano-Chemical Coupling and Anisotropy in Protein-Membrane Systems").

Chapter 4 – Multi-scale organization in communicating active matter*

Project Contributions

I am the main contributor to this project under the supervision of Prof. Dr. Erwin Frey and with external collaborator Prof. Dr. Igor Aranson. Dr. Ivan Maryshev contributed to the project with an early implementation of the analysis on the collective information content.

Associated Publications

The contents of Chapter 4 are adapted from the published article (Ref. [3]) in

Multi-scale organization in communicating active matter
by Alexander Ziepke, Ivan Maryshev, Igor S. Aranson, and Erwin Frey.
Published in *Nature Communications* **13**, 6727 (2022).
Reproduced with permission, CC BY 4.0.

Chapter 5 – Acoustic signaling enables collective perception and control in active matter systems*

Project Contributions

I am the main contributor to this project under the supervision of Prof. Dr. Erwin Frey and with external collaborator Prof. Dr. Igor Aranson.

Associated Publications

The contents of Chapter 5 are adapted from the article (Ref. [4]) in

Acoustic signaling enables collective perception and control in active matter systems
by Alexander Ziepke, Ivan Maryshev, Igor S. Aranson, and Erwin Frey.
Reproduced with permission, CC BY 4.0.
Preprint available at arXiv.2410.02940.

* The contents of these chapters are edited versions of published manuscripts or manuscripts currently in preparation.

Project Abstracts

Geometric control of protein pattern formation in bulk-boundary systems

In this project, we develop an analytical framework to describe pattern-forming reaction-diffusion systems involving species that diffuse within a bulk volume and species that are bound to a spatially modulated, enclosing confinement. Specifically, we account for the effects of geometric deformations in an enclosing tubular structure by deriving an effective, dimensionally reduced description. This description also accounts for reactive interaction between bulk- and boundary species at the modulated confinement. The presented approach enables an analytic analysis of the linear stability of the homogeneous steady state as well as of the emergent patterns. For deformed geometries, our analysis relies on a perturbative treatment that considers spatial deformations as weak deviations from the undeformed tubular shape. Beyond the initial formation of patterns, we investigate the influence of geometric deformations on long-term pattern dynamics, particularly focusing on coarsening processes.

Context. Biological protein systems often exhibit complex interactions among multiple protein species, particularly through dynamic exchanges between the cytosolic bulk and the membrane[6–8]. These interactions give rise to spatially organized patterns, which are essential for critical biological processes such as cell division and polarization[9–12]. Similarly, the functional design of some chemical microfluidic devices with coated reactive surfaces relies on the reactions at the surface and exchange with a bulk volume[13–16].

Studies on protein systems with bulk-boundary coupling have demonstrated that geometric confinement strongly influences pattern formation[17]. For example, by tuning the ratio between reactive and geometric length scales in models of elliptical cells, one can control the emergence of long-axis or short-axis polarization[18]. Furthermore, experiments on reconstituted Min protein systems in deformed PDMS channels reveal that confining geometric shapes significantly affect pattern length scales and oscillatory behavior[19–21].

Given the crucial role of geometric constraints in reaction-diffusion dynamics, there have been recent efforts in understanding pattern formation within modulated geometries[22] and on deformable surfaces[23]. However, so far, a comprehensive framework combining membrane and bulk dynamics within spatially deformed tubular geometries, along with a systematic investigation of the relevant contributions in such a controlled, dimensionally reduced setting, has been missing.

Research Question. Here, we first aim to simplify the theoretical description of protein reaction-diffusion dynamics with reactive bulk-boundary interactions at an enclosing deformed tubular surface, by reducing the system to a single spatial dimension. This reduction makes the system more amenable to analytical analysis. Subsequently, we study how spatial modulations of the geometry influence the emergent protein patterns and whether they can stabilize specific length scales in the long-term dynamics, thereby arresting coarsening processes.

Results. Assuming narrow tubes relative to the length scale of bulk gradients, we simplify the system by integrating out the angular and radial degrees of freedom within the tubular geometry. This reduction yields an effective one-dimensional equation that describes protein reaction-diffusion dynamics, including reactive interactions at the deformed tubular surface.

Using this reduced equation, we perform a perturbative linear stability analysis, which reveals how the geometry of the confinement influences the emergent protein patterns. In particular, we predict that geometric deformations localize the patterns and control their characteristic length scale. These predictions are validated through numerical simulations of the full reaction-diffusion system within the tubular domain, showing excellent agreement with our analytical results.

Beyond the initial pattern formation, we analyze the impact of geometric deformations on coarsening dynamics. Our findings demonstrate that spatial modulations of the confinement can arrest coarsening. We identify the system's intrinsic tendency toward interface minimization as the key mechanism underlying long-term pattern localization and stabilization within deformed geometries. By combining the diffusive mass transfer rate during coarsening[24,25] with the interface minimization tendency, given by effective advective contributions in the reduced equations, we derive a criterion for geometric deformations that effectively halt the coarsening process.

Relevance. The study of bulk-boundary coupled systems and geometric length-scale selection is of significant relevance for cellular protein systems. Here, the development of a systematic understanding of cellular division and self-organization is an ongoing research effort. The dimensionally reduced description may prove useful to answer the question, which fundamental mechanisms and aspects need to be taken into account. Moreover, when the underlying assumptions hold, solving the one-dimensional effective equation can substantially reduce computational costs in comparison to full 3D numerical simulations, facilitating both analytical and numerical studies. Also for the inverse question of how do confinements need to be shaped to give rise to specific patters, our approach may serve as a starting point for design of chemical reactors or dynamic membrane confinements for artificial cells.

Importantly, our approach can also be extended to include physical membrane mechanics and dynamic membrane deformations, which interact in feedback with the confined protein patterns. Such an extension enables the study of mechano-chemical coupling in confined bulk-boundary systems, positioning the framework as a versatile and generic model for exploring complex geometric interactions in biological and artificial systems.

Phase separation on deformable membranes: interplay of mechanical coupling and dynamic surface geometry

This project focuses on the interplay between phase-separation- and elastic membrane dynamics through mechanical coupling. We study proteins embedded in a two-dimensional elastic membrane, where these proteins are assumed to induce a concentration-dependent spontaneous curvature. As a result, the proteins' demixing dynamics couples to the dynamic membrane, leading to protein-induced deformations. In turn, via their intrinsic curvature, proteins can sense and respond to geometric deformations.

The mechanical deformations of the membrane give rise to a non-local coupling between protein concentrations on the membrane and thereby effect the proteins' phase-separation dynamics. To describe this phenomenon, we develop a covariant model equation for the phase-separation dynamics on the dynamic membrane manifold. We analyze the resulting behavior numerically using Monge parametrization and explore its long-term thermodynamic implications.

Context. Phase separation is a fundamental mechanism for the formation of structures and chemically enriched reactive compartments at the cellular level[26,27]. Thereby, the phase-separation dynamics can take place on two-dimensional surfaces. For example, lipids within lipid bilayer membranes show phase-separation into structures such as lipid rafts[28,29], while the demixing of membrane-associated proteins can give rise to high-density protein clusters[30,31]. These variations in lipid composition and densities of attached proteins can, in turn, induce membrane deformations[32,33].

Recent theoretical work on phase separation in ternary lipid mixtures has demonstrated that a membrane curvature that depends on the lipid densities, can lead to length-scale selection of emergent patterns, controlled by the membrane-mediated mechanical interactions[34]. Similarly, numeri-

cal simulations have shown that the phase separation of membrane-bound proteins is significantly influenced by the mechanical coupling between protein densities and membrane spontaneous curvature[35].

However, these studies omitted key contributions to the dynamics by employing uncontrolled expansions. For instance, Ref.[34] neglected terms that account for temporal changes in the effective membrane area, thereby only approximately conserving mass. Additionally, both studies neglected contributions of the spatial variations in the surface metric, which play a significant role for the protein-protein (or lipid-lipid) interactions driving the demixing behavior.

Research Question. Here, we address the problem of formulating a covariant description of demixing dynamics on deformable membrane surfaces and thereby extend the present descriptions. Additionally, we aim to systematically expand the full model to determine the characteristics of pattern formation from the fully mixed state as well as the long-time characteristic length scale of the system using thermodynamic arguments.

Results. In numerical simulations of the approximation free dynamical equations, we observe a significant impact of geometric coupling on the demixing dynamics. By tuning the strength of the induced spontaneous curvature, the stability of the fully mixed state exhibits a transition from stable, to a conserved Turing (type I) instability, and finally to the classical long-wavelength Cahn-Hilliard (type II) instability[36,37]. Notably, in contrast to the uninterrupted coarsening dynamics seen in the phase-separating system without geometric coupling, a characteristic, persistent length scale emerges at intermediate spontaneous curvature values.

To quantify this emergent length scale, we account for the system's relaxation to thermodynamic equilibrium. By applying a weakly bending approximation for the membrane and integrating out the membrane-deformation modes, we derive a thermodynamic prediction for the final length scale in the demixed state. This selected length scale is tunable via the strength of the protein-induced spontaneous curvature. Our analytical prediction is validated through numerical simulations, which show excellent agreement

Relevance. The emergence of length scales in phase-separating systems typically requires active driving or a form of non-local coupling. In this study, we introduce such a coupling through dynamic mechanical deformations of a two-dimensional membrane surface, which interacts with the phase-separating protein densities. Our results demonstrate that this system indeed gives rise to distinct patterns, suggesting that membrane-mediated coupling can act as a minimal mechanism for controlling the length scales of demixed phases.

Our study reveals quantitative differences compared to the previous work by Yu et al.[34], which we attribute to the controlled system expansion. Moreover, we observe a qualitative tuning of instabilities in the fully mixed state, highlighting the significant role of mechanical effects in both the initiation of phase separation and the determination of resulting length scales.

MULTI-SCALE ORGANIZATION IN COMMUNICATING ACTIVE MATTER

In this project, we investigate the role of long-range communication in self-propelled active agents through chemical signaling. The signaling transmission is sustained by the agents, which can either relay chemical signals or remain inactive, depending on their internal dynamic state. Additionally, we introduce a feedback mechanism, coupling the agents' motion to the collectively established chemical field, such that agents preferentially move toward regions of higher chemical concentration. We explore the resulting emergent dynamics and self-organization properties of this chemically communicating active matter using a combination of agent-based numerical simulations and continuous field modeling.

Context. In biological systems, communication among active agents is essential for enabling collective organization and functionality. Individual units must coordinate their behaviors to achieve a collective functioning, which often creates evolutionary advantages. For example, in organoid and tissue formation, mechanochemical cues guide cellular organization, differentiation, and spatial positioning[38,39]. Bacteria utilize chemical signaling to coordinate their movement[40,41], while social insects like ants rely on pheromone trails to communicate locations of food sources[42]. Larger animals, such as fish and birds, use visual or acoustic signals for long-distance communication to achieve complex coordinated behavior. A particular example of chemical signaling is seen in *Dictyostelium discoideum*, when cells release cyclic AMP to drive aggregation and fruiting body formation under starvation conditions[43–45]. Despite the critical role of inter-agent communication in driving collective behavior within active matter systems, its fundamental role for self-organization is yet not fully understood.

Research Question. Inspired by these biological examples and motivated by the overall importance of exchanging information between agents for collective organization, we investigate the role of communication in the aggregation process of active matter with chemical signaling. Specifically, we aim to identify minimal motifs required for effective physical long-range communication and examine how these mechanisms interact with the system's emergent collective behavior.

Results. In the active matter system with chemical communication, a long-range chemical communication is established through relaying of chemical signals by triggered emission of molecules by the dispersed agents. This form of communication enables a self-organized hierarchical aggregation process employing diverse collective structures with distinct behaviors at different stages. At smaller scales, chemically mediated agent-agent interactions first lead to the formation of collectively propagating droplets, which then coalesce into streams and eventually converge toward stationary, localized vortex states. The vortices, hosting internal spiral wave dynamics, continuously emit chemical waves into their surroundings, acting as self-organized centers of aggregation that guide the subsequent structure formation.

To assess the role of communication in the aggregation process, we quantify the emergent order by measuring the system's dynamic information content. Thereby, we establish a qualitative link between the observed collective organization and the signal processing capabilities of individual agents. Thus, the system's hierarchical organization and order formation are fundamentally driven by the collectively established chemical signaling landscape and the signal processing capabilities of the individual agents.

Relevance. The work sheds light on the mechanisms driving self-organization and structure formation in communicating active matter. Chemical signaling, which enables long-range communication via signal relaying, plays a crucial role in the aggregation process. The collectively established chemical signaling field can be seen as a shared reservoir of information to which agents have access through their signal processing machinery.

A key finding is that the use of distinct phenotypes at various stages of the self-organization process improves effectiveness of aggregation. It requires an adaptive differentiation of agents and an emergence of organizational units. We have demonstrated that such a behavior can be effectively achieved through chemical communication providing valuable insights for designing self-organized aggregation behaviors in artificial active matter systems.

By linking individual signal processing to collective self-organization, our results highlight the essential role of information processing in driving emergence and self-organization. Importantly, the observed non-linear responses to signals can be readily implemented in technical systems, such as microrobots, offering promising applications in microrobotics and other artificial systems.

ACOUSTIC SIGNALING ENABLES COLLECTIVE PERCEPTION AND CONTROL IN ACTIVE MATTER SYSTEMS

In this project, we investigate emergent phenomena in self-propelled active agents coupled through acoustic interactions. We develop a model for swarming agents equipped with internal oscillators that emit acoustic signals into their surroundings. These agents, in turn, perceive the collective acoustic field and synchronize their individual oscillations with the detected signals. Furthermore, the agents align their direction of motion towards larger acoustic amplitudes which creates a coupling between the acoustic signaling and the self-propulsion behavior.

Context. In our study on chemically communicating active matter[3], we observed that chemical signaling relies on the propagation of information through signal relaying by active agents. Without this relaying mechanism, chemical interactions are constrained by the relatively slow process of diffusive transport. As a result, both the propagation speed of signals and the distance over which the signals remain effective before dilution are inherently limited by diffusion.

In contrast, wave-based signaling, such as by acoustic or electromagnetic waves, offers the advantage of rapid signal propagation, enabling communication across larger distances, even when agents are sparsely distributed. For instance, animals like bats, birds, and whales rely on acoustic signals to communicate over large distances where diffusive transport would be impossible or impractically slow.

In the field of robotics, the development of synthetic swarms could greatly benefit from incorporating acoustic or electromagnetic interactions to facilitate communication between agents. However, despite the significant potential of wave-like signaling not only for such applications, a minimal system that implements acoustic communication in an active matter framework so far remained absent.

Research Question. We address the question of how a wave-like signaling between oscillatory agents enables self-organization and synchronized collective behavior. What are the organizational principles underlying wave-like coupling of active matter and which functionality can systems gain from it?

Results. To investigate the role of acoustic coupling in active matter, we conduct numerical simulations of an agent-based model and corresponding continuous field equations. Our findings reveal that acoustic signaling between oscillatory units drives self-organization into distinct collective states, each characterized by unique behaviors and acoustic signatures. These emergent structures include localized blob solutions, motile larvae, and fast-moving snakes, each enabling the agents to achieve diverse collective functionalities.

Notably, due to the self-organized differentiation of agent behaviors, the collective structures exhibit remarkable resilience, such as phenotype stability under strong perturbations. Additionally, they develop the ability to collectively orchestrate responses to external stimuli and environmental changes. Beyond the acoustic interactions between individual agents, agents within aggregates emit collective signals with distinct acoustic signatures. This facilitates communication across emergent collectives, enabling information transfer between collective structures on larger spatial scales.

Furthermore, collectives can sense their surroundings by detecting reflections of their emitted signals, allowing them to respond by modulating their acoustic output and behavior. Similarly, the collectives can be influenced by externally applied control signals which allows for external triggering of phenotype transitions and controlling the aggregates' motion in space.

Importantly, all of these emergent properties arise from the inherent non-locality of signals transmitted through acoustic waves.

Relevance. This study highlights the fundamental organizational principles of swarms, where simple individual units exchange information to develop collective behavior and coordinated responses to external cues. In potential technological implementations and applications of active matter systems, such as microrobotics, individual units are typically small compared to the size of forming

collectives. They may possess limited processing power and should operate under conditions in which a full external supervision is challenging. Consequently, achieving an autonomous collective functionality is essential.

Here, we demonstrate that such a functionality can emerge as a cooperative property through acoustic information exchange between individual agents. This work marks an important step toward functional active matter and offers design principles for future microrobotic swarms capable of performing complex tasks, as well as collectively sensing and responding to their environment.

Contents

* The contents of these chapters are edited versions of published manuscripts or manuscripts currently in preparation as indicated on pages xi-xii.

1

Introduction

1

Emergent patterns are a hallmark of biological systems, arising from simple local interactions that lead to complex, organized structures. At the cellular level, reaction-diffusion processes drive protein pattern formation, enabling critical functions such as cell polarization and division. On larger scales, collectives of active agents, such as cells or bacteria, self-organize into dynamic patterns and structures through energy consumption and microscopic interactions. These phenomena illustrate how local rules and interactions can give rise to robust, large-scale organization, a principle relevant to both living systems and synthetic active materials. In this thesis, we extend the study of such systems by introducing non-local interactions. Specifically, we examine how mechanical interactions with deforming geometries influence pattern selection in protein reaction-diffusion systems, and how long-range communication in active matter drives the emergence of novel patterns, structures, and cooperative functionalities.

1.1 STRUCTURE FORMATION IN BIOLOGY

Structure formation is a key ingredient for life in which increasingly complex structures emerge from simpler individual parts. The idea of 'More is different', brought forward by Anderson[46,47], is that the sum of many individual parts gives rise to a collective behavior governed by new laws, where emergent phenomenology is qualitatively different and hard to capture or predict based on the laws and language of the individual parts. For example, individual molecules can combine to form macromolecules, which then organize into complex structures such as biological cells. At this level, new properties emerge and cells exhibit life-like behaviors, such as growth and reproduction, which are absent at the molecular level. Groups of cells, in turn, form tissues and organs, which together constitute entire organisms. Remarkably, when these organisms interact in groups, they give rise to collective behaviors like the synchronized flight of bird flocks or the coordinated swimming patterns of schooling fish.

For the collective behavior the constituting components interact with each other while these interactions create emergent phenomena. For instance an ideal gas can be seen as a naive extension of single atoms to collective numbers of atoms. However, in the ideal gas description one fully neglects the interactions which lead to the collective properties of real gases that deviates from the simpler ideal gas model. Real gasses exhibit phase-transitions and critical phenomena, all these aspects arrive due to the interactions of gas molecules. Similarly, biological processes relying on physics and chemistry, living systems exhibit complex phenomena like metabolism, reproduction, and consciousness. These phenomena in principle still follow the underlying laws, e.g. of quantum mechanics, however, their description requires a different language. Emergent principles like evolutionary fitness, genetic coding, and neural network dynamics govern behavior at higher levels of complexity and implement a new vocabulary of relevant quantities to consider at the collective level. The emergent collective phenomena introduce new, scale-specific laws to replace the microscopic laws that are simply no longer adequate for description. New principles emerge that are specific to the scale of the collective. Thus, for an appropriate description, one chooses a model on the scale of the emergent patterns and collective structures.

Emergence is a crucial concept in biological systems as their complex behaviors and functions involve collective interactions at multiple scales. In biology, protein interactions can lead to liquid-liquid phase separation, a minimal mechanism for structure formation in cellular systems[26]. Liquid-liquid phase separation relies on the minimal basis of collective phenomenon as it solely includes energetic interactions between neighboring particles of different types. Such phase-separating systems are fully described by thermodynamic considerations and free energy minimization. However, they exhibit an emergent phenomenon known as demixing, where ordered structures spontaneously form from an initially homogeneous and noisy state. These collective structures are macroscopic, with sizes significantly larger than those of the individual units.

Moreover, through nonlinear reactions, proteins can form complex collective macroscale patterns with stationary, traveling wave, or oscillatory dynamics that are organizing mechanisms behind cell polarization, mechanic contraction waves, or mid-cell localization of the cellular division machinery[48–52]. Such reaction-diffusion systems comprise a broad class of physical models that describe the

dynamics of diffusing species with local reactions such as state changes, or attachment and recruitment processes on reactive surfaces. The collective dynamics of the constituting species, which is typically driven out of equilibrium by active processes, yields emergent patterns at scales that are large compared to the extend of single constituents.

Another important example in which novel phenomena emerge from collective behavior is active matter systems. Here, energy consumption at the level of individual units, e.g. for self-propulsion of these units, drives the system out of equilibrium leading to remarkable examples of collective emergent behavior, relevant in a multitude of biological structure forming system[53–56]. For instance, upon division of eukaryotic cells, mitotic spindle formation ensures segregation of the two copies of DNA (sister chromatites in daughter cells) during mitosis within the mother cells[57–59]. This process relies on the polarization of microtubules and their alignment at the cellular centrosomes. Thereby, motor proteins exert a force on these microtubules, assuring separation of the gene copies. The emergent polar order of microtubules is a key ingredient for the cooperative aligned functioning of the motor proteins. Furthermore, active motion of cells such as in the social amoeba *Dictyostelium discoideum*[60] or of bacteria[61] yields cooperative behavior such as aggregation or dynamic tissue remodeling during morphogenesis[62,63]

Altogether, liquid-liquid phase separation and reaction-diffusion dynamics are key mechanisms for structure formation in cellular systems. Active matter, is yet another broad field in which cooperativity of large numbers of individual units gives rise to emergence. In this thesis, we will cover examples of emergent behavior through a form of non-local coupling in these fields.

1.1.1 LIQUID-LIQUID PHASE-SEPARATION

A particular mechanism of structure formation, relevant to biological system is liquid-liquid phase separation[27]. It is based on the classical demixing mechanism as described by the Flory-Huggins theory of spinodal decomposition where different energetic interaction between solute and solvent particles give rise to formation of spatially demixed states[64]. In the context of biological systems, such a demixing behavior is of large relevance for the formation of cellular structures and membrane-less compartments. The formation of such compartments allows for an enrichment of molecules inside and enables a tuning of reactive conditions. For instance germ cell initialization in *Caenorhabditis elegans* is established by condensation of P granules and their subsequent localization[26]. Through liquid-liquid phase separation, cells can control enzymatic reactions[65,66] and it is believed to be an important mechanism behind several cellular mechanisms such as signaling and stress response[67–69].

On its own, liquid-liquid phase separation is a thermodynamic effect and the demixing occurs after parameter quenching as a thermodynamic equilibrium process. These systems often exhibit Ostwald ripening and the coarsening process prevails stable structure formation and the system's ability for length scale selection[70]. What is required in addition to the demixing dynamics for the system to yield stable patterns and structures with a distinct length scale? In cellular systems, one can argue that coarsening is typically slow and other downstream mechanisms such as active reactions can either stabilize structures at some time and length scale or the dynamics is actively driven, preventing coarsening[71]. For instance, one can achieve stationary size distributions of demixed droplets through constant nucleation and coalescence events[72]. Droplet sizes an localization of liquid condensates can be regulated by active chemical reactions[73–75].

Recent studies on mechanically coupled phase-separating systems reveal the possibility for stable finite length-scale patterns in liquid-liquid phase separation. Changing the preferred curvature of the lipid membrane they constitute, the mechanical feedback between phase-separation dynamics and changing geometric properties can yield stable pattern length scales without coarsening[34]. Another systems in thermodynamic equilibrium that exhibits such a finite length scale is phase-separation of block copolymer melts where the length scale can be associated to a present non-local coupling[76]

In Chapter 3, we will show that the mechanical interactions of phase-separating proteins attached to an elastic surface lead to an effective non-local coupling. This coupling is responsible for the emergence of finite pattern length scales, even in the absence of active driving[2].

1

1.1.2 REACTION-DIFFUSION SYSTEMS

Reaction-diffusion systems are a core element for describing pattern formation in various chemical and biological systems[77–80]. They comprise the local transformation of species into others (reaction) and a spatial coupling that flattens concentration gradient (diffusion). For instance, applications of reaction-diffusion modeling range from pattern dynamics in the Belouszov-Zhabotinsky-reaction[81,82] over surface waves on catalytic Pt-surfaces[83–85], to cellular protein patterns[86–88].

Reaction-diffusion processes are relevant in various biological systems as they are a remarkable example for non-equilibrium pattern and structure formation[89]. To understand their role in biological systems, one needs to address large-amplitude patterns, geometrically confined systems, bulk-boundary coupling, and especially relevant for synthetic cells: mechano-chemical coupling. In the following we focus on protein reaction-diffusion dynamics and recapitulate general aspects of their pattern forming capabilities with particular focus on mass-conservation and the role of a reactive coupling at an enclosing surface.

A LATERAL INSTABILITY YIELDS PATTERN FORMATION

As discussed by Turing in his seminal paper[89], reaction-diffusion systems with at least two coupled species can give rise to spatial pattern formation through the coupling of local reaction kinetics and spatial diffusion. Thereby, diffusion acts to reduce concentration gradients by promoting spatial homogenization, distributing molecules uniformly across space. Additionally, the reaction kinetic locally drive the system towards stationary states (fixed points) for which the reactions are in a dynamic equilibrium, converting species into one another while retaining the average concentrations constant. Typically, reaction dynamics drive the system towards stable fixed points establishing stationary concentration ratios between the different species, or more complicated general stable attractors. Individually, both diffusion and reaction mechanisms appear to drive the system toward a homogeneous steady state. However, as Turing demonstrated, their combined effects in a reaction-diffusion system with two coupled species can give rise to spatial patterns that Turing argued could template downstream morphogenesis.

The key insight from Turing's work lies in the fact that the diffusive coupling between chemical species with different diffusive length scales can induce a lateral instability and drive the formation of spatial patterns. Turing realized that, even if a system is stable under homogeneous perturbations (and thus returns to its fixed point), the introduction of diffusion can destabilize the system with respect to heterogeneous perturbations. This spatially extended instability, known as Turing instability, serves as a general mechanism for the emergence of patterns[90]. However, recently it has been explored that, mass-conservation of the species introduces a new twist to this paradigmatic pattern-forming mechanism[80,88,91–94].

MASS-CONSERVING SYSTEMS

Mass-conserving reaction-diffusion systems play a crucial role in modeling biological pattern formation. Particularly, in cellular systems, proteins or lipids are confined by or, respectively, embedded within the cell membrane, and changes in protein numbers due to a net production or degradation are negligible on the typical timescale of pattern dynamics. Therefore, mass conservation is overall granted which has several implication on the pattern formation mechanisms[88,94].

Mass-conserving reaction-diffusion models have been widely used to study biological phenomena, including polarity formation in cells[80,86,91,95]. Examples include models for the localization of budding sites in yeast *Saccharomyces cerevisiae*[93,96,97] or the establishment of long-axis polarization in *C. elegans*[18], to name a few. The Min protein system in *Escherichia coli* serves as a paradigmatic model for cellular pattern formation due to its generic functioning, representative for a broad range of cellular systems, and the possibility for it to be reconstituted in vitro[48,98]. Oscillations of the Min system provide a striking example where mass-conserving reaction-diffusion modeling successfully captures experimental observations. The modeling approaches yield qualitative and quantitative

agreement and allow for insights into relevant yet unexplored molecular interactions and parameter dependence of exhibited behavior[99,100]. The minDE pole-to-pole oscillations are critical for the mid-cell localization of the division machinery[49,101,102]. Advanced models of the Min system have achieved quantitative agreement with both in vivo and in vitro experiments, enhancing our understanding of the mechanisms underlying cellular division[100]. Moreover, the reconstituted Min system, embedded within giant unilamellar vesicles[103,104], represents a promising module for bottom-up approaches aimed at reconstructing division machinery in artificial cells[105,106]. Other notable examples of mass-conserving reaction-diffusion systems include the confined dynamics of Rho enzymes in starfish oocytes, which guide surface contraction waves during meiotic anaphase[5,52,107,108], and conserved models for head-tail polarization dynamics in Dictyostelium discoideum, which compared to non-conserving models demonstrate increased robustness and enhanced propagation speed during polarity formation[109], among many others.

Beyond its biological relevance, mass conservation has a profound qualitative impact on pattern formation. Unlike non-conserved systems, mass-conserving systems exhibit neutral stability of the homogeneous steady state with respect to changes in the local mass. This property fundamentally alters the nature of pattern-forming instabilities. For instance, while linear stability analysis can predict lateral instabilities in general reaction-diffusion systems, the presence of a conservation law introduces further constraints that affect the dynamics of pattern formation. Reactive nullclines, which provide critical insights into the dynamics of well-mixed systems, become directly linked through the conservation law, effectively reducing the dimensionality of the analysis [1]. In conserving systems, the conserved quantity (e.g., the total mass of a protein) acts as a control parameter that influences local reactive equilibria. Although local dynamics cannot change this parameter, spatial heterogeneities in its distribution drive variations in local equilibria, leading to the emergence of patterns[80,88,94]. This perspective enables a geometric approach to analyzing lateral instabilities and the mass-redistribution instability, which underlies pattern formation.

In Chapter 2, we apply this geometric framework to describe the influence of confinement on pattern formation in mass-conserving reaction-diffusion systems inspired by biological protein systems with bulk-boundary coupling[94].

PATTERNS FORMING PATTERNS

Already in his founding discussion Alan Turing pointed out that biological systems may employ a hierarchy of patterns, transitioning from one to another and thereby, successively, increasing organizational complexity[89]. As discussed above, pattern formation is typically studied by means of a linear stability analysis, in which the reaction-diffusion dynamics is linearly expanded around the considered homogeneous steady state. However after the onset of the pattern formation instability, non-linear effects can dominate the subsequent dynamics. Secondary instabilities of the evolving patterns can lead to pulsations, or fingering instabilities of interfaces (equivalent to a Mullins-Serkerka instability[110,111]) in which the interfaces begin to undulate and break open[112–114]. For instance, depending on curvature and width of pulses, wave instabilities occur in the Belousov-Zhabotinski reaction[115,116] which lead to the propagation of unstable wave segments[117]. The developing nonlinear wave solutions can form stationary or propagating waves with varying shapes. Wave trains exhibit anomalous dispersion relations where the interaction of different peaks in the solution influences the collective's propagation velocity[118,119]. Reaction-diffusion waves show nonlinear properties like pining at obstacles[120] or depinning through wave-wave interactions[121].

In addition to secondary instabilities, temporal variations in system parameters can drive the dynamic evolution of patterns. For example, aging effects in chemical reactions can lead to a temporal drift in the observed oscillation periods[122]. Changes in reaction conditions that trigger transitions in observed patterns can also be caused by geometric factors. Externally induced cell deformations have been shown to affect internal protein pattern dynamics, as demonstrated in in vitro experiments on Min protein oscillations within chemical reactors of varying shapes[21]. Similarly, dynamic surface

[1] For example, in a two-component system with conservation law $m + c = \text{const}$, nullclines $f(m, c) = 0$ and $g(m, c) = 0$ collapse into a single constraint, $g(m, c) = -f(m, c) = 0$.

contraction waves in starfish oocytes have been found to significantly alter the behavior of enclosed protein concentration patterns[5,52].

These higher-order effects often produce patterns and dynamics that deviate from the initially predicted length scales emerging from a homogeneous state. Therefore, a detailed analysis of potential long-term dynamics is essential to connect the onset of pattern formation to the system's actual temporal behavior.

Another generic mechanism that leads to a dynamic change of pattern length scales in many reaction-diffusion systems is coarsening. As for Ostwald ripening of binary mixtures in thermodynamic equilibrium, coarsening also appears in reaction-diffusion systems and especially with existing conservation laws[24,25,123–126]. For some of these systems, the conserved equations can be reexpressed in terms of relaxational dynamics with an effective free energy Lyapunov functional[127–129]. Therefore, these systems relax to a minimum of an effective free energy by coarsening and the pattern length scales successively grow until they reach system size. However, it has been reported that coarsening can be interrupted for instance by weakly breaking mass-conservation[24,25] or through spatial parameter heterogeneities in the reactive domain[130]. We will show in chapters 2 and 3 how geometric deformations of an enclosing confinement and mechanical coupling to a deformable membrane can yield interrupted coarsening. Developing an analytic description for the coarsening dynamics beyond the onset of pattern formation, we can derive predictions for geometrically or mechanically controlled pattern length scale selection.

CONFINED BULK-BOUNDARY SYSTEMS

As apparent from the above examples, many pattern-forming systems are confined to spatially restricted geometries. For example, intracellular proteins are confined within the cell body being either dissolved within the cytosol or attached to the cellular membrane[51,131–133]. These proteins often exhibit interdependent dynamics driven by reactive interactions, such as protein attachment, detachment, or recruitment, which predominantly occur at the enclosing surface[134]. Consequently, the boundary plays a central role in the system's reaction dynamics, enabling an interplay between the geometry and biochemical processes.

The interaction between geometry and proteins can be explicit in form of a direct curvature sensing, whereby proteins with a specific intrinsic curvature preferentially attach to regions with similar curvature, locally altering attachment and detachment rates, and other reaction parameters[135–137]. This leads to spatially heterogeneous reaction conditions induced by a geometric deformation of the enclosing membrane. In turn, these proteins may induce membrane curvature changes to align the membrane shape with their intrinsic curvature, potentially creating a feedback loop between protein patterning and membrane deformation[137]. This cooperative mechanical feedback can even produce quasi-nonlocal mechanical coupling, as we will explore in Chapter 3. For instance, lipids phase separate in lipid rafts within membranes due to variations in their mechanical properties[34]. Similarly, BAR domain proteins induce anisotropic curvature and show preferential binding when attaching to lipid membranes. This direct geometric feedback mechanism yields an effective curvature sensing and a curvature mediated recruitment[138,139].

In the context of bulk-boundary systems, the protein DivIVA in *Bacillus subtilis* provides an example of direct curvature sensing. It preferentially binds to negatively curved membranes, diffusing through the cytosol and forming persistent aggregates at cell poles to prevent polar localization of the cellular division machinery[140,141].

Beyond such a direct sensing of surface curvature by preferential protein binding, the reactions driven at the membrane surface allow the system to indirectly probe geometry through the formation of collective patterns. For instance, Min protein patterns in elliptical geometries are influenced by the changing bulk-to-boundary ratios between center and polar positions. The patterns respond to such geometric differences through the cytosolic gradients that emerge via the reactive coupling at the enclosing boundaries. Thereby the system changes its exhibited behavior between long-axis and short-axis polarization depending on the length scale of these cytosolic gradients[142]. In a similar fashion long axis polarization is implemented by PAR proteins in *C. elegans*[18,143–145]. In another example, stable bipolar patterns of Min proteins in elliptical confinements demonstrate how surface

curvature is effectively sensed through cytosolic gradients[17]. In an in vitro setting, the Min protein system has been shown to develop stable self-organized oscillations along the long axis due to an effective geometry sensing on the pattern scale[146]. Additionally, wave-pinning mechanisms of Rho GTP concentration waves yield insights into the confining geometry through the bulk-boundary coupling process[147].

From a bottom-top theoretical perspective, extensive research has examined diffusive transport in spatially confined geometries. For spatially modulated confinements, such as channels or tubes, wider regions act as entropic barriers[148–150], requiring more time for particles to sample the domain and diffuse further. In tubular confinements, diffusion along the central axis can be described using a space-dependent diffusion coefficient, incorporating the effects of varying tube radii. The effective diffusion coefficient is given by the Lifson-Jackson equation[151]. The overarching Fick-Jacobs framework describes diffusion within spatially modulated tubes under the assumption that perpendicular concentration gradients equilibrate rapidly, enabling projection onto the central axis[152–154]. These techniques have been extended to study confined bulk reaction-diffusion systems, revealing the impact of spatial modulations on traveling wave behavior in channels[155,156] and tubes[157].

Recently, work on pattern formation on the surfaces of deformed cylinders yielded a pinning of emergent patterns at particular deformation sites and hinted towards a geometric selection of emergent pattern lengths. For cylinders with spatially modulated surfaces, the authors applied a conformal mapping approach to solve the linear dispersion relation of the forming patterns on the modulated geometries[23]. Regarding pattern formation in a bulk volume, confined by modulated geometries, authors in Ref.[22] performed a linear stability analysis for particular examples where analytical solutions to the reduced diffusion equation are known. Their study yields a geometric mode selection within the deformed domains.

Concerning the biologically relevant bulk-boundary systems, so far, effective one-dimensional descriptions have generally relied on ad hoc implementations of differing rates at the cellular poles, accounting for smaller bulk-to-surface ratios with heuristic adjustments[86]. Thus, theoretical descriptions of pattern formation in quasi-1D bulk-boundary systems, incorporating bulk and boundary diffusion with reactive interactions at deformed surfaces, remain incomplete.

In Chapter 2 of this work, we address the challenge of analytically describing confined reaction-diffusion systems with bulk-boundary coupling. We present a dimensional reduction approach to derive effective one-dimensional equations that capture the effects of geometric deformations in tubular confinements. By employing a direct parametrization and expanding for weak perturbations from an undeformed cylindrical shape, our framework provides a unified approach to studying bulk and boundary dynamics in a one-dimensional description. We investigate the influence of varying bulk-to-boundary ratios on pattern formation and demonstrate geometric control over pattern length scales and the geometric interruption of coarsening processes.

1.1.3 PATTERN FORMATION IN *Motile Active Matter*

In a broad definition, active matter represents systems that are driven out of equilibrium by active processes with energy insertion at the level of individual constituents[158]. In these systems the energy input at the microscale and its transfer from single constituent to larger structures drives collective self-organization[56]. In this thesis, we consider a subset of these systems by focusing on motile or (self)-propelled active matter. Here the induced energy at the level of individual agents translates into an active motion of the agents that is distinguishable from random Brownian dynamics. This active motion can be produced by the individual agents themselves, like the crawling motion of cells[54,55] or as seen in the active motion of chemical Janus particles[159]. The energy can also be supplied by mechanical excitation on the individual agent level. For instance, vibrated granular rods exhibit coarsening dynamics driven by effective attraction through their shape anisotropy and develop vortex type of motion in confinements[160–162]. An external generation of motion occurs also in the actin motility assay, which constitutes an experimental setting for studying emergent behavior in filamentous active matter. Within this setup, actin filaments show motion induced by interactions with active motor proteins that are fixed on a cover lip, yielding an actively driven behavior of the

filaments[163,164].

Key aspects of active matter are the propulsion via internal mechanisms such as auto-motility or motion via active interactions among agents. Self-propulsion of agents necessitates also a direction of agents in which they move. This could be along gradients in an external field as in the Keller-Segel model for chemotactic active matter[165]. In many other cases, the agents are directly equipped with an internal degree of freedom determining their intrinsic direction of motion. Often, the alignment of these orientations plays a crucial role in active matter systems[166]. One typically distinguishes polar and nematic active agents. Polar agents have an orientation with a direction in space, whereas nematic agents only have an orientation, but don't break the forward/backward invariance on the orientation line. Also the alignment of agents with the direction of their neighbors can be polar or nematic in nature. For instance there can be different ranges of angles between the orientations of two colliding agents that either lead to a nematic or a polar alignment. The coexistence of ranges for both polar and nematic alignment between actin filaments in the actin motility assay has shown to bring forward also a coexistence of spatially separated polar and nematic order[164].

Examples of self-propelled active matter systems cover a large range of scales. Active matter descriptions are applied to the collective motility of cells such as bacteria[55] or social amoeba[43,45]. The description of these systems by methods in the active matter field, yield an understanding of their chemotactic motion[165,167,168] and collective behavior[5545]. But the framework of active matter is not restricted to such microscopic systems. Equivalent descriptions can be applied for motion and collective behavior of animals also on larger scales with different applicability and necessary assumptions and approximations. The framework of active matter yields insights into collective organization processes underlying the behavior of social insects such as ants[169], the flocking and murmuration behavior of birds[170], the swarming and predator-response of schools of fish[171,172].

In all these systems, the formalism of propelled active matter is applied to investigate the collective emergent behavior. Based on detailed studies of the individual dynamics, one typically tries to infer and explore the emergent behavior using experimental observation or numerical simulations.

In the field of self-propelling active matter one distinguishes wet and dry systems[53,173]. Dry active matter describes systems in the overdamped limit. All momenta are transferred into a substrate and effective motion of agents is overdamped. In contrast 'wet' active matter considers the case in which agents exhibit a momentum. It is called 'wet' because their treatment requires the incorporation of a medium that transfers momenta between agents over a flow field which results in hydrodynamic interactions between active swimmers[174,175]. Focusing on aspects such as general organization and long-range communication between active agents, we in this thesis will focus on the overdamped dry active matter.

Potentially one of the field founding events was the observation of flocking birds which led to the question of what are the minimal ingredients necessary to obtain such a behavior? The celebrated Vicsek model[166], describing Langevin dynamics of individual self-propelled agents with a persistent direction of motion and polar alignment with neighboring agents, showed a non-equilibrium phase transition. For sufficiently strong interactions, agents align into a polar flock formation. Corresponding phenomenological field equations yielded the theoretical insights into the transition between the isotropic and the polar flocking state[176]. The system is found to exhibit true long-range order in a two-dimensional system, breaking the Mermin-Wagner theorem, valid for systems in thermodynamic equilibrium and thereby highlighting the active nature of the system's alignment interactions[177].

Another, emergent phenomenon that arises in persistently self-propelled particles with steric repulsion, may appear counterintuitive on first thought. With repulsion alone as the only interaction between agents that perform persistent random walks, one observes an effective attraction and cluster formation[178–180]. When two agents collide, they cannot immediately escape the collision area due to the persistence in their orientation, which only slowly changes. Before the agents change their direction due to the random fluctuations and can escape the head-to-head collision, other agents collide and block the route to escape. This can successively lead to large-scale collective cluster formation. Certainly, the occurrence of this phenomenon depends on the overall agent density and the rate of stochastic reorientation. This effect reminiscent of aggregation at boundaries[181–183] is called motility induced phase-separation. Initially, it was theoretically predicted on the basis of

hydrodynamic field equations for a density of active Brownian particles with density-dependent velocity[178], and soon also observed in various agent-based numerical simulations that include steric repulsion[179,180,184–186].

DESCRIBING ACTIVE MATTER

For active matter systems, there are various ways of description. Just like describing the motion of each particle, e.g., in molecular dynamics simulation for reaction-diffusion systems, a possible way are agent-based simulations. Here one considers the dynamics of the individual active agents and formulates them on the basis of Langevin equations by putting in microscopic rules for agent behavior and agent-agents interactions. Such rules potentially include the agent's motility and dynamic spatial orientation, orientational- or positional noise, and steric repulsion interactions, among others. Depending on the complexity of these interactions, this approach already makes a numerical study of significantly large systems feasible.

However, on the scale of emergent collective structures, order parameters are typically used to describe the mesoscale organization of the system. For instance, the agent density is such an order parameter. Averaging over local distributions of agents, it transfers information about the individual agents' positions into a mesoscale continuous quantity. In a similar way, one can define order parameters for the degree of polar alignment between agents or a nematic tensor, that identifies the local average orientation in space and the degree of alignment of agents within this direction.

Thus, beyond agent-based models, hydrodynamic field equations offer a description of self-propelling active matter directly at the level of the order parameters. There are field theories which work on the level of scalar active matter, describing the dynamics of the agent density supplemented by different dynamics such as chemotaxis[165] or density-dependent velocities[178]. These models, can be seen as out of equilibrium extensions to classical phase-separating systems[187].

The continuous hydrodynamic models can be motivated from symmetry considerations[188,189] including conservation laws. For instance Toner and Tu used a phenomenological model to describe the isotropic to polar flocking transition in Ref.[176]. Even though phenomenological equations allow for reproduction of behavior observed in various experimental or agent-based numerical studies[188,190], they don't enable a mapping between the phenomenological and the underlying microscopic parameters. A general mapping between microscopic interactions and continuous 'hydrodynamic' field equations can be involved. There are various approaches which have been developed mainly over the last decade[191–193]. The overall idea is, to start from the microscopic behavior of individual agents and apply a coarse graining scheme, to finally arrive at continuous field equations for the order parameters.

There are approaches on the basis of Fokker-Planck Equations[194] or others that try to include multi-agent collisions to account for dynamics within high density phases[195]. Others, that base on a Smoluchowski equation[196] include interactions in form of physical potentials but thereby do not yield the dependencies between the microscopic and hydrodynamic parameters and require phenomenological stabilizing terms[197].

In this work, we focus on the Boltzmann-Ginzburg-Landau framework for deriving hydrodynamic field equations from the microscopic dynamics of agents[191,198–200]. The starting point is a Boltzmann equation for the state probability density, which includes the agent interactions through transition probabilities between densities of different states. Assuming molecular chaos and low agent densities, the state probability density is expanded into Fourier modes of the spatial orientation. This procedure generates a hierarchy of coupled equations for the Fourier moments. Importantly, this hierarchy involves couplings to higher-order moments, including two- or multi-moment interactions which necessitates a suitable closure scheme. The Boltzmann-Ginzburg-Landau framework has proven effective in describing various systems, including the behavior of inelastically aligning microtubule assemblies[198,201,202] and the dynamics of actin filaments in motility assays[203].

In chapter 4, we derive hydrodynamic field equations for chemically communicating polar active matter on the basis of such a Boltzmann approach. In chapter 5, we use similar equations with phenomenological parameters for the description of polar active matter with acoustic interactions.

1.2 NON-LOCAL COUPLING

In the case of Turing instabilities, we observed that coupling dynamics across different length scales can lead to instabilities that drive pattern formation in a system. This highlights a fundamental principle: introducing additional couplings or degrees of freedom can unlock new emergent phenomena. Here, we explore two biologically and technologically relevant systems that exhibit increased complexity and richness when non-local interactions are incorporated.

Through non-local coupling, the individual elements of the systems gain access to information from distant positions, extending interactions beyond immediate neighbors. This qualitatively novel aspect can give rise to emergent phenomena, such as long-range correlations, synchronized behavior, or self-organized patterns that are not present in systems with purely local interactions.

The types of non-local coupling explored in this thesis are twofold. In the first part, we focus on geometric coupling. We begin by considering bulk-boundary reaction-diffusion dynamics in static geometric confinements, which introduce a spatial heterogeneity in the system. While this does not represent a dynamic non-local coupling, it addresses important geometric aspects for confined cellular pattern formation and lays the groundwork for Chapter 3. There, we will investigate geometric coupling that arises dynamically through membrane deformations, in interplay with phase-separating protein dynamics. By reducing the pattern-forming mechanism to demixing dynamics, we are able to isolate the role of mechanical coupling for patterning in the system. As we will demonstrate, these dynamic geometric deformations generate an effective non-local mechanical coupling within the system.

In chapters 4 and 5 we will discuss a very different type of non-local coupling. Namely, large distance communication in active matter systems. Also for these systems the non-local interactions will give access to information about distant parts of the domain and thereby yield qualitatively new, emergent phenomena.

1.2.1 GEOMETRIC AND MECHANICAL COUPLING

Geometry and mechanical coupling play a fundamental role in biological pattern formation. Geometric confinement, such as the cell membranes, can impose spatial heterogeneities that influence the distribution and dynamics of chemical species, leading to the emergence of complex geometrically controlled patterns. Additionally, mechanical deformations, such as protein-induced changes in membrane shapes, can dynamically couple to the pattern-forming reaction-diffusion processes, creating a feedback between geometry and chemical dynamics. Investigating these effects provides key insights into how patterns form and adapt in confined, living systems and, in turn, yield potential principles for designing synthetic cells.

Of particular relevance for intracellular pattern formation are protein reaction networks that incorporate bulk dissolved and boundary-bound species. The nonlinear reaction kinetics at the deformed surface enables the systems to sense geometric properties such as local bulk-boundary ratios and changes in available reactive bulk volume and surface are. Therefore, bulk-boundary systems are a class of reaction-diffusion equations that is particularly amenable to geometric deformations.

In the first part of this thesis, Chapter 2, we consider the coupling of a bulk-boundary protein system to a static external modulation of an enclosing cylindrical geometry. The pattern forming system is confined to this tubular domain while surface species and bulk species interact via reactions on the surface. The externally imposed geometric deformation introduces a positional information in the system as it causes a parameter variation over the domain and thereby breaks translational symmetry. This broken symmetry, gives rise to a geometric pattern selection in the system. We present an approach to introduce a geometric context into one-dimensional reaction-diffusion models, which extends the applicability of such models to bulk-boundary systems with spatial modulations of the enclosing confinement. Within this framework, we can predict the evolving patterns with a very good agreement to numerical simulations.
Finally, we investigate the long-time dynamics of the system. In particular, we will find that geometric deformations can induce forces on the interfaces that counteract the coarsening dynamics that would arise in the system without geometric modulation. We can predict necessary modulations for

arrested coarsening at different length scales.

In Chapter 3, we discuss a minimal model for mechanical coupling of a phase-separating system with geometric deformations. In particular, we study a system of proteins embedded into a two-dimensional deformable manifold. The latter is characterized by a Canham-Helfrich free energy with preferred curvature that is induced by the presence of one species of the demixing system. We find that the geometric deformations implement an effective non-local coupling between the phase-separating protein densities. This leads to a stabilization of patterns with finite wavelength in the system.

Both these studies investigate the impact of geometric confinements and mechanical coupling on pattern forming systems. We identify that geometric deformations can induce a non-local coupling between pattern forming species. We find, that simple forms of non-local information in the system, be it through an externally induced break of translational symmetry or through self-organized mechanical coupling via modulated membrane surfaces, give rise to geometrically controlled pattern length scales and a selection of final steady states.

1.2.2 LONG-RANGE COMMUNICATION

In active matter systems, steric repulsion and alignment due to shape anisotropies of agents implements a local form of interactions. Agents directly respond to their neighbors by physical cues. As such, actin filaments in motility assays align with each other for avoiding overlap[163] and active Brownian particles which experience steric repulsion form clusters via motility-induced phase-separation[180]. Thus, even on the basis of such local interactions, systems can develop large-scale collective structures. If these structures are dense aggregates, they can even achieve a form of large-distance information transfer, where information is propagated through fast/physical subsequent nearest neighbor interactions, forming a continuous force chain[204]. However this is limited to dense packing of agents as it requires direct adjacency between interacting agents for information transfer.

In the second part of this thesis we ask for the general principles of long-scale communication. How can agents achieve efficient information transfer and collectively employ the gathered information in terms of collective decision-making.

In general, introducing non-local interactions has been shown to make the system more responsive to external stimuli and to enable it to self-organize over larger ranges[205,206]. For instance, swarming active matter with a long-ranging visual coupling between agents yields potentially non-reciprocal interactions and rich phenomenology[207,208].

Inspired by its relevance for biological systems such as for bacterial navigation and slime mold aggregation, there are various studies on chemically interacting active matter[209] starting from the original studies of Patlak[210] and Keller and Segel[165,167]. For instance, cyclic AMP signaling plays an important role for fruiting body formation in Dictyostelium cells[45,211,212]. Upon starvation, the cells emit chemical signals into their surrounding where they diffuse and transmit information to distant cells[43,213]. Similarly, ants and other social insects apply chemical signaling, leaving trails of pheromones behind, that give information about beneficial paths and potential food sources and warning for threats[214,215]. Here, ants perceive very local information about pheromone levels, however an effective long-scale communication arises through a history of information given by persistent pheromone traces in the environment. Combined with the active motion of the ants, this translates into a type of long-scale interaction. A chemical field can represent a distributed memory of the collective. The time scale of that memory is determined by the inverse pheromone decay rate and diffusive spread.

Chemical communication has been explored in various experimental systems[216]. For instance, chemical interactions can help to optimize the collective behavior of self-propelled Janus particles[217] or facilitate emergent, chemically controlled oscillations in colloidal systems, that regulate collective self-assembly and dispersal[218]. In other experiments, self-propelled autochemotactic droplets exhibit avoidance of their previous trajectories, as they leave persistent chemorepellent traces in the environment. These lasting chemical cues can even result in the active droplets becoming trapped within

their own paths[219]. Chemically activated colloidal Janus particles exhibit dynamic aggregate formation[220] and an agent density-depending dynamic switching between large and small clusters. Thus, the agents can employ changes in the chemical field to perceive densities and cluster sizes[221]. Most of these systems involve a localized diffusive spreading of chemical signals and thereby implement a local organization of the collective behavior.

In contrast, in Chapter 4, we introduce a non-linear chemical signal relaying mechanism which will lead to a distant spreading of chemical waves and thereby transport signals to other positions. In particular, we consider a system of self-propelled active agents that are equipped with a Schmitt-trigger-like internal dynamics. Upon encountering a chemical signal with significant strength, above a given threshold, agents actively relay the signal by also emitting chemical molecules into their surrounding. In turn, information propagates not diffusively, but is actively relayed as a nonlinear trigger wave by the present agents. Given this functionality, the system exhibits a rich organization into a variety of collective structures. Thereby, we show that the aggregation process occurs by employing a hierarchy of different states.

Having established the role of non-local coupling for the self-organization process in chemically communicating active matter, we will turn our focus towards what type of emergent functionality can arise through a non-local coupling.

A step in this direction are swarmalator models for chiral active matter[222]. Here, the agents exhibit a persistent rotation while self-propelling. The rotational motion of agents is coupled to the rotation of others. Thereby, the agents can synchronize these oscillators, typically via intermediate ad-hoc synchronization rules. This resembles a version of the celebrated Kuramoto model for interacting and synchronizing oscillators, with variable interaction partners due to the varying spatial distances induced by the agent's/oscillator's motion. Swarmalator models with local or global coupling between the agents, for instance, show aggregation into vortex clusters and rings[222,223]. Similar behavior could be reconstructed in collectives of oscillating chiral active agents, called Weasle balls[224]. In contrast to the theoretical models, here the mutual synchronization is mediated by steric effects between the active spheres and their circular two-dimensional confinement. In current swarmalator models, the intrinsic oscillators of the agents are directly coupled to their chiral motion, preventing them from serving as independent degrees of freedom that can explicitly facilitate communication. We aim to explore an alternative approach that incorporates synchronization between the agents' intrinsic degrees of freedom into their collective dynamics. The interactions of oscillators and the motion of agents will be interlinked through bi-directional feedback but remain distinct properties, allowing the agents to communicate information that is not identical to their motility behavior. In chapter 5, we discuss a system of self-propelled active agents that have an oscillatory state as an internal degree of freedom. Representing the state of an oscillator that emits acoustic waves into the surrounding, the agents can synchronize and perceive states from others via acoustic coupling.

In this study, we go beyond existing models by equipping active agents with internal states that possess intrinsic traits while also being influenced by mutual coupling, mediated through a collectively established chemical or acoustic field. This enables the communication of information that is distinct from, and additional to, the agents' self-propulsion dynamics.

2

Geometric control of protein pattern formation in bulk-boundary systems

This chapter comprises contents of a manuscript, currently in preparation[1]
Detailed contribution information on pages XI-XII.

We present a reduction approach to capture geometric effects on confined reaction-diffusion systems with bulk-boundary coupling. Our approach yields an effective one-dimensional reaction-diffusion-advection equation that incorporates the influence of spatio-temporally modulated boundaries in a rotationally symmetric cylindrical geometry. This reduction enables the use of various analytical tools, such as phase-space analysis, to study mass-conserving reaction-diffusion systems. Through this analysis, we identify an instability condition whereby spatial boundary modulations can either induce or suppress pattern formation. Using a perturbative linear stability analysis that includes these geometric deformations, we predict conditions for length-scale selection and pattern localization based on boundary geometry. Additionally, we apply the reduced model to examine how geometry can interrupt coarsening. Our findings show that interface minimization within deformed geometries acts as a primary driver behind coarsening interruption. This work deepens our understanding of geometrically controlled pattern formation in confined geometries, with particular relevance for intracellular protein systems. Our framework also provides an analytic approach for studying mechano-chemical coupling in general quasi-one-dimensional bulk-boundary systems.

2.1 INTRODUCTION

Pattern formation in biological and chemical systems represents a fundamental self-organization mechanism to induce an initial symmetry breaking of biochemical species. This symmetry breaking underlies various subsequent organization processes, including cell division, polarization, and specification[9–12].

Various experimental and numerical studies have demonstrated the importance of mechano-chemical coupling[2,34,137,225–227] and geometric modulations in controlling confined pattern formation[18,19,86]. For instance, the Min protein system exhibits externally controllable reaction patterns driven by varying geometry[228], and elliptic reaction domains can induce different stable bi-polar patterns as in *E. coli* cells, not observed in planar geometries[17].

In cellular systems, membranes naturally provide spatial confinement by enclosing the cytosolic bulk volume, serving as reactive interfaces where protein attachment, detachment, or recruitment processes occur[6–8]. These non-trivial boundary interactions enrich the influence of geometric modulation on confined pattern formation.

Despite their inherently two- or three-dimensional nature, many confined pattern-forming systems exhibit length-scale separation, where the dynamics predominantly occurs along a single spatial dimension[87,228]. This reduction in dimensionality provides an opportunity for analytical modeling. Given the biological significance of protein systems with bulk-boundary coupling and the pronounced effects of geometric confinement on pattern dynamics[120,229–231], we aim to derive an analytically tractable theoretical model for describing and predicting these geometric effects. To this end, we extend approaches for confined bulk diffusion systems[22,151,157,232–235] by deriving a one-dimensional reduction of reaction-diffusion (RD) systems with bulk-boundary coupling at a spatio-temporally modulated membrane boundary (Fig. 2.1). By integrating out the cytosolic bulk volume, we develop a framework for a reduced description of bulk-boundary systems with spatiotemporal domain modulations which extends beyond existing models on spatially modulated tubular surfaces[22,23]. This framework allows us to study geometry-controlled pattern formation using established analytical tools such as linear stability analysis[89], geometric phase-space analysis for mass-conserving systems[88,94], and singular perturbation theory[155,236]. Applying these techniques to generic two-component mass-conserving reaction-diffusion models, we predict geometrically controlled pattern formation, derive criteria for length scale selection and pattern localization, and establish conditions for geometrically interrupted coarsening. These predictions are validated against full three-dimensional numerical simulations of the deformed bulk-boundary system.

The presented theory systematically incorporates geometric effects into one-dimensional RD models, moving beyond previous ad-hoc effective formulations, e.g., using space-dependent rates[86]. Our approach, therefore, provides an analytically accessible theory that applies to a range of biological and chemical systems, such as intracellular communication via membrane tunneling nanotubes[237,238], mechano-chemical feedback in vein networks of *Physarum polycephalum*[239,240], and

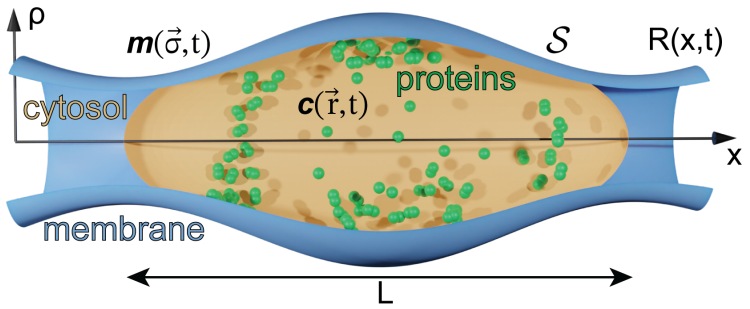

Figure 2.1: Schematic of a system of cytosol (orange) $\boldsymbol{c}(\vec{r},t)$ and membrane (blue) species $\boldsymbol{m}(\vec{\sigma},t)$, Eq. (2.1), of proteins (green) in a rotationally symmetric tube with spatially varying radius $R(x,t)$. The interaction of both species can be described via reactive boundary conditions, Eq. (2.2), at the modulated membrane $\mathcal{S}$, which is given as a two-dimensional surface in $\mathbb{R}^3$; $\psi : U \to \mathcal{S} \subset \mathbb{R}^3$ with parametric coordinates $\vec{\sigma} \in U \subset \mathbb{R}^2$.

polar pattern formation in elongated cells[146,241].

Our analysis reveals that spatially varying bulk-boundary ratios and interface minimization are key mechanisms driving geometric pattern selection and localization. We find that the diffusive interface minimization is also the driving mechanism behind geometrically interrupted coarsening. Together, our results suggest that these principles represent general mechanisms governing the pattern formation of confined bulk-boundary reaction-diffusion systems. These principles are therefore likely to be broadly relevant across diverse biological and chemical systems.

The paper is organized as follows; after stating the considered setup of coupled bulk-boundary systems in spatially varying confinement in section 2.2, in section 2.3, we outline the derivation of the reduced one-dimensional reaction-diffusion description. In section 2.4, we make use of the one-dimensional reduction of the system to gain insights into geometrically controlled pattern formation by applying a phase-space analysis of a generic two-component mass-conserving reaction-diffusion system. In section 2.5, we go beyond this initial analysis and derive predictions for geometrically controlled pattern and length-scale selection through interrupted coarsening and compare them with results of 1d and full 3d numerical simulations.

2.2 CONFINED BULK-BOUNDARY SYSTEMS

To model confined reaction networks with bulk-boundary coupling (Fig. 2.2), we consider a general class of coupled reaction-diffusion equations

$$\partial_t \boldsymbol{m}\,(\vec{\sigma},t) = D_{\mathrm{m}}\Delta_{\mathrm{m}}\boldsymbol{m} + \boldsymbol{f}_{\mathrm{m}}(\boldsymbol{m}) + \boldsymbol{f}_{\mathrm{mc}}(\boldsymbol{m},\boldsymbol{c}|_{\mathcal{S}})\,, \tag{2.1a}$$

$$\partial_t \boldsymbol{c}(\vec{r},t) = D_{\mathrm{c}}\Delta_{\mathrm{c}}\boldsymbol{c} + \boldsymbol{f}_{\mathrm{c}}(\boldsymbol{c})\,. \tag{2.1b}$$

Throughout this work, we adopt the terminology of biochemical reaction-diffusion systems, although the proposed approach is applicable to a broader class of systems. Specifically, we denote by $\boldsymbol{m}(\vec{\sigma},t) \in \mathbb{R}^p$ and $\boldsymbol{c}(\vec{r},t) \in \mathbb{R}^n$ the surface ($\vec{\sigma} \in U \subset \mathbb{R}^2$) and volume ($\vec{r} \in \mathbb{R}^3$) concentrations of the p membrane and n cytosolic protein species, respectively; see Fig. 2.1. For simplicity, we assume that diffusion constants only depend on whether proteins diffuse on the membrane or in the cytosol, but are otherwise the same. We distinguish between chemical reactions that exclusively involve membrane-bound and cytosolic proteins ($\boldsymbol{f}_m(\boldsymbol{m})$ and $\boldsymbol{f}_{\mathrm{c}}(\boldsymbol{c})$), or both of them ($\boldsymbol{f}_{\mathrm{mc}}(\boldsymbol{m},\boldsymbol{c}|_{\mathcal{S}})$); the latter may include protein attachment to and detachment from the membrane as well as protein membrane recruitment. Consequently, these reactions depend on the cytosolic protein concentrations adjacent to the membrane $\mathcal{S}$[80]. The reaction-diffusion equations are supplemented by reactive boundary conditions for the cytosolic species,

$$D_{\mathrm{c}}\,(\vec{n}\cdot\nabla)\;\boldsymbol{c}|_{\mathcal{S}} = \boldsymbol{g}\,(\boldsymbol{m},\boldsymbol{c}|_{\mathcal{S}})\,, \tag{2.2}$$

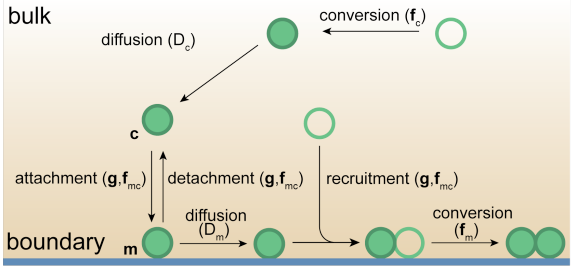

Figure 2.2: Exemplary reaction scheme with generic interactions for bulk-boundary protein systems. Besides bulk and boundary diffusion (D_c, D_m), species can occur either dissolved in the bulk ($\boldsymbol{c}$) or bound to the boundary ($\boldsymbol{m}$). They can undergo distinct reaction kinetics within the bulk ($\boldsymbol{f}_c$), and at the boundary ($\boldsymbol{f}_m$, $\boldsymbol{f}_{mc}$) involving reactive boundary conditions ($\boldsymbol{g}$, Eq. (2.2)) for the bulk species.

with outward pointing surface normal unit vector $\vec{n}$ at the enclosing boundary $\mathcal{S}$. The quantity $\boldsymbol{g}(\boldsymbol{m}, \boldsymbol{c}|_{\mathcal{S}})$ represents the reactive boundary contributions to the cytosolic species associated with the membrane term $\boldsymbol{f}_{\mathrm{mc}}$.

As shown in Fig. 2.2, proteins can either be dissolved in the cytosol (bulk) or bound to the membrane (boundary). Within the cytosol and on the membrane, they show diffusive dynamics with respective diffusion coefficients D_c and D_m. Here, to illustrate the basic principles, we exemplify some generic protein interactions that can be captured by the reaction-diffusion equations, Eqs. (2.1), and the boundary condition, Eq. (2.2). Note, however, that the scope of the model encompasses a wide range of systems beyond these specific cases; for a more realistic set of interactions, we refer the reader to Refs.[18,31,80,88,93,95,97,99,242]. For example, proteins within the bulk may undergo state conversions, such as ATP hydrolysis, which are incorporated into the bulk reaction dynamics $\boldsymbol{f}_c(\boldsymbol{c})$. To illustrate this interaction in a representative scenario with two bulk species ($n = 2$), the bulk reactive contributions could take the form

$$\partial_t \begin{pmatrix} c_1 \\ c_2 \end{pmatrix} = D_c \Delta_c \begin{pmatrix} c_1 \\ c_2 \end{pmatrix} + \begin{pmatrix} \lambda c_2 \\ -\lambda c_2 \end{pmatrix} , \tag{2.3}$$

for a linear conversion from species c_2 to c_1. Importantly, a significant part of the reactive interactions typically occurs on the membrane. For instance, attachment, detachment, and recruitment of proteins contributes both to the reactive term $\boldsymbol{f}_{mc}$ and the reactive boundary condition $\boldsymbol{g}$. Exemplarily, attachment with rate k_{attach} and auto-recruitment with rate k_{recruit} of a single species $p = n = 1$ from the bulk (c) to the boundary (m) would yield

$$\boldsymbol{f}_{mc}\left(m, c|_{\mathcal{S}}\right) = \left(k_{\text{attach}} + k_{\text{recruit}} m\right) c|_{\mathcal{S}} , \tag{2.4}$$

and the corresponding reactive boundary condition for the bulk species

$$\boldsymbol{g}\left(m, c|_{\mathcal{S}}\right) = -\left(k_{\text{attach}} + k_{\text{recruit}} m\right) c|_{\mathcal{S}} , \tag{2.5}$$

that preserves total mass-conservation, $n = c + m$. The reactive contribution $\boldsymbol{g}$ represents the impact of the reactions $\boldsymbol{f}_{mc}$ at the boundary on the bulk species as mediated through the reactive boundary conditions. Finally, the reaction-diffusion equations, Eqs. (2.1), consider reaction kinetics ($\boldsymbol{f}_m(\boldsymbol{m})$) that only involve membrane-bound species. As such, a local conversion of one species into another boundary species (e.g., m_1 into m_2) would give the contributions

$$\boldsymbol{f}_m\left(\boldsymbol{m}\right) = \begin{pmatrix} -m_1 \\ m_1 \end{pmatrix} , \tag{2.6}$$

and have no further effect on the bulk reactive boundary conditions. As a final note, it is important to highlight that the reactive boundary conditions inherently generate bulk concentration gradients perpendicular to the boundary. These boundary conditions encode that the chemical reactions link-

ing membrane and cytosolic proteins act as localized sinks or sources at the membrane, driving changes in concentration. Through diffusive transport into the bulk, this generates concentration gradients that extend into the bulk over a characteristic length scale $\ell_c \sim \sqrt{D_c \tau}$ [88]. Here τ denotes the timescale of the reaction process at the boundary, e.g., attachment, $\tau = 1/k_{\text{attach}}$, Eq. (2.5), and D_c is the species' bulk diffusion constant. If this length scale ℓ_c is small compared to the bulk's extend perpendicular to the boundary, the variations in bulk concentrations with increasing distance to the boundary can significantly influence the dynamics of the reaction-diffusion system.

2.3 DIMENSIONAL REDUCTION

In the following, we consider a tube-like membrane with a spatially modulated and time-dependent radius $R(x,t)$ of finite length L, as illustrated in Fig. 2.1. Using cylindrical coordinates with $\vec{r} = (x, \rho\cos\phi, \rho\sin\phi)^T$, the boundary $\mathcal{S}$ (membrane) is given by a surface of revolution which can parametrically be written as

$$\vec{r}(x,\phi) = (x, R(x,t)\cos\phi, R(x,t)\sin\phi)\,. \tag{2.7}$$

In cylindrical geometry, the reaction-diffusion equation of the cytosolic protein density, Eq. (2.1b), reads

$$\partial_t \boldsymbol{c} = D_\mathrm{c}\left(\frac{1}{\rho}\partial_\rho\left(\rho\,\partial_\rho \boldsymbol{c}\right) + \frac{1}{\rho^2}\partial_\phi^2 \boldsymbol{c} + \partial_x^2 \boldsymbol{c}\right) + \boldsymbol{f}_c(\boldsymbol{c})\,. \tag{2.8}$$

The outward-pointing surface normal vector of the boundary $\mathcal{S}$ is given by,

$$\vec{n} = \frac{1}{\gamma}\left(\vec{e}_\rho - R'(x,t)\,\vec{e}_x\right), \tag{2.9}$$

where $\vec{e}_\rho$ and $\vec{e}_x$ are unit vectors in radial direction and along the cylinder axis, respectively (Fig. 2.3), and a prime denotes the derivative with respect to the center line coordinate x. Here, $\gamma = \sqrt{1+R'^2}$ is the local dilation factor of a meridian, i.e., a line on the surface aligned with the centerline direction. Using this, the boundary condition, Eq. (2.2), can be rewritten as

$$D_\mathrm{c}\left(\partial_\rho - R'\partial_x\right)\boldsymbol{c}|_{\mathcal{S}} = \gamma\,\boldsymbol{g}(\boldsymbol{m}, \boldsymbol{c}|_{\mathcal{S}})\,. \tag{2.10}$$

We start the derivation of the dimensionally reduced equations from the integral form of the reaction-diffusion equation for the bulk species $\boldsymbol{c}$,

$$\frac{\mathrm{d}}{\mathrm{d}t}\int_V \mathrm{d}V\,\boldsymbol{c}(\vec{r},t) = D_\mathrm{c}\int_{\partial V}\mathrm{d}S\,\vec{n}\cdot\nabla\boldsymbol{c} + \int_V \mathrm{d}V\,\boldsymbol{f}_c\,. \tag{2.11}$$

This equation states that changes in the particle numbers of each individual bulk component within a volume V are either due to particle fluxes through the boundary ∂V with surface element $\vec{n}\,\mathrm{d}S$ or due to reactions within the bulk V. Now, consider a thin slice of the modulated cylinder as integration volume V, bounded by the membrane surface $\partial V|_{\mathcal{S}}$ and two parallel discs $\mathcal{F}_x$ and $\mathcal{F}_{x+\Delta x}$ that are perpendicular to the cylinder axis and separated by an (infinitesimal) distance Δx apart (Fig. 2.3); a disc at x_0 is defined by

$$\mathcal{F}_{x_0} = \left\{\vec{r}\,\middle|\, x = x_0,\ \rho\in[0, R(x_0,t)],\ \phi\in[0,2\pi)\right\}. \tag{2.12}$$

For the following analysis, we assume that cytosolic diffusion is sufficiently fast such that the resulting cytosolic diffusion length ℓ_c is much larger than the lateral extension of the system, i.e., the radius of the cylinder: $\ell_\mathrm{c} \sim \sqrt{D_\mathrm{c}\tau} \gg R(x,t)$; here τ denotes some characteristic time of the chemical reactions. Under this condition, crucial for the dimensional reduction, the bulk density can be considered spatially uniform perpendicular to the cylinder's center axis, implying rotational symmetry

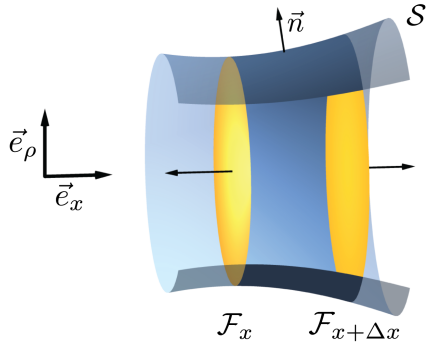

Figure 2.3: Schematic of a bulk section confined by a spatially varying tubular membrane surface $\mathcal{S}$, Eq. (2.7), (blue) with outward-pointing surface normal vector $\vec{n}$, Eq. (2.9), and two parallel discs perpendicular to the cylindrical axis (yellow) separated by a distance Δx.

and the absence of gradients in the radial direction: $c(\vec{r},t) \equiv c(x,t)$. This allows us to express the left-hand side of Eq. (2.11) as

$$\frac{\mathrm{d}}{\mathrm{d}t}\int_V \mathrm{d}V\, \boldsymbol{c}(\vec{r},t) \;= \partial_t\big(\pi R^2 \Delta x\, \boldsymbol{c}\big) = \pi R^2\, \Delta x\, \partial_t \boldsymbol{c} + 2\pi R\, \dot{R}\, \Delta x\, \boldsymbol{c}\,, \tag{2.13}$$

where a dot indicates the temporal derivative. There are two different contributions to the change in the bulk concentration: one due to temporal changes in the density and the other due to dynamic changes in the cross-sectional area. Next, we consider the boundary term, $\int_{\partial V} \mathrm{d}S\, \vec{n}\cdot\nabla \boldsymbol{c}$, which can be split into three contributions; one on the enclosing boundary $\mathcal{S}$ and two contributing at the parallel discs $\mathcal{F}_x$. Using the reactive boundary conditions, Eq. (2.10), the first contribution can be written as

$$D_\mathrm{c} \int_{\partial V|_\mathcal{S}} \mathrm{d}S\, \vec{n}\cdot\nabla \boldsymbol{c} = 2\pi R\,(\gamma\,\Delta x)\,\boldsymbol{g}\,, \tag{2.14}$$

where $\gamma\,\Delta x$ denotes the length of the infinitesimal boundary element of the curved surface. For the diffusive flux through a disk $\mathcal{F}_x$ in positive x-direction, we obtain

$$\int_{\partial V|_{\mathcal{F}_x}} \mathrm{d}F_x\, \vec{e}_x\cdot\nabla \boldsymbol{c} = \pi R^2(x)\, \partial_x \boldsymbol{c}(x,t)\,. \tag{2.15}$$

Subtracting the cytosolic fluxes through the two parallel discs at positions $x+\Delta x$ and x, and using the limit

$$\lim_{\Delta x\to 0} \frac{R^2\partial_x \boldsymbol{c}|_{x+\Delta x} - R^2\partial_x \boldsymbol{c}|_x}{\Delta x} = \partial_x\big(R^2\partial_x c\big)|_x\,, \tag{2.16}$$

one finds that the bulk flux difference (divided by Δx) can be written as the spatial derivative $\partial_x\big(D_\mathrm{c}\pi R^2\partial_x c\big)$. The latter expression is the gradient (along the cylinder axis) of the total diffusive flux $\pi R^2 D_\mathrm{c}\partial_x c$ through the area πR^2. Finally, the reactive contributions within the bulk volume read

$$\int_V \mathrm{d}V\, \boldsymbol{f}_c = \pi R^2 \Delta x\, \boldsymbol{f}_c\,. \tag{2.17}$$

Thus, collecting all the terms and dividing also the remainder by Δx, we obtain the reduced one-dimensional description

$$\partial_t(\pi R^2 \boldsymbol{c}) = D_\mathrm{c}\partial_x(\pi R^2\partial_x \boldsymbol{c}) + 2\pi R\gamma\, \boldsymbol{g} + \pi R^2\, \boldsymbol{f}_c\,, \tag{2.18}$$

which can be interpreted as follows: For each bulk component, the temporal change of the bulk line density, $\widetilde{c} = \pi R^2 \boldsymbol{c}$, is driven by the gradient of the total diffusive flux along the cylindrical axis (first term) [1], net particle exchange with the membrane (second term), and total reactions in the reactive volume (third term).

Similar to the protein line density in the cytosol, $\widetilde{c} = \pi R^2\, \boldsymbol{c}$, one can also define an analogous line density on the membrane, $\widetilde{\boldsymbol{m}} = 2\pi\gamma R\, \boldsymbol{m}$. It corresponds to the protein area density $\boldsymbol{m}$ on the membrane multiplied by the locally available membrane area $2\pi R\gamma$. Following the same reasoning as above, one can derive the dynamics for this membrane line density. Alternatively, as shown in appendix Section 2.8.1, the reduced membrane dynamics can also be obtained using an approach outlined in Refs.[243,244]. The combined set of effective equations for both line densities can then be expressed as:

$$\partial_t \widetilde{\boldsymbol{m}} = D_{\mathrm{m}} \partial_x \boldsymbol{J}_{\mathrm{m}} + 2\pi\gamma R \left(\boldsymbol{f}_{\mathrm{m}}(\boldsymbol{m}) + \boldsymbol{f}_{\mathrm{mc}}(\boldsymbol{m}, \boldsymbol{c}) \right), \tag{2.19a}$$

$$\partial_t \widetilde{\boldsymbol{c}} = D_{\mathrm{c}} \partial_x \boldsymbol{J}_{\mathrm{c}} + \pi R^2 \boldsymbol{f}_{\mathrm{c}}(\boldsymbol{c}) + 2\pi\gamma R\, \boldsymbol{g}(\boldsymbol{m}, \boldsymbol{c}). \tag{2.19b}$$

These equations have a physically plausible geometric interpretation: Following Fick's law, the currents $\boldsymbol{J}_{\mathrm{m}}$ and $\boldsymbol{J}_{\mathrm{c}}$ of the diffusive fluxes are determined by gradients in the actual surface and volume densities:

$$\boldsymbol{J}_{\mathrm{m}} = 2\pi R \gamma^{-1} \partial_x \boldsymbol{m}\,, \quad \boldsymbol{J}_{\mathrm{c}} = \pi R^2 \partial_x \boldsymbol{c} \tag{2.20}$$

The geometric prefactors reflect the fact that currents on the membrane are proportional to the surface area elements $2\pi R$ and bulk cross-section πR^2, respectively, and that the gradients on the membrane are given by derivatives with respect to the line elements s along the membrane $\partial_s = \gamma^{-1}\partial_x$. The reactive contributions changing the relative masses of the species locally, are weighted with the locally available reactive bulk volume and surface area, respectively. Thus, reactions at the membrane ($\boldsymbol{f}_{\mathrm{m}}, \boldsymbol{f}_{\mathrm{mc}}, \boldsymbol{g}$) acquire a factor $2\pi\gamma R$ and cytosolic reactions $\boldsymbol{f}_{\mathrm{c}}$ are weighted with the corresponding bulk volume πR^2.

The dimensionally reduced reaction-diffusion equations, Eqs. (2.19), can be reformulated in terms of the volume and area densities as:

$$\partial_t \boldsymbol{m} = \frac{D_{\mathrm{m}}}{\gamma^2} \left[\partial_x^2 + \left(\frac{R'}{R} - \frac{R' R''}{\gamma^2} \right) \partial_x \right] \boldsymbol{m} - \left(\frac{\dot{R}}{R} + \frac{R' \dot{R}'}{\gamma^2} \right) \boldsymbol{m} + \boldsymbol{f}_{\mathrm{m}} + \boldsymbol{f}_{\mathrm{mc}}\,, \tag{2.21a}$$

$$\partial_t \boldsymbol{c} = D_{\mathrm{c}} \left[\partial_x^2 + \frac{2R'}{R} \partial_x \right] \boldsymbol{c} - \frac{2\dot{R}}{R} \boldsymbol{c} + \boldsymbol{f}_{\mathrm{c}} + \frac{2\gamma}{R}\, \boldsymbol{g}\,. \tag{2.21b}$$

As compared to the original three-dimensional reaction-diffusion equation, Eqs. (2.1), these contain new types of terms, all originating from the spatial and temporal modulation of the membrane. For the cytosolic line density, these have the following interpretation: The term $\frac{2\gamma}{R}\boldsymbol{g}$ is an effective reaction term due to the bulk-boundary coupling with the prefactor accounting for the local relation of surface area, $2\pi R\gamma$, to bulk volume, πR^2. The term $-\frac{2\dot{R}}{R}\boldsymbol{c}$ acts as an effective source-sink term with the delatation prefactor $(\partial_t \pi R^2)/(\pi R^2) = 2\dot{R}/R$. It indicates that a temporal increase (decrease) in the local cross-section effectively reduces (increases) the corresponding local volume density $\boldsymbol{c}$. Finally, the contribution $\frac{2R'}{R}\partial_x \boldsymbol{c}$ is an effective drift term with the prefactor acting as an effective drift velocity. It originates from $(\partial_x \pi R^2)/(\pi R^2) = 2R'/R$, i.e., a spatial dilatation of the accessible cross-sectional area. For the membrane line density, there are similar interpretations that can be inferred from the analysis presented in appendix Section 2.8.1.

[1] Notably, the diffusive contributions to Eq. (2.18) yield an effective space-dependent diffusion constant, recovering the classical Fick-Jacobs result for diffusion in spatial confinements[149]: $\partial_t \tilde{c} = \partial_x \left[D_c R^2 \partial_x \frac{\tilde{c}}{R^2} \right]$.

2.4 GEOMETRICALLY CONTROLLED PATTERN FORMATION IN TWO-COMPONENT SYSTEMS

In this section, we apply our geometric reduction approach to a specific example, highlighting the insights it offers into the effects of bulk-boundary coupling. We focus on static surfaces of revolution as enclosing boundaries to examine how spatially varying tube radii, $R(x)$, influence pattern formation and dynamics.

Specifically, we investigate generic reaction-diffusion models involving a single protein species that can exist either bound to the membrane or dissolved in the cytosol. We consider reaction kinetics in which no reactions occur exclusively on the membrane or in the cytosol, that is $\boldsymbol{f}_{\mathrm{m}} = \boldsymbol{f}_{\mathrm{c}} = 0$, but always involve particle exchange between the membrane and the cytosol, $\boldsymbol{f}_{\mathrm{mc}} = -\boldsymbol{g} = f(m, c)$, ensuring mass conservation. This allows us to isolate the effects arising solely from bulk-boundary coupling and geometric modulation.

In this setting, the effective one-dimensional reaction-diffusion dynamics reduces to

$$\partial_t m = \frac{D_{\mathrm{m}}}{\gamma^2}\left[\partial_x^2 + \left(\frac{R'}{R} - \frac{R'R''}{\gamma^2}\right)\partial_x\right] m + f(m,c) \tag{2.22a}$$

$$\partial_t c = D_{\mathrm{c}}\left[\partial_x^2 + \frac{2R'}{R}\partial_x\right] c - \frac{2\gamma}{R}\, f(m,c)\,. \tag{2.22b}$$

As we discussed in the preceding section, in the cytsolic dynamics the reaction term is weighted by a factor corresponding to the area to volume ratio. Moreover, the spatial modulation in the cross-sectional area introduces drift terms for both the dynamics of the membrane and the cytosolic density. Since the drift velocities v_{drift} scale approximately as R'/R, these drift terms imply that interfaces in the concentration profiles shift toward narrower sections of the tube, indicating a tendency of diffusive coupling to minimize interface length. In the following sections, we will explore how these effective reactive and advective contributions influence pattern formation and localization within spatially modulated tubular geometries.

The chemical reactions considered conserve the total number N of particles in the systems:

$$N = \int_0^L \mathrm{d}x\, \left(2\pi\gamma R\, m + \pi R^2 c\right). \tag{2.23}$$

This defines an effective line density for the total amount of particles

$$n(x,t) = 2\pi\gamma(x) R(x)\, m(x,t) + \pi R^2(x)\, c(x,t)\,. \tag{2.24}$$

Since the dynamics conserve mass, this density must obey a continuity equation, as can be inferred from Eqs. (2.22) or, equivalently, Eqs. (2.19),

$$\partial_t n(x,t) = \partial_x\left[D_m \frac{2\pi R}{\gamma}\partial_x m + D_c\, \pi R^2 \partial_x c\right]. \tag{2.25}$$

The total current is a sum of the effective diffusive fluxes on the membrane and in the cytosol, cf. Eq. (2.20).

2.4.1 MASS-REDISTRIBUTION INSTABILITY

In this section, we consider the stability of a homogeneous steady state (HSS) (m^*, c^*) against spatial perturbations. It is given by the intersect between the reactive nullcline, $f(m^*, c^*) = 0$ and the reactive subspace that follows from the constraint on the total protein mass:

$$N = m^* V_{\mathcal{S}} + c^* V_B\,, \tag{2.26}$$

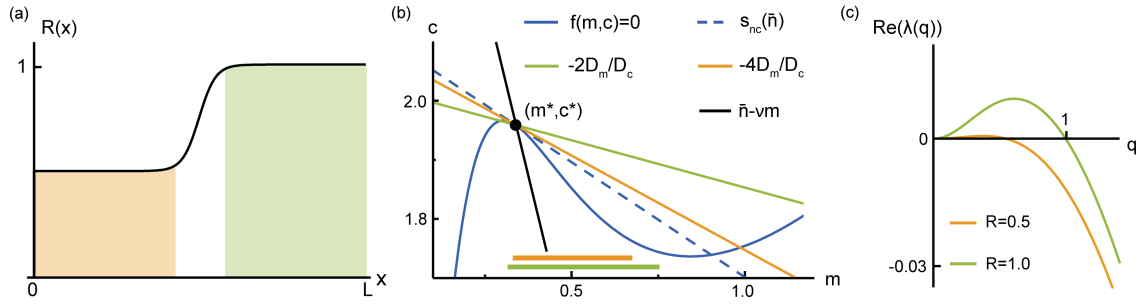

Figure 2.4: Phase-space analysis of geometrically controlled pattern formation. (a) Tube radius $R(x)$, Eq. (2.33), with a narrow transition of two compartments with $R \sim 0.5$ and $R \sim 1$. (b) Representation of the phase-space conditions for lateral instability: a system is laterally unstable if and only if the nullcline's slope (dashed blue (dark gray) line) at the homogeneous steady state (m^*, c^*) is smaller than the critical value (solid green (light gray) and orange (medium gray) lines for $R = 1$ and $R = 0.5$, respectively). The homogeneous steady state is given as the intersect of reactive nullcline (blue, dark gray) and the reactive subspace (black, Eq. (2.27)). The total range of lateral instability in the two domains is indicated by the green (medium gray) and the narrower orange (light gray) bars. (c) Dispersion relations for both parts of the geometry. Linear growth rates $\mathrm{Re}(\lambda(q))$ are larger in the broader part ($R = 1$, green (medium gray)) compared to the narrower section ($R = 0.5$, orange (lighter gray)). The parameters are set to $D_\mathrm{c} = 0.5$, $D_\mathrm{m} = 0.04$, $k = 0.07$, $L = 20$, and $N = 108$.

with V_S and V_B denoting the total membrane area and cytosolic volume, respectively. This relation can be written as

$$c(m^*) = \bar{n} - \nu\, m^*\,, \tag{2.27}$$

where $\bar{n}$ denotes the average mass density if all proteins were dissolved in the cytosol, and $\nu := V_S/V_B$ is the total surface to volume ratio; for an illustration see Fig. 2.4(b). Note that we restrict the discussion to the specific case where only a single stable homogeneous steady state (HSS) exists. In general, the surface-to-volume ratio, ν, can modify the slope of the relationship in Eq. (2.27), potentially introducing additional intersections with the reactive nullcline and leading to multistable behavior[94].

These steady state concentrations (m^*, c^*) lead to a mass line density

$$n^*(x) = 2\pi\gamma(x)R(x)\, m^* + \pi R^2(x)\, c^*\,, \tag{2.28}$$

which is spatially inhomogeneous due to the spatial modulation of the membrane. To study the stability of a HSS we use the dynamic equation for the total density, Eq. (2.25), and expand it around this nonuniform steady state, $n(x,t) = n^*(x) + \delta n(x,t)$. To leading order this yields an effective diffusion equation

$$\partial_t \delta n \approx \partial_x \big(D_\mathrm{eff}(x)\, \partial_x \delta n\big) \tag{2.29}$$

with a space-dependent diffusion coefficient:

$$D_\mathrm{eff}(x) = D_m\, \frac{2\pi R}{\gamma}\, \partial_n m^* + D_c\, \pi R^2\, \partial_n c^*\,. \tag{2.30}$$

This effective diffusion equation exhibits an instability, termed mass-redistribution instability[94], when there is anti-diffusion, $D_\mathrm{eff} < 0$. Thus, the condition for such an instability of the HSS translates to a criterion on the slope of the nullcline at the homogeneous steady state:

$$s_\mathrm{nc} = \frac{\partial_n c^*}{\partial_n m^*} < -\frac{2}{\gamma(x)\, R(x)}\, \frac{D_m}{D_c}\,. \tag{2.31}$$

This criterion is analogous to the slope criterion for a flat geometry[94], yet there are crucial differences. First, even for a cylinder with a constant radius R_0, there is a dependence on geometry:

the instability can be triggered by altering the cylinder's radius, thereby changing only a geometric feature of the system. Second, for surfaces of revolution with a spatially varying radius $R(x)$, the criterion becomes a local one, depending on the local size of the radius as well as the slope of the surface through the metric factor $\gamma(x) = \sqrt{1 + (R'(x))^2}$. As a result, for example, some regions along the cylinder might exhibit instability while others do not.

To exemplify these general criteria we consider a reaction kinetics of the form

$$f(m, c) = \left(k + \frac{m^2}{1 + m^2}\right) c - m\,, \tag{2.32}$$

with a linear attachment and detachment term as well as a nonlinear recruitment term that saturates at high membrane densities. Such a kinetics has previously been employed in conceptual models for cell polarity[12,87,92,94,245]. For the geometric confinement, we choose a hyperbolic tangent with a smooth transition of width $l_{\text{inter}} = 2$, between domains of different radii 0.5 and 1 at the center of the domain, $x = L/2$ (Fig. 2.4(a)):

$$R(x) = \frac{1}{2} + \frac{1}{4}\left[1 + \tanh\left(\frac{2}{l_{\text{inter}}}\left(x - \frac{L}{2}\right)\right)\right]\,. \tag{2.33}$$

We impose no-flux boundary conditions at the cylinder ends.

For the specific case shown in Fig. 2.4, the slope criterion, Eq. (2.31), predicts a mass-redistribution instability in the left and right domain of the revolving surface, as the condition on a mass-redistribution instability is fulfilled for both $R = 1$ and $R = 0.5$; the nullcline's slope $s_{\text{nc}}(n)$ (dashed blue line) at the HSS is steeper than the slope of the corresponding stability lines, green (medium gray) and orange (light gray), respectively. Comparing the conditions in the two spatial domains, we observe that the overall parameter region of total protein masses $\bar{n}$ exhibiting lateral instability is broader for the part with larger bulk volume, as indicated by the bars at the bottom of Fig. 2.4(b). This is in accordance with the dispersion relations obtained from linear stability analysis giving the growth rates $\mathrm{Re}(\lambda(q))$ of modes with wave vector q, Fig. 2.4(c), which show larger growth rates in the spatial domain with the larger radius; see appendix Section 2.8.2 for details on the classical linear stability analysis.

2.4.2 NUMERICAL SOLUTIONS

To investigate the implications of a spatially varying geometry beyond the linear stability analysis, we performed numerical simulations of Eq. (2.22) with reaction kinetics given by Eq. (2.32) and geometry as specified by Eq. (2.33) in Wolfram Mathematica[246]. Figure 2.5 shows corresponding kymographs illustrating the time evolution of membrane and cytosolic densities. Consistent with the slope criterion for a mass-redistribution instability, spatially inhomogeneous density profiles emerge predominantly in the domain with the larger cross-section. This behavior is in accordance with the higher linear growth rates, $\mathrm{Re}[\lambda(q)]$, predicted for larger local tube radii. Once these mesa-shaped profiles have formed, our simulations show that they subsequently translocate toward the narrower region of the system. This traveling wave behavior arises from the geometry-induced advection terms in Eqs. (2.22), which imply a drift velocity $v_{\text{drift}} \sim -R'/R$, directed toward narrower parts of the tube. This translocation process can be understood as a tendency of the system for interface minimization: At smaller tube radii, both the length of the membrane interface and the area of the cytosolic interface between high and low protein density decrease[145]. This will be discussed in more depth in section 2.6 where we will show that this is the driving mechanism behind geometrically interrupted coarsening.

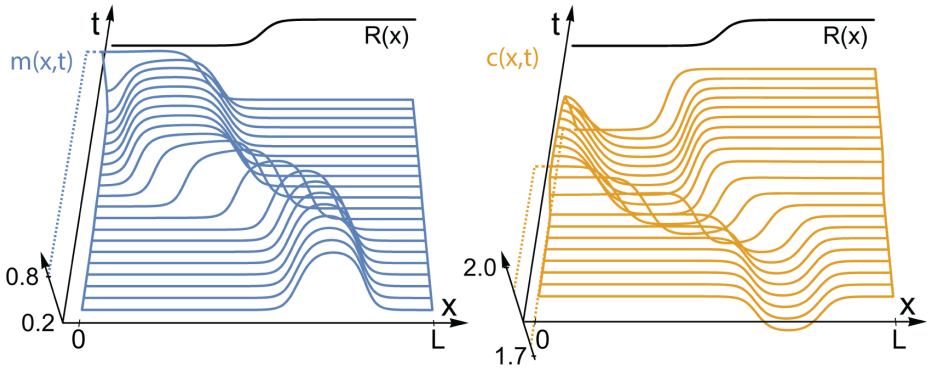

Figure 2.5: Kymographs of membrane (blue, left) and cytosol concentrations (orange, right) in a tube geometry with local radius $R(x)$ as given in Eq. (2.33). Neighboring lines differ by a time interval of 1000 units starting after initial transients ($t = 3000$) when a pattern evolved from the initial homogeneous steady state $(m^*, c^*) \approx (0.34, 1.96)$ perturbed with Gaussian zero-mean white noise with an amplitude of 0.1% of the concentration value; during the initial phase a pattern governed by the fastest growing mode of the dispersion relation emerges, later dominated by the contributions in the broader section of the tube. Parameters as listed in Fig. 2.4.

2.5 STABILITY ANALYSIS OF PATTERN FORMATION IN MODULATED GEOMETRIES

As demonstrated by the elementary example in the previous section, geometric deformations can significantly influence the dynamics of protein systems with bulk-boundary coupling. In this section, we systematically investigate how spatial deformations of the membrane can lead to mode selection in emerging patterns employing a linear stability analysis of the dimensionally reduced equations, Eqs. (2.22), for weak geometric modulations. This approach yields growth rates for lateral instabilities driven by geometric effects. We compare these analytical findings with numerical simulations of the full three-dimensional corrugated tube with bulk-boundary coupling.

2.5.1 PERTURBATIVE LINEAR STABILITY ANALYSIS

The dimensionally reduced one-dimensional description, Eqs. (2.22), facilitates an analytic treatment of the lateral stability of homogeneous steady states (HHS) in a geometrically modulated system. To investigate the impact of a deformed geometry on pattern formation, we perform an asymptotic perturbation expansion in the deviations from a flat geometry, extending the classical linear stability analysis.

In a domain of length L, we assume that the tube-like boundary profile is described by a spatially varying radius

$$R(x) = R_0 + \epsilon R_1(x)\,, \tag{2.34}$$

where R_0 represents the spatially constant component, given by

$$R_0 = \frac{1}{L}\int_0^L \mathrm{d}x\, R(x)\,, \tag{2.35}$$

and $\epsilon\, R_1(x)$ denotes a weak modulation of the tube radius with $\epsilon \ll 1$. Inserting this weakly modulated profile into Eqs. (2.22) and expanding up to the first order in ϵ, one obtains

$$\partial_t m = D_m\left[\partial_x^2 + \epsilon\frac{R_1'}{R_0}\partial_x\right] m + f(m,c)\,, \tag{2.36a}$$

$$\partial_t c = D_c\left[\partial_x^2 + \epsilon\frac{2R_1'}{R_0}\partial_x\right] c - \frac{2}{R_0}f(m,c) + \epsilon\frac{2R_1}{R_0^2}f(m,c)\,. \tag{2.36b}$$

To analyze the linear stability of the HSS, (m^*, c^*), we perturb these densities by expanding $m(x,t)$ and $c(x,t)$ as $m(x,t) = m^* + \delta m(x,t)$ and $c(x,t) = c^* + \delta c(x,t)$, respectively. Furthermore, we adopt a factorization ansatz to separate temporal and spatial dynamics as

$$\begin{pmatrix} \delta m(x,t) \\ \delta c(x,t) \end{pmatrix} = \begin{pmatrix} \delta m(x) \\ \delta c(x) \end{pmatrix} \exp(-\lambda_t t)\,. \tag{2.37}$$

This allows us to rewrite Eqs. (2.36) as an the eigenvalue equation for the spatial part

$$\lambda_t \begin{pmatrix} \delta m \\ \delta c \end{pmatrix} = \left[\mathcal{D}_0 + \epsilon\mathcal{D}_1 + \mathcal{J}\right] \begin{pmatrix} \delta m \\ \delta c \end{pmatrix}\,, \tag{2.38}$$

where for brevity we omitted the arguments in $\delta m(x)$ and $\delta c(x)$. Here, the zeroth order diffusion operator is given by

$$\mathcal{D}_0 = \begin{pmatrix} D_m\partial_x^2 & 0 \\ 0 & D_c\partial_x^2 \end{pmatrix}\,, \tag{2.39}$$

the first order correction reads

$$\mathcal{D}_1 = \begin{pmatrix} D_m\frac{R_1'}{R_0}\partial_x & 0 \\ 2\frac{R_1}{R_0^2}f_m^* & 2D_c\frac{R_1'}{R_0}\partial_x + 2\frac{R_1}{R_0^2}f_c^* \end{pmatrix}\,, \tag{2.40}$$

and the Jacobian of the reaction kinetics, evaluated at the HSS has the form

$$\mathcal{J} = \begin{pmatrix} f_m^* & f_c^* \\ -\frac{2}{R_0}f_m^* & -\frac{2}{R_0}f_c^* \end{pmatrix}\,. \tag{2.41}$$

Equation (2.38) is a linear operator equation comprising a constant term (eigenvalue), λ_t, obtained via the separation ansatz, a spatially dependent differential operator, $\mathcal{D}_0 + \epsilon\mathcal{D}_1$, and a constant matrix term, $\mathcal{J}$. To highlight the distinct nature of these terms, the equation can be reordered as

$$\left[\lambda_t \begin{pmatrix} 1 & 0 \\ 0 & 1 \end{pmatrix} - \mathcal{J}\right] \begin{pmatrix} \delta m \\ \delta c \end{pmatrix} = \left[\mathcal{D}_0 + \epsilon\mathcal{D}_1\right] \begin{pmatrix} \delta m \\ \delta c \end{pmatrix}\,. \tag{2.42}$$

Since, the operator on the left-hand side of this equation is space-independent, also the right-hand side needs to evaluate to a product with a matrix Λ_{spatial}, constant in space, thus, satisfying the equation

$$\Lambda_{\text{spatial}} \begin{pmatrix} \delta m \\ \delta c \end{pmatrix} = \begin{pmatrix} \lambda_{mm} & \lambda_{mc} \\ \lambda_{cm} & \lambda_{cc} \end{pmatrix} \begin{pmatrix} \delta m \\ \delta c \end{pmatrix} = \left[\mathcal{D}_0 + \epsilon\mathcal{D}_1\right] \begin{pmatrix} \delta m \\ \delta c \end{pmatrix}\,. \tag{2.43}$$

In the following, we seek to calculate the matrix Λ_{spatial} perturbatively to replace the spatial contributions $[\mathcal{D}_0 + \epsilon\mathcal{D}_1]$ in Eq. (2.38). Without geometric deformations ($\epsilon = 0$), the solution to equation (2.43) is given by Fourier modes,

$$\{\delta m^{(0)}, \delta c^{(0)}\} \in \{\cos(qx), \sin(qx)\}\,. \tag{2.44}$$

For a domain with length L and periodic boundary conditions, the wave numbers are given by $q = 2\pi n/L$ with $n \in \mathbb{N}$. Indicating the dependence on the mode number q, we rename $\Lambda_{\text{spatial}} \equiv \Lambda_q$, and the zeroth order of equation (2.43) ($\epsilon = 0$) reads

$$\Lambda_q^{(0)} \equiv \begin{pmatrix} \lambda_{mm}^{(0)} & \lambda_{mc}^{(0)} \\ \lambda_{cm}^{(0)} & \lambda_{cc}^{(0)} \end{pmatrix} = \begin{pmatrix} -D_m q^2 & 0 \\ 0 & -D_c q^2 \end{pmatrix}\,. \tag{2.45}$$

Next, we consider the effects of the weak spatial deformation by expanding the terms in orders of ϵ,

$$\Lambda_q = \Lambda_q^{(0)} + \epsilon\,\Lambda_q^{(1)} + \mathcal{O}(\epsilon^2)\,, \tag{2.46}$$

and the vector $(\delta m, \delta c)^T$ around the zeroth order eigenvector of $\mathcal{D}_0$ (Eq. (2.44)),

$$\begin{pmatrix}\delta m\\ \delta c\end{pmatrix} = \begin{pmatrix}\delta m^{(0)}\\ \delta c^{(0)}\end{pmatrix} + \epsilon\begin{pmatrix}\delta m^{(1)}\\ \delta c^{(1)}\end{pmatrix} + \mathcal{O}(\epsilon^2) \tag{2.47}$$

$$\equiv |\boldsymbol{u}^{(0)}\rangle + \epsilon|\boldsymbol{u}^{(1)}\rangle + \mathcal{O}(\epsilon^2)\,, \tag{2.48}$$

where we introduced the vector notation $|\boldsymbol{u}\rangle = (\delta m, \delta c)^T$ for brevity. Then, to first order in ϵ, Eq. (2.43) reads:

$$\Lambda_q^{(0)}|\boldsymbol{u}^{(1)}\rangle + \Lambda_q^{(1)}|\boldsymbol{u}^{(0)}\rangle = \mathcal{D}_0|\boldsymbol{u}^{(1)}\rangle + \mathcal{D}_1|\boldsymbol{u}^{(0)}\rangle\,. \tag{2.49}$$

To calculate, the corrections $\Lambda_q^{(1)}$, we multiply the equation with the left eigenvectors of $\mathcal{D}_0$. Note that to order $\epsilon = 0$, the boundary and the bulk modes are decoupled, such that $\delta m^{(0)}$ and $\delta c^{(0)}$ are independent and the two independent eigenvectors spanning the eigenspace of the operator $\mathcal{D}_0$ are

$$|\boldsymbol{u}_m^{(0)}\rangle = \begin{pmatrix}\delta m^{(0)}\\ 0\end{pmatrix} \quad \text{and} \quad |\boldsymbol{u}_c^{(0)}\rangle = \begin{pmatrix}0\\ \delta c^{(0)}\end{pmatrix}\,. \tag{2.50}$$

Thus, choosing these two eigenvectors as basis vectors $|\boldsymbol{u}_\alpha^{(0)}\rangle$ with $\alpha, \beta \in \{m, c\}$, we obtain the following relation for the components $\lambda_{ij}^{(1)}$ ($i, j \in \{m, c\}$) of the matrix $\Lambda_q^{(1)}$:

$$\langle \boldsymbol{u}_\alpha^{(0)} \mid \Lambda_q^{(0)}\boldsymbol{u}_\beta^{(1)}\rangle + \langle \boldsymbol{u}_\alpha^{(0)} \mid \Lambda_q^{(1)}\boldsymbol{u}_\beta^{(0)}\rangle = \langle \boldsymbol{u}_\alpha^{(0)} \mid \mathcal{D}_0\boldsymbol{u}_\beta^{(1)}\rangle + \langle \boldsymbol{u}_\alpha^{(0)} \mid \mathcal{D}_1\boldsymbol{u}_\beta^{(0)}\rangle\,, \tag{2.51}$$

with the scalar product

$$\langle \boldsymbol{v}|\boldsymbol{u}\rangle = \int_0^L \boldsymbol{v}\cdot\boldsymbol{u}\,\mathrm{d}x\,. \tag{2.52}$$

Given the diagonallity of $\Lambda_q^{(0)}$, the first term can be rewritten as

$$\langle \boldsymbol{u}_\alpha^{(0)} \mid \Lambda_q^{(0)}\boldsymbol{u}_\beta^{(1)}\rangle = \lambda_{\alpha\alpha}^{(0)}\langle \boldsymbol{u}_\alpha^{(0)} \mid \boldsymbol{u}_\beta^{(1)}\rangle\,. \tag{2.53}$$

Using the orthonormality of the basis vectors, Eq. (2.50), the second term on the left-hand side yields

$$\langle \boldsymbol{u}_\alpha^{(0)} \mid \Lambda_q^{(1)}\boldsymbol{u}_\beta^{(0)}\rangle = \lambda_{\alpha\beta}^{(1)}K_{\text{norm}}\,, \tag{2.54}$$

with the norm

$$K_{\text{norm}} = \begin{cases}\langle \boldsymbol{u}_\alpha^{(0)} \mid \boldsymbol{u}_\alpha^{(0)}\rangle & \text{, for } \alpha = \beta\\ \langle \delta m^{(0)}\,\delta c^{(0)}\rangle & \text{, for } \alpha \neq \beta\end{cases}\,. \tag{2.55}$$

Finally, we can use the self-adjointness of $\mathcal{D}_0$ such that

$$\langle \boldsymbol{u}_\alpha^{(0)}|\mathcal{D}_0\boldsymbol{u}_\beta^{(1)}\rangle = \langle \mathcal{D}_0\boldsymbol{u}_\alpha^{(0)}|\boldsymbol{u}_\beta^{(1)}\rangle = \lambda_{\alpha\alpha}^{(0)}\langle \boldsymbol{u}_\alpha^{(0)}|\boldsymbol{u}_\beta^{(1)}\rangle\,, \tag{2.56}$$

and Eq. (2.51) yields the result

$$\lambda_{\alpha\beta}^{(1)} = \frac{\langle \boldsymbol{u}_\alpha^{(0)}|\mathcal{D}_1\boldsymbol{u}_\beta^{(0)}\rangle}{K_{\text{norm}}}. \tag{2.57}$$

The matrix $\Lambda_q^{(1)}$ with components $\lambda_{ij}^{(1)}$ captures the relevant contributions for pattern formation that arise from the geometric deformation to the first order in ϵ. Incorporating this correction matrix in Eq. (2.38) by replacing $[\mathcal{D}_0 + \epsilon\mathcal{D}_1] = \Lambda_q$, we can now consider all parts of the linear operator equation. This substitution leads to the dispersion relation $\lambda_t \equiv \lambda_t(q)$, which characterizes the linear growing modes in deformed tubes. Up to the first order in ϵ, it is given as the solution of the eigenvalue equation

$$\begin{aligned}\lambda_t(q)\begin{pmatrix}\delta m\\ \delta c\end{pmatrix} &= [\Lambda_q + \mathcal{J}]\begin{pmatrix}\delta m\\ \delta c\end{pmatrix}\\ &= \begin{pmatrix}\lambda_{mm}^{(0)}(q) + \epsilon\lambda_{mm}^{(1)}(q) + f_m^* & \lambda_{mc}^{(0)}(q) + \epsilon\lambda_{mc}^{(1)}(q) + f_c^*\\ \lambda_{cm}^{(0)}(q) + \epsilon\lambda_{cm}^{(1)}(q) - \frac{2}{R_0}f_m^* & \lambda_{cc}^{(0)}(q) + \epsilon\lambda_{cc}^{(1)}(q) - \frac{2}{R_0}f_c^*\end{pmatrix}\begin{pmatrix}\delta m\\ \delta c\end{pmatrix},\end{aligned} \tag{2.58}$$

with the zeroth order values $\Lambda_q^{(0)}$ stated in Eq. (2.45) and the corrections $\lambda_{ij}^{(1)}$ from Eq. (2.57), given by

$$\lambda_{mm}^{(1)}(q) = D_m\int_0^L \mathrm{d}x\,\delta m^{(0)}\frac{R_1'}{R_0}\partial_x\delta m^{(0)} \tag{2.59a}$$

$$\lambda_{cc}^{(1)}(q) = \int_0^L \mathrm{d}x\,\delta c^{(0)}\left(f_c^*\frac{2R_1}{R_0^2} + D_c\frac{R_1'}{R_0}\partial_x\right)\delta c^{(0)} \tag{2.59b}$$

$$\lambda_{cm}^{(1)}(q) = f_m^*\int_0^L \mathrm{d}x\delta c^{(0)}\frac{2R_1}{R_0^2}\delta m^{(0)} \tag{2.59c}$$

$$\lambda_{mc}^{(1)}(q) = 0\,. \tag{2.59d}$$

By solving for the eigenvalues λ_t of the matrix $\Lambda_q + \mathcal{J}$, Eq. (2.58), we obtain the growth rates of the various modes q that emerge from the linear instability of the HSS (m^*, c^*). Within the matrix $\Lambda_q^{(1)}$, one observes an additional off-diagonal coupling $\lambda_{cm}^{(1)}(q)$ between modes of the membrane (first) and the cytosolic (second) component that arises from the geometric perturbations. Beyond the homogeneous term $\sim f_m^*/R_0$, this additional coupling $\lambda_{cm}^{(1)}(q)$ incorporates the first-order geometric deformation $\epsilon R_1(x)$ of the tube's radius. It directly reflects the spatial variations in bulk-to-boundary ratios, which in consequence play a determinant role in the geometric mode selection. Notably, in finite-sized domains, $x \in [0, L]$, with periodic boundary conditions, the geometric deformations lift the degeneracy between sine and cosine modes, Eq. (2.45). Thus, the maxima of this perturbative dispersion relation determine the geometric pattern selection, specifying both the characteristic length scales and the spatial positioning (e.g., sine/cosine modes) of the evolving patterns. The explicit evaluation of the eigenvalue equation, Eq. (2.58), is performed in Wolfram Mathematica, see appendix Section 2.8.4. We will discuss particular examples and the implications of our findings for geometrically induced mode selection later, in Section 2.5.3

2.5.2 TRANSLATIONAL STABILITY OF THE FASTEST GROWING MODE

As discussed in Section 2.4, spatial deformations introduce effective advective contributions in the dimensionally reduced equations, Eq. (2.21), resulting in the motion of emergent patterns along the tube's center axis. Having established the geometrically influenced growth rates of the different Fourier modes in Section 2.5.1, we now examine their translational stability. Specifically, we assess whether a small positional offset relative to the geometric deformation causes the modes to return to their original positions or drift further away. Translationally stable modes will recover their initial positions, while unstable modes will amplify the spatial deformations. Such a translational shift would alter the geometrically selected pattern, leading to deviations from the predictions of the perturbative linear stability analysis (Section 2.5.1).

In contrast to the previous section, where we analyzed the stability of a spatially uniform state against spatial perturbations, we are now interested in the stability of the emerging periodic pattern against translations. We proceed by following the standard procedure from the perturbation theory of linear operators[247–250]. To this end, we first consider again the dynamic equation, the emergent modes originate from,

$$\partial_t \boldsymbol{u}(x,t) = [\mathcal{D}_0 + \epsilon\mathcal{D}_1 + \mathcal{J}]\,\boldsymbol{u}(x,t)\,, \tag{2.60}$$

with the Jacobian $\mathcal{J}$, linearized around the HSS. We next, rewrite this equation with the previously used separation ansatz $\boldsymbol{u}(x,t) = \boldsymbol{u}(x)e^{\lambda_t t}$ and combine the terms into a single linear operator $\mathcal{L}$,

$$0 = [\mathcal{D}_0 + \epsilon\mathcal{D}_1 + \mathcal{J} - \lambda_t(q)]\,\boldsymbol{u}(x) = \mathcal{L}\boldsymbol{u}(x)\,, \tag{2.61}$$

with the eigenvalue and its correction $\lambda_t(q) = \lambda_t^{(0)}(q) + \epsilon\lambda_t^{(1)}(q)$ as calculated in Section 2.5.1. In the following, we want to consider explicitly, the dynamics of the mode, predicted to arise from the perturbative linear stability analysis, namely $\boldsymbol{u}_{q,0}$ with wave number $q = \hat{q}$, i.e. the allowed mode with the largest growth rate. For this mode, the zeroth order equation ($\epsilon = 0$) without the spatial deformation gives

$$0 = \left[\mathcal{D}_0 + \mathcal{J} - \lambda_t^{(0)}(\hat{q})\right]\boldsymbol{u}_{\hat{q},0}(x) = \mathcal{L}_0\boldsymbol{u}_{\hat{q},0}(x)\,. \tag{2.62}$$

In the following, we want to consider the impact of the spatial deformations on this mode as a solution to equation (2.60). In particular, we are interested in the translational dynamics, that is motion along the x-direction, of the emergent Fourier mode. Therefore, we decompose the solutions to Eq. (2.61) in terms of a complete basis of $\mathcal{L}_0$, including perturbation-induced spatial translations of the solution with velocity ϵv,

$$\boldsymbol{u}(x,t) = \boldsymbol{u}_{\hat{q},0}(x - \epsilon v t) + \epsilon\boldsymbol{u}_{q\neq\hat{q},1}(x,t)\,. \tag{2.63}$$

Here the term $\boldsymbol{u}_{q\neq\hat{q},1}$ includes all the potential deformations that could arise through the geometric perturbations.

For convenience, we introduce the short-hand coordinate $\xi = x - vt$, for the reference frame, co-moving with the perturbed solution. Inserting this ansatz into Eq. (2.60) yields the first order balance, $\sim \mathcal{O}(\epsilon)$,

$$-v\boldsymbol{u}'_{\hat{q},0}(\xi) + \partial_t\boldsymbol{u}_{q\neq\hat{q},1}(x,t) = \mathcal{L}_0\boldsymbol{u}_{q\neq\hat{q},1}(x,t) + \mathcal{D}_1\boldsymbol{u}_{\hat{q},0}(\xi) - \lambda_t^{(1)}(\hat{q})\boldsymbol{u}_{\hat{q},0}(\xi)\,. \tag{2.64}$$

Stationary solutions $\boldsymbol{u}_0$ to Eq. (2.62) are translationally invariant, meaning that $\boldsymbol{u}_0(x)$ and $\boldsymbol{u}_0(x+\Delta x)$ are both solutions. This translational invariance implies that the derivative of the stationary solution, $\boldsymbol{u}'_0(x)$, satisfies $\mathcal{L}_0\boldsymbol{u}'_0(x) = 0$. Thus, also $\boldsymbol{u}'_{\hat{q},0}(x)$ is a Goldstone mode associated with the translational symmetry and serves as the generator of this symmetry. Conversely, the adjoint mode $\boldsymbol{W}^\dagger_{\hat{q}}$ to the eigenvalue zero of the adjoint linear operator $\mathcal{L}_0^\dagger$, $\mathcal{L}_0^\dagger\boldsymbol{W}^\dagger_{\hat{q}} = 0$, serves as a projector of inputs such as $\mathcal{D}'_1\boldsymbol{u}_{\hat{q},0}$ onto the translational mode, which is why the objects $\boldsymbol{W}^\dagger$ are sometimes also called the *translational response vectors*. Thus, to assess the perturbation-induced translational velocity v of the emerging mode $\boldsymbol{u}_{\hat{q},0}$, we multiply Eq. (2.64) from left with the null space eigenvector $\boldsymbol{W}^\dagger_{\hat{q}}(\xi)$ of wavenumber $\hat{q}$. This yields

$$\begin{aligned} v\langle\boldsymbol{W}_{\hat{q}}(\xi) \mid \boldsymbol{u}'_{\hat{q},0}(\xi)\rangle + \langle\boldsymbol{W}_{\hat{q}}(\xi) \mid \partial_t\boldsymbol{u}_1(x,t)\rangle = \\ \langle\boldsymbol{W}_{\hat{q}}(\xi) \mid \mathcal{L}_0\boldsymbol{u}_1(x,t)\rangle + \langle\boldsymbol{W}_{\hat{q}}(\xi) \mid \left(\mathcal{D}_1(x) - \lambda_t^{(1)}(\hat{q})\right)\boldsymbol{u}_{\hat{q},0}(\xi)\rangle\,, \end{aligned} \tag{2.65}$$

with the same scalar product as above, $\langle\boldsymbol{v} \mid \boldsymbol{u}\rangle = \int_{-\infty}^{\infty}\boldsymbol{v}\cdot\boldsymbol{u}\,\mathrm{d}x$. We observe that the first term on the right-hand side of Eq. (2.65) vanishes as $\mathcal{L}_0^\dagger\boldsymbol{W}^\dagger_{\hat{q}} = 0$. For the remaining deformation contributions, $\langle\boldsymbol{W}_{\hat{q}} \mid \partial_t\boldsymbol{u}_{q\neq\hat{q},1}\rangle$, we make the following considerations: Firstly, as we project $\partial_t\boldsymbol{u}_1$ onto

the eigenmode $\boldsymbol{W}_{\hat{q}}^{\dagger}$ with a given wave number $\hat{q}$, only contributions with wavenumber $\hat{q}$ from $\partial_t \boldsymbol{u}_1$ can contribute to this term due to orthogonality of the eigenmodes for different wave numbers q. Thus, the only contributions of this term could arise through changes of the wavevector by terms $\epsilon \mid \partial_t \boldsymbol{u}_1\rangle \sim \epsilon \mathcal{D}_1 \mid \epsilon \boldsymbol{u}_1\rangle$. However, these are of higher order in ϵ and are therefore neglected.

We continue by solving Eq. (2.65) for the translational velocity v,

$$v = \frac{\langle \boldsymbol{W}_{\hat{q}}(\xi) \mid \left(\mathcal{D}_1(x) - \lambda_t^{(1)}(\hat{q})\right) \boldsymbol{u}_{\hat{q},0}(\xi)\rangle}{\langle \boldsymbol{W}_{\hat{q}} \mid \boldsymbol{u}'_{\hat{q},0}\rangle} \,. \tag{2.66}$$

This relation resembles the solution of the perturbative eigenvalue corrections, Eq. (2.57), requiring a vanishing velocity $v = 0$, as we derived $\langle \boldsymbol{W}_{\hat{q}} \mid \left(\lambda_t^{(1)}(\hat{q}) - \mathcal{D}_1\right) \boldsymbol{u}_{\hat{q},0}\rangle = 0$ in Section 2.5.1. Thus, the perturbation-induced velocity at the modes position of emergence vanishes. However, we now want to analyze if these modes are also translationally stable. To assess the translational stability of the emergent mode $\boldsymbol{u}_{\hat{q},0}(\xi)$, we consider a shift, between the mode and the spatial deformations by introducing an offset $\mathcal{D}_1(x) \to \mathcal{D}_1(x + \delta\,\Delta x)$. This is equivalent to shifting the solution in the opposite direction. For this offset, we now seek to calculate the velocity $v(\Delta x)$. For small offsets, $\Delta x \ll 1$, we can expand

$$\mathcal{D}_1(x + \Delta x) \approx \mathcal{D}_1(x) + \Delta x \mathcal{D}_1'(x) \,. \tag{2.67}$$

Plugging this into the velocity equation, Eq. (2.66), we obtain

$$\frac{v(\Delta x) - v}{\Delta x} = \frac{1}{K_0} \langle \boldsymbol{W} \mid \mathcal{D}_1' \boldsymbol{u}_0\rangle \,. \tag{2.68}$$

with the stationarity of the emergent mode, $v(0) = v = 0$, as given by Eq. (2.66) and normalization factor $K_0 = \langle \boldsymbol{W} \mid \boldsymbol{u}_0'\rangle$. This equation yields the velocity $v(\Delta x)$ for a given small offset Δx of the solution $\boldsymbol{u}_0$ from its stationary position in the fixed spatial deformation $\mathcal{D}_1$. If velocity changes $v(\Delta x)$ have an opposite sign as offsets Δx, the geometric perturbation will move the emerging solution back to its original steady state position, which identifies stable configurations. In contrast, if $v(\Delta x)/\Delta x > 0$, the considered pattern is translationally unstable.

Next, we evaluate this stability criterion for the emergent mode, predicted by the perturbative linear stability analysis, Eq. (2.58).

We predict the emergence of a periodic wave $\boldsymbol{u}_0 = \left(\delta m^{(0)}, \delta c^{(0)}\right)^T$ with $\left\{\delta m^{(0)}, \delta c^{(0)}\right\} \in \{\sin, \cos\}$ and wavevector q as the maximum of the dispersion relation $\lambda_t(q) > 0$, Eq. (2.58). The two components of the eigenvectors are coupled via the bulk-boundary reaction kinetics, therefore they are not independent, but exhibit the same mode and a fixed ratio between the membrane $\delta m^{(0)}$ and the bulk mode amplitude $\delta c^{(0)} = \alpha \delta m^{(0)}$, $\boldsymbol{u}_0 = \left(\delta m^{(0)}, \alpha \delta m^{(0)}\right)^T$ with coupling factor α. To study the translational stability of this mode, we compute all the terms that appear in Eq. (2.68). We obtain the translational response vector $\boldsymbol{W}^{\dagger}$ as the left eigenvector of $\mathcal{L}_{\boldsymbol{u}_0}$ corresponding to a vanishing eigenvalue, $0 = \mathcal{L}_{\boldsymbol{u}_0}^{\dagger} \boldsymbol{W}^{\dagger}$ through partial integration of the terms in $\mathcal{L}_{\boldsymbol{u}_0}^{\dagger}$. It is given as $\boldsymbol{W}^{\dagger} = \begin{pmatrix} \delta m^{(0)\prime} & \tilde{\alpha} \delta m^{(0)\prime} \end{pmatrix}$ with respective coupling factor $\tilde{\alpha}$. Then, the spatial positions, where emergent modes $\boldsymbol{u}_0$ are stationary under the spatial deformation $\sim \mathcal{D}_1$ can be calculated as

$$0 = v = -\frac{1}{K_0} \int \mathrm{d}x \left[\frac{R_1'}{R_0} \left(D_m + 2\alpha\tilde{\alpha} D_c\right) \left(\delta m^{(0)\prime}\right)^2 + \frac{2R_1}{R_0^2} \tilde{\alpha} \left(f_m^* + \alpha f_c^*\right) \delta m^{(0)} \delta m^{(0)\prime} \right] , \tag{2.69}$$

with normalization factor $K_0 = \langle \boldsymbol{W} | \boldsymbol{u}_0'\rangle$. Note that here we assume that the reaction dynamics are still within the linear pattern-forming regime, thus, we evaluate the reactive contributions in Eq. (2.69) at the homogeneous steady state. To assess the stability of these points with respect to translational offsets of the emerging modes, we consider the linearized changes of velocity v for a

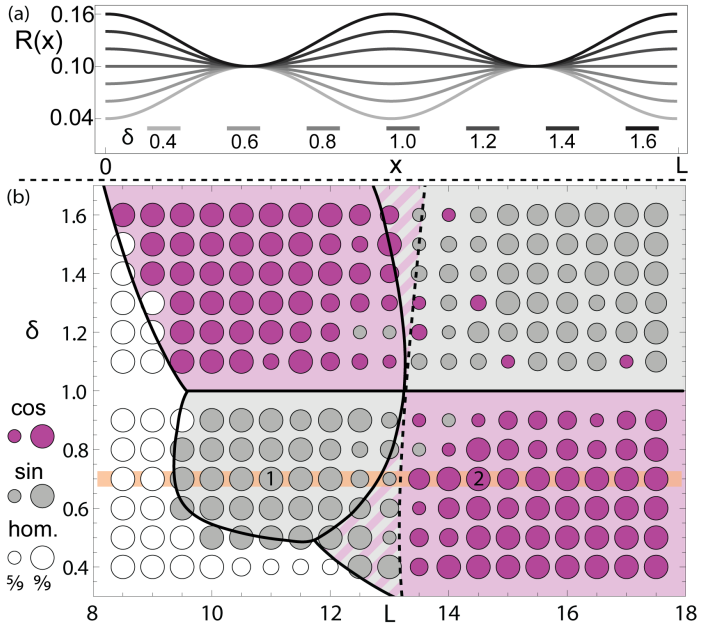

Figure 2.6: *Geometry-induced pattern selection.* (a) Tube radius modulation $R(x)$, Eq. (2.71), for various corrugation parameters δ (light to dark). (b) Phase space of dominant emerging modes (cosine - purple/dark gray, sine - gray) for varying geometric deformation parameter δ and domain length L. Empty circles denote the absence of a lateral instability of the HSS. The size of the circles indicates confidence of the result obtained from nine numerical simulations (smallest circle, indicated mode occurs 5 out of 9 times; largest circle, 9 out of 9 times), with nine different initial conditions for each data point. Analytic predictions for dominant mode (solid line, shaded areas) and stability transition (dashed line, striped area), Eq. (2.58), match the observed behavior. The remaining parameters are set to $D_c = 50$, $D_m = 0.15$, and $k = 0.08$. Details on emergent modes along $\delta = 0.7$ (horizontal orange line) and examples for data points $L = 11$ (1) and $L = 14.5$ (2) are shown in Fig. 2.7.

given induced offset Δx:

$$\frac{\Delta v}{\Delta x} = -\frac{1}{K_0}\int_0^L \mathrm{d}x \left[\frac{R_1''}{R_0}\left(D_m + 2\alpha\tilde{\alpha}D_c\right)\left(\delta m^{(0)\prime}\right)^2 + \frac{2R_1'}{R_0^2}\tilde{\alpha}\left(f_m^* + \alpha f_c^*\right)\delta m^{(0)}\delta m^{(0)\prime}\right] . \tag{2.70}$$

The sign of the term $\Delta v/\Delta x$ will determine the translational stability for the emergent modes. For the following comparison with results of numerical simulations, we evaluate the stability condition (Eq. (2.70)) using Wolfram Mathematica[246].

2.5.3 MODE SELECTION IN A PERIODIC CONFINEMENT

To illustrate our approach, we focus on a representative case featuring a single externally imposed geometric length scale, specifically a periodic radial deformation defined by

$$R(x) = 0.05\left[1 + \delta - (1-\delta)\cos(4\pi\, x/L)\right] , \tag{2.71}$$

shown in Fig. 2.6(a) for different corrugation parameters δ. This spatial modulation, characterized by a single length scale $L/2$, serves as a minimal test setup to study geometry-induced pattern selection and evaluate the potential of the proposed perturbative approach. We investigate how variations in the corrugation parameter δ and the system length L influence the emerging patterns. Unlike the planar tube case ($\delta = 1$), a non-uniform corrugation ($\delta \neq 1$) lifts the degeneracy between sine and cosine modes. In the following, we use the dispersion relation $\lambda_t(q)$, obtained as the solution of the eigenvalue problem (Eq. (2.58)), the result of the perturbative analysis. As a particular example, we consider the lateral stability of the HSS $(m^*, c^*) \approx (0.40, 1.84)$ for the reaction kinetics defined by Eq. (2.32) with parameter $k = 0.08$.

SIMULATIONS IN FULL THREE-DIMENSIONAL GEOMETRY

Numerical simulations of the full three-dimensional setup with periodic boundary conditions at $x \in [0, L]$, show that the HSS is laterally unstable across a broad range of system lengths L and deformation parameter δ; see Fig. 2.6(b). Within this range, the instabilities are predominantly characterized by the emergence of either sine (gray) or cosine (purple) modes, as shown in Fig. 2.6(b). The simulations were performed using COMSOL Multiphysics®[251] implementing Eqs. (2.1) and (2.2), and using initial conditions corresponding to a HSS perturbed with Gaussian zero-mean white noise with an amplitude of 0.1% of the concentration values; see appendix Section 2.8.4 for details. For each indicated combination of the parameters L and δ, we performed a set of nine independent numerical simulations with different realizations of the initial noise. The color of the disks in Fig. 2.6 indicates the predominant modes (sine/cosine) and the size of the disks signifies the fraction of these dominant modes in the simulations; from 5 out of 9 (smallest) to 9 out of 9 (largest disks). Dominant cosine modes (purple) are present in the quadrants $\delta > 1$, $L \lesssim 13$ and $\delta < 1$, $L \gtrsim 13$, whereas sine modes (gray) predominantly occur for $\delta < 1$, $L \lesssim 13$ and $\delta > 1$, $L \gtrsim 13$. As stated before, for the deformation-free case, $\delta = 1$, translational invariance leads to a degeneracy between sine- and cosine modes, and the two cannot be distinguished. For smaller system sizes ($L \lesssim 9$), we observe a region where the HSS remains laterally stable (white disks). In these cases, the present unstable wavelengths exceed the system size, preventing their growth into a pattern. As a result, the system remains in its HSS.

Inverting the amplitude of the spatial corrugation from $\delta > 1$ to $\delta < 1$ swaps the positions of the minima and maxima in the radial modulation, with $\delta > 1$ inducing outward modulation and $\delta < 1$ corresponding to inward-directed deformation from the reference radius $R(x) = 0.1$; see Fig. 2.6(a).

This inversion of the amplitude can also be interpreted as an effective phase shift of the spatial modulation by $\Delta x = L/4$. Consequently, we also expect a phase shift by the same amount in the selected emergent modes which would manifest in an exchange of sine and cosine modes in the numerical simulations as $\sin\left(2\pi(x + L/4)/L\right) = \cos\left(2\pi\, x/L\right)$. However, in Fig. 2.6(b) we do not observe a complete anti-symmetry of sine and cosine with respect to the case of a flat tube geometry ($\delta = 1$). In contrast, we see a strong dependence of the range of stable homogeneous steady states (white disks) on L that does not reflect the trivial interchange of sine and cosine modes due to the effective profile shifting by $\Delta x = L/4$ at $\delta \gtrless 1$. This asymmetry arises because variations in the corrugation parameter δ also alter the average tube radius R_0. Since the bulk volume scales as R_0^2 and the surface area as R_0, changes in δ modify the balance between cytosolic and membrane concentrations, a critical factor in pattern selection[17]. Specifically, outward-directed membrane deformations ($\delta > 1$) increase the available bulk volume, thereby extending the range of lateral instability, as demonstrated in Sec. 2.4. Conversely, inward-directed deformations ($\delta < 1$) decrease the bulk volume and the local, available mass, narrowing the range of lateral instability. This explains the larger regime of stable HSS for $\delta < 1$ in Fig. 2.6(b).

Altogether, the phase diagram, Fig. 2.6(b), reveals the impact of different geometric modulations with strength $\delta \gtrless 1$ and domain length L on observed dominant modes arising from lateral instability. Spatial modulations of the confining membrane boundary can alter the average bulk-boundary ratio, as well as the overall accessible bulk volume and surface area, thereby shifting the maximum of the dispersion relation and with it the characteristic length scale of the emerging patterns. Moreover, spatial deformations lift the degeneracy between sine and cosine modes, leading to the localization of the emerging high-density regions along the tube's center axis.

COMPARISON WITH LINEAR STABILITY ANALYSIS IN SPATIALLY MODULATED TUBE GEOMETRY

Next, we compare these numerical findings with analytic predictions derived from perturbative linear stability analysis. As detailed in Section 2.5.1, we determine the dispersion relation $\lambda_t(q)$ from solving the eigenvalue problem, Eq. (2.58), for sine and cosine modes. Notably, the analytic predictions (shaded regions, solid black lines in Fig. 2.6(b)) align closely with the domain boundaries (local prevalence of colored disks) identified in the numerical simulations. Specifically, predictions for lateral stability (white background), cosine-mode instability (purple background), and sine-mode

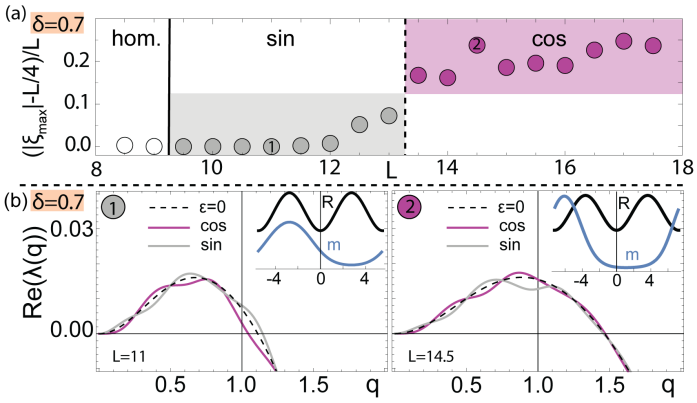

Figure 2.7: *Examples of geometric-induced mode selection.* Dominant modes of numerical simulations are characterized by the location $\xi_{\max}$ of the maximum of the protein concentration on the membrane, as illustrated in panel (a) for the cutline along $\delta = 0.7$ in Fig. 2.6. (b) Dispersion relations for sine and cosine modes together with the boundary profiles R and emerging protein concentrations on the membrane, m, projected onto the tubes' center-axis for $L = 11$ (1) and $L = 14.5$ (2), respectively (see insets). Parameters as in Fig. 2.6.

instability (gray background) generally correspond well with the modes observed in simulations (represented by colored disks). However, we observe some deviations between the numerically measured modes and the analytic predictions around a system length of $L \approx 13$ (purple-gray striped regions). In the purple-gray striped region of Fig. 2.6(b), the modes with the largest growth rates experience translational instability as discussed in Section 2.5.2. This displacement transforms the modes into new, phase-shifted patterns. From the analysis in Section 2.5.2, we obtain an analytical transition line (dashed line in Fig. 2.6) which marks the onset of translational instability in the predicted modes. Within the striped regions, the dominantly emerging modes (sine for $\delta > 1$, cosine for $\delta < 1$) are expected to become translationally unstable, dynamically transitioning into phase-shifted states. The three-dimensional numerical simulations (appendix Section 2.8.4) confirm this behavior, showing the translationally stable modes instead of the ones predicted by LSA. For instance, for the parameter combination $\delta = 0.5$, $L = 12.5$, the perturbative LSA, Eq. (2.58), identifies the cosine mode as having the largest linear growth rate, suggesting it should emerge. However, the analytic treatment of translational stability of that mode (Section 2.5.2) reveals that the geometric deformations induce a spatial shift, rendering the cosine mode with the largest growth rate translationally unstable. Instead, a sine mode is found to be translationally stable under these conditions. Consistent with this prediction, numerical simulations for $\delta = 0.5$, $L = 12.5$ yield patterns corresponding to the sine mode.

In the following, we investigate in more depth the geometric mode selection process. We discuss how emergent modes are determined numerically and how the numerical solutions are related to the analytically obtained dispersion relations. In Fig. 2.7, the positions $\xi_{\max}$ of the maximum of the protein concentration profiles on the membrane, developing in numerical simulations, are given for various system length L along the cutline $\delta = 0.7$ in Fig. 2.6. We identify the developing pattern as sine-like (gray) if the position $\xi_{\max}$ of the concentration maximum is located close to a quarter of the system length, $x = L/4$. Then, the developing pattern resembles a sine-mode with period L and fulfills the criterion $(|\xi_{\max}| - L/4)/L < 1/8$. Conversely, if the maximum position is closer towards the center or the outer edges of the domain, i.e., $(|\xi_{\max}| - L/4)/L > 1/8$, we identify the emergent mode as a cosine mode. For the cutline along $\delta = 0.7$, Fig. 2.7(a), we first observe the stability of the HSS for lengths $L \leq 9$. For increasing system lengths, we then observe a transition towards sin mode emergence and a switch towards cosine mode selection at $L \approx 13$. Panels (b) illustrate the dispersion relations corresponding to system length $L = 11$ (1) and $L = 14.5$ (2), respectively. We observe that in both cases the dispersion of sine (gray) and cosine modes (purple) split off the dispersion relation from the planar tube (dashed black line). Given the limited system size L, the only unstable rescaled wavevector is located at $q = 1$. For the dispersion relation shown

in panel (1), we observe that the real part of the sine mode dispersion relation is larger compared to the cosine mode at the relevant wavenumber $q = 1$. Thus, one expects a sine mode to evolve. The inset in the panel illustrates the location of the membrane concentration pattern (blue) that evolves in numerical simulations of the setup with respect to the radius modulation R (black solid line). Indeed, we observe a localization of the concentration maximum close to $x = L/4$, resembling a sine mode. In contrast, for the parameters $L = 14.5$ shown in panel (b)(2), the maximum of the dispersion relation is of cosine type. The membrane concentration pattern (blue) evolving in numerical simulation indeed is shifted closer to the cosine configuration.

2.5.4 GEOMETRY CONTROLS EMERGENT PATTERNS

In conclusion, we performed a perturbative linear stability analysis incorporating geometric coupling between bulk and boundary modes to predict the geometry-induced selection of emerging patterns. By accounting for effective advective terms in the reaction-diffusion equations, our analysis reliably predicted mode selection at the onset of the lateral instability, capturing potential translational instabilities that influence the dominant modes. Our approach enables an analysis of how spatial modulations of the membrane can lead to specific pattern length scales and localization, allowing us to predict the resulting patterns analytically.

We have performed the perturbative linear stability analysis for a two-component mass-conserving reaction-diffusion system (Eqs. (2.22)) and presented results for a representative single-mode spatial deformation. However, the proposed approach is equally applicable and effective for more complex reaction kinetics involving multiple species in arbitrary but weak deformations.

Instead of analytically predicting the behavior of the system for given radial modulations, one could address the opposite question of how to design a deformation to obtain a desired patterning. Our analytical framework could be used as a starting point for designing geometric confinements in bulk-boundary systems to achieve desired target patterns.

Our perturbative linear stability analysis successfully predicts the initial length scales and localization of geometrically selected patterns in the linear regime. However, these predictions of the initial dynamics following the lateral instability may be modified by subsequent nonlinear effects, such as coarsening, a phenomenon commonly observed in many cellular protein systems[24,252]. To address this, we next investigate how geometric deformations affect coarsening dynamics, bridging the initial patterns with the final steady-state outcomes shaped by spatial modulations of the confining geometry.

2.6 GEOMETRY-INDUCED INTERRUPTED COARSENING

In the preceding sections, we explored the geometric selection of patterns arising from mass-redistribution instabilities using a linear stability analysis of a one-dimensional effective set of equations obtained through dimensional reduction, Eqs. (2.22). However, non-linear pattern evolution can involve a range of complex downstream dynamics, potentially leading to final states that differ significantly from the initial patterns. An important phenomenon in long-time dynamics is coarsening where the merging of solutions and mass transfer between them result in a progressive increase in pattern length scales.

Recently, it has been shown in the context of protein reaction-diffusion systems with sufficiently many conservation laws, that this behavior is generally uninterrupted, with pattern length scales continuing to grow until they approach the system size[24,25]. Our numerical analysis of such systems in spatially modulated confinement (see Fig. 2.5) reveals qualitative differences in the long-term dynamics. In particular, we found that spatial modulations induce a drift of pattern profiles such that the length of the interface between low- and high-density domains is minimized. In this section, we investigate how geometric modulations of the membrane can interrupt the coarsening process in two-component mass-conserving reaction-diffusion systems.

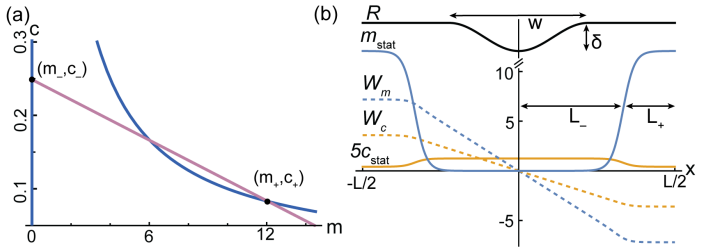

Figure 2.8: *Plateau coarsening in the Brusselator core network.* (a) Reactive nullcline (blue, dark gray) and flux-balance subspace, Eq. (2.73) (purple, lighter gray), of the mass-conserving Brusselator-core model, Eqs. (2.72). An interface solution connects two plateaus that approach (m_-, c_-) and (m_+, c_+) on an infinite domain. (b) Stationary solution $(m_{\text{stat}}, c_{\text{stat}})$ connecting two high-density plateaus with equal masses located at the boundaries of a finite domain $[-L/2, L/2]$. As plateaus are saturated, coarsening is mediated by interface shifts. A geometric deformation R, Eq. (2.92) with width w and amplitude δ affects interface positions and may arrest coarsening. Geometric interface shifts can be computed using the solution's translational response functions (W_m, W_c)

To simplify the analysis, we reduce the reaction kinetics to the polynomial form

$$f(m, c) = m^2 c - k\, m\,, \tag{2.72}$$

which represents the mass-conserving *Brusselator-core* model[24,25], a reduced form of the well-known Brusselator reaction network[253,254] that realizes local mass-conservation. This model incorporates recruitment of the bulk species c to the membrane and detachment of the membrane species m from the surface at a rate k. The model's nonlinear dynamics is characterized by the nullcline, $f(m, c) = 0$, (shown in blue/dark gray) in Fig. 2.8(a). For stationary solutions, $(m_{\text{stat}}(x), c_{\text{stat}}(x))$, to two-component mass-conserving reaction-diffusion systems, the total mass distribution needs to be constant, $\partial_t n(x, t) = 0$. Thus, integrating the dynamic equation of the mass-density $n(x, t)$, Eq. (2.25), for a tube with constant radius, $R(x) = R_0$, yields the flux-balance relation[94]

$$\eta_{\text{stat}} = \frac{2}{R_0}\frac{D_m}{D_c}\, m_{\text{stat}}(x) + c_{\text{stat}}(x)\,, \tag{2.73}$$

with constant offset value η_{stat}; see appendix Section 2.8.3 for details. The prefactor of $m_{\text{stat}}(x)$ weights the contributions of the diffusive fluxes between membrane surface and bulk volume. The value of the constant η_{stat} is determined by a balance of all reactive contributions within the domain[94].

2.6.1 PLATEAU COARSENING IN UNIFORM TUBES

To illustrate the emergence of coarsening and its dependence on spatial modulations of the membrane, we analyze a minimal configuration comprising two connected, equally-sized plateaus, as depicted in Fig. 2.8(b). This analytically tractable setting captures the essential features of coarsening dynamics in confined mass-conserving reaction-diffusion systems as it allows us to study the mass transfer between the two plateaus as well as the geometric impact on it. This stationary solution $(m_{\text{stat}}, c_{\text{stat}})$ of Eq. (2.22) for a constant tube radius $R(x) = R_0$ features two domains of high membrane concentration, $m_{\text{stat}} \approx m_+$, each with a length L_+. These domains are located at the no-flux domain boundaries at $x \in \{-L/2, L/2\}$ and are connected by a central trough of width $2L_-$, where the membrane concentration approaches a lower value $m_{\text{stat}}(0) \approx m_-$. As concentration gradients almost vanish within the plateaus, the corresponding concentrations approximately assume the steady-state values (m_+, c_+) and (m_-, c_-) (black dots in Fig. 2.8). Since the plateau concentrations are fixed by these steady-state values, changes in a plateau's mass are primarily reflected in shifts of its interface position. Namely, an increase or decrease in a plateau's mass causes its interfaces to shift outward or inward with respect to its center of mass, respectively. Neglecting

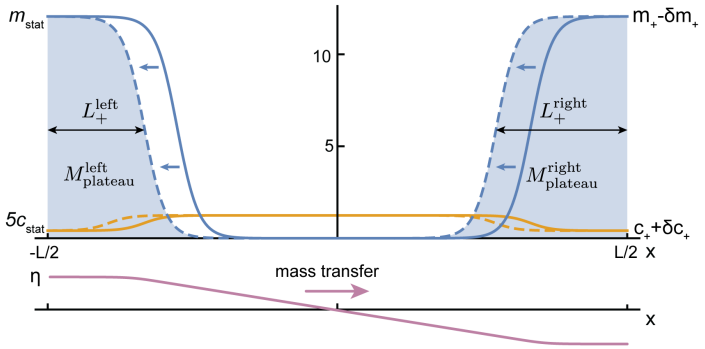

Figure 2.9: *Coarsening between two mesas.* Illustration of mass-transfer between two plateaus. Changes in the plateau masses M_{plateau} are mediated by interface shifts (blue arrows) changing the plateau lengths L_+. As the total system mass is conserved, both interfaces need to move in the same direction. Due to finite plateau lengths, the concentration saturation values (m_+, c_+) differ from infinitely extended solutions, see appendix Section 2.8.3. The deviations of these concentrations involve a spatial gradient in the mass-redistribution potential η between the two plateaus. This gradient causes the coarsening mass transfer with rate σ_c.

contributions from the interface itself, the total mass within a plateau can be approximated as

$$M_{\text{plateau}} = L_+ \left(2\pi R_0 m_+ + \pi R_0^2 c_+\right) , \tag{2.74}$$

where the plateau length L_+ is taken up to the inflection point of its interface (Fig. 2.8(b)).

Extending the approach from Refs.[24,25] to tubular geometries with constant radius $R(x) = R_0$, we observe that the two-plateau solution is only metastable, with any small density difference $\delta M = M_{\text{plateau}}^{\text{right}} - M_{\text{plateau}}^{\text{left}}$ between the left and the right plateau being amplified. As shown in appendix Section 2.8.3, we find

$$\partial_t \, \delta M = \sigma_c \, \delta M \, , \tag{2.75}$$

with the mass transfer rate

$$\sigma_c = -\frac{6k}{1 - D_m/D_c} \, \frac{\ell_m}{L_-} \, \exp\left(-2L_+/\ell_m\right) , \tag{2.76}$$

where $\ell_m := (D_m/k)^{1/2}$ denotes a diffusion length corresponding to the width of the protein density interface on the membrane.

This coarsening rate is notably independent of the tube radius R_0. This is due to a balance of effects: while the mass of proteins transported on the membrane and in the cytosol scales with the perimeter of the tube and the tube's surface area, respectively, the diffusive fluxes responsible for the mass transfer also scale with these same factors, cf. the expressions for the total currents, Eq. (2.20). This implies that the coarsening rate is effectively identical to that for a one-dimensional line[24,25]; see appendix Section 2.8.3.

Hence, the conclusions drawn are the same as in Refs.[24,25]: The rate of mass transport decreases linearly with the distance $2L_-$ between the plateaus and decreases exponentially with the length of the plateaus, L_+. The coarsening process occurs by a synchronized shift of the two interfaces towards the plateau with the smaller mass (left plateau in Fig. 2.9).

2.6.2 SPATIAL DEFORMATIONS SHIFT INTERFACES

Next, we introduce a spatial deformation of the tube between the two density plateaus and using the dimensionally reduced reaction-diffusion equations, Eq. (2.21), we investigate how this affects the interface profiles and the coarsening dynamics.

As discussed in Section 2.4, spatial deformations generate effective advection terms in the reaction-

diffusion equations that can lead to geometry-induced shifts of interface positions. In the following, we will calculate these shifts, by expanding around the symmetric solution with two equally sized high-concentration plateaus. This analysis yields an additional geometry-induced mass-transfer rate σ_g such that the total mass-transfer between the plateaus reads

$$\partial_t \delta M = \sigma_{\text{total}} \delta M = (\sigma_c + \sigma_g)\, \delta M\,. \tag{2.77}$$

As we will see below, the mechanisms underlying these two mass-transfer rates are fundamentally different.

To quantify the impact of the geometry-induced contributions, we start from the dimensionality-reduced dynamics, Eqs. (2.36), that are expanded for weak spatial modulations, $R(x) = R_0 + \epsilon R_1(x)$. In contrast to our analysis of translational stability of the Fourier modes at the onset of the instability of the spatially homogeneous state (Section 2.5.2), this requires analyzing how spatial deformations affect patterns showing (sharp) interface profiles. To this end, we consider—as in the previous subsection—a two-plateau pattern, $\boldsymbol{u}_0(x) = \big(m_{\text{stat}}(x), c_{\text{stat}}(x)\big)$, which is a solution to the stationary equation in the absence of spatial deformations,

$$0 = \mathcal{D}_0 \boldsymbol{u}_0 + \begin{pmatrix} 1 \\ -\frac{2}{R_0} \end{pmatrix} f(\boldsymbol{u}_0)\,. \tag{2.78}$$

We are interested in the dynamics of such a profile in the presence of weak spatial modulations as described by Eq. (2.36), namely under the dynamics

$$\partial_t \boldsymbol{u} = \mathcal{D}_0 \boldsymbol{u} + \begin{pmatrix} 1 \\ -\frac{2}{R_0} \end{pmatrix} f(\boldsymbol{u}) + \epsilon \mathcal{D}_1 \boldsymbol{u} + \epsilon \begin{pmatrix} 0 \\ 2\frac{R_1}{R_0^2} \end{pmatrix} f(\boldsymbol{u})\,, \tag{2.79}$$

with perturbative differential operator

$$\mathcal{D}_1 = \begin{pmatrix} \frac{R_1'}{R_0}\partial_x & 0 \\ 0 & \frac{2R_1'}{R_0}\partial_x \end{pmatrix}. \tag{2.80}$$

Anticipating that the spatial modulations of the membrane can induce a motion of the pattern with velocity $v(t)$ along with deformations of the overall shape of the solution we make the following ansatz

$$\boldsymbol{u}(x,t) = \boldsymbol{u}_0\big(x - \varphi(t)\big) + \epsilon\, \boldsymbol{u}_1(x,t)\,, \tag{2.81}$$

with the time-dependent offset position $\varphi(t)$ of the solution $\boldsymbol{u}_0$,

$$\varphi(t) = \int_{t_0}^{t} \mathrm{d}t'\, \epsilon v(t')\,. \tag{2.82}$$

We define the initial solution at $t = 0$ as $\boldsymbol{u}_0(x)$ with $\varphi(0) = 0$ and introduce the shorthand notation for the coordinates in the co-moving reference frame, $\xi := x - \varphi(t)$ Inserting this expansion into Eq. (2.79) yields

$$\begin{aligned} \epsilon\, \partial_t \boldsymbol{u}_1(x,t) - \epsilon\, v\, \boldsymbol{u}_0'(\xi) = \big[\mathcal{D}_0 + \epsilon \mathcal{D}_1\big]\,(\boldsymbol{u}_0 + \epsilon \boldsymbol{u}_1) \\ + \begin{pmatrix} 1 \\ -\frac{2}{R_0} \end{pmatrix} f(\boldsymbol{u}_0) + \epsilon \begin{pmatrix} 0 \\ \frac{2R_1}{R_0} \end{pmatrix} f(\boldsymbol{u}_0) + \epsilon \mathcal{J}_{\boldsymbol{u}_0} \boldsymbol{u}_1 + \mathcal{O}(\epsilon^2)\,, \end{aligned} \tag{2.83}$$

with the Jacobian (evaluated at $\boldsymbol{u}_0$)

$$\mathcal{J}_{\boldsymbol{u}_0} = \begin{pmatrix} f_m & f_c \\ -\frac{2}{R_0} f_m & -\frac{2}{R_0} f_c \end{pmatrix}\Bigg|_{\boldsymbol{u}_0}. \tag{2.84}$$

Thus, using Eq. (2.78), one finds to first order ($\mathcal{O}(\epsilon)$),

$$\begin{aligned}\partial_t \boldsymbol{u}_1 - v\,\boldsymbol{u}_0' &= \mathcal{D}_0\boldsymbol{u}_1 + \mathcal{J}_{\boldsymbol{u}_0}\boldsymbol{u}_1 + \mathcal{D}_1\boldsymbol{u}_0 + \begin{pmatrix}0\\ \frac{2R_1}{R_0}\end{pmatrix} f(\boldsymbol{u}_0)\\ &\equiv \mathcal{L}_{\boldsymbol{u_0}}\boldsymbol{u}_1 + \mathcal{D}_1\boldsymbol{u}_0 + \begin{pmatrix}0\\ \frac{2R_1}{R_0}\end{pmatrix} f(\boldsymbol{u}_0)\,,\end{aligned} \tag{2.85}$$

with the *linear stability operator* $\mathcal{L}_{\boldsymbol{u}_0}$ evaluated at the stationary zeroth order solution $\boldsymbol{u}_0$. We assume that shape deformations of the profile decay sufficiently fast such that one can consider the stationary limit where $\partial_t \boldsymbol{u}_1 = 0$. Then one gets

$$-v\,\boldsymbol{u}_0' = \mathcal{L}_{\boldsymbol{u_0}}\boldsymbol{u}_1 + \mathcal{D}_1\boldsymbol{u}_0 + \begin{pmatrix}0\\ \frac{2R_1}{R_0}\end{pmatrix} f(\boldsymbol{u}_0)\,. \tag{2.86}$$

As for the consideration of the translational stability in Section 2.5.2, we now multiply equation (2.85) from the left with the translational response vector $\boldsymbol{W}^\dagger(\xi)$

$$-v\,\langle \boldsymbol{W}(\xi)|\boldsymbol{u}_0'(\xi)\rangle = \langle \boldsymbol{W}(\xi)|\mathcal{L}_{\boldsymbol{u}_0}|\boldsymbol{u}_1(x)\rangle + \langle \boldsymbol{W}(\xi)|\mathcal{D}_1(x)|\boldsymbol{u}_0(\xi)\rangle + \langle \boldsymbol{W}(\xi)\mid \begin{pmatrix}0\\ \frac{2R_1(x)}{R_0}\end{pmatrix} f(\boldsymbol{u}_0(\xi))\rangle\,. \tag{2.87}$$

Finally, by the same reasoning as in the analysis of the translational stability of Fourier modes in Section 2.5.2, using $\langle \boldsymbol{W}|\mathcal{L}_{\boldsymbol{u}_0} = 0$, we obtain the geometry-induced velocity as

$$v(\varphi(t)) = -\frac{1}{K_0}\left(\langle \boldsymbol{W}|\mathcal{D}_1(x)|\boldsymbol{u}_0\rangle + \langle \boldsymbol{W}\mid f(\boldsymbol{u}_0)\begin{pmatrix}0\\ \frac{2R_1}{R_0}\end{pmatrix}\rangle\right)\,, \tag{2.88}$$

with normalization factor $K_0 = \langle \boldsymbol{W}|\boldsymbol{u}_0'\rangle$. Note that as the right-hand side of the equation only depends implicitly on time through the time-dependent off-set potions $\varphi(t)$, we also reexpress the velocity by the positional argument $\varphi(t)$. This equation gives the translational velocity of quasi-stationary profiles $\boldsymbol{u}_0(\xi)$ in response to the geometric deformation, as encoded in the operator $\mathcal{D}_1(x)$ and spatial modulation $R_1(x)$. From this expression for the geometry-induced interface velocity, we can deduce a linear rate σ_g of interface shifting to compare with the coarsening rate σ_c (Eq. (2.76)).

Consider now a small deviation δM of mass between the two plateaus, see Fig. 2.9. Such a shift in plateau masses is proportional to a shift in interface positions, $\delta M \sim \Delta x$, and we need to consider the solution shifted by $\varphi(t) = \Delta x$. By this relation, one can connect the geometric mass-transfer rate σ_g to the deformation-induced translational velocity, Eq. (2.88), as

$$\epsilon v = \partial_t \varphi(t) = \partial_t \Delta x = \sigma_g \Delta x\,. \tag{2.89}$$

In the following we seek to calculate the geometry-induced propagation velocity for a solution $\boldsymbol{u}_0(x-\varphi(t))$ that is slightly shifted away from the initial symmetric position $\boldsymbol{u}_0(x)$. Thus, we consider the spatial shift $\varphi(t) = \Delta x$. Will this solution be moved back towards the symmetric case or will the offset from the symmetric configuration grow over time? Similarly to what we have considered for the stability of the emergent patterns in Section 2.5.2, we now investigate if the tube deformation leads to a relaxation back to the case of two equal plateau masses or whether the geometric shift Δx between the symmetric solution $\boldsymbol{u}_0$ and the geometric modulation will increase due to the geometrically induced velocity v, Eq. (2.88). Note that the geometric deformation only contributes in areas where $\mathcal{D}_1$ is non-vanishing. Thus, we can neglect any boundary contributions that otherwise would arise from the spatial shifting. This way we can consider the analogous case of shifting the geometry instead of the solution.

For small shifts Δx, we can expand the velocity v by expansion of the spatial deformation contri-

butions, $R(x+\Delta x) \approx R(x) + R'(x)\Delta x$, as

$$\begin{aligned}\sigma_g &= \epsilon \frac{v}{\Delta x} \approx \epsilon \frac{v(0)}{\Delta x} + \epsilon \frac{\partial v(x)}{\partial x}|_{x=0} \\ &= -\frac{\epsilon}{K_0} \langle \boldsymbol{W}(x)| \left(\mathcal{D}_1'(x) \mid \boldsymbol{u}_0(x)\rangle + f(\boldsymbol{u}_0) \mid \begin{pmatrix} 0 \\ \frac{2R_1}{R_0} \end{pmatrix} \rangle \right) . \end{aligned} \tag{2.90}$$

Here we assumed that for the symmetric plateau solution, no translation is induced by the geometry. This is the case for geometric deformations that are symmetric with respect to the center plane, between the two plateaus, i.e. at $x = 0$ in Fig. 2.8(b). Explicitly writing the scalar products yields the geometric mass-transfer rate

$$\sigma_g = -\frac{\epsilon}{K_0} \int \mathrm{d}x \left[W_m \frac{D_m R_1''(x)}{R_0} m_{\text{stat}}' + W_c \frac{2 D_c R_1''(x)}{R_0} c_{\text{stat}}' + W_c \frac{2R_1'}{R_0^2} f\left(m_{\text{stat}}, c_{\text{stat}}\right) \right] . \tag{2.91}$$

This puts us now in the position to calculate a necessary geometric deformation to arrest the coarsening of two plateau solutions shown in Fig. 2.10 with the transition line at $\sigma_c = \sigma_g$.

2.6.3 SPATIAL DEFORMATIONS ARREST COARSENING

As a concrete example, we consider a radial modulation of the tube given by an indentation of width w and amplitude δ (Fig. 2.8(b)):

$$R = 1 - \begin{cases} \frac{\delta}{2}\left(1 - \cos\left(\frac{2\pi(\frac{w}{2}+x)}{w}\right)\right) & , -\frac{w}{2} \le x \le \frac{w}{2}, \\ 0 & , \text{else}, \end{cases} \tag{2.92}$$

and set the system length to $L = 9$. We set up the system with a two-plateau solution $\boldsymbol{u}(x,t) \approx \boldsymbol{u}_0$ as given in Appendix 2.8.3.

Figure 2.10 shows the analytically calculated boundary between uninterrupted and interrupted coarsening, as given by $\sigma_{\text{total}}(\delta, w) = 0$, in dependence on the deformation parameters w and δ; see appendix Section 2.8.4 for details on the evaluation of the expressions of the mass transfer rates σ_c (Eqs. (2.76)) and σ_g (Eq. (2.91)).

We observe that as the width w of the membrane indentation increases, the deformation amplitude δ required to arrest coarsening decreases. From the geometric mass-transfer rate, Eq. (2.91), we can see that the translational response of the solution is governed by terms $\sim m_{\text{stat}}', c_{\text{stat}}'$ which are located around the plateau interfaces, here exemplarily positioned at $x \in [-L/3, L/3]$. Therefore, wider indentations interact more strongly with the solution as they reach towards the interface positions, allowing weaker deformations to effectively counteract coarsening.

We validate the predicted transition line $\delta_c(w)$ between uninterrupted and arrested coarsening through numerical simulations of the 1d effective Eqs. (2.21) in COMSOL Multiphysics®, see appendix Section 2.8.4 for details. We find that the numerical results align perfectly with the analytical predictions (Fig. 2.10). From the kymographs of the membrane protein concentration $m(x,t)$ (insets in Fig. 2.10) we see the qualitative differences between unarrested and arrested coarsening. For the indentation amplitude $\delta = \delta_c(1 - 5\%)$, coarsening progresses as expected, whereas, for $\delta = \delta_c(1 + 5\%)$, the solution remains in the two-plateau configuration, even at simulation times two orders of magnitude longer than the coarsening completion took in the unarrested case. This indicates that the geometric deformations are sufficiently strong to counteract diffusive mass transfer, thereby arresting coarsening.

Taken together, this example demonstrates that geometric deformations can counteract the mass transfer that in a planar system would lead to coarsening and uninterrupted growth of pattern length scales. This geometry-induced control of the pattern length scale is mediated by the system's tendency for interface length minimization. Spatial deformations of the confinement guide interface motion and thereby determine long-time pattern evolution. Here, we have performed the analysis

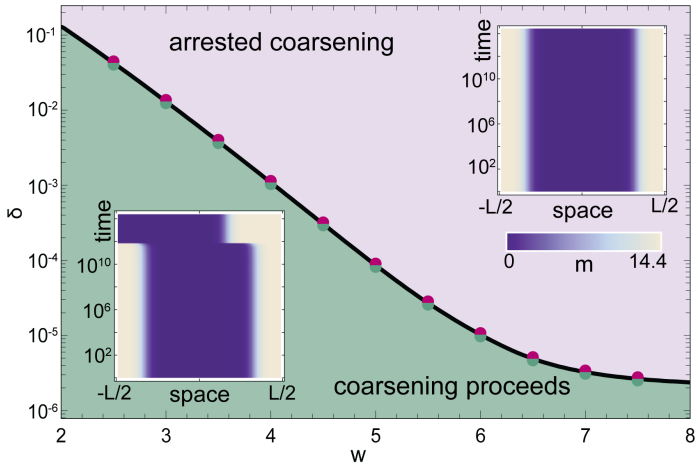

Figure 2.10: *Geometrically arrested coarsening.* Geometric deformations with amplitudes δ and widths w induce coarsening arrest (purple/light gray shaded) in contrast to uninterrupted coarsening (green, dark gray shaded). The analytically predicted transition line (black) results from comparing analytic coarsening rates σ_c, Eq (2.76), and geometric interface shifting rate σ_g, Eq. (2.91). Purple (dark gray) and green (lighter gray) dots represent the results of numerical simulations of Eq. (2.22) with Brusselator-core reaction kinetics, Eq. (2.72), yielding arrested and unarrested coarsening, respectively. Insets show membrane concentration kymographs of two exemplary solutions for arrested (top right) and unarrested (bottom, left) coarsening dynamics at deformation width $w = 4$. The selected amplitude parameters δ are located at deformations at $\pm 5\%$ of the analytically predicted transition values.

exemplarily for the Brusselator core model, Eq. (2.72), for which all necessary analytical expressions can be calculated. For more complex reaction kinetics, obtaining these expressions will require numerical evaluation, though the underlying approach remains viable.

2.7 CONCLUSION

In this work, we developed a minimal model to explore the role of geometry in bulk-boundary coupled reaction-diffusion systems. Our approach considers a reaction-diffusion system with reactive exchange between the bulk and boundary components within a radially modulated, rotationally symmetric cylinder. By performing a dimensionality reduction, we introduce a geometric context to one-dimensional reaction-diffusion formulations, which allows for analytic tractability and provides insights into the effects of confinement on pattern formation and dynamics.

The reduction of full reaction-diffusion dynamics to an effective one-dimensional model relies on key assumptions: that lateral bulk gradients are small relative to the axial gradients driven by boundary reactions, and that the cylindrical geometry is narrow compared to the relevant diffusion lengths. This quasi-1D reduction, which holds for many observed patterns in elongated cells and microfluidic settings, enabled us to integrate out radial and angular dependencies, leading to a simplified reaction-diffusion-advection equation that accurately captures the role of geometric modulation.

Using this reduced model, we found that a spatial modulation of the confinement directly influences pattern formation by varying the bulk-boundary ratio. This spatial variation modifies local reactive equilibria, thus driving pattern selection and localization. Through a perturbative linear stability analysis of weakly modulated geometries, we predicted the modes of the emerging patterns and their spatial positioning, with results that aligned well with full 3D simulations. This strong correspondence validates both the reduced theory and the analytical insights it provides, showing that geometry significantly influences emergent patterns.

Beyond initial pattern formation, many biological systems exhibit coarsening, a process where patterns evolve to span the entire system. Here, we examined how geometric confinement can prevent coarsening and stabilize specific pattern scales. By analyzing the effects of radial modulation, we found that interface minimization plays a key role, as the geometry can effectively arrest coarsening

by counteracting mass transfer and thereby stabilize distinct pattern scales.

Our study highlights the critical role of geometric confinements on pattern formation and length-scale selection. We identify the modulation of the bulk-boundary ratios and interface minimization as primary geometric effects. These insights suggest that these mechanisms are broadly relevant to confined systems, offering a general framework to understand and manipulate pattern formation in both biological and synthetic settings.

Our approach highlights a pathway for designing confinement geometries to achieve targeted pattern configurations, which could be useful in applications such as protein pattern formation in vesicle-like systems or in chemical reactors with customized confinement shapes. The presented theory thus opens avenues for precise control over pattern dynamics and localization in various confined environments.

2.8 APPENDIX

2.8.1 REDUCED MEMBRANE DYNAMICS

For completeness, we include a derivation of the one-dimensional dynamics of surface-bound protein species, closely following the presentation in Ref.[243] and extending it by a coupling to enclosed bulk protein species. As before, we use a parametric representation of the reactive surface $\mathcal{S}$, Eq. (2.7), in terms of the angular variable ϕ and the position x along the cylinder axis:

$$\vec{X}(x,t) = \begin{pmatrix} x \\ R(x,t)\cos\phi \\ R(x,t)\sin\phi \end{pmatrix} . \tag{2.93}$$

The surface tangent vectors are given by

$$\vec{X}_x = \frac{\partial \vec{X}}{\partial x} = \begin{pmatrix} 1 \\ R'\cos\phi \\ R'\sin\phi \end{pmatrix} = \vec{e}_x + R'\,\vec{e}_\rho\,, \tag{2.94}$$

$$\vec{X}_\phi = \frac{\partial \vec{X}}{\partial \phi} = \begin{pmatrix} 0 \\ -R\sin\phi \\ R\cos\phi \end{pmatrix} = R\,\vec{e}_\phi\,. \tag{2.95}$$

with norms $h_1 = |\vec{X}_x| = \sqrt{1+R'^2}$ and $h_2 = |\vec{X}_\phi| = R$. In the following, we consider the dynamics of the chemical components on the surface, $\boldsymbol{m} \in \mathbb{R}^{\mathrm{p}}$, in a given subsection $\Gamma \subset \mathcal{S}$; see Fig. 2.11 for an illustration.

The area concentrations need to fulfill the balance equation

$$\begin{aligned} \frac{\mathrm{d}}{\mathrm{d}t}\int_{\Gamma(t)} \mathrm{d}S_X\, \boldsymbol{m}(\vec{X},t) &= D_{\mathrm{m}} \int_{\partial\Gamma(t)} \mathrm{d}l\, \vec{n}_{\partial\Gamma}\cdot\nabla\boldsymbol{m} \\ &\quad + \int_{\Gamma(t)} \mathrm{d}S_X \left[\boldsymbol{f}_{\mathrm{m}}(\boldsymbol{m}) + \boldsymbol{f}_{\mathrm{mc}}(\boldsymbol{m},\boldsymbol{c}|_{\mathcal{S}})\right], \end{aligned} \tag{2.96}$$

where $\mathrm{d}S_X$ denotes the surface element and $\mathrm{d}l$ the line element along the curve $\partial\Gamma$ bounding the surface area Γ, whose normal $\vec{n}_{\partial\Gamma}$ lies in the tangent plane $T_{\mathcal{S}}$ of $\mathcal{S}$. Similar to Eq. (2.11), the continuity equation for membrane species states that the total change in the number of surface-bound proteins within an area Γ is either due to diffusive fluxes through the bounding line $\partial\Gamma$ or chemical reactions within the domain Γ.

In order to further evaluate the various terms in Eq. (2.96), we need a few basic relations from differential geometry. Let the boundary $\partial\Gamma$ be described in parametric form by $x_0(s)$ and $\phi_0(s)$ with s denoting the arclength. Then the tangent vector on $\partial\Gamma$ can be written as $\vec{t}_{\partial\Gamma} = x_0'(s)\vec{X}_x + \phi_0'(s)\vec{X}_\phi$. As the normal vector is element of the tangent space on $\mathcal{S}$, $\vec{n}_{\partial\Gamma} \in T_{\mathcal{S}}$, it can be written in terms of the

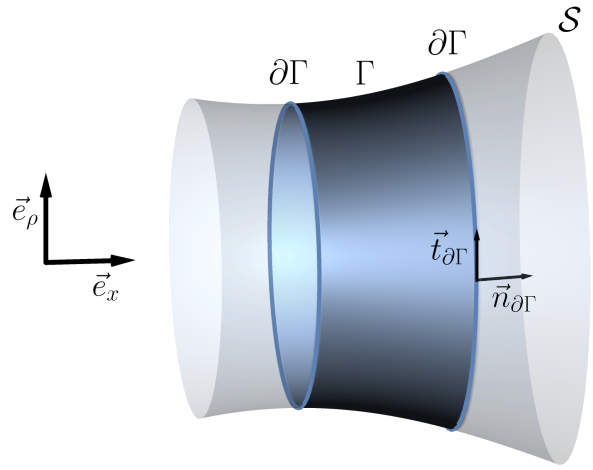

Figure 2.11: Schematic of a small surface element $\Gamma \subset \mathcal{S}$. Its perimeter curve $\partial\Gamma$ can be described by means of the local tangent space vectors $\vec{X}_x$ and $\vec{X}_\phi$. The curves normal and tangent vector are given by $\vec{n}_{\partial\Gamma}$ and $\vec{t}_{\partial\Gamma}$, respectively.

surface tangent vectors: $\vec{n}_{\partial\Gamma} = \alpha\vec{X}_\phi + \beta\vec{X}_x$. The parameters α and β can be determined from the normalization condition and orthogonality to the tangent vector of $\partial\Gamma$. This gives

$$\vec{n}_{\partial\Gamma} = -\frac{x_0' h_1}{h_2|\vec{t}_{\partial\Gamma}|}\vec{X}_\phi + \frac{\phi_0' h_2}{h_1|\vec{t}_{\partial\Gamma}|}\vec{X}_x\,. \tag{2.97}$$

Using the explicit form for the surface gradient

$$\nabla \boldsymbol{m} = \left(\frac{1}{h_1^2}\,\partial_x \boldsymbol{m}\right)\vec{X}_x + \left(\frac{1}{h_2^2}\,\partial_\phi \boldsymbol{m}\right)\vec{X}_\phi \tag{2.98}$$

and the line element $\mathrm{d}l = |\vec{t}_{\partial\Gamma}|\,\mathrm{d}s$, the interface fluxes in Eq. (2.96) can be written as

$$\int\limits_{\partial\Gamma(t)} \mathrm{d}l\,\vec{n}_{\partial\Gamma}\cdot\nabla\boldsymbol{m} = \int\limits_{\partial\Gamma(t)} \mathrm{d}s\left[\frac{h_2\phi_0'}{h_1}\partial_x\boldsymbol{m} - \frac{h_1 x_0'}{h_2}\partial_\phi\boldsymbol{m}\right] = -\int\limits_{\partial\Gamma(t)} \mathrm{d}x_0\,\frac{h_1\partial_\phi\boldsymbol{m}}{h_2} + \int\limits_{\partial\Gamma(t)} \mathrm{d}\phi_0\;\frac{h_2\partial_x\boldsymbol{m}}{h_1} \tag{2.99}$$

and applying Stoke's theorem yields

$$\int\limits_{\partial\Gamma(t)} \mathrm{d}l\,\nabla\boldsymbol{m}\cdot\vec{n}_{\partial\Gamma} = \int\limits_{\Gamma} \mathrm{d}x_0\mathrm{d}\phi_0\left(\partial_{\phi_0}\left[\frac{h_1}{h_2}\partial_{\phi_0}\boldsymbol{m}\right] + \partial_{x_0}\left[\frac{h_2}{h_1}\partial_{x_0}\boldsymbol{m}\right]\right). \tag{2.100}$$

We note that due to an implicit time dependence, one has

$$\frac{\mathrm{d}}{\mathrm{d}t}\int\limits_{\Gamma}\boldsymbol{m}(\vec{X}(x_0,\phi_0,t),t)h_1h_2\mathrm{d}x_0\mathrm{d}\phi_0 = \int\limits_{\Gamma}\left[\left(m_t + \nabla\boldsymbol{m}\vec{X}_t\right)h_1h_2 + \boldsymbol{m}\partial_t\left(h_1h_2\right)\right]\mathrm{d}x\mathrm{d}\phi\,. \tag{2.101}$$

Altogether, the continuity equation reads

$$0 = \int\limits_{\Gamma}\left\{h_1h_2\partial_t\boldsymbol{m} + \boldsymbol{m}\partial_t\left(h_1h_2\right) - D_{\mathrm{m}}\left[\partial_\phi\frac{h_1}{h_2}\partial_\phi\boldsymbol{m} + \partial_x\frac{h_2}{h_1}\partial_x\boldsymbol{m}\right] - (\boldsymbol{f}_m + \boldsymbol{f}_{mc})h_1h_2\right\}\mathrm{d}x\mathrm{d}\phi\,, \tag{2.102}$$

which needs to hold for every sufficiently small surface segment Γ. For the concrete geometry, Eq. (2.93), we substitute $h_1 = \gamma$ and $h_2 = R$. Neglecting angular gradients, i.e. $\partial_\phi \boldsymbol{m} = 0$, one gains the one-dimensional reaction-diffusion equation

$$\partial_t \boldsymbol{m} = \frac{D_\mathrm{m}}{\gamma^2}\partial_x^2 \boldsymbol{m} + \frac{D_\mathrm{m}}{\gamma^2}\left(\frac{R'}{R} - \frac{R'R''}{\gamma^2}\right)\partial_x \boldsymbol{m} - \left(\frac{\dot{R}}{R} + \frac{R'\dot{R}'}{\gamma^2}\right)\boldsymbol{m} + \boldsymbol{f}_m(\boldsymbol{m}) + \boldsymbol{f}_{mc}(\boldsymbol{m}, \boldsymbol{c})\,. \tag{2.103}$$

In analogy to the derived reduction for the cytosolic species, one obtains effective advective contributions. These account for the space-dependent impact of mass transport on surface concentrations. In contrast to the bulk case, there are two factors that affect the accessible surface area, namely the local circumference of the tube and the curvature-dependent boundary line element in x-direction.

2.8.2 LINEAR STABILITY ANALYSIS FOR A PIECEWISE CONSTANT PROFILE.

Complementary to the discussion in the main text based on the dynamics of the total mass, we here perform a classical linear stability analysis of the HSS for a system within a geometry with an approximately piecewise constant boundary profile, Eq. (2.33) with a comparably sharp interface with width $l_\mathrm{inter} \approx 2 = 0.1\,L$; see Fig. 2.4(b).

Neglecting the impact of the interface, we perform a linear stability analysis for the two 'separate' domains, with locally constant radii $R_1 = 0.5$ and $R_2 = 1$. Specifically, we analyze the dynamics of perturbations $(\delta m, \delta c)$ around the HSS (m^*, c^*), Eq. (2.22), which for a constant tube-radius reads

$$\partial_t \delta m = D_m \partial_x^2 \delta m + f_m^* \delta m + f_c^* \delta c\,, \tag{2.104a}$$

$$\partial_t \delta c = D_c \partial_x^2 \delta c - \frac{2}{R}\left(f_m^* \delta m + f_c^* \delta c\right)\,. \tag{2.104b}$$

Here, we linearized the reaction term

$$f(m^* + \delta m, c^* + \delta c) \approx 0 + f_m^* \delta m + f_c^* \delta c\,. \tag{2.105}$$

and abbreviated $f_\alpha^* := \partial_\alpha f(m,c)|_{(m^*,c^*)}$ for $\alpha \in \{c, m\}$.

Using Fourier modes, $(\delta m_q, \delta c_q) \sim \exp[iqx + \lambda(q)t]$, Eqs. (2.104) becomes an eigenvalue problem

$$\lambda(q)\begin{pmatrix}\delta m_q \\ \delta c_q\end{pmatrix} = \left[-\begin{pmatrix}D_m & 0 \\ 0 & D_c\end{pmatrix} q^2 + \begin{pmatrix}f_m^* & f_c^* \\ -\frac{2}{R}f_m^* & -\frac{2}{R}f_c^*\end{pmatrix}\right]\begin{pmatrix}\delta m_q \\ \delta c_q\end{pmatrix}\,. \tag{2.106}$$

Solving this eigenvalue problem for a given tube radius, one obtains the distinct dispersion relations shown in Fig. 2.4(c). For a constant tube radius $R(x) = R_0$, we consistently recover the slope criterion, Eq. (2.31).

For a cylindrical geometry with a spatially constant radius $R(x) \equiv R$, the impact of the R-dependent bulk-boundary ratio on the HSS of the enclosed reaction-diffusion system can be incorporated by re-scaled reaction rates. Namely, using the line densities for constant tube radii, i.e., $\gamma = 1$, $\tilde{m} = 2\pi\, R m$ and $\tilde{c} = \pi\, R^2\, c$, we can transform

$$f(m,c) = \tilde{f}(\tilde{m}, \tilde{c}) = \left[\frac{k_\mathrm{on}}{\pi R^2} + \frac{k_\mathrm{fb}}{\pi R^2}\frac{\tilde{m}^2}{4\pi^2 R^2\left(k_\mathrm{d}^2 + \frac{\tilde{m}^2}{4\pi^2 R^2}\right)}\right]\tilde{c} - \frac{k_\mathrm{off}}{2\pi R}\tilde{m} = \left[\tilde{k}_\mathrm{on} + \tilde{k}_\mathrm{fb}\frac{\tilde{m}^2}{\tilde{k}_\mathrm{d}^2 + \tilde{m}^2}\right]\tilde{c} - \tilde{k}_\mathrm{off}\tilde{m}\,. \tag{2.107}$$

For the re-scaled reaction kinetics, pattern formation can be analogously described as done in Ref.[94]. In consequence, spatially varying tube radii will lead to heterogeneous reaction conditions due to the dependence on bulk-boundary ratios.

2.8.3 PLATEAU-COARSENING IN UNDEFORMED TUBES

In this appendix, we show the calculations to obtain an analytic expression for the coarsening rate between two plateaus in an undeformed tube. We follow Refs.[24,25] by adapting their discussion to a tubular geometry. First, we seek to calculate the quasi-stationary plateau solutions, Fig. 2.8, in an uncorrugated tube with constant radius $R(x) = R_0$. We start with the dimensionally reduced dynamic equations, Eqs. (2.21),

$$\partial_t m = D_m \partial_x^2 m + f(m,c) \tag{2.108}$$

$$\partial_t c = D_c \partial_x^2 c - \frac{2}{R_0} f(m,c)\,. \tag{2.109}$$

Adding both equations for the temporal evolution of the mass-density $n(x,t) = 2\pi\gamma R m + \pi R^2 c$, we obtain

$$\partial_t n = 2\pi R D_m \partial_x^2 m + \pi R^2 D_c \partial_x^2 c\,. \tag{2.110}$$

For stationary solutions $(m,c)(x,t)=(m_{\text{stat}}(x), c_{\text{stat}}(x))$, the dynamics of the mass-density is stationary, $\partial_t n = 0$ and the right-hand side of the equation can be integrated as

$$\eta_{\text{stat}} = \frac{2}{R_0}\frac{D_m}{D_c} m_{\text{stat}} + c_{\text{stat}} \equiv \tilde{d}\, m_{\text{stat}} + c_{\text{stat}}\,, \tag{2.111}$$

with a constant mass-redistribution-potential offset η_{stat}. This equation states a flux-balance relation for the stationary solutions. The factor $\tilde{d}$ weights the contributions of diffusive fluxes between membrane surface and bulk volume. To construct the two-plateau solution, we dissect it into two symmetric parts each of which consisting of a single interface as a continuous transition from a low-density plateau $m_{\text{stat}}(x\to-\infty)=m_-$ in one side of the domain, to a high-density plateau $m_{\text{stat}}(x\to\infty)=m_+$ on the other side. To obtain this elementary stationary single interface solution we need to calculate the corresponding constant value of $\eta_{\text{stat}}^{\infty}$. It can be obtained by inserting the flux-balance relation, Eq. (2.111) into the stationary membrane equation,

$$0 = D_m \partial_x^2 m_{\text{stat}} + \tilde{f}(m_{\text{stat}}, \eta_{\text{stat}}^{\infty})\,, \tag{2.112}$$

where we reexpressed the reactive contributions as $\tilde{f}(m_{\text{stat}}, \eta_{\text{stat}}) = f(m_{\text{stat}}, \eta_{\text{stat}} - \tilde{d}\, m_{\text{stat}})$. Next, we multiply the equation with $\partial_x m_{\text{stat}}$ and integrate over space $x \in (-\infty, \infty)$. Rewriting the integral in terms of membrane concentrations, one obtains

$$0 = \int_{m_{\text{stat}}(-\infty)}^{m_{\text{stat}}(\infty)} \tilde{f}(m, \eta_{\text{stat}^\infty})\mathrm{d}m\,, \tag{2.113}$$

where we applied the no-flux boundary conditions at the outer boundaries. Upon integration, the relation yields

$$0 = \left[-\frac{\tilde{d}}{4}m^4 + \frac{\eta_{\text{stat}}^{\infty}}{3}m^3 - \frac{k}{2}m^2\right]_{m=m_{\text{stat}}(-\infty)=m_-}^{m_{\text{stat}}(\infty)=m_+}. \tag{2.114}$$

The lower and upper plateau values (m_-, m_+) can be obtained from the intersection of the FBS, Eq. (2.111), with the reactive NC (Fig. 2.8 (a)). The nullcline of the Brusselator-core is given by

$$0 = -\tilde{d}m^3 + \eta_{\text{stat}} m^2 - km\,, \tag{2.115}$$

giving the relevant solutions $m_- = 0$ and $m_+ = \sqrt{2k/\tilde{d}}$. Thus, solving Eq. (2.114) for η_{stat}, we obtain the value

$$\eta_{\text{stat}}^{\infty} = 3\sqrt{\frac{\tilde{d}k}{2}}\,. \tag{2.116}$$

Having calculated the plateau values as well as the flux-balance offset, we are in the position to calculate the infinite single-interface plateau solution by solving Eq. (2.112). The solution is given by

$$m_{\text{stat}}^{\infty} = \sqrt{\frac{k}{2\tilde{d}}}\left(1 + \tanh\left(-\sqrt{\frac{k}{D_m}}\frac{x}{2}\right)\right)\,, \tag{2.117a}$$

$$c_{\text{stat}}^{\infty} = \eta_{\text{stat}}^{\infty} - \tilde{d}\, m_{\text{stat}}^{\infty}\,. \tag{2.117b}$$

To construct a combined finite length solution of two high-density plateaus as discussed in the main text, Fig. 2.8(b), one effectively considers no-flux boundaries at finite positions instead of being located at $\pm\infty$. Accordingly, we introduce a system length $L = 2\,(L_- + L_+)$ with high- and low-density plateau lengths L_+ and L_-, respectively. In the sharp interface limit, the plateau lengths are bounded by the solution's inflection points (Fig. 2.9) such that the total system mass $M = L\,\bar{n}$ of the two-plateau solution can be estimated as

$$\frac{L}{2}\bar{n} \approx L_- n_- + L_+ n_+\,. \tag{2.118}$$

Then, a given system mass fixes the plateau lengths and directly relates them to the plateau densities $n_\pm$ via

$$L_\pm(L) = \pm\frac{L}{2}\frac{\bar{n} - n_\mp}{n_+ - n_-}\,. \tag{2.119}$$

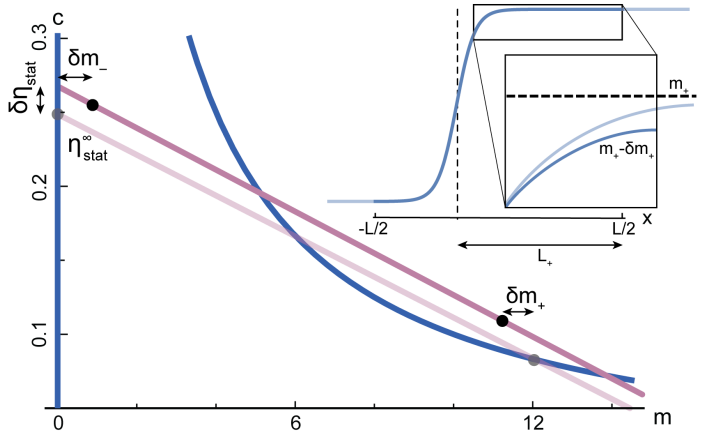

Figure 2.12: *Qualitative illustration of varying plateau densities.* Stationary solutions to Eqs. (2.21) on a finite domain exhibit a shift of the flux-balance subspace (purple) by $\delta\eta_{\text{stat}}$. Thereby, concentration saturation values within the plateaus of finite length L_+ are shifted by δm_+.

On the finite domain, the plateau values of the infinitely extended solution, Eqs. (2.117), cannot be attained. Instead, finite solutions approach plateau values that depend on their lengths. The single interface solution shown in Fig. 2.12 has a finite plateau length L_+. Therefore its membrane concentration value at the domain boundary $x = L/2$ will saturate below the one of the infinite solution as $m_s(L/2) = m_+ - \delta m_+$. Additionally, for a finite plateau length, it can be shown that

the flux-balance subspace of the solution is shifted from the infinite one $\eta_{\text{stat}}^{\infty}$ by $\delta\eta_{\text{stat}}$[24,25]. This has direct consequences for a solution consisting of two high-concentration plateaus of slightly varying masses: As plateaus with different masses have different plateau lengths L_+, they attain different saturation concentrations. These variations in saturation values lead to differences in the local mass-redistribution potential η and the solution is no longer stationary. In turn, coarsening is driven by the differences in η through

$$\partial_t n(x,t) = D_c \pi R_0^2 \partial_x^2 \eta(x,t)\,. \tag{2.120}$$

Thus, to analyze the coarsening dynamics in a system with two high-density plateaus, as shown in Fig. 2.9, we can calculate the respective differences from the saturation values of the infinitely extended solution. These will yield differences in the local mass-redistribution potential, which drives the mass transport between the two plateaus.

The deviations from the infinite plateau values can be obtained by linearizing the stationary membrane equation, Eq. (2.112), for $m_{\text{stat}}(x) = m_\pm \mp \delta m_\pm$,

$$0 = D_m \partial_x^2 \delta m_\pm + \tilde{f}_m|_{m_\pm} \delta m_\pm\,. \tag{2.121}$$

One finds that the saturation values of the infinite domain are approached exponentially as

$$m_{\text{stat}}^{\infty}(x) - m_\pm = \mp a_\pm \exp\left(\mp x/\ell_\pm\right)\,, \tag{2.122}$$

with length scale $\ell_\pm^2 = -D_m/\tilde{f}_m|_{m_\pm}$. Here, the amplitude for the Brusselator core reaction kinetics, Eq. (2.72), with the infinite-domain solutions, Eq. (2.117), is given by

$$a_\pm = \sqrt{\frac{2k}{\tilde{d}}}\,. \tag{2.123}$$

Next, to calculate the differences in η_{stat} from the infinite-plateau values, we take into account the concentration deviations $(\delta m_-, \delta m_+)$, Eq. (2.122), within the finite-sized plateaus by expanding Eq. (2.113) around the infinite-domain plateau values to the lowest order in $\delta m_\pm$ and the finite-domain correction to the mass-redistribution potential $\delta\eta_{\text{stat}} = \eta_{\text{stat}}(L_-, L_+) - \eta_{\text{stat}}^{\infty}$,

$$0 = \int_{m_- + \delta m_-}^{m_+ + \delta m_+} \tilde{f}\left(m, \eta_{\text{stat}}^{\infty} + \delta\eta_{\text{stat}}\right) \mathrm{d}m \tag{2.124}$$

$$\approx \frac{1}{2}\tilde{f}_m|_{m_+} \delta m_+^2 - \frac{1}{2}\tilde{f}_m|_{m_-} \delta m_-^2 \tag{2.125}$$

$$+ \delta\eta_{\text{stat}} \int_{m_-}^{m_+} \mathrm{d}m \tilde{f}_\eta(m, \eta_{\text{stat}}^{\infty})\,. \tag{2.126}$$

Solving the latter expression for $\delta\eta_{\text{stat}}$ and taking the derivative with respect to the plateau lengths $L_\pm$ yields

$$\partial_{L_\pm}\eta_{\text{stat}} = \pm\frac{8k}{l_\pm \tilde{d}} \frac{\tilde{f}_m|_{m_\pm}}{F_\eta} \exp\left(-2L_\pm/\ell_\pm\right)\,, \tag{2.127}$$

with shorthand notation

$$F_\eta = \int_{m_-}^{m_+} \mathrm{d}m\, \tilde{f}_\eta\left(m, \eta_{\text{stat}}^{\infty}\right)\,. \tag{2.128}$$

This equation expresses how the mass-redistribution potential η changes when varying the finite plateau length. Starting from a configuration with almost equal lengths, this yields the coarsening rate. Differences in the mass-redistribution potential between two plateau solutions will then drive the flux of mass from one plateau to the other. In the following, we will relate the lengths of the

plateaus directly to plateau masses to finally obtain an expression for the mass redistribution due to coarsening.

In principle, mesa coarsening can occur through two different mechanisms. Namely, on the one hand, high-concentration plateaus can increase their size by shifting their interfaces outwards. Alternatively, two high-concentration mesas can merge by translation towards each other, effectively given by a shrinking low-concentration plateau in between. These two coarsening modes generally have different coarsening rates. For the setup of the two high-concentration plateaus at the outer no-flux boundary conditions discussed in the main text, independent translation of the high-concentration plateaus is not allowed as the overall length of the connecting low-concentration plateau is fixed through mass conservation, $M \approx (n_+ - n_-)\, L_+$. Thus, only the first coarsening mode contributes here. This relation allows us to translate the plateau length change due to coarsening to a change in respective plateau masses via

$$\frac{\partial M}{\partial L_+} = n_+ - n_- \,, \tag{2.129}$$

and we rewrite

$$\partial_{L_+} \eta_{\text{stat}} = (n_+ - n_-)\, \partial_M^+ \eta_{\text{stat}} \,. \tag{2.130}$$

To arrive at the coarsening rate that describes the mass-transfer between two plateaus with almost equal masses, we expand the mass-redistribution dynamics about two plateaus with equal masses

Finally, this gives the linear coarsening rate

$$\begin{aligned} \sigma_c(L) &= -\frac{D_c\, \pi R_0^2}{L_-} \partial_M \eta_{\text{stat}} \\ &= -\frac{6\sqrt{k D_m}}{L_-\,(1 - D_m/D_c)} \exp\left(-2\sqrt{\frac{k}{D_m}} L_\pm\right) . \end{aligned} \tag{2.131}$$

This rate describes the onset of the mass-redistribution dynamics between the two plateaus with minimal mass difference. Neglecting tube corrugations, for a given average tube radius R_0, the latter expression gives the growth rate of mass-differences between two high-concentration plateaus, i.e., $\delta M = M_2 - M_1$, with

$$\partial_t \delta M = \sigma_c(L)\, \delta M \,. \tag{2.132}$$

Noteworthy, the coarsening rate is independent of the tube radius. For all radii, mass-transfer is weighted by the mass differences as expressed through the plateau length. As, in turn, mass fluxes are also weighted by the potential diffusive transport and, thus, the local bulk area, contributions cancel out.

Within planar tubes with constant radii, the coarsening proceeds uninterrupted leading to a final solution with a single high-density plateau located at one side of the domain. However, given that coarsening occurs through the common shift of the plateau interfaces, geometric deformations can affect the coarsening dynamics. The contributions of this geometric effect we want to calculate in the following.

2.8.4 NUMERICAL EVALUATION AND SIMULATIONS

For the analytic solution of derived expressions, i.e., calculations of the combined profiles, response functions, and evaluation of the coarsening criteria, we implemented the derived expressions in Wolfram (Mathematica 14.2)[246]. We complement the analytic treatment with numerical simulations of the derived one-dimensional reaction-diffusion advection equation, Eq. (2.21), as well as the full equations Eq. (2.1) and Eq. (2.2) in a three-dimensional corrugated cylinder geometry. All numerical simulations have been executed with the stated parameters using COMSOL Multiphysics®[251]. As

long as the assumption of relaxing bulk gradients perpendicular to the tube surface is met, the 1d projected dynamics align nicely with the 3d numerical simulations. Note the agreement between analytic predictions and full 3d numerical simulations in Fig. 2.6.

3

Phase separation on deformable membranes: interplay of mechanical coupling and dynamic surface geometry

The self-organization of proteins into enriched compartments and the formation of complex patterns are crucial processes for life on the cellular level. Liquid-liquid phase separation is one mechanism for forming such enriched compartments. When phase-separating proteins are membrane-bound and locally disturb it, the mechanical response of the membrane mediates interactions between these proteins. How these membrane-mediated interactions influence the steady state of the protein density distribution is thus an important question to investigate in order to understand the rich diversity of protein and membrane-shape patterns present at the cellular level. This work starts with a widely used model for membrane-bound phase-separating proteins. We numerically solve our system to map out its phase space and perform a careful, systematic expansion of the model equations to characterize the phase transitions through linear stability analysis and free energy arguments. We observe that the membrane-mediated interactions, due to their long-range nature, are capable of qualitatively altering the equilibrium state of the proteins. This leads to arrested coarsening and length-scale selection instead of simple demixing and complete coarsening. In this study, we unambiguously show that long-range membrane-mediated interactions lead to pattern formation in a system that otherwise would not do so. This work provides a basis for further systematic study of membrane-bound pattern-forming systems.

3.1 INTRODUCTION

Self-organization in the absence of external guiding cues is a key principle in the creation and maintenance of cellular structures. One important mechanism for forming structures and enriched compartments is liquid-liquid phase separation[26,27], whereby local interactions between components like proteins or lipids induce demixing into a dense and a dilute phase[64]. Phase separation also occurs on cellular lipid membranes, where it leads to the formation of domains such as lipid rafts[28,29] or enriched protein clusters[30,31]. Such domains are crucial for cellular functions such as polarization[255], sensing[33,256], and membrane transport[257].

In all these cases, the lipid bilayer membrane acts as an elastic manifold with embedded proteins. This can lead to mutual feedback between the spatial organization of membrane-bound proteins and the mechanical properties of the membrane via interactions that are influenced by the geometry of the membrane surface. For instance, intracellular proteins can alter properties like the bending rigidity of lipid bilayer membranes[225,258] or may cause deformations due to their intrinsic curvature[137,259,260]. A well-studied instance of phase-separating membrane-bound proteins that induce curvature involves BAR domains, which form high-density and dilute regions on the membrane[227,260]. Lipid-demixing in multi-component membranes is another example of biological liquid-liquid phase separation, in which lipid-localization can affect local membrane curvature[32] as well as the local protein composition[33]. This highlights the importance of the dynamic interplay between phase-separation dynamics and mechanical deformations of surfaces.

Theoretical and experimental studies have explored how membrane curvature influences the demixing and positioning of lipids and membrane-embedded proteins in response to externally induced (static) membrane deformations[261–263]. In particular, it has been reported that local curvature induced by micropipette aspiration induces curvature-dependent lipid sorting in biomembranes[264]. Other experimental studies demonstrated phase separation and sorting of lipid rafts in giant unilamellar vesicles upon induction of varying curvatures[265–267].

The crucial role of membrane curvature for pattern formation of curvature-sensing and curvature-inducing proteins and lipids has also inspired various theoretical studies on the dynamic interplay between membrane mechanics and liquid-liquid phase separation[268–271]. These theoretical analyses primarily focus on the onset of phase separation and membrane deformations from the initial spatially uniform and flat state, but often do not investigate the subsequent (nonlinear) dynamics leading to a steady state. Two recent studies have gone beyond the emergence of patterns and studied these nonlinear dynamics that result from the interplay between phase separation and mechanical deformations[34,35]. Using an expansion of their model equations that assumes weak membrane deformations, these authors find that phase separation is altered by the membrane-mediated interactions between proteins[35] and that membrane-mediated lipid-lipid interactions lead to a length-scale selec-

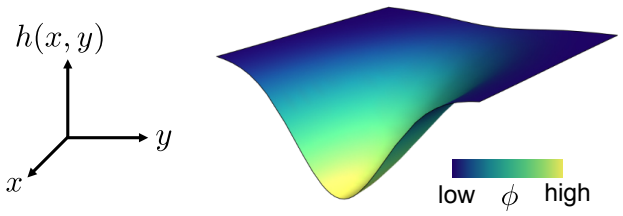

Figure 3.1: Illustration of the model for phase separation on a deformable membrane surface, in which protein density and membrane conformations are mechanically coupled. On the membrane surface, represented in the Monge parametrization by a height field $h(x, y)$, proteins induce local curvature that scales with their concentration $\phi(x, y)$ (color code). This figure is reproduced from Ref.[2] under license [CC BY 4.0].

tion of emerging patterns[34]. However, these theoretical studies leave aside two crucial aspects of the dynamics. Firstly, the analysis in Ref.[34] neglects the impact of temporal changes in membrane surface area on protein and lipid concentrations, thereby only approximately preserving mass-conservation on the deformable surface for weak deformations. Second, both studies disregard significant contributions from spatial changes in the membrane metric, that affect local interactions between the phase-separating components and the entropic contributions mediated by changes in membrane area. Consequently, the question of how the dynamic interplay between membrane geometries and curvature-inducing phase-separating proteins affects protein dynamics remains unresolved.

Here, we investigate how membrane-mediated interactions influence phase separation of membrane-bound proteins. We model the thermodynamics of the protein-lipid system using the Flory-Huggins free energy for a symmetric binary mixture[272,273]. The mechanical deformations of the liquid membrane are described by the Canham-Helfrich free energy[274,275], which accounts for bending energy and surface tension. The dynamics of protein densities and membrane deformations are assumed to be coupled mechanically. Specifically, we follow the well-established literature[268] and examine proteins that cause spontaneous local curvature proportional to their density on the membrane. This assumption is supported by experimental studies of BAR domains[138,227,276] and clathrin complexes[277,278], where the coupling forces the membrane to locally conform to the (potentially anisotropic) curvature induced by the protein coating, as illustrated in Fig. 3.1. In a similar fashion, recent experiments emphasize the induction of membrane curvature by lipid-membrane-attached MinD proteins in giant vesicles which gives rise to blebbing and protein-controlled vesicle shape oscillations[231,279].

What are the implications of the coupling between protein densities and membrane deformations for the dynamics of phase separation? While the proteins undergo phase separation and aggregation in droplet-like domains, they induce membrane deformations, which, in turn, alter the dynamics of the protein density. In particular, a dynamically deforming membrane affects the protein dynamics through a spatially and temporally varying surface metric, changing the local concentration gradients of proteins and their interactions with neighboring proteins.

We present a general covariant description of phase-separation dynamics on dynamic membrane surfaces. Our theory fully accounts for the effects of spatio-temporal changes in the governing metric, mass-conservation, and the mechanical coupling through isotropic protein-induced curvatures. This framework is versatile and can be applied to analyze more complex phase-separating systems involving multiple components or active out-of-equilibrium contributions.

For the generic model system discussed, we find that mechanical coupling induces two distinct phase-separating (spinodal) instabilities: a classical long-wavelength Cahn-Hilliard instability, which is also present in the absence of geometric coupling, and a conserved Turing instability, characterized by a band of unstable modes that are bound away from zero wavevector but including it as a marginal mode[280]. Depending on the mechanical coupling parameters, we observe steady-state patterns with geometrically arrested coarsening dynamics and we determine the pattern length scales based on thermodynamic arguments. Overall, our study uncovers the mechanical coupling via deformable membranes as a mechanism behind membrane-mediated pattern formation and provides a conceptual basis for systematic investigation of membrane-bound pattern-forming systems.

The paper is organized as follows: Section 3.2 introduces our model for liquid-liquid phase separation on dynamic membranes with mechanical coupling. We combine free energy contributions for the fluid membrane and protein-protein interactions and implement the geometric coupling via a spontaneous curvature of the proteins. Additionally, we introduce dimensionless parameters and identify those crucial for tuning the strength of the interactions between the elastic (membrane) and chemical (protein) contributions to the free energy. Finally, we give the dynamic equations that govern the evolution of the membrane shape and the protein density. These equations comprehensively describe the spatiotemporal variations of the membrane metric. They detail how the elastic properties of the membrane affect protein-protein interactions and mechanical coupling. In section 3.3, we present the results of our numerical simulations, establishing that our system exhibits arrested coarsening and length-scale selection for strong coupling between membrane and protein densities. In section 3.4, we connect numerical and analytical findings on the basis of linear stability analysis. We examine the problem from two perspectives. Firstly, we conduct a classical linear stability analysis of the dynamic equations, identifying different types of instability with their associated dispersion relations of unstable modes. Secondly, we study the soft modes of an expanded, effective free energy of the proteins, which we determine by integrating out the degrees of freedom related to membrane fluctuations. Consistently, this approach provides analytical expressions for distinguishable instability types and the initial pattern length scale. In section 3.5, we further develop this thermodynamic reasoning and successfully predict the onset of arrested coarsening. Additionally, we derive an analytic estimate for the mechanical length-scale selection of the final steady-state patterns. Finally, we discuss our findings and shortly outline how our work may be generalized to other systems in section 3.6. This study is supported by six appendices (Section 3.7): Appendix 3.7.1 provides the derivation of the dynamic equations, while Appendix 3.7.2 gives details of the numerical simulations. In appendices 3.7.3 and 3.7.4, we describe in detail the linear stability analysis based on the dynamic equations and the effective free energy, respectively. We comment on the comparison between the two approaches in Appendix 3.7.5. Appendix 3.7.6 contains details on the distance measure applied to obtain the steady-state pattern length scales in the numerical simulations.

3.2 PROTEIN-MEMBRANE DYNAMICS

To investigate the influence of mechanical interactions on the phase separation of proteins, we construct a minimal dynamical model that takes into account both protein-protein and membrane-mediated interactions. We assume that the protein-membrane system relaxes towards thermodynamic equilibrium via gradient dynamics that respect conservation laws. To model this process, we establish dynamic equations based on the principles of non-equilibrium thermodynamics. Crucially, when formulating the free energy functional and the corresponding dynamic equations, one has to consider dynamical changes in the surface metric that arise from the deformations of the membrane surface.

3.2.1 FREE-ENERGY FUNCTIONAL

We base our study on the free energy functional

$$\mathcal{F}[\phi, C] = \int \mathrm{d}A \left\{ f[\phi, g_{ab}] + e[\phi, C] \right\}, \tag{3.1}$$

comprised of the functionals for the free energy densities of the proteins on the membrane, $f[\phi, g_{ab}]$, and the local conformations of the membrane itself, $e[\phi, C]$. Both of these functionals, as we will discuss in detail below, depend on the protein area fraction ϕ on the membrane and the membrane conformation, given in terms of the curvature C, which is the sum of the principal curvatures, and the metric tensor g_{ab} of the membrane surface, where $a, b \in \{1, 2\}$. Moreover, for a parametrization (u, v) of the membrane surface, the infinitesimal surface element is given by $\mathrm{d}A = \sqrt{g}\,\mathrm{d}u\,\mathrm{d}v$, where g is the determinant of the metric tensor of the curved membrane surface.

We assume that the functional of the free energy density for the proteins is given by the standard Flory-Huggins (FH) theory for a symmetric binary mixture (of proteins and lipids)[90,272,273]

$$f[\phi, g_{ab}] = \rho_s \, k_B T \Big[f(\phi) + \frac{\chi}{4\rho_s} \, |\boldsymbol{\nabla}\phi|^2 \Big] \,, \tag{3.2}$$

with the local part

$$f(\phi) := \phi \ln \phi + (1-\phi) \ln(1-\phi) + \chi \, \phi \, (1-\phi) \,. \tag{3.3}$$

In particular, ϕ denotes the protein area fraction on the membrane with a saturation density $\rho_s = 1/v$ given as the inverse of the two-dimensional molecular volume v. In the following, we will measure all lengths in units of $a \equiv \sqrt{v}$, setting $\rho_s = 1$. While the first two terms describe entropic mixing, the terms proportional to the (dimensionless) Flory-Huggins parameter χ characterize the interaction between the proteins. Since the membrane is generally deformed, the differential operator $\boldsymbol{\nabla}$ denotes the covariant derivative on the curved membrane, such that $|\boldsymbol{\nabla}\phi|^2 = (\partial_a \phi)(\partial_b \phi) g^{ab}$. Thus, the FH free energy density becomes a functional of the membrane conformation. For the functional of the free energy density of the membrane conformations, we assume a Canham-Helfrich form[274,275]

$$e[\phi, C] \equiv e(\phi, C) = \frac{\kappa}{2} \big(C - C_0 \phi \big)^2 + \sigma \,. \tag{3.4}$$

It accounts for the free energy costs associated with membrane curvature C and area changes, characterized by two parameters, the surface tension σ and bending rigidity κ. We consider a total spontaneous membrane curvature mediated by the proteins bound to the membrane. For simplicity, we assume a linear dependence on the protein concentration ϕ with a proportionality factor C_0[281], which describes the mechanical coupling in the system. Hence, the coupling constant C_0 determines the extent to which the proteins influence the curvature of the membrane.

Assuming the absence of overhangs, we describe the membrane deformation using a Monge parametrization, representing the membrane surface as a height profile $\mathbf{r} = (x, y, h(x,y))^T$. Then, the membrane curvature[282] is given by

$$C = \boldsymbol{\nabla}_\perp \cdot \left[\frac{\boldsymbol{\nabla}_\perp h}{\sqrt{1 + (\boldsymbol{\nabla}_\perp h)^2}} \right] , \tag{3.5}$$

where $\boldsymbol{\nabla}_\perp = \hat{\mathbf{x}} \, \partial_x + \hat{\mathbf{y}} \, \partial_y$ denotes the two-dimensional gradient operator on the base plane, with unit vectors $\hat{\mathbf{x}}$, $\hat{\mathbf{y}}$ spanning the parametrization domain. The metric tensor is given by

$$g_{ab} = \begin{pmatrix} 1 + (\partial_x h)^2 & (\partial_x h)\,(\partial_y h) \\ (\partial_y h)\,(\partial_x h) & 1 + (\partial_y h)^2 \end{pmatrix} \tag{3.6}$$

and its determinant is $g = 1 + (\boldsymbol{\nabla}_\perp h)^2$.

3.2.2 COUPLED GRADIENT DYNAMICS OF PROTEIN DENSITY AND MEMBRANE CONFORMATION

We assume that the temporal evolution of the height field $h(x,y,t)$ and the concentration field $\phi(x,y,t)$ follow gradient dynamics, neglecting hydrodynamic effects other than friction. For the fluid membrane conformations, we use relaxational dynamics

$$\partial_t h = -\gamma \, \frac{\delta \mathcal{F}}{\delta h} \,, \tag{3.7}$$

where γ is a positive Onsager coefficient; accounting for fluid dynamics beyond friction would require a more elaborate approach[283].

To set up the equation for the protein dynamics, one starts from the conservation law for the number of proteins, which for an arbitrary domain Ω with boundary $\partial\Omega$ on the membrane surface

reads

$$\partial_t \int_\Omega \mathrm{d}A\, \phi = -\int_{\partial\Omega} \mathrm{d}l\, \mathbf{J}\cdot\mathbf{n}\,, \tag{3.8}$$

where $\mathbf{J}$ denotes the protein density current and $\mathbf{n}$ the outer normal of Ω. Using Stoke's theorem and the surface element $\mathrm{d}A = \sqrt{g}\,\mathrm{d}x\mathrm{d}y$, and noting that a dynamically deforming membrane surface has a time-dependent metric, this results in a modified continuity equation[244,284]

$$\frac{1}{\sqrt{g}}\,\partial_t\,(\sqrt{g}\,\phi) = -\boldsymbol{\nabla}\cdot\mathbf{J}\,. \tag{3.9}$$

Close to thermodynamic equilibrium the particle current $\mathbf{J}$ is given by the gradient of the chemical potential, $\mathbf{J} = -M\boldsymbol{\nabla}\mu$, with a constant mobility M related to the diffusion constant D and the thermal energy scale by the Einstein relation $M = D/k_\mathrm{B}T$[285]. The chemical potential μ is given by the functional derivative of the free energy functional with respect to the area fraction, $\mu = \delta\mathcal{F}/\delta\phi$. This results in a covariant form of the Cahn-Hilliard equation[286,287] that accounts for a time-dependent metric,

$$\frac{1}{\sqrt{g}}\,\partial_t\,(\sqrt{g}\phi) = M\,\boldsymbol{\nabla}^2\frac{\delta\mathcal{F}}{\delta\phi}\,, \tag{3.10}$$

where $\boldsymbol{\nabla}^2$ is the Laplace-Beltrami operator

$$\boldsymbol{\nabla}^2 = \frac{1}{\sqrt{g}}\,\partial_a\left[\sqrt{g}\,g^{ab}\partial_b\right]\,. \tag{3.11}$$

Note that Eq. (3.10) gives the protein dynamics in a covariant form and therefore, is valid for arbitrary surfaces that give rise to the metric g_{ab}. Thus it introduces no further approximations beyond the Monge representation and should, therefore, be exact as long as overhangs in the membrane conformations are negligible.

Taken together, Eqs. (3.7) and (3.10) describe the coupled close-to-equilibrium dynamics of proteins and fluid membranes. The proteins undergo phase separation, simultaneously inducing spontaneous curvature on the deformable membrane. This mechanical coupling influences the bending dynamics of the membrane, which in turn affects the protein dynamics through geometric effects encoded in the dynamic metric of the membrane surface.

3.2.3 NON-DIMENSIONALIZATION AND CHOICE OF PARAMETERS

We now further non-dimensionalize the set of dynamic equations, Eqs. (3.7) and (3.10). In addition to rescaling length in units of the protein size $a \equiv 1/\sqrt{\rho_\mathrm{s}}$ we rescale time by the corresponding diffusive time scale $\tau \equiv 1/(D\rho_\mathrm{s})$. The main dimensionless parameters determining the mechanical feedback are the bending rigidity $\kappa/k_\mathrm{B}T \to \kappa$, expressed in units of the thermal energy $k_\mathrm{B}T$, the FH parameter χ, and the protein-induced curvature $C_0/\sqrt{\rho_\mathrm{s}} \to C_0$ in units of the protein size. To focus on the impact of these key parameters on the mechanical feedback, we keep the dimensionless surface tension $\sigma/(k_\mathrm{B}T\rho_\mathrm{s}) \to \sigma$ and the Onsager coefficient $\gamma\rho_\mathrm{s}k_\mathrm{B}T/D \to \gamma$ constant throughout the following analysis.

All parameter ranges are chosen to mirror typical values found for membrane proteins, for instance, BAR domains or clathrin[260,288]; see Table 3.1. Accordingly, we choose the system size $L = 2\,\mu\mathrm{m}$, the bending rigidity in the range $\kappa = 0 - 40\,k_\mathrm{B}T$ [289], the spontaneous protein curvature in the range $C_0 = 0 - 0.04\,\mathrm{nm}^{-1}$ [290], the membrane surface tension $\sigma \approx 1\cdot 10^{-4}\,\mathrm{pN\,nm}^{-1}$ [291], and the protein size $1/\sqrt{\rho_\mathrm{s}} \approx 55\,\mathrm{nm}$ [292]. Note that there is a wide range of values of σ reported in the literature since it can describe different physics. Here we choose a small value of sigma, which represents the cost of pulling area from a reservoir of thermal fluctuations.

To focus on the impact of membrane-mediated interactions on the evolving patterns, we fix the

Table 3.1: Ranges of values of the dimensionless parameters in units of the chosen scales (indicated within brackets) taken from Refs.[289–292], as specified in the main text.

χ	> 0	protein interaction
$C_0\,[\sqrt{\rho_s}]$	$0 - 1.2$	protein curvature
$\sigma\ [k_\mathrm{B}T\rho_\mathrm{s}]$	0.16	surface tension
$\kappa\ [k_\mathrm{B}T]$	$0 - 40$	bending rigidity
$\gamma\ [D/k_\mathrm{B}T\rho_\mathrm{s}]$	1	Onsager coefficient

protein interaction parameter to $\chi = 3$ throughout this study, unless stated otherwise. Due to mass conservation, the total protein mass is fixed and is determined by the initial condition. As our initial condition, we choose a flat membrane with a homogeneous density of $\phi_0(x, y) = 0.3$, thus the initial average area fraction is $\bar{\phi} = \frac{1}{A}\int \mathrm{d}A\,\phi(x, y) = 0.3$.[1] This choice results in spinodal decomposition on flat membranes, as for $\bar{\phi} = 0.3$ the FH parameter $\chi = 3$ significantly exceeds the spinodal line $\chi_s \approx 2.38$. Additionally, we assume that the time scale of the protein dynamics is comparable to that of the membrane dynamics $\gamma = 1$.

3.2.4 DYNAMIC EQUATIONS AND THEIR INTERPRETATION

We close this section by summarizing the dynamic equations in their dimensionless form. The dynamics of the protein density is given by a generalized Cahn-Hilliard equation that fully accounts for the dynamics of the metric tensor,

$$\frac{\partial_t(\sqrt{g}\,\phi)}{\sqrt{g}} = \boldsymbol{\nabla}^2\left[\partial_\phi f(\phi) + \partial_\phi e(\phi, C) - \frac{\chi}{2}\boldsymbol{\nabla}^2\phi\right], \tag{3.12}$$

where the additional term $\partial_\phi e(\phi, C) = -\kappa C_0\phi\,(C - C_0\phi)$ describes the coupling of the protein density to the membrane curvature. The local term now reflects the competition between minimizing the free energy of the protein system and minimizing the mechanical deformation energy of the membrane.

In the absence of a coupling to a protein density, the membrane dynamics is driven by the surface tension σ and the bending rigidity κ of the membrane[293]

$$\frac{1}{\gamma}\,\partial_t h = \sigma\,C - \kappa\left[\boldsymbol{\nabla}^2 C + \frac{C}{2}\left(C^2 - 4C_\mathrm{G}\right)\right], \tag{3.13}$$

where $C_\mathrm{G} = g^{-2}\det[\partial_a\partial_b h]$ denotes the Gaussian curvature. Accounting for the mechanical coupling we obtain (see appendix Section 3.7.1 for details)

$$\begin{aligned}\frac{1}{\gamma}\,\partial_t h = &\left[f[\phi, g_{ab}] + e(\phi, C)\right]C - \kappa\boldsymbol{\nabla}^2(C - C_0\phi)\\ &+ \kappa\,(C - C_0\phi)\,(-C^2 + 2C_\mathrm{G})\\ &- \tfrac{1}{2}\chi\,C^{ab}\,(\partial_a\phi)(\partial_b\phi)\,,\end{aligned} \tag{3.14}$$

where $C_{ab} = g^{-1/2}\partial_a\partial_b\,h$ denotes the curvature tensor. This still has the overall structure of the dynamic shape equation, Eq. (3.13), with a few essential new features. The first term now has as a prefactor the total free energy functional including the contributions from the protein interactions. The spatial gradients in the curvature are now given relative to the spontaneous curvature imposed by the protein density distribution. The third contribution from the bending rigidity is no longer

[1] Note that in our system, the total mass $\int \mathrm{d}A\,\phi(x, y)$ is conserved. Thus, if the considered surface area $A = \int \mathrm{d}A$ changes over time due to deformations, this will result in dynamic changes in the average protein area fraction $\bar{\phi}$.

weighted with the membrane curvature but with its deviation from the protein-imposed preferred curvature. The final term couples the curvature tensor to the gradients in the protein distribution. Notably, upon defining the deviatoric stress tensor

$$\Sigma^D_{ab} = \frac{\chi}{2}\left[\frac{1}{2}(\partial_c\phi)(\partial_d\phi)g^{cd}g_{ab} - (\partial_a\phi)(\partial_b\phi)\right], \tag{3.15}$$

one can rewrite the equation as

$$\begin{aligned}\frac{1}{\gamma}\,\partial_t h = &\left[f(\phi) + e(\phi, C)\right] C - \kappa\boldsymbol{\nabla}^2(C - C_0\phi)\\ &+ \kappa\,(C - C_0\phi)\,(-C^2 + 2C_{\mathrm{G}})\\ &+ C^{ab}\,\Sigma^D_{ab}\,.\end{aligned} \tag{3.16}$$

Now the first term contains only the local free energy contributions and the gradients in the protein density are absorbed into the deviatoric stress tensor (last term). To leading order in the curvature, this equation reduces to

$$\frac{1}{\gamma}\,\partial_t h = \sigma(\phi)\,C - \kappa\boldsymbol{\nabla}^2(C - C_0\phi) + C^{ab}\,\Sigma^D_{ab}\,, \tag{3.17}$$

with an effective tension term

$$\sigma(\phi) = \sigma + f(\phi) + \tfrac{1}{2}\kappa\,C_0^2\,\phi^2\,. \tag{3.18}$$

This effective tension incorporates the original surface tension σ, a thermodynamic term related to the protein free energy density $f(\phi)$, and one mechanical term that arises from the protein-induced curvature C_0.

Finally, linearizing in the height profile with $g_{ab} = \delta_{ab} + \mathcal{O}(h^2)$ one obtains:

$$\begin{aligned}\frac{1}{\gamma}\,\partial_t h = &\,\sigma(\phi)\,\boldsymbol{\nabla}^2_\perp h - \kappa\boldsymbol{\nabla}^2_\perp(\boldsymbol{\nabla}^2_\perp h - C_0\phi)\\ &+ \Sigma^D_{ab}\,(\partial_a\partial_b h)\,,\end{aligned} \tag{3.19}$$

where we assume summation over repeated indices. For these three terms, we now have the following physical interpretation. The first term represents a generalized surface tension, which includes the bare membrane tension, a surfactant-like term due to the local free energy costs for the protein density, and a mechanical term due to the spontaneous curvature induced by the proteins. The second term accounts for the bending cost of the membrane relative to the configuration defined by the protein-induced spontaneous curvature profile $C_0\phi$. The third term describes the coupling between the deviatoric stress of the protein density and the curvature tensor of the membrane.

3.3 OSTWALD RIPENING AND ARRESTED COARSENING

In this section, we present results from numerical solutions (appendix Section 3.7.2) of the dynamic equations, Eqs. (3.12) and (3.14), to analyze the impact of the mechanical feedback on protein pattern formation and the system's coarsening behavior as a function of the protein-induced curvature C_0. As discussed in the previous section, we choose the remaining parameters such that on a flat, non-deformable membrane, the homogeneous steady state $\phi(x, y) = \bar{\phi}$ is unstable against small spatial perturbation, i.e., the system is in the spinodal decomposition regime.

For small induced spontaneous curvatures, such as $C_0 = 0.05$, the influence of membrane geometry on the phase separation dynamics of proteins is nearly negligible, resulting in dynamics similar to classical Ostwald ripening described by the Cahn-Hilliard equation, cf. Fig. 3.2(a). After an initial perturbation of the homogeneous steady state $\phi_0 = 0.3$, multiple high-density droplets form, and

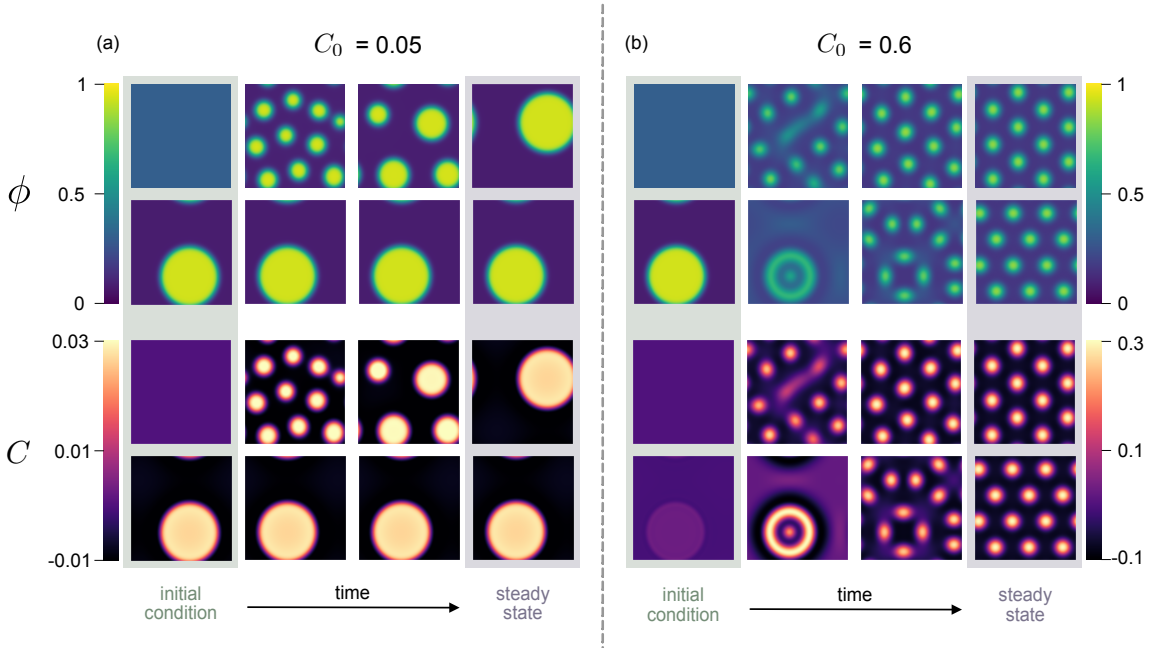

Figure 3.2: Time evolution of the protein area fraction $\phi(x, y, t)$ (color scale, top) and corresponding membrane curvature $C(x, y, t)$ (color scale, bottom) for two different protein-induced curvatures $C_0 = 0.05$ (a) and $C_0 = 0.6$ (b). The respective upper and lower time sequences show the dynamics that emerge from two distinct initial conditions: a protein area fraction $\phi_0(x, y) = 0.3 + \xi$ with Gaussian zero-mean white noise ξ of amplitude $\sim 5 \times 10^{-4}$ (upper rows), and a single droplet (lower rows). The remaining dimensionless parameters are chosen as follows $\sigma = 0.16$, $\gamma = 1$, $\kappa = 20$, and $\chi = 3$. Spinodal decomposition and coarsening dynamics are observed for $C_0 = 0.05$. The final steady state is a single droplet. In contrast, for $C_0 = 0.6$, the steady state comprises multiple droplets. Starting from a random protein distribution, droplets form by spinodal decomposition, but the coarsening process is eventually arrested. Moreover, an initial single droplet state is unstable and splits into multiple droplets. This figure is reproduced from Ref.[2] under license [CC BY 4.0].

larger droplets subsequently grow at the expense of smaller ones (top row in Fig. 3.2(a)). The Ostwald ripening process continues until only a single droplet remains[294,295]. Consistently, when simulations are initialized with a single droplet, it remains stable over time; see the second row in Fig. 3.2(a) for $C_0 = 0.05$.

In contrast, when the protein-induced curvature is increased to $C_0 = 0.6$, the effects of the mechanical feedback become increasingly prominent. The onset of pattern formation from a homogeneous steady state is similar for $C_0 = 0.05$ and $C_0 = 0.6$, but is delayed for the larger value of protein-induced curvatures; see Fig. 3.2(b). Remarkably, in contrast to standard Cahn-Hilliard dynamics, the mechanical feedback arrests the Ostwald ripening process, and a regular pattern with a preferred droplet size emerges as the system's steady state. To verify that the mechanical deformations induce a length-scale selection, we also performed numerical simulations of the dynamics starting from a single droplet as an initial condition; Fig. 3.2(b), second row. One observes that the initial droplet nearly dissolves into the surrounding low-density phase, giving rise to a pattern with twelve droplets. We attribute this to the high cost of membrane deformation associated with large protein aggregates, which leads to a gradual dissolution of a single droplet into several smaller ones.

In summary, the mechanical coupling through protein-induced curvature not only arrests the Ostwald ripening process but also facilitates the selection of a well-defined wavelength in the final steady-state patterns. In the following chapters, we use linear stability analysis and thermodynamic arguments to investigate the underlying mechanism.

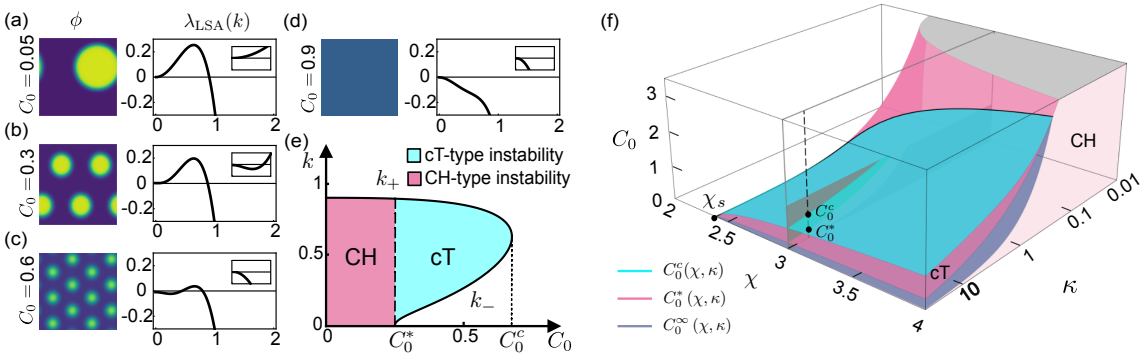

Figure 3.3: Linear stability analysis; (a-d) Dispersion relations $\lambda_{\mathrm{LSA}}(k)$ (right) and the corresponding steady-state concentration profiles $\phi(x, y)$ (left) for $\chi = 3$ and varying protein-induced curvatures $C_0 = 0.05, 0.3, 0.6$, and 0.9, respectively. Color scale as in Fig. 3.2 for $\phi \in [0, 1]$. Insets show zoom-ins of the dispersion relations at small wave numbers k. (e) Band of unstable modes (k_-, k_+) as a function of the protein-induced curvature C_0. For $C_0 < C_0^*$, there is a long wavelength *Cahn-Hilliard-type* (CH-type) instability with the band extending to zero wavevector, $k_- = 0$. Above the threshold value C_0^* (dashed line), the dispersion relation changes from a CH-type long wavelength instability (magenta) to a *conserved Turing-type* (cT-type) instability, in which the band of unstable modes is bound away from $k = 0$, but connects to the marginal mode $k = 0$ (cyan). Above a critical value C_0^c, lateral instabilities are absent (dotted line). (f) Bifurcation diagram derived from the dispersion relation of the effective free energy λ, Eq. (3.29), as a function of the protein-induced curvature C_0, the FH parameter χ, and the bending stiffness κ, which shows the boundaries for a CH-type instability (magenta, middle) and a cT-type instability (cyan, upper). Also shown is the boundary between coarsening and arrested coarsening (dark blue, lower) derived from the effective free energy functional (C_0^∞, Eq. (3.34)). The dashed line indicates the parameters corresponding to (a-d) and the gray plane the parameter ranges of C_0 and κ corresponding to the simulation results shown in Fig. 3.5. All other model parameters as specified in Table 3.1. This figure is reproduced from Ref.[2] under license [CC BY 4.0].

3.4 LINEAR STABILITY ANALYSIS

To better understand the dynamics and the emerging patterns, we perform a linear stability analysis (LSA) of the coupled protein and membrane dynamics, Eq. (3.12) and Eq. (3.14), around a spatially homogeneous steady state. We start with a linear stability analysis of the full dynamic equations and investigate the dispersion relation for varying protein-induced curvature C_0. In addition, we exploit the thermodynamic nature of the system to obtain analytical expressions for the dispersion relation and the phase boundaries using free energy arguments.

3.4.1 LINEAR STABILITY ANALYSIS OF THE DYNAMIC EQUATIONS

To perform a linear stability analysis of Eqs. (3.12) and (3.14) around a spatially homogeneous state we consider small perturbations $\delta h(\mathbf{x})$ and $\delta\phi(\mathbf{x})$ with respect to a steady state with spatially uniform concentration and height fields (ϕ_0, h_0); the detailed mathematical analysis is given in appendix Section 3.7.3.

Figure 3.3(a-d) displays the corresponding dispersion relations $\lambda_{\mathrm{LSA}}(k)$, i.e., growth rates as a function of the wavevector k, for a set of different protein-induced curvatures C_0 and fixed values for $\chi = 3$ and $\kappa = 20$. Depending on the magnitude of C_0, we observe qualitatively different instabilities. For small parameter values, e.g., $C_0 = 0.05$, the instability is of type-II[36], i.e., a long wavelength instability with a band of unstable modes $(0, k_+)$ extending to zero wavevector. This is the same type of instability as obtained for the spinodal decomposition regime of the Cahn-Hilliard model in flat geometry (*Cahn-Hilliard-type instability*). Above a threshold value $C_0^* \approx 0.25$, the dispersion relation becomes qualitatively different and exhibits a band of unstable modes (k_-, k_+) that is bound away from $k = 0 < k_-$ such that long wavelength modes are stable; note however that the dispersion relation approaches zero in the limit $k \to 0$. We refer to this type-I[36] lateral instability as a *conserved Turing-type instability*, following a recent suggestion in Refs.[37,280]. For even larger protein-induced curvature above the threshold value $C_0^c \approx 0.68$, LSA predicts linear stability of the homogeneous steady state as the largest growth rates $\lambda_{\mathrm{LSA}}(k)$ for all modes are non-positive, Fig. 3.3(d). We attribute this to the stabilizing effect of the mechanical feedback. Since curvature mismatches are

always associated with energetic costs, these costs must exceed the free energy gain from the protein mixing entropy at a certain threshold value of protein-induced curvature, so that the homogeneous steady state becomes energetically favorable.

3.4.2 EFFECTIVE FREE ENERGY IN THE WEAKLY BENDING LIMIT AND LINEAR STABILITY ANALYSIS

Since we are considering the dynamics of a system relaxing into thermodynamic equilibrium, we can take advantage of the fact that the equilibrium steady state is encoded in the free energy functional. Our starting point is the free energy functional, Eq. (3.1), together with the corresponding expressions for the local free energies for the protein density ϕ and the membrane height undulations h, Eq. (3.2) and Eq. (3.4), rewritten in their non-dimensional form, Eqs. (3.12) and (3.14).

WEAKLY BENDING APPROXIMATION

If one assumes that the gradients in the height fluctuations of the membrane are weak, the surface element can be approximated as

$$\mathrm{d}A \approx \mathrm{d}x\,\mathrm{d}y\left(1+\tfrac{1}{2}|\boldsymbol{\nabla}_\perp h|^2\right). \tag{3.20}$$

Note that this yields a surface tension term for the membrane of the form $\frac{1}{2}\sigma\int \mathrm{d}^2x\,(\boldsymbol{\nabla}_\perp h)^2$ but in the same way also multiplies all the terms in the Flory-Huggins free energy. This has, as we will see below, important implications for the equilibrium steady state patterns since it gives rise to an effective surface tension. Moreover, we approximate the membrane curvature by its leading order term

$$C \approx \boldsymbol{\nabla}_\perp^2 h\,, \tag{3.21}$$

where $\boldsymbol{\nabla}_\perp^2 = \partial_x^2 + \partial_y^2$. Taken together, this weakly bending approximation results in a free energy functional which is quadratic in the height fluctuations, and the part depending on the bending modes is given by

$$\begin{aligned}\mathcal{F}_{\text{bend}} = \int \mathrm{d}^2x \Big\{ &\tfrac{1}{2}\kappa\big(\boldsymbol{\nabla}_\perp^2 h - C_0\phi\big)^2 \\ &+ \tfrac{1}{2}\Big[\sigma + f(\phi) + \tfrac{1}{2}\kappa C_0^2\phi^2 + \tfrac{1}{4}\chi(\boldsymbol{\nabla}_\perp\phi)^2\Big](\boldsymbol{\nabla}_\perp h)^2\Big\}\,.\end{aligned} \tag{3.22}$$

To proceed further, we assume that in the term proportional to $(\boldsymbol{\nabla}_\perp h)^2$ one can replace the protein density field ϕ by its spatial average $\bar{\phi}$ such that the free energy becomes quadratic in both the protein density and the height field.

Then, the corresponding harmonic part of the total free energy functional can approximately be written in Fourier space as follows:

$$\begin{aligned}\mathcal{F}_{\text{bend}} \approx \sum_k \Big\{ &\tfrac{1}{2}\left[\kappa k^4 + \sigma(\bar{\phi})k^2\right]|h_k|^2 \\ &+\tfrac{1}{2}\kappa C_0^2|\phi_k|^2 + \kappa C_0 k^2 h_k\phi_k^*\Big\}\,,\end{aligned} \tag{3.23}$$

with the effective tension

$$\sigma(\bar{\phi}) = \sigma + f(\bar{\phi}) + \tfrac{1}{2}\kappa\, C_0^2\bar{\phi}^2\,. \tag{3.24}$$

The two additional terms, other than the membrane surface tension σ, arise from the changed free energy costs or gains associated with protein coverage of the membrane (second term) and the induced spontaneous curvature (third term). These contributions can be interpreted as a type of “surfactant" effect. Just as surfactants alter the properties of liquid interfaces by modifying surface tension, these additional terms adjust the membrane’s surface energy. Specifically, the proteins’ influence can either stabilize or destabilize the membrane, akin to how surfactants can either reduce

or enhance surface tension. We focus on parameter regimes where this effective surface tension remains positive, as a negative value would signify an instability in the overall system.

Given the harmonic form of the coupling term in Eq. (3.23), one can perform the path integral in the partition sum over the bending modes by completing the square. Thereby, one obtains an effective coupling term of the form

$$\mathcal{F}_{\text{coupling}} = \frac{1}{2}\sum_k \left[\kappa C_0^2 - \frac{(\kappa\, C_0)^2 k^2}{\sigma(\bar{\phi}) + \kappa k^2}\right] |\phi_k|^2 \,, \tag{3.25}$$

where the summation runs over all Fourier modes compatible with the chosen boundary conditions (typically chosen as periodic boundary conditions). Combining this effective coupling term with the remainder of the FH free energy gives us the following effective total free energy functional

$$\begin{aligned}\mathcal{F}_{\text{eff}}[\phi_k] = \frac{1}{2}\sum_k \left[\kappa C_0^2 - \frac{(\kappa C_0)^2 k^2}{\sigma(\bar{\phi}) + \kappa k^2} + \tfrac{1}{2}\chi k^2\right] |\phi_k|^2 \\ + \int \mathrm{d}^2x\; f(\phi)\,.\end{aligned} \tag{3.26}$$

Importantly, the effective coupling term, which is due to the long-range nature of the membrane-mediated interactions, changes the physics at large length scales. In contrast to the original stiffness term $\frac{1}{4}\chi\, k^2|\phi_k|^2$ in the FH free energy, it behaves differently at long wavelengths. Thus, for a finite surface tension $\sigma(\bar{\phi})$, one finds asymptotically in the long wavelength limit, $|k| \ll \sigma(\bar{\phi})/\kappa$,

$$\mathcal{F}_{\text{coupling}} \approx \frac{1}{2}\sum_k \left[\kappa C_0^2 - \frac{(\kappa\, C_0)^2}{\sigma(\bar{\phi})}\, k^2\right] |\phi_k|^2 \,. \tag{3.27}$$

This reduces the magnitude of the stiffness term and can even make it negative, transforming a Cahn-Hilliard-type instability into a conserved Turing-type instability, as we will discuss next.

LINEAR STABILITY ANALYSIS OF EFFECTIVE FREE ENERGY

With the above form of the effective free energy one can write down the dynamics in the limit where membrane dynamics is equilibrated on the timescale of the protein density dynamics as

$$\partial_t \phi = \boldsymbol{\nabla}^2 \frac{\delta \mathcal{F}_{\text{eff}}}{\delta \phi}\,. \tag{3.28}$$

Linear stability analysis then gives for the growth rates of the Fourier modes,

$$\lambda(k) = -k^2\left[f''(\bar{\phi}) + \kappa\, C_0^2 + \tfrac{1}{2}\chi_{\text{eff}}(k)\, k^2\right], \tag{3.29}$$

where $\chi_{\text{eff}}(k)$ denotes the stiffness parameter renormalized by the bending modes and the generalized surface tension,

$$\chi_{\text{eff}}(k) = \chi - \frac{2\,(\kappa\, C_0)^2}{\sigma(\bar{\phi}) + \kappa\, k^2}\,. \tag{3.30}$$

In addition, the leading order term $-f''(\bar{\phi})\, k^2$, which determines the position of the spinodal in the CH model through the sign change of the curvature of the free energy density $f''(\bar{\phi})$, is shifted by a constant $\kappa\, C_0^2$, depending on the spontaneous curvature.

Figure 3.3(f) shows the bifurcation diagram resulting from the dispersion relation of the effective model, Eq. (3.29), as a function of the FH parameter, bending stiffness, and spontaneous curvature. It demonstrates that, depending on the values of these parameters, the spatially uniform state can become unstable through either a CH-type or conserved Turing-type instability. These transitions

align with the transitions obtained from the full model (see appendix Section 3.7.5). In the regime where the instability is of CH-type, i.e., a long-wavelength instability, the spinodal line is given by the condition $f''(\bar{\phi}) + \kappa\, C_0^2 = 0$, resulting in

$$2\chi = \frac{1}{\bar{\phi}\,(1-\bar{\phi})} + \kappa\, C_0^2\,. \tag{3.31}$$

Below this spinodal surface, the dynamics is essentially equivalent to those described by the standard Cahn-Hilliard model. This involves an initial phase of spinodal decomposition followed by a subsequent coarsening process.

However, this CH-type transition with a long wavelength instability can be pre-empted by a finite wavelength conserved Turing-type instability, where a band (k_-, k_+) of modes becomes unstable. This band emerges if the following condition is met (see appendix Section 3.7.4)

$$\begin{aligned} {C_0^c}^2 = \frac{4}{\bar{\phi}^2\left(\bar{\phi}^2\chi - 16\kappa\right)}\Bigg(&\bar{\phi}^2 f''(\bar{\phi}) + \sigma_{\mathrm{FH}}\Big(4 - \frac{1}{2\kappa}\bar{\phi}^2\chi\Big) \\ &- 2\sqrt{\bar{\phi}^2 f''(\bar{\phi})\left(4\kappa f''(\bar{\phi})/\chi - 2\sigma_{\mathrm{FH}}\right) + 4\sigma_{\mathrm{FH}}^2}\Bigg)\,, \end{aligned} \tag{3.32}$$

where one has $f''(\bar{\phi}) = 1/[\bar{\phi}(1-\bar{\phi})] - 2\chi$ and we defined $\sigma_{\mathrm{FH}} := \sigma + f(\bar{\phi})$. The resulting bifurcation surface is depicted as the cyan upper surface $C_0^c(\chi,\kappa)$ in Fig. 3.3(f). The boundary between the conserved Turing-type and CH-type transitions is given by equating Eq. (3.31) and Eq. (3.32); see the thick black line in Fig. 3.3(f). For parameter ranges with an initial conserved Turing-type instability, Eq. (3.31) delineates the change from this conserved Turing-type to a CH-type dispersion relation.

Comparing the dispersion relation of the full model, $\lambda_{\mathrm{LSA}}(k)$ with that of the effective model, Eq. (3.29), two observations can be made. First, the effective dispersion relation is obtained from the full dispersion relation in the limiting case of a strong timescale separation between the protein density dynamics and the membrane dynamics. However, in our numerical simulations we chose comparable timescales, i.e. $\gamma = 1$, for both dynamics. As membrane deformations are rather weak, we still observe a co-localization of deformations with protein aggregates, and hysteresis from previous membrane configurations is still negligible. Second, the phase boundaries for the Cahn-Hilliard and conserved Turing-type instabilities remain unchanged even if there is no separation of time scales; see appendix Section 3.7.5.

3.5 THERMODYNAMICS AND LENGTH-SCALE SELECTION

To better characterize the emergence of the finite pattern length scale and the arrest of coarsening, we simulated the system dynamics across a larger region in parameter space, for a fixed value of $\chi = 3$ and encompassing variations in protein-induced curvature ($C_0 \in [0, 1.2]$) and membrane bending stiffness ($\kappa \in [0, 40]$). Figure 3.4 shows the corresponding results for the inter-droplet distance (see appendix Section 3.7.6) in the stationary state. It reveals the existence of two distinct phase boundaries.

First, a *spinodal line* (cyan) marks the onset of the instability of a spatially uniform state against small perturbations. In the parameter range shown, this transition is a conserved Turing-type instability, given by Eq. (3.32); there is excellent agreement between the predicted and the numerically observed transition (Fig. 3.4). Below the spinodal line, our numerical simulations show that the system initially undergoes spinodal decomposition and Ostwald ripening. However, this coarsening process does not reach completion; instead, it eventually arrests, and results in the formation of a spatial pattern with periodic arrangements of droplets of finite size. This is distinct from the Ostwald ripening process that we observe in a parameter regime where the transition is driven by a Cahn-Hilliard-type long wavelength instability. Upon decreasing the protein-induced curvature C_0 for a fixed value of the bending rigidity κ, our simulations show that both the distance between the droplets and their size increase; see the black dashed line and the corresponding panels for the

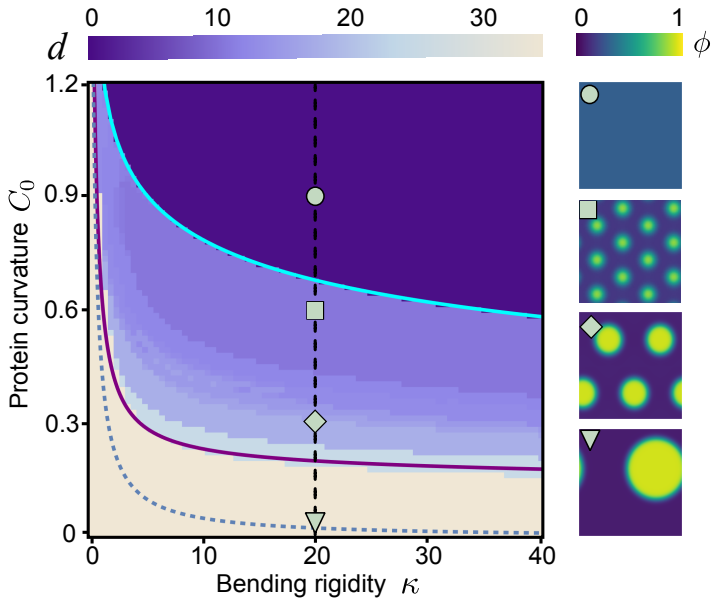

Figure 3.4: Inter-droplet distance d (color code) in the final stationary state of numerical simulations of the system described by Eq. (3.12) and Eq. (3.14), for different values of protein-induced curvature C_0 and bending rigidity κ in a square domain with side length $L = 2\mu\text{m}$. The spinodal line for the conserved Turing-type transition (C_0^c, cyan, light gray) marks the onset of pattern formation predicted by linear stability analysis; see Eq. (3.32). With decreasing protein-induced curvature (C_0), the length scale of the emerging droplet pattern increases (black dashed line at $\kappa = 20$); the panels on the right show corresponding snapshots of these patterns at the parameters indicated by the green symbols. The transition from a finite number of droplets to a single droplet in a finite size system is indicated by a solid purple (dark gray) line (C_0^L, Eq. (3.37)). The phase boundary between an infinitely extended system that shows arrested coarsening and one that exhibits Ostwald ripening is shown by the dashed blue (medium gray) line (C_0^∞, Eq. (3.34)). All system parameters as in Fig. 3.3, where parameter ranges of C_0 and κ are indicated as a gray plane. This figure is reproduced from Ref.[2] under license [CC BY 4.0].

patterns in Fig. 3.4. Eventually, in the finite-sized system simulated here, there is a threshold line for the protein-induced curvature below which the system exhibits only a single droplet, cf. solid purple line in Fig. 3.4.

3.5.1 THERMODYNAMIC LENGTH-SCALE SELECTION

Why does the system exhibit coarsening arrest within an intermediate range of protein-induced curvature and bending rigidity? One way to address this question would be to use methods from nonlinear dynamics and perform a weakly nonlinear analysis along the lines introduced by Matthews and Cox[296], which accounts for the presence of the long wavelength marginal mode at $k = 0$. In the present case, however, there is a more straightforward approach, as the dynamics relax to a thermal equilibrium state determined—at the mean-field level—by the minimum of the free energy functional. In general, thermodynamic systems with only short-ranged interactions show Ostwald ripening with the equilibrium state given by complete phase separation. Here, however, we have long-ranged interactions between the proteins mediated by the elastic deformation of the membrane surface. It is known that the balance between the short-ranged forces driving phase separation and the long-ranged forces that impose ordering constraints can lead to the formation of patterns. A classical example are block copolymer melts, where the long-range interaction is mediated by connections between different chemical sequences in the copolymer chain[76]. In the present context, there is an intriguing twist to this narrative due to the significance of geometric effects inherent in the metric of the membrane surface.

The length scale of the final pattern can be determined from the effective free energy functional derived in the previous section, Eq. (3.26). Following the approach in Ref.[76], this length scale is

obtained by finding the wave vector that minimizes the effective free energy functional density,

$$k_{\min}^2 = C_0 \sqrt{\frac{2\sigma(\bar{\phi})}{\chi}} - \frac{\sigma(\bar{\phi})}{\kappa}\,. \tag{3.33}$$

This relation shows that thermodynamically one should have a transition from microphase separation (arrested coarsening) to full coarsening for $k_{\min} = 0$, equivalent to

$$C_0^{\infty} = \frac{1}{\kappa}\sqrt{\frac{\chi\,\sigma(\bar{\phi})}{2}}\,. \tag{3.34}$$

Substitution of the effective surface tension, Eq. (3.24), and solving for C_0^{∞} yields

$$C_0^{\infty} = \sqrt{\frac{\chi(\sigma + f(\bar{\phi}))}{2\kappa^2\left(1 - \chi\bar{\phi}^2/(4\kappa)\right)}}\,; \tag{3.35}$$

see the dashed blue line in Fig. 3.4.

3.5.2 FINITE SIZE EFFECTS

On comparing our numerical simulations with the above thermodynamic results we have to account for finite size effects. The wavevector $k_{\min}$ defines the inter-droplet distance

$$d = \frac{2\pi}{k_{\min}} \tag{3.36}$$

of the steady-state pattern. Figure 3.5 compares the simulation data for the cutline $\kappa = 20$ in Fig. 3.4 alongside this analytical expression for the inter-droplet distance. The average distance between droplets decreases with increasing protein curvature C_0 and we observe good agreement with the simulation results. However, as we consider a finite-size system, the inter-droplet distance takes

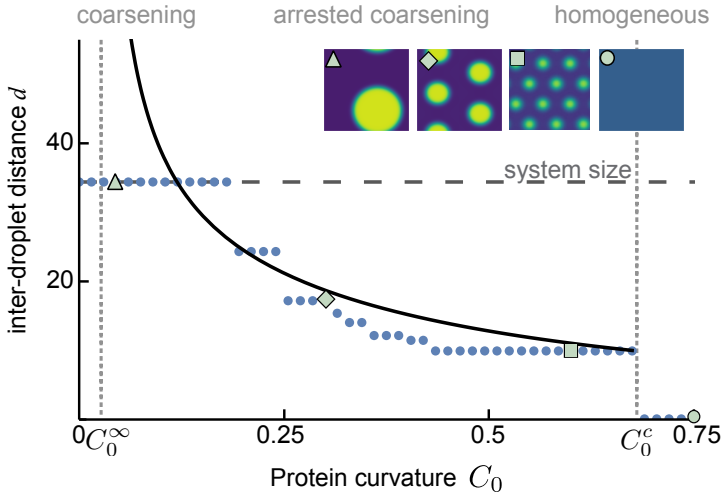

Figure 3.5: Comparison of the analytical result for inter-droplet distance Eq. (3.36) (black line) and the simulation results for the cutline $\kappa = 20$ in Fig. 3.4 (blue dots). Both are in a good agreement, with minor deviations due to finite size effects and the harmonic approximation used to derive the effective free energy. The panels on top show the pattern corresponding to the length scale indicated by the green symbols. The system size, given by the horizontal dashed line, restricts the maximum possible distance. The regime showing microphase separation is limited by C_0^{∞} (Eq. 3.34) and C_0^{c} (Eq. 3.32) as indicated by the vertical dashed lines. This figure is reproduced from Ref.[2] under license [CC BY 4.0].

on discrete values. Moreover, since the hexagonal symmetry of the periodic arrangement of the droplets is not consistent with the square domain used in the simulations, there are geometric frustration effects; for a discussion see appendix Section 3.7.6. Finally, there may also be deviations between the simulation results and the thermodynamic expression, because we have used harmonic approximations in the derivation of the effective free energy (Sec. 3.4.2).

Figure 3.5 also illustrates that the inter-droplet distance is limited by the system size and the boundary between coarsening an arrested coarsening is shifted compared to an infinite system. The maximum distance between two droplets in our finite domain is $d_2 = L/\sqrt{2}$. Thus, we estimate the boundary between microphase separation (two or more droplets) and complete Ostwald ripening (one droplet) for our finite square domain with length L through the condition

$$d = \frac{L}{\sqrt{2}}\,. \tag{3.37}$$

The corresponding critical value of the protein-induced curvature $C_0^L(\kappa)$ is shown in Fig. 3.4 as the purple line. As the system size increases and finite-size effects decrease, we expect the agreement between the analytically predicted and numerically measured pattern length scales to improve even further, in addition to the already good agreement for the finite-size system. Specifically, as the systems become larger, we anticipate that the critical transition lines will converge, i.e., $C_0^L \to C_0^\infty$ in the limit $L \to \infty$. Since we do not anticipate any fundamentally new effects to arise at larger scales, we will omit the technical challenge of performing numerical simulations of larger systems here.

3.6 DISCUSSION

In this study, we investigated phase separation on membranes that dynamically evolve their shape, by integrating a Flory-Huggins theory for symmetric binary mixtures with a Canham-Helfrich theory for fluid elastic membranes. Specifically, we focused on systems where the density of molecules undergoing phase separation induces spontaneous membrane curvature, thereby facilitating a coupling with the membrane's mechanical deformations.

We employed a general covariant framework to describe phase-separation dynamics on membranes with dynamically evolving geometry, deliberately avoiding the use of small deformation or dilute phase expansions that are commonly used to simplify the analysis. The resulting set of coupled dynamic equations for protein density and membrane conformations account for the effects of spatiotemporal variations in the prevailing surface metric, ensure mass conservation, and capture the mechanical coupling arising from protein-induced curvatures.

The analysis of these dynamic equations shows that liquid phase separation on deformable membranes exhibits three qualitatively different phenomenologies. First, we observe a regime with stable, *spatially homogeneous* steady states, where proteins maintain a mixed state with a uniform concentration across a flat membrane. Second, we find a regime characterized by a fully coarsened phase-separated steady state, where proteins aggregate into a single high-density droplet surrounded by a low-density phase. Finally, we also find a regime of arrested coarsening, where protein aggregation is counteracted by the energetic cost of membrane deformation induced by the mechanical coupling to the protein density. In this regime, the length scale of the emergent pattern is determined by the trade-off between the thermodynamics of protein mixing and membrane bending energy costs.

An interesting and notable feature of phase separation on deformable membranes is that the dispersion relation changes from a standard Cahn-Hilliard-type long wavelength instability to a conserved Turing-type instability above a certain threshold value for the spontaneous curvature. The Cahn-Hilliard instability leads to Ostwald ripening, where smaller droplets dissolve into larger ones, resulting in coarsening of the phase-separated structures over time. In contrast, the conserved Turing instability, characterized by a band of unstable modes and a marginal mode at zero wavevector in the dispersion relation, drives the formation of spatial patterns with a finite wavelength. Since we study the dynamics of a protein-membrane system that relaxes to a thermodynamic equilibrium,

one can take advantage of the fact that the thermal equilibrium state is encoded in the free energy functional. By minimizing this effective free energy density, where membrane conformations were integrated out, we were able to determine the length scale of the patterns. The analytical results obtained through this method showed excellent agreement with our numerical simulations.

Similar to recent findings in Ref.[34], our results highlight that curvature-mediated interactions, in conjunction with phase separation, can serve as a minimal motif for pattern formation with a well-defined length scale, determined by the material parameters of the system. Notably, this mechanism does not depend on complex biochemical pathways but rather on generic features of the membrane's lipid composition[34] or protein interaction with the membrane[279,297]. The dynamics of the membrane and the density field discussed in our work are qualitatively similar to those in Ref.[34], but differ in several key aspects. First, we avoid expanding the membrane dynamics beyond the intrinsic limits of Monge representation. Second, we incorporate the effects of the surface metric in the Flory-Huggins free energy, resulting in an effective membrane tension. Finally, we account for the metric in the time derivative of protein density to ensure accurate protein mass conservation. These differences lead to distinct predictions for the phase diagram, particularly in how the phase boundaries depend on model parameters such as the protein-induced curvature.

In our current analysis, we have neglected the in-plane lipid flow within the membrane. Extending recent work[35], which incorporates this flow, to the nonlinear Monge regime explored here would be a valuable next step. Additionally, another promising research avenue would involve accounting for the fluid flow of the surrounding liquid beyond the Rouse approximation used in our present study.

Finally, an intriguing open research question that could be explored by adapting our theoretical framework is how dynamics and steady states are affected in systems with broken detailed balance. This includes systems where the de-mixing dynamics is described by the nonreciprocal Cahn-Hilliard equations[280,298–300] and various pattern-forming systems[87,88,94,239,244]. For instance, two-component mass-conserving reaction-diffusion system on deformable surfaces, exhibit geometrically induced pattern-forming instabilities and the occurrence of oscillations and traveling waves, not present without geometric coupling[244]. The general correspondence between Cahn-Hilliard models and reaction-diffusion systems with conservation laws[24,301] promises the possibility of directly applying the approaches presented here to such systems and extending them to even more general active matter.

3.7 APPENDIX

3.7.1 NON-DIMENSIONALIZED DYNAMIC EQUATIONS

As discussed in the main text, we base our study on the non-dimensionalized effective free energy functional

$$\begin{aligned}\mathcal{F} = \int \mathrm{d}A \Big[&\sigma + \frac{\kappa}{2}\left(C - C_0\phi\right)^2 \\ &+ \left(\phi \ln \phi + (1-\phi)\ln(1-\phi)\right) \\ &+ \chi\phi(1-\phi) + \frac{\chi}{4}|\boldsymbol{\nabla}\phi|^2 \Big] .\end{aligned} \tag{3.38}$$

We assume in the following that all quantities are non-dimensionalized as discussed in Sec. 3.2.3. In order to derive dynamic equations for the membrane height field h and the protein density ϕ, we assume gradient dynamics towards minima of the effective free energy functional $\mathcal{F}$. In particular, we assume relaxational (model A) dynamics for the height field,

$$\partial_t h = -\gamma \frac{\delta \mathcal{F}}{\delta h} , \tag{3.39}$$

and Cahn-Hilliard (model B) dynamics for the conserved protein field ϕ,

$$\frac{1}{\sqrt{g}}\,\partial_t\left(\sqrt{g}\phi\right) = \boldsymbol{\nabla}^2\frac{\delta\mathcal{F}}{\delta\phi}\,. \tag{3.40}$$

To derive the explicit form of the dynamic equations, we need to perform the variation of the free energy functional with respect to the height field h and the protein area fraction ϕ. For the dynamics of the height field, we make use of the fact that the variations of the curvature, metric, and metric tensor, respectively, are given by[282]

$$\delta C = \left(\Delta + C^2 - 2C_{\mathrm{G}}\right)\frac{\delta h}{\sqrt{g}}\,, \tag{3.41}$$

$$\delta g = -2\,g\,C\,\frac{\delta h}{\sqrt{g}}\,, \tag{3.42}$$

$$\delta g^{ab} = 2\,C^{ab}\,\frac{\delta h}{\sqrt{g}}\,. \tag{3.43}$$

Here

$$C_{ab} = \frac{1}{\sqrt{1+(\boldsymbol{\nabla}_\perp h)^2}}\begin{pmatrix}\partial_x^2 h & \partial_{yx}^2 h\\ \partial_{xy}^2 h & \partial_{yy}^2 h\end{pmatrix} \tag{3.44}$$

denotes the extrinsic curvature tensor, C is the total curvature, defined in the main text, Eq.(3.5), and

$$C_{\mathrm{G}} = \frac{\det[\boldsymbol{\nabla}_\perp\boldsymbol{\nabla}_\perp h]}{(1+(\boldsymbol{\nabla}_\perp h)^2)^2} \tag{3.45}$$

is the Gaussian curvature.

Given the free energy functional $\mathcal{F}$, Eq. (3.38), we find for the local part of the functional

$$\begin{aligned}\delta\int \mathrm{d}A\, f_{\mathrm{tot}}[\phi, g_{ab}, C] &= \delta\int \mathrm{d}x\mathrm{d}y\sqrt{g}\, f_{\mathrm{tot}}[\phi, g_{ab}, C]\\ &= \int \mathrm{d}x\mathrm{d}y\left[\frac{1}{2\sqrt{g}}\delta g\, f_{\mathrm{tot}} + \sqrt{g}\,\delta f_{\mathrm{tot}}\right]\\ &= \int \mathrm{d}A\left[-f_{\mathrm{tot}}C\frac{\delta h}{\sqrt{g}} + \delta f_{\mathrm{tot}}\right].\end{aligned} \tag{3.46}$$

Here the total free energy density is given by the sum of the Canham-Helfrich and the Flory-Huggins free energy Eq. (3.38):

$$\begin{aligned}f_{\mathrm{tot}}[\phi, g_{ab}, C] &= f[\phi, g_{ab}] + e[\phi, C]\\ &= f\left(\phi\right) + \frac{\chi}{4}(\partial_a\phi)(\partial_b\phi)g^{ab} + e(\phi, C)\,,\end{aligned} \tag{3.47}$$

where we have used $|\boldsymbol{\nabla}\phi|^2 = (\partial_a\phi)(\partial_b\phi)g^{ab}$.

By combining the variation of the curvature C (Eq. (3.41)) and the metric tensor g_{ab} (Eq. (3.43)) with the above results, one obtains the variation of the free energy functional

$$\begin{aligned}\delta\mathcal{F} &= \int \mathrm{d}A\Big[-C\big(f\left[\phi, g_{ab}\right] + e\left[\phi, C\right]\big)\frac{\delta h}{\sqrt{g}} + \frac{\chi}{4}(\partial_a\phi)(\partial_b\phi)\delta g^{ab} + \partial_C e\left[\phi, C\right]\delta C\Big] \\ &= \int \mathrm{d}A\Big[-C\big(f\left[\phi, g_{ab}\right] + e\left[\phi, C\right]\big)\frac{\delta h}{\sqrt{g}} + \frac{\chi}{2}(\partial_a\phi)(\partial_b\phi)C^{ab}\frac{\delta h}{\sqrt{g}} + \partial_C e\left[\phi, C\right]\big(\Delta + C^2 - 2C_{\mathrm{G}}\big)\frac{\delta h}{\sqrt{g}}\Big] \\ &= \int \mathrm{d}x\mathrm{d}y\Big[-C\big(f\left[\phi, g_{ab}\right] + e\left[\phi, C\right]\big) \\ &\qquad + \frac{\chi}{2}(\partial_a\phi)(\partial_b\phi)C^{ab} + \Delta\partial_C e[\phi, C] + (\partial_C e\left[\phi, C\right])\big(C^2 - 2C_{\mathrm{G}}\big)\Big]\delta h\,. \end{aligned} \tag{3.48}$$

In the last step we have integrated the term $(C - C_0\phi)\,\Delta h$ twice by parts and assumed vanishing boundary terms. Insertion of the equations for the free energy densities gives the variation of the free energy functional with respect to the height field

$$\begin{aligned}\frac{\delta\mathcal{F}}{\delta h} =& -C\left[\phi\ln\phi + (1-\phi)\ln(1-\phi) + \chi\phi(1-\phi) + \frac{\chi}{4}|\boldsymbol{\nabla}\phi|^2 + \frac{\kappa}{2}\left(C - C_0\phi\right)^2 + \sigma\right] \\ &+ \frac{\chi}{2}\left(\partial_a\phi\right)\left(\partial_b\phi\right)\,C^{ab} + \Delta\kappa(C - C_0\phi) + \kappa(C - C_0\phi)\left(C^2 - 2C_{\mathrm{G}}\right). \end{aligned} \tag{3.49}$$

From this, we can read off the dynamic equations for the height field

$$\frac{1}{\gamma}\,\partial_t h = \left[f[\phi, C] + e(\phi, C)\right]C - \kappa\boldsymbol{\nabla}^2(C - C_0\phi) + \kappa\left(C - C_0\phi\right)\left(-C^2 + 2C_{\mathrm{G}}\right) - \frac{\chi}{2}\,C^{ab}\left(\partial_a\phi\right)(\partial_b\phi)\,. \tag{3.50}$$

Analogously, the dynamic equation for the protein concentration reads

$$\begin{aligned}\frac{1}{\sqrt{g}}\partial_t(\sqrt{g}\phi) =& \boldsymbol{\nabla}^2\left[\partial_\phi e\left(\phi, C\right) + \partial_\phi f\left(\phi\right) - \frac{\chi}{2}\boldsymbol{\nabla}^2\phi\right] \\ =& \boldsymbol{\nabla}^2\left[-C_0\kappa(C - C_0\phi) + \ln\left(\frac{\phi}{1-\phi}\right) + \chi(1 - 2\phi) - \frac{\chi}{2}\boldsymbol{\nabla}^2\phi\right]. \end{aligned} \tag{3.51}$$

3.7.2 NUMERICAL SIMULATIONS

We solved Eq. (3.12) and Eq. (3.14) numerically in two spatial dimensions using finite element methods with the commercially available software COMSOL Multiphysics v.6.1[251]. The simulations were performed on a square domain with side length $L = 2\,\mu\mathrm{m}$ and periodic boundary conditions. As an initial condition, we used one droplet or a homogeneous protein density $\phi_0(x, y) = 0.3$ perturbed by Gaussian zero-mean white noise with an amplitude $\sim 5\times10^{-4}$. The total protein mass was chosen to be the same for the one droplet and the homogeneous protein density.

3.7.3 LINEAR STABILITY ANALYSIS

We perform a linear stability analysis (LSA) around the spatially homogeneous state $(h_0, \bar{\phi})$. To this end, we introduce small perturbations of the concentration field $\phi = \bar{\phi} + \delta\phi$ and the height field $h = h_0 + \delta h$ with respect to the spatially homogeneous state and linearize the dynamic equations, Eq. (3.12) and (3.14),

$$\partial_t\begin{pmatrix}\delta h\\ \delta\phi\end{pmatrix} = J\cdot\begin{pmatrix}\delta h\\ \delta\phi\end{pmatrix} \tag{3.52}$$

with the Jacobian

$$J = \begin{pmatrix} J_{hh} & J_{h\phi} \\ J_{\phi h} & J_{\phi\phi} \end{pmatrix}, \tag{3.53}$$

where

$$\begin{aligned} J_{hh} &= -\frac{1}{2}\gamma k^2 \big[2\bar{\phi}\left(\chi - \ln\left(1-\bar{\phi}\right) + \ln\bar{\phi}\right) && \text{(3.54a)} \\ &\quad + 2\left(\kappa k^2 + \sigma + \ln\left(1-\bar{\phi}\right)\right) + \bar{\phi}^2\left(\kappa C_0^2 - 2\chi\right)\big], \\ J_{h\phi} &= \gamma\kappa(-C_0)k^2, && \text{(3.54b)} \\ J_{\phi\phi} &= -\frac{k^2}{2\left(\bar{\phi}-1\right)\bar{\phi}}\big[\bar{\phi}^2\left(\chi\left(k^2-4\right) + 2\kappa C_0^2\right) && \text{(3.54c)} \\ &\quad - \bar{\phi}\left(\chi\left(k^2-4\right) + 2\kappa C_0^2\right) - 2\big] \\ J_{\phi h} &= \kappa(-C_0)k^4. && \text{(3.54d)} \end{aligned}$$

The largest eigenvalue of the Jacobian determines the highest growth rate. The analysis of analytical expressions is implemented in Mathematica 13.1[246]. Solving for the largest eigenvalues of the Jacobian J as a function of wavevector k yields the dispersion relations and the bifurcation diagram shown in Fig. 3.3.

3.7.4 LINEAR STABILITY ANALYSIS FOR THE REDUCED MODEL WITH AN EFFECTIVE FREE ENERGY

In this chapter we analyze the dispersion relation obtained from the effective free energy functional, Eq. (3.29). We determine the region in the (χ, κ, C_0) phase space, where a conserved Turing-type instability exists, by investigating the roots k_- and k_+ of the dispersion relation Eq. (3.29)

$$k_+ = \frac{1}{\sqrt{\chi\kappa}}\Big[-\left(\tfrac{1}{2}\chi\sigma\left(\bar{\phi}\right) + \kappa f''(\bar{\phi})\right) + \sqrt{\left(\tfrac{1}{2}\chi\sigma\left(\phi\right) + \kappa f''(\bar{\phi})\right)^2 - 2\chi\kappa\sigma\left(\bar{\phi}\right)\left(f''(\bar{\phi}) + \kappa C_0^2\right)}\Big]^{\frac{1}{2}}, \tag{3.55a}$$

$$k_- = \frac{1}{\sqrt{\chi\kappa}}\Big[-\left(\tfrac{1}{2}\chi\sigma\left(\bar{\phi}\right) + \kappa f''(\bar{\phi})\right) - \sqrt{\left(\tfrac{1}{2}\chi\sigma\left(\bar{\phi}\right) + \kappa f''(\bar{\phi})\right)^2 - 2\chi\kappa\sigma\left(\bar{\phi}\right)\left(f''(\bar{\phi}) + \kappa C_0^2\right)}\Big]^{\frac{1}{2}}, \tag{3.55b}$$

A conserved Turing-type instability can only exist in the regions where k_- is defined. From this, two conditions can be derived

$$0 = -\left(\tfrac{1}{2}\chi\sigma\left(\bar{\phi}\right) + \kappa f''(\bar{\phi})\right) - \sqrt{\left(\tfrac{1}{2}\chi\sigma\left(\bar{\phi}\right) + \kappa f''(\bar{\phi})\right)^2 - 2\chi\kappa\sigma\left(\bar{\phi}\right)\left(f''(\bar{\phi}) + \kappa C_0^2\right)}, \tag{3.56a}$$

$$0 = \left(\tfrac{1}{2}\chi\sigma(\bar{\phi}) + \kappa f''(\bar{\phi})\right)^2 - 2\chi\kappa\sigma(\bar{\phi})\left(f''(\bar{\phi}) + \kappa C_0^2\right). \tag{3.56b}$$

We recover the critical protein induced-curvature $C_0^*(\chi, \kappa)$ from the first equality, Eq. (3.56a). However, this solution is only valid if the condition $\left(\frac{1}{2}\chi\sigma\left(\bar{\phi}\right) + \kappa f''(\bar{\phi})\right) \leq 0$ is fulfilled. The black solid line in Fig. 3.3(f) depicts the boundary, given by $\left(\frac{1}{2}\chi\sigma\left(\bar{\phi}\right) + \kappa f''(\bar{\phi})\right) = 0$. The second equality is equivalent to the condition $k_- = k_+$, which determines the spinodal for the conserved Turing regime

$$C_0^{\mathrm{c}} = \left[\frac{4}{\bar{\phi}^2\left(\bar{\phi}^2\chi - 16\kappa\right)}\left(\bar{\phi}^2 f''(\bar{\phi}) + \sigma_{\mathrm{FH}}\left(4 - \tfrac{1}{2\kappa}\bar{\phi}^2\chi\right) - 2\sqrt{\bar{\phi}^2 f''(\bar{\phi})\left(\tfrac{4\kappa f''(\bar{\phi})}{\chi} - 2\sigma_{\mathrm{FH}}\right) + 4\sigma_{\mathrm{FH}}^2}\right)\right]^{\frac{1}{2}}, \tag{3.57}$$

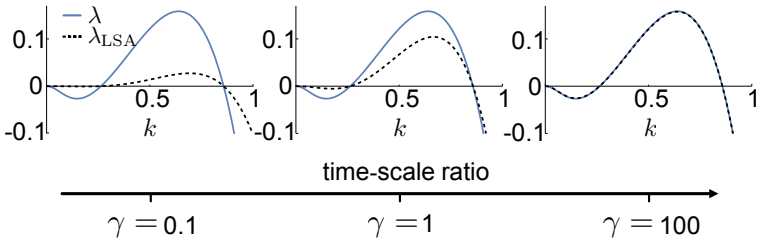

Figure 3.6: Comparison of the dispersion relation of the full model λ_{LSA} (dashed line) with that of the effective free energy functional λ (solid line). The dispersion relations agree in the limit of strong time-scale separation. The ranges of unstable modes agree independently of the time-scale separation, i.e., $\gamma \gg 1$. The parameters are the same as in Fig. 3.3; specifically we chose $C_0 = 0.5$ and vary γ. This figure is reproduced from Ref.[2] under license [CC BY 4.0].

where $\sigma_{\mathrm{FH}} = \sigma + f(\bar{\phi})$.

So far, we have derived the critical protein-induced curvature for the transition from a conserved Turing-type to a Cahn-Hilliard type instability, as well as the critical protein-induced curvature that defines the spinodal in the conserved Turing-type instability region. Next, we aim to determine the spinodal for the region with a Cahn-Hilliard-type instability, given by $k_+ = 0$. Again, we recover the protein induced curvature $C_0^*(\chi, \kappa)$ as a solution, which is only valid for $\frac{1}{2}\chi\sigma + \kappa f''(\phi_0)) \geq 0$.

Taken together, $C_0^*(\chi, \kappa)$, defines a surface in the parameter space (depicted as the magenta manifold in Fig. 3.3(f)), at which a sign change in the dispersion relation at the origin occurs. Below the magenta surface, the dispersion relation at the origin is positive, leading to a CH-type instability. Above the black line ($\frac{1}{2}\chi\sigma + \kappa f''(\phi_0)) \geq 0$) on this surface, $C_0^*(\chi, \kappa)$ also satisfies the equation $k_+ = 0$, thus defining the boundary between a homogeneous system and a phase-separated system. Below the black line ($\frac{1}{2}\chi\sigma + \kappa f''(\phi_0)) \leq 0$) on this surface, $C_0^*(\chi, \kappa)$ solves the equation $k_- = 0$, thereby defining the boundary between a CH-type and cT-type instability. In this case, the spinodal is given by C_0^c and is shown as the cyan surface in Fig. 3.3(f).

3.7.5 Comparison of Linear Stability Analyses of Dynamic Equations and Free Energy

We compare the dispersion relation derived from the standard linear stability analysis $\lambda(k)$ with that derived from the effective free energy functional. The dispersion relation derived from the effective free energy functional, in which the height fluctuations have been integrated out, is valid if we can assume that the height field has already equilibrated on the timescale of the protein dynamics. For a positive effective surface tension this is equivalent to saying that dynamic changes in the height field have to be fast compared to the protein dynamics. The dispersion relations for different time-scale ratios are shown in Fig. 3.6. We make two important observations: The effective dispersion relation $\lambda(k)$ follows from the full dispersion relation $\lambda_{\mathrm{LSA}}(k)$ in the limit of strong time-scale separation. Second, the roots of the dispersion relations agree independently of the time-scale separation, and, thus, also the phase boundaries C_0^c and C_0^*, derived in appendix Section 3.7.4, don't depend on the time-scales.

While the detailed form of the dispersion relations is distinct from the expressions obtained by analyzing the effective free energy (see appendix Section 3.7.5), the zeros (marginal modes) of the dispersion relations, Eqs. (3.55b) and (3.55a), agree. Thus, the bifurcation diagrams that differentiate between regions where the homogeneous state is stable and various types of lateral instabilities are the same for the full LSA and the LSA based on the effective free energy functional. This reflects that the underlying system is thermodynamic, implying that the final steady state should be independent of specific timescales. By integrating out the height field dynamics to quadratic order, one effectively assumes a factorization of the contributions within the free energy. This factorization directly translates into the resulting effective dispersion relation, thereby preserving its characteristic roots.

3.7.6 DISTANCE MEASURE

In this section, we explain the method used to define an inter-droplet distance on the basis of the integer number of droplets N and compare it with the inter-droplet distance as measured by averaging over mutual center-to-center distances of neighboring droplets. Due to geometric frustration, deviations from the regular lattice may occur, leading to slight variations in the inter-droplet distances.

We define the number-derived inter-droplet distance as the characteristic length scale of the pattern

$$d_N = \sqrt{\frac{A}{N}}\,, \tag{3.58}$$

where N is the number of droplets in a domain with area A. In Fig. 3.7, we compare the number-derived inter-droplet distance (blue circles) to the measured distances from simulation snapshots (magenta dots). The latter is determined by averaging over the distances to all the droplets that can be reached without intersecting another droplet. We use periodic boundary conditions to calculate the distance for droplets close to the boundary of the system. Since the simulations are performed in a finite domain (grey box), the pattern can be geometrically frustrated and deviate from the regular lattice for some parameter values, as shown in panels ii) and iii) in Fig. 3.7. The number-derived droplet distance agrees very well with the minimal distance from the simulation snapshots.

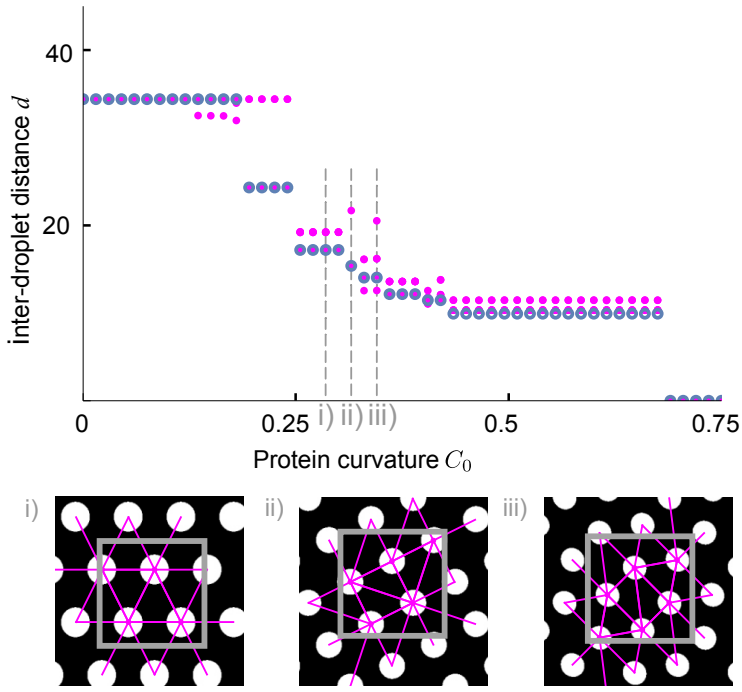

Figure 3.7: Droplet distances in numerical simulations as determined from center-to-center distances (pink dots) and as derived from the droplet number (blue circles) as a function of the protein induced curvature C_0. The measured center-to-center distance of the droplets is obtained by averaging over the distances to all neighbors that can be reached without intersecting another droplet in the finite domain (gray box). Bottom panels i)-iii) show three simulation snapshots for different values of C_0 as indicated by dashed lines. The center-to-center distances to the neighboring droplets are indicated by pink lines in the snapshots. Geometric frustration can be observed in panels ii) and iii). This figure is reproduced from Ref.[2] under license [CC BY 4.0].

4

Multi-scale organization in communicating active matter

The emergence of collective motion among interacting, self-propelled agents is a central paradigm in non-equilibrium physics. Examples of such active matter range from swimming bacteria and cytoskeletal motility assays to synthetic self-propelled colloids and swarming microrobots. Remarkably, the aggregation capabilities of many of these systems rely on a theme as fundamental as it is ubiquitous in nature: communication. Despite its eminent importance, the role of communication in the collective organization of active systems is not yet fully understood. Here we report on the multi-scale self- organization of interacting self-propelled agents that locally process information transmitted by chemical signals. We show that this communication capacity dramatically expands their ability to form complex structures, allowing them to self-organize through a series of collective dynamical states at multiple hierarchical levels. Our findings provide insights into the role of self-sustained signal processing for self-organization in biological systems and open routes to applications using chemically driven colloids or microrobots.

4

4.1 INTRODUCTION

Active matter encompasses a broad class of non-equilibrium systems that transduce energy stored in the environment into mechanical motion. In its most common form, locally interacting, self-propelled agents form coherent collective states that exceed the size of a single agent by orders of magnitude. Examples range from a variety of biological systems such as swimming bacteria[55,302,303], cytoskeletal motility assays[163,304,305], swarms, and flocks and schools of larger animals[306], to synthetic self-propelled colloids[307,308] and swarming microrobots[309,310]. There is broad agreement that self-propulsion, local alignment, and random disorientation of simple agents are fundamental microscopic determinants that can explain the occurrence of large-scale collective behavior. However, in addition to local short-range interactions, such as alignment and collisions, many biological and synthetic systems exhibit various types of long-range signaling strategies. The social amoeba Dictyostelium discoideum uses cell-to-cell cyclic adenosine monophosphate (cAMP) concentration waves and chemotaxis to induce aggregation under harsh conditions[45,311], insects rely on sound to coordinate the formation of cohesive swarms[312], protein waves control cargo transport[313], some active colloids form oscillating clusters using long-range chemical Ag/AgCl coupling[218,314], microrobots and robotic fish use infrared, electrical and acoustic signals to communicate[315,316]. Signal transduction allows organisms to develop successful survival techniques that give them an evolutionary advantage over non-communicating organisms[217,317]. Communication facilitates the emergence of novel dynamic steady states, such as large streams and localized vortices[45]. Without communication, such states are not generic and are observed only under specific boundary conditions, particle chirality, or density-dependent feedback mechanisms[318,319]. Despite its importance, the role of communication in the context of active matter remains largely unexplored.

A significant body of literature focuses on self-propelled particles with diffusive (chemotactic) interactions. Studies on chemotactic colloids report on the formation of localized clusters and colliding polar bands, both established through motility-induced phase-separation (MIPS)[216,320,321]. There, the chemical interactions between different agents are mostly linear and passive, e.g., with a constant emission of the signal by the individual agents[322,323]. Distinct from these earlier studies, we ask about the role of an active, non-trivial agent's response (decision-making) to detected signals. The information processing and decision-making should enable the complex hierarchical organization akin to living matter that does not occur in systems with passive chemical signaling.

To reveal the fundamental role of interparticle communication for self-organization, we chose to study a system of self-propelled units (agents) with local polar-alignment interactions. In addition, each agent can perform a specific task, namely, to detect and relay a signal transmitted between agents. Inspired by social amoebae that use cyclic adenosine monophosphate (cAMP) for communication[211], and Gram-negative bacteria that employ acyl-homoserine-lactone (AHL) molecules as quorum-sensing signals[324,325], we consider agents that broadcast a signal in the form of a chemical substance into the environment, where it spreads diffusively. Once the local level of the signal exceeds a certain threshold, agents tend to produce and propagate it. Thus, the agents act like a Schmitt trigger, a simple nonlinear electronic circuit with hysteresis[326]. Such a signal transduction

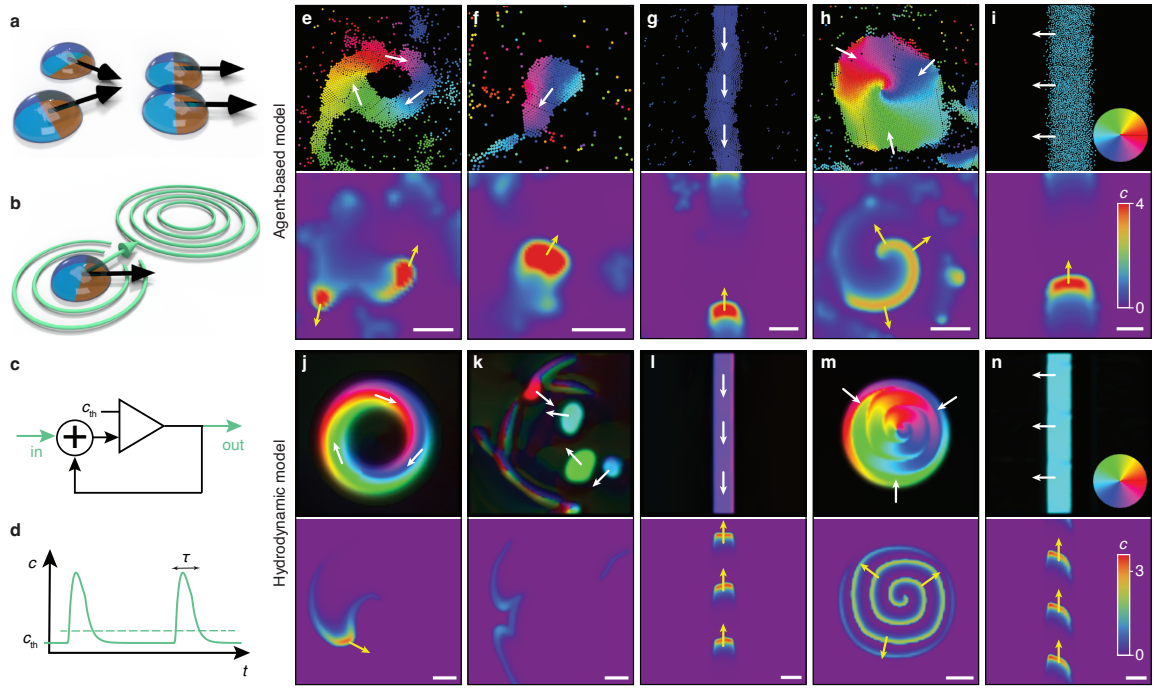

Figure 4.1: *Schematics of the agent-based model for communicating active matter and summary of collective dynamic states.* (a), Polar self-propelled particles undergo alignment in binary collisions. (b), A diffusible signal (green) aligns the cells' orientation vectors. (c), Schematic of a Schmitt trigger with variable threshold c_{th}. (d), Temporal response $c(t)$ of the agents' signaling system with characteristic time scale τ. (e)-(n), Representative collective dynamic states in the agent-based ((e)-(i)) and the hydrodynamic model ((j)-(n)). The snapshots illustrate aggregation and vortex formation following initial ring formation ((e), (j)), where remnant spiral wave arms induce chemical wave propagation in the ring after the spiral core vanished due to depletion in its center ('whispering gallery'-modes); active droplets ((f), (k)), with a collective response to external stimuli; a collective stream ((g), (l)), where agents propagate towards the source of communication waves; a large vortex with a spiral wave ((h), (m)), and a polar band ((i), (n)). White scale bars indicate a length of 10 units. Colors indicate the polar orientation of particles (top panels) and the chemical concentration c (bottom panels). White and yellow arrows illustrate the direction of motion of the particles (top panels) and the propagation direction of signaling activity (bottom panels), respectively. Parameters are defined in section 4.6.7. This figure is reproduced from Ref.[3] under license [CC BY 4.0].

system constitutes a spatially extended excitable medium that generically exhibits spiral waves of signaling activity. These waves can control the spatial self-organization of the agents by entraining their direction of self-propulsion. Thus, unlike existing models of amoeboid or bacterial aggregation[213,327–330], self-propelled motion, rather than Brownian motion, is the primary mode of transport in our system. In contrast to Vicsek-type models[166], the model incorporates the ubiquitous signaling found in biological systems. It thus provides insight into specific behaviors such as aggregation in social amoebae[44] and oscillatory colloids[218] and sheds light on the fundamental properties of active matter consisting of agents with "on-board" signal processing capabilities. The combination of chemical communication and internal information processing leads to an aggregation process involving collective dynamic states at multiple scales. We identify the decision-making machinery of the individual active agents as the driving mechanism for the collectively controlled self-organization of the system.

4.2 MODEL

We consider an agent-based description of communicating active matter, in which each agent moves with velocity $\boldsymbol{v} = v_0\boldsymbol{n}$ and is endowed with signal detection and relaying capability whose activity depends on an internal state variable s. The dynamics of the agents' positions $\boldsymbol{r}_i = (x_i, y_i)^T$ is

described by

$$\frac{\mathrm{d}\boldsymbol{r}_i}{\mathrm{d}t} = v_0 \boldsymbol{n}_i + \sum_{j[r_{ij}<2r_p]} f_{ij}\,, \tag{4.1}$$

where $\boldsymbol{n}_i = (\cos\varphi_i, \sin\varphi_i)^T$ is the unit vector in the direction of the i-th agent's orientation φ_i, with $i = 1, \ldots, N$; N is the total number of agents in the domain. While the speed v_0 of each particle is assumed to be constant, their direction of motion $\boldsymbol{n}$ can change – owing to inelastic binary collisions that favor polar alignment (Fig. 4.1a) or in response to a chemical signal (Fig. 4.1b). Within an interaction radius r_c, agents align in a polar fashion, i.e., the interaction of an agent with a neighbor causes both agents to turn towards the average orientation angle with the alignment rate Γ. If agents approach each other below a critical distance $2r_\mathrm{p}$, they obey a hard-core repulsion interaction cast as an isotropic short-range force f_{ij} between the agents in Eq. (4.1). Akin to chemotaxis, the agents align with a certain sensitivity ω along the concentration gradient $\varphi_c = \tan^{-1}(\partial_y c/\partial_x c)$ of the local maximum of the chemical signal concentration c. These competing alignment processes are generally error-prone, which is accounted for by a white-noise term ξ_i with amplitude $\sqrt{2D_R}$. Specifically, we assume that the dynamics of the agent's orientation φ_i over time t is given by the Langevin equation

$$\frac{\mathrm{d}\varphi_i}{\mathrm{d}t} = -\Gamma \sum_{j,[r_{ij}<r_c]} \frac{\sin(\varphi_i - \varphi_j)}{|\boldsymbol{r}_i - \boldsymbol{r}_j|} + \omega \sin(\varphi_c - \varphi_i) + \xi_i\,, \tag{4.2}$$

incorporating binary inelastic collisions between neighboring agents with spatial distance $r_i j = |\boldsymbol{r}_i - \boldsymbol{r}_j|$, chemotactic reorientation of agents along the concentration gradient of chemical signaling molecules[198], and noise, respectively. The orientation along chemical gradients is implemented similarly to the agents' polar alignment with their neighbors. For instance, in social amoeba the ability of chemotaxis is stable over large ranges of concentrations and alignment can be assumed to be independent of the absolute signal strength[212]. Signal detection and self-sustained relaying are modeled by a Schmitt trigger (Fig. 4.1c): if the signal amplitude (i.e., chemical concentration) is above some threshold value ($c > c_\mathrm{th}$), an agent in a quiescent state ($s_0 = 0$) switches into an excited state ($s_\mathrm{ex} > 0$), and over a period τ it broadcasts the signal (Fig. 4.1d), i.e., releases a certain amount of the chemical into the environment, where it diffuses (with diffusion constant D_c) and is also degraded with rate α. This yields the chemical signal dynamics

$$\partial_t c = D_c \nabla^2 c - \alpha c + \beta \sum_{i=1}^{N} f(|\boldsymbol{r} - \boldsymbol{r}_i|)\,\phi(s_i, c)\,, \tag{4.3}$$

with a Gaussian spatial source distribution $f(|\boldsymbol{r}|)$, Laplace operator ∇^2, and temporal derivative ∂_t. The agents act as sources of the chemical signal as

$$\beta\phi(s_i, c) = \beta(1 - s_i)\Theta(c - c_\mathrm{th})\,, \tag{4.4}$$

with Heaviside-type signal detection and production rate β. The threshold value c_th as well as the source strength depend on the internal state, whose dynamics, for simplicity, is assumed to be linearly adapting to the signal concentrations,

$$\frac{\mathrm{d}s_i}{\mathrm{d}t} = \epsilon\,(c - s_i)\,. \tag{4.5}$$

The response of the agents' state s_i to recent stimuli mimics adaptation of receptor sensitivity and productiveness of the signal-emission. Taken together, the model incorporates the fundamental ingredients of a system of self-propelled active matter capable of communication; see section 4.6.1 for a more extensive description of the agent-based model. Exemplary aggregation dynamics of a system without active decision making are studied in section 4.6.6. As a complementary approach based on this microscopic model, we derive a hydrodynamic theory formulated in terms of the agents' density

field $\rho(\boldsymbol{r},t)$, the polarization field $\boldsymbol{p}(\boldsymbol{r},t)$, the internal state variable $s(\boldsymbol{r},t)$, and the concentration of the chemical signal $c(\boldsymbol{r},t)$, all of which depend on the spatial position $\boldsymbol{r}$ and time t,

$$\partial_t\rho(\boldsymbol{r},t) = -v_0\nabla\cdot\boldsymbol{p} + D_\rho\nabla^2\rho\,, \tag{4.6a}$$

$$\partial_t\boldsymbol{p}(\boldsymbol{r},t) = \sigma\,(\rho-1)\,\boldsymbol{p} - \delta|\boldsymbol{p}|^2\boldsymbol{p} + D_p\nabla^2\boldsymbol{p} - \chi\boldsymbol{p}\cdot\nabla\boldsymbol{p} - Q(\rho)\nabla\rho + \rho\omega\nabla c\,, \tag{4.6b}$$

$$\partial_t c(\boldsymbol{r},t) = D_c\nabla^2 c - \alpha c + \rho\beta\Theta\,(c-c_{\text{th}})\,(1-s)\;, \tag{4.6c}$$

$$\partial_t s(\boldsymbol{r},t) = D_\rho\nabla^2 s - \epsilon\,(s-c) - v_0\boldsymbol{p}\cdot\nabla s\,. \tag{4.6d}$$

The hydrodynamic model comprises a coupled set of partial differential equations for these fields with basically the same parameters as the agent-based model (see section 4.6.2 for details and section 4.6.5 for a derivation of the hydrodynamic theory from the agent-based model). In the absence of communication, e.g., $c \equiv 0$, the parameters σ and δ regulate the emergence of polar order above a mean-field critical density $\rho_c = 1$ when polar alignment interactions outweigh angular diffusion. Based on the large-scale field equations, we can study the dynamics of communicating active matter on length- and time-scales, not accessible with agent-based numerical simulations due to their high computational costs.

4.3 COLLECTIVE DYNAMIC STATES

Communicating active matter exhibits unprecedentedly rich spatiotemporal dynamics and collective states, both during aggregation and in the final non-equilibrium steady state. The agent-based model and the hydrodynamic theory show that the emergence of order occurs through the hierarchical formation of distinct collective dynamic states (Supplementary Movie 1[331]). These states include directed particle streams in which the agents move towards the source of chemical waves, ring-like streams with agents migrating along closed paths, compact motile droplets (active droplets), and large vortices that serve as sources of chemical spiral waves (Fig. 4.1e-n). The juxtaposition of the spatial organization of the particles (Fig. 4.1e-n, top panels) and the concentration field of the chemical signal (Fig. 4.1e-n, bottom panels) reveals a tight interdependence between the collective states of active matter and the chemical patterns.

Each of the collective dynamic states has a specific dynamics and a degree of stability. Vortices are well-localized and are stabilized by spiral waves trapped inside these dense aggregates. Their polarization vector $\boldsymbol{p}$ is oriented perpendicular to the outer vortex boundary and points inward, preventing agents from escaping and, therefore, stabilizing the vortex (Fig. 4.1h,m). While vortices are stable and robust, ring-like particle streams (Fig. 4.1e,j), retained by "whispering-gallery" waves, are long-lived but metastable and are typically engulfed by neighboring vortices (Supplementary Movie 9[331]). Active droplets (Fig. 4.1f,k) lack an intrinsic source of excitable waves, and their direction of migration is generally determined by external signal gradients. They dissolve in the absence of guiding stimuli. A particle stream (Fig. 4.1g,l) can be considered a limiting case of a ring-like stream (with an infinite radius of curvature and planar signaling waves). It establishes an efficient collective long-distance particle transfer towards the source of the signaling waves. Finally, we also observe bands resembling the polar bands that develop in non-communicating Vicsek-like models[166] (Fig. 4.1i,n). However, if agents in polar bands are coupled to chemical signaling waves propagating along the bands, as shown in Fig. 4.1i,n, this will induce a change of the agents' orientation and may lead to a transition towards stream-type solutions as depicted in Fig. 4.1g,l. Given these phenomenological observations, we ask two fundamental questions: How can different collective dynamic steady states be selected by tuning characteristic properties of the particle dynamics and the communication process? How can one characterize the hierarchical self-organization process and quantify the information processing involved? Figure 4.2 shows the (qualitative) phase diagram with the representative collective dynamic states as a function of the agents' mobility and signal sensitivity. In contrast to the isotropic-polar transition in Vicsek-type systems at $\rho = 1$[176], order here emerges at much lower densities, depending on the signal sensitivity (Figure 4.6). This is due to the alignment of the polar particles with the collectively established signaling field. At a given particle

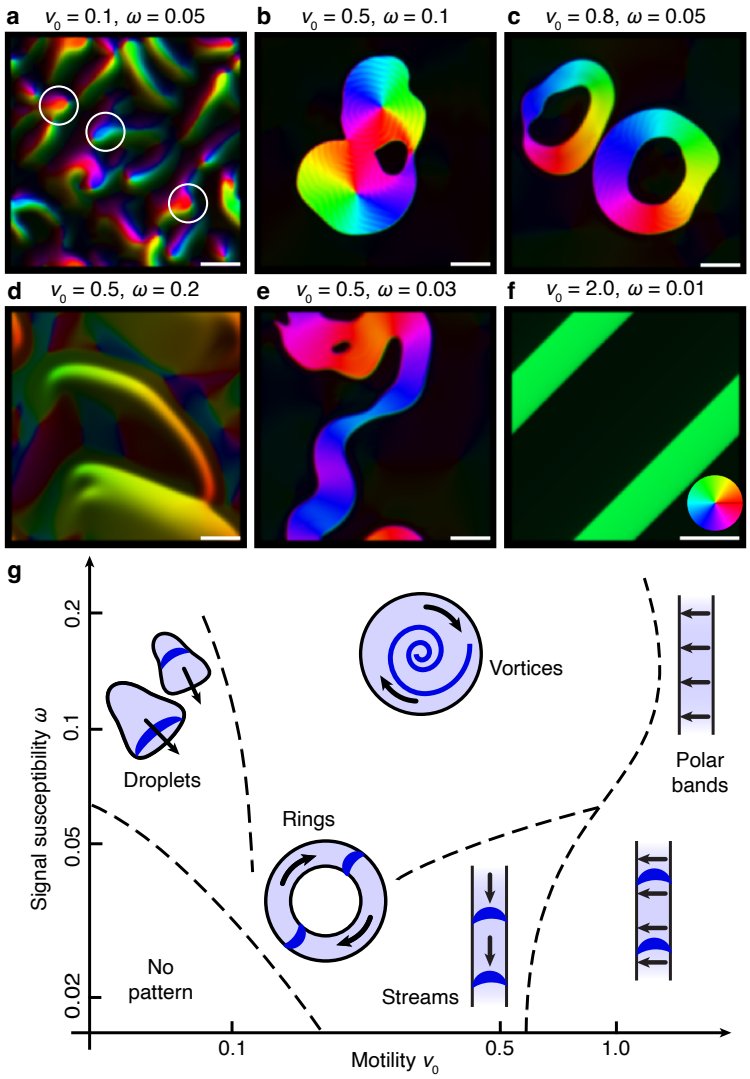

Figure 4.2: *Principal collective dynamic states in the hydrodynamic model.* The phase diagram of dominant (meta-stable) dynamic states in the $\omega - v_0$ (signal susceptibility and motility) parameter space is shown in the lower panel (g), and snapshots of corresponding numerical simulations of the hydrodynamic model, starting from a homogeneous initial density $\rho_0 = 0.6$ and random initial excitations of the signaling system are depicted in the upper panels. Colors indicate the polar orientation within the aggregates. (a), active droplets (three are highlighted by white circles), (b), vortex states, (c), ring solutions, (d), "silent" polar bands, (e), streams, (f), polar bands with signaling activity. See Supplementary Movies 2-7[331]. The polar relaxation rate is set to $\sigma = 0.02$, remaining parameters are given in section 4.6.7. White bars indicate a length of 50 units. This figure is reproduced from Ref.[3] under license [CC BY 4.0].

density, the dominant collective dynamic state in the asymptotic non-equilibrium steady state is determined by the relative fraction of motility and signaling effects. Vortices and rings are the dominant structures in a parameter regime with low motility and high signaling sensitivity. Thereby, vortices exhibit a balance between the persistent self-propulsion promoting agents away from the localized vortices and chemotactic attraction towards the vortex' center due to persistent spiral wave activity in the signaling field. If self-propulsion outweighs the attractive force established by collective signaling, vortices split up, and ring-like states become the predominant solution. If self-propulsion is rather weak and dominated by diffusion effects, the steady-state is governed by active droplets. Conversely, for vanishing signal sensitivity, the model reduces to a Vicsek-type model[166], and only polar bands are found. These can either host persistent signaling activity or remain in the quiescent state of the signaling machinery, just like system-spanning polar bands in Vicsek-like models. Next,

we asked how the hierarchical aggregation process from a disordered arrangement of particles to the final nonequilibrium steady state can be understood based on our characterization of the various collective dynamic states (Fig. 4.1). To this end, we focus on a parameter regime with intermediate polarity relaxation times and a balance between motility and signaling effects, which ultimately gives rise to vortex states.

4.4 HIERARCHICAL SELF-ORGANIZATION

Our agent-based simulations and numerical integration of the hydrodynamic theory consistently show that the hierarchical self-organization process is facilitated by an intricate interplay of self-propulsion, signaling, and information processing (Fig. 4.3, Supplementary Movie 8[331]). Initially, small-scale density fluctuations form, out of which droplets, streams, and small clusters later emerge. These initial aggregation processes are facilitated by short distance signaling waves and a local mutual entrainment. At later stages, the aggregation is orchestrated by spiral waves of signaling activity. Interestingly, there is competition between the spiral waves: Those that occupy larger and denser areas (mounds) accordingly have a higher frequency and displace smaller spiral waves (Figure 4.5). As a result, higher particle density provides a positive feedback mechanism that favors the formation of larger aggregation centers[332]. The aggregation stage is characterized by competition between particle clusters, which is quite different from that of non-signaling active matter [e.g. motility-induced phase separation (MIPS)], where the number of clusters scales as $N_c \sim t^{-\eta}$ with $\eta \approx 2/3$ [180]. In our hydrodynamic model, we observe multi-scaling behavior, indicating qualitatively distinct types of processes (Fig. 4.3a,b) for the time evolution of the cluster number and the density and polarization fields. Initially, we observe $N_c \sim 1/t$ (Fig. 4.1a), consistent with interface-controlled Ostwald ripening of clusters[70]. Once the streams have formed, there is a qualitative change in the aggregation process. The aggregation rate is now limited by the persistent directed motion of clusters and streams which migrate towards the aggregation centers. This leads to a much faster decay of the cluster number, even compared to the ballistic coalescence of clusters which would correspond to $\eta = 2$. This 'streaming phase' is followed by the formation of a few localized vortices that contain most agents. Due to the low particle density in between the vortices and the resulting lack of signal transmission, the interaction between these structures is strongly attenuated, and the coarsening process is slow. Since the signaling field decays exponentially (with diffusion length $L_c \sim \sqrt{D_c/\alpha}$), one expects a logarithmic coarsening law $N_c \sim 1/\ln t$ [333], consistent with the slow decay seen in our numerical data (Fig. 4.3c).

Thus, the ability to process information and make decisions results in the radically different organization of polar active matter. Ordering begins below the threshold of the polar-isotropic transition. The process leading to the formation of large vortices as robust attractors in the final stage of aggregation is much faster than that observed in non-signaling active matter or active matter with passive chemical signaling[320]. This is because it can exploit multi-scale collective intermediate states, whose respective frequencies are quantified in Fig. 4.3c. This classification confirms the observed phenomenology. The initial phase is dominated by coarsening of droplets. Once organizing vortices emerge, they establish persistent signaling waves. This causes a rapid decrease in the number of droplets and induces progressive aggregation through the formation of streams towards the vortices. In the final phase, a slow coarsening process occurs among the vortices with a corresponding logarithmic decrease in their number. Information processing drives self-organization Since each agent is endowed with a decision-making capability, we also sought to characterize the course of information processing during the multi-scale hierarchical aggregation process. To this end, we quantified the time evolution of the information content $I(t)$ in the system, using the computable information content of a lossless compressed configuration of the physical fields c, ρ, $\boldsymbol{p}$ and s [334,335]. In particular, we consider the file sizes obtained by the Lempel-Ziv-Welch compression algorithm[336] as implemented in the PNG file format (see section 4.6.4). The system's information content changes over time as individual agents process information in response to external stimuli employing their self-propulsion and intrinsic signal processing capability (Schmitt triggers). In the absence of signaling, self-propulsion and local interactions are unable to create order at subcritical densities due

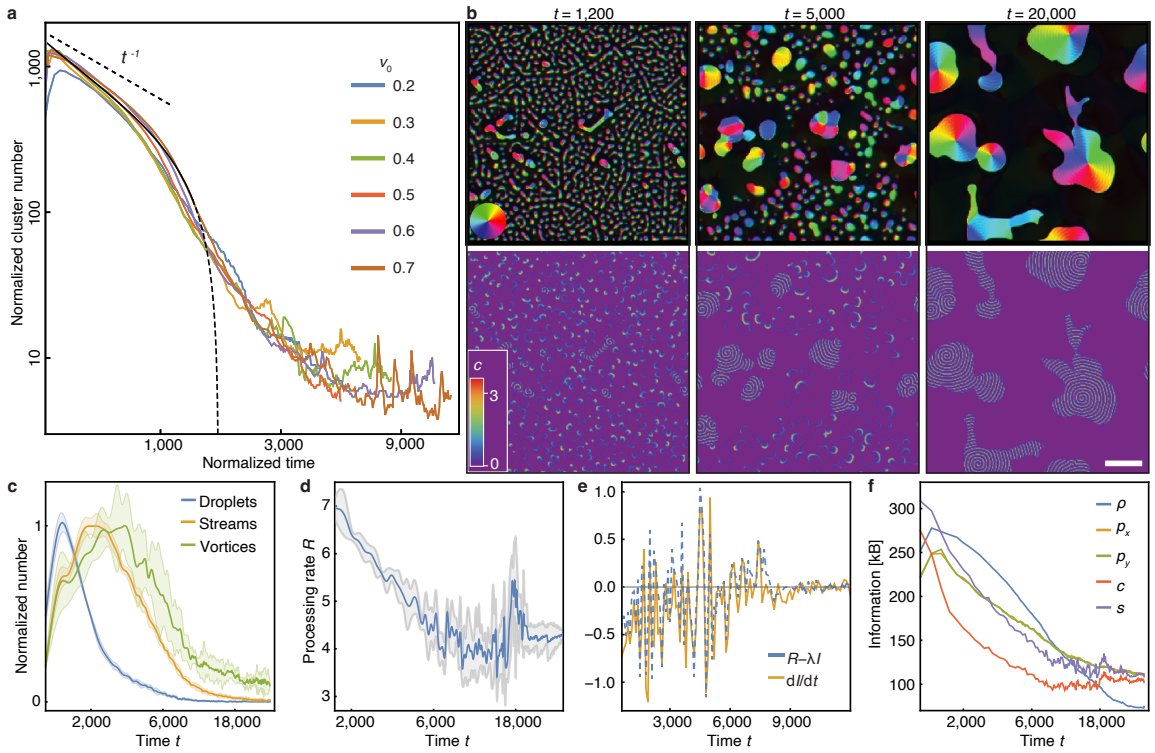

Figure 4.3: *Hierarchical self-organization and information processing.* (a) Time dependence of the cluster number N_c for different values of the mobility parameter v_0 in rescaled quantities $t \cdot v_0$ and $N_c/\sqrt{v_0}$. The unlabeled black line indicates the estimate $N_c \sim \left(N_0 - \kappa t^2\right)/t$. (b) Simulation snapshots at time t, displaying droplet ripening, vortex-controlled aggregation, and merging of vortices. The scale bar indicates a length of 100 units. Colors indicate polar orientation (top panels) and signaling concentration (bottom panels), respectively. (c) Time-resolved classification of collective dynamic states averaged over six simulation runs; the lighter shades define intervals of standard deviations. Initially, droplets grow and aggregate to form streams and vortices. (d) Time evolution of the information processing rate R of the signaling system and standard deviations (grey) averaged over six simulation runs. (e) Comparison of the rate of change $\mathrm{d}I/\mathrm{d}t$ of the stored information as predicted from Eq. (4.7) (blue) and the temporal derivative of compressed file sizes (orange). (f) Time dependence of the information content of the various fields, Eqs. (4.6). Parameters are $omega = 0.05$ and the values given in section 4.6.7. Panels (b)-(f) show simulation results and analysis for $v_0 = 0.5$. See section 4.6.4 for details. This figure is reproduced from Ref.[3] under license [CC BY 4.0].

to dominant angular diffusion; accordingly, the information content will decline exponentially with some decay rate λ as the system approaches the disordered homogeneous state. Here, however, there is information processing which leads to self-organization and induces order. We quantify the information processing by the rate R of agents transitioning to the refractory state, i.e., agents that emit a signal in response to a stimulus and therefore process information (Fig. 4.3d). Altogether, we expect the system's information content to follow the dynamics

$$\frac{\mathrm{d}I}{\mathrm{d}t} \sim R - \lambda I \tag{4.7}$$

with a fitting parameter λ. That, in turn, implies that the temporal change in the stored information depends exclusively on the initial information content and the measured processing rate R. The basic hypothesis, Eq. (4.7), is validated by our numerical simulations (Fig. 4.3e). On a qualitative level, it agrees very well with the predicted evolution of information content. In particular, the prediction captures not only the overall trend but also coincides with important landmark points of the evolution. This affirms our assertion that the signaling machinery is key for information processing and the driving mechanism behind self-organization in the system. The rate of change of the encoded information approaches a final state in which the order generated by persistent signaling

offsets the loss of correlation created by the agents' self-propulsion. An analysis of the amount of information stored in the various fields also reveals the different stages of the aggregation process (Fig.4.3f). We observe that the amount of information stored in the density field decreases and eventually approaches a comparably low value once the mass has accumulated in only a few stable vortices. This reflects the results of the cluster number analysis (Fig. 4.3a), including the qualitative change in aggregation dynamics between the dominance of ripening and the dominance of the guided movement of active droplets. In contrast to the homogeneous density field, the information content of the polarity field saturates at higher values, which correlates with the presence of persistent vortex states. Interestingly, the information content of the chemical concentration field c exhibits a super-exponential decay. This confirms that information processing is mainly performed by the signaling machinery, which makes it an essential factor in the organization of the aggregation process. Moreover, it approaches its baseline information level earlier than the density field, indicating the transition towards the phase of nearly isolated vortex states.

4.5 DISCUSSION

In conclusion, we have introduced a new class of active matter equipped with self-sustaining signaling capabilities: it allows self-propelled agents to communicate and process information. Communication and decision-making enable hierarchical self-organized aggregation to emerge via a sequence of distinct collective dynamic states. While our model is generic and does not rely on specific biological or chemical details, the observed phenomenology closely resembles the aggregation dynamics of social amoebae, including the formation of stable vortices[45] and metastable rings[43]. Communication induces a non-trivial self-organized attraction that gives rise to the formation of a rich variety of collective dynamic states. The exhibited behavior in terms of collective dynamic states and the collectively controlled aggregation process is a clear advance compared to current models of chemotactic colloids. Besides the variety of observed states, communication and active information processing introduce a new framework of collective organization. It allows for much faster aggregation times and a controlled competition between aggregation centers as high-density clusters can enlarge their basin of attraction. There are several potential extensions to the model, such as locally coupled self-propelled relaxation oscillators, signaling nematic active matter, or self-propelled agents coupled via sound or electromagnetic waves, which may have direct relevance to technological applications such as self-organizing swarms of minimal drones or functional micro-robots. Information processing could be introduced by modifying the chemistry of colloids and droplets, thus allowing experimentally accessible realizations to be directly established for silver-chloride Janus colloids exhibiting chemical oscillations and synchronization[218,314], and for self-propelled emulsions hosting the Belousov-Zhabotinsky reaction[337], to name but two. Decision-making can also be implemented using simple electronic circuits in mass-manufactured microrobots. These may open new avenues for applications of active matter in nanoscience and robotics.

4.6 APPENDIX

4.6.1 A DETAILED DESCRIPTION OF THE AGENT-BASED MODEL

In the agent-based model, we consider self-propelled particles with radius r_p in a two-dimensional square periodic domain with side length L. The particles move with constant speed v_0 in the plane. The dynamics of the agents' positions r_i is described by Eq. (4.1). The direction of movement can be changed by polar alignment during collision events, chemotactic responses to signaling molecules, or stochastic fluctuations. If two agents come within a distance of less than $2r_\mathrm{p}$, they are repositioned according to the following hard-core repulsion rule: overlapping particles are shifted in the direction of their distance vector by equal amounts until a distance of $2r_\mathrm{p}$ is restored. Within an interaction radius $r_c > 2r_\mathrm{p}$, agents align in a polar fashion, i.e. the interaction of an agent i with a neighbor j causes both agents to turn towards the average orientation angle with the alignment rate Γ. The

agents also align with the direction $\varphi_c = \tan^{-1}(\partial_y c/\partial_x c)$ of the local maximum of the chemical signal concentration c with the susceptibility coefficient ω. Both alignment interactions are imperfect, which we account for by adding zero-mean white noise ξ_i with amplitude $\sqrt{2D_R}$:$\langle \xi_i(t)\xi_j(t')\rangle = 2D_R\delta_{ij}\delta(t-t')$. In total, the dynamics of the agent's orientation φ_i is given by the Langevin equation, Eq. (4.2).

The system of agents establishes self-sustaining chemical signaling as a means of information processing and transmission. Each agent is equipped with an internal state variable $s_i \in [0,1]$ that determines whether or not it perceives the environment and transmits signals by emitting a chemical substance. We take the magnitude of s_i to be the refractoriness of an agent to external signals, i.e., a measure of how responsive it is to relay a signal: $s_i = 0$ then corresponds to the state with the lowest refractoriness (highest susceptibility). The agents are assumed to sense the environment by linearly adapting to the local concentration level c of the chemical field with rate ϵ, Eq. (4.3), and act as nonlinear sources of the chemical signal c. This release of chemicals depends on both the internal state of the agents and the environment. We assume the source strength to be of the threshold form, Eq. (4.4), where β denotes the release rate and c_{th} a threshold above which agents can detect and relay signals and below which they remain quiescent; $\Theta(x)$ denotes the Heaviside step function with

$$\Theta(x) \equiv \begin{cases} 1 & \text{,for } x > 0, \\ 0 & \text{,else.} \end{cases} \tag{4.8}$$

The agent's signaling receptors are assumed to undergo state-dependent changes in susceptibility that implement potential saturation effects and adaptation to varying levels of signaling molecules in the environment. Specifically, we take the threshold value c_{th} to be a linear function of the state variable s_i,

$$c_{\text{th}}(s_i) = (s_i + b)/a\,, \tag{4.9}$$

implementing a higher threshold for signal detection at larger state values of the refractoriness s_i. The parameter b sets the baseline threshold and the factor $1/a$ specifies the linear increase of the threshold $c_{\text{th}}(s_i)$ with growing state values. Additionally, to implement the agents' ability to process detected signals and respond to them, the release of chemicals shall depend on the internal state s_i of an agent: In terms of their signal production, agents in the most susceptible state ($s_i = 0$) react most vigorously to super-threshold stimuli. The rate of signal release is assumed to decrease linearly $(1 - s)$ with increasing s_i. Note that for the set of parameters used in this study, section 4.6.7, the states s_i do not exceed values of one. Therefore, agents are always either quiescent and do not contribute to the chemical signaling field or act as sources for it. Taken together, the interplay between the internal dynamics s and the chemical field c in a well-mixed environment is given by

$$\frac{\mathrm{d}s}{\mathrm{d}t} = \epsilon\,(c - s)\,, \tag{4.10a}$$

$$\frac{\mathrm{d}c}{\mathrm{d}t} = -\alpha c + \beta\phi\,(s, c)\,, \tag{4.10b}$$

which also accounts for degradation of the emitted signal at a rate α. Equations (4.10) constitute a nonlinear two-component system, which shows excitable behavior; see Supplementary Fig. 4.4a for an illustration of the phase-space flow. The quiescent state, corresponding to $c = s = 0$, is linearly stable and has a finite domain of attraction. However, if for $s = 0$ the input signal c_{in} exceeds the threshold $c_{\text{in}} > c_{\text{th}}\,(s = 0) = b/a$, the system performs a long excursion in phase space before returning to $c = s = 0$; see the red phase space trajectory in Supplementary Fig. 4.4a. Note that the amplitude of the response (extent of the red trajectory in phase space) is mainly determined by the phase-space flow and only weakly depends on the initial input strength c_{in}. This ensures a sufficiently strong transmission of any super-threshold signals. The phase-space trajectory in Supplementary Fig. 4.4a yields the excitation pulse displayed in Supplementary Fig. 4.4b, which shows fast excitation and emission of signals and a slower refractory dynamics that restores the

susceptible state ($c = s = 0$). The duration of the refractory period τ is determined by the inverse of the relaxation rate ϵ^{-1}. Taken together, the excitable dynamics resemble the behavior of a Schmitt trigger (Fig. 4.1c), a circuit with closed negative feedback, which exhibits hysteresis-like dynamics representative of e.g. relaxation oscillators. In particular, the appropriate delay between the fast production of signaling molecules and the slower adaptation of the agent's internal state can be achieved by choosing $\beta/\epsilon \ll 1$, resulting in a relaxation dynamics with a rapid response to a stimulus followed by a slower refractory period. Model parameters are summarized in section 4.6.7.

To formulate the spatial dynamics of the signaling molecules in terms of a concentration field c, one must specify how the molecules emitted by the agents are distributed in their vicinity. We use a source distribution given by a normalized Gaussian profile $f \sim \exp\left[-(x^2+y^2)/(2w^2)\right]$ with characteristic width $w \equiv 2r_{\mathrm{p}}$. In addition, we account for the center-of-mass diffusion (with diffusion coefficient D_c) and degradation with rate α, so that together with the source terms for each agent one obtains Eq. (4.3). We choose the decay rate α to be of the same order of magnitude as the positive source contributions, terms $\sim \beta$, to the signaling field c for average agent densities. On the scale of individual agents, signal diffusion is assumed to be fast compared to the agents' self-propulsion velocity, $1 \ll D_c/\left(r_p v_0\right)$. The parameters used in the numerical simulations are specified in Table 4.1.

4.6.2 A DETAILED DESCRIPTION OF THE HYDRODYNAMIC MODEL

In this section, we give a detailed description of the hydrodynamic model, Eqs. (4.6), that we introduced in the main text for communicating active-matter systems. This dynamic field theory is formulated in terms of a set of evolution equations for the following fields: the number density of particles ρ, the vector order parameter characterizing the particles' local average polar alignment $p = \langle n_i \rangle$, the concentration of the signaling species c, and the state of refractoriness s. A representative vortex solution with internal spiral-wave activity of the signaling fields is shown in Supplementary Fig. 4.4a. We observe an approximately circular high-density cluster within which the particle orientation revolves around its center and aligns with the density gradients at the interface to the outer low-density regime. This vortex state is accompanied by the emergence of a spiral wave established inside the high-density domain by the chemical field and the adapting signaling states of the agents. The time evolution of the agent's density field $\rho(r,t)$, Eq. (4.6a), is given by an advection-diffusion equation, which accounts for advective transport due to the particles' self-propulsion with speed v_0 and diffusion of the center of mass with diffusion constant D_ρ. The center-of-mass diffusion has no direct counterpart in the agent-based model as it has been neglected there. However, for completeness and to regularize density gradients, it is included in the hydrodynamic theory. The direction of self-propulsion, described by the polar field $\boldsymbol{p}(\boldsymbol{r},t)$, can be changed by interparticle interactions, stochastic fluctuations, and signaling-induced reorientations: The first three terms in Eq. (4.6b), for the time evolution of the polarity field correspond to a time-dependent Ginzburg-Landau model describing the dynamics close to an isotropic-polar phase transition; units for the density ρ are chosen such that the critical density is set to unity. The persistence parameter σ defines the relaxation time, the parameter δ sets the magnitude of polar order, and D_p implements the elasticity in a one-Frank-constant approximation. Moreover, to make the model more general, we include a term $\chi \boldsymbol{p} \cdot \nabla \boldsymbol{p}$ that accounts for self-advection. In the numerical simulations, the corresponding parameter χ is set to a small value and does not contribute critically to the qualitative behavior of the system. The coupling between the orientational order and density combines both self-advective and steric effects incorporated in the function

$$Q(\rho) = \frac{v_0}{2}\left[\exp\left(-32\rho\right) + \exp\left(16(\rho-2)\right)\right] . \tag{4.11}$$

The steric effects can be modeled as an effective pressure. As derived in section 4.6.5, see Eq. (4.27), we include the low-density contribution as an amplitude $Q(\rho \to 0) = v_0/2$. For increasing densities, we assume that collective effects arising from particle interactions counteract the steric repulsion, and therefore reduce the amplitude of the function $Q(\rho)$. Complementing this, for high densities,

the effective pressure contributions outweigh the collective effects again due to the finite volume of agents. Therefore, the amplitude $Q(\rho)$ increases at a critical maximum density of $\rho = 2$. The coupling of the polar order to signaling encoded by the chemical concentration field enters in Eq. (4.6b) via the term $\omega\nabla c$. It describes the alignment of the polarization field in the direction of the local maximum of the signal concentration c with susceptibility parameter ω. The dynamics of the chemical concentration field c, Eq. (4.6c), is a direct transfer from the agent-based model, Eq. (4.3). Coarse-graining the equation, we replace the discrete sum of Gaussian source terms $\sum_i f(|\boldsymbol{r} - \boldsymbol{r}_i|)$ by a density-dependent continuous contribution $\sim \rho(\boldsymbol{r}, t)$. The dynamics of the state variable s, Eq. (4.6d), includes diffusive, reactive, and advective contributions. Here, the first term simply corresponds to the center-of-mass diffusion of the particles as in Eq. (4.6a). The second term corresponds to the relaxation of the local state variable s to the corresponding local value of the signaling field c, where ϵ denotes the relaxation rate. Therefore, the magnitude of the rate ϵ controls the timescale over which the internal signaling state s adapts to the chemical concentrations c. Finally, the term $\sim \boldsymbol{p}\cdot\nabla s$ incorporates the local change of the agents' signaling states s by means of their self-propulsion. The regularizing prefactor $v = v_0 \tanh(|\boldsymbol{m}|/\rho)/|\boldsymbol{p}|$ ensures the boundedness of effective self-propulsion velocities for low densities $\rho \to 0$.

4.6.3 NUMERICAL IMPLEMENTATION

We integrate the agent-based model, Eqs. (4.1)-(4.5), on a square periodic domain with side length L over discretized time intervals Δt. For each time step, the continuous particle positions and orientations are updated following Eqs. (4.1), (4.2) and the hard-core repulsion rule, using an Euler-Maruyama scheme. For efficient identification of potential interaction partners at each time step, particles are assigned to virtual grid cells. We check for collisions within a particle's grid cell and its surrounding cells. Agents that pass through a virtual grid cell's boundaries are reassigned to their new grid cell. Based on the updated agent positions, we compute the agents' source contributions, $\sim \beta$ to the continuous signaling field c. Subsequently, we solve the temporal dynamics of the signaling field, Eq. (4.3), in Fourier space by a forward Euler integration scheme and then obtain the representation in real space by inverse Fourier transform. We apply a fast Fourier transform algorithm for these transformations. Concluding the calculations for a given time, we update the internal states of the agents using the same forward Euler time integration scheme for Eq. (4.5). For the simulations with 4000 agents, shown in Fig. 4.1, we use a total system size of 200×200, resolved by 200 Fourier modes per spatial direction and a time step of $Deltat = 0.01$. The depicted solutions are neither dependent on the selected spatial or temporal resolution which we verified by corresponding simulations with higher accuracy.

The set of continuous hydrodynamic equations, Eqs. (4.6), is solved in a square periodic domain by a quasi-spectral method and a semi-implicit time integration with discretized time steps Δt. For each time step, we make use of fast Fourier transform of the field quantities to calculate their spatial derivatives. Also, we compute the Fourier transform of the nonlinear contributions to the dynamics, and apply an exponential time differencing scheme of second order (ETD2) to integrate the complete set of equations in Fourier space over a time interval Δt 52. In doing so, all linear contributions to the dynamics, Eqs. (4.6), are implicitly solved for, while nonlinearities are included explicitly via their first-order forward finite difference approximation. The eigenvalues and pseudoinverse of the matrix representation of the linear dynamics of Eqs. (4.6), necessary for ETD2, are calculated once at the beginning of the runtime using the linear algebra library Eigen[338]. We initialize the system with homogeneous densities and polarity fields with small zero-mean white noise perturbations. The chemical system is initialized by exciting randomly positioned and oriented two-dimensional Gaussian kernels of characteristic lengths ranging from 20 to 30 units and widths of 5 units. The model parameters are given in section 4.6.7. For all simulations, time steps and spatial resolutions have been adapted to optimize runtime while ensuring that results do not depend on the chosen discretization.

4.6.4 QUANTIFICATION OF THE AGGREGATION PROCESS

The self-sustaining signaling mechanism we consider has a threefold effect on the formation and organization of large-scale structures in the active polar system. Firstly, signaling enables pattern formation from a homogeneous density, even below the critical density ($\rho_c \equiv 1$) for the polar ordering transition. Secondly, stronger chemotactic susceptibility of the polar orientation to the established signaling significantly increases the rate of the self-organization process, as can be seen in Supplementary Figure 4.6. Starting from an initially spatially uniform density ρ_0, the aggregation times T_{aggr} for crossing the isotropic-to-polar ordering transition at $\rho_c \equiv 1$ decrease significantly for larger signal susceptibilities ω. And thirdly, spiral waves as sources of persistent signaling activity can stabilize the emerging vortex structures, as can be seen from the results of the numerical simulations, e.g., Fig. 4.3. To gain a better understanding of the principles underlying the signal-driven self-organization process and to quantify the degree and type of ordering, we use cluster classification analysis and quantify the time evolution of the information content in the system. Both methods are presented in more detail below. In our numerical simulations, we observe that distinct collective states dominate the different phases of aggregation; see Fig. 4.3, Supplementary Movie 8[331]. During an initial phase, droplets of agents are formed and undergo Ostwald-type ripening. Once spiral waves are established as persistent signaling sources, the droplets show directed motion towards the strongest of these sources, i.e., they become 'active' droplets. The coalescence of these active droplets leads to the formation of collective density streams. Eventually, streams and active droplets approach the source of the organizing signal, where they condense into stable clusters. The interplay of aggregation due to the intrinsic signaling and the self-propulsion of the polar active matter typically results in localized vortex solutions. As a means of classifying the various collective states discussed above, namely droplets, streams and vortices, we analyze clusters with densities $\rho > 0.7$ (above the system's average density, which we typically set to $\rho_0 = 0.6$) by quantifying their total mass, spatial extension along their main axes, and the direction of the effective self-propulsion of the cluster. The latter represents the direction of the cluster's center-of-mass motion, $\sim \int \boldsymbol{p}(\boldsymbol{r}, t)\, \mathrm{d}\boldsymbol{r}$. In particular, we measure the spatial extension of clusters along their main axes (axes with largest spatial extent), the angle between the main axis and the averaged cluster polarity, and the intrinsic vorticity $\nabla \times \boldsymbol{p}$ of the orientational field. We classify a given aggregate as a stream if the shape factor (the ratio of major to minor diameter) is larger than 1.4 and the angle between the major axis and polarity is smaller than $\pi/4$; if the shape factor is less than 1.4 and the mean vorticity inside the domain exceeds a value of 0.01, the aggregate is classified as a vortex. Clusters characterized as neither streams nor vortices are classified as droplets. Information about domain position, orientation and shape is obtained by using the first three central moments of the binarized domain with density threshold $\rho = 0.7$. As a measure for emerging order in the system, and to quantify the impact of the signaling machinery on the aggregation process, we consider the total amount of information stored in the system. Following main text references[334,335], the information content can be obtained by lossless compression of the system's data, i.e., the data points of the discretized continuous fields, Eqs. (4.6), for a given time. We analyze the fields at discrete time points with step size $\Delta t = 200$ for total simulation times of $t_{\text{sim}} = 40,000$. In order to measure the information content of the system for a given time, we saved the data of all the separate fields into a collective image with a spatial discretization of 128 by 128 pixels per field and 256 grey values per pixel. Subsequently we use the lossless compression in the PNG format to compute the stored information content. The resulting file sizes then give a corresponding amount of stored information as discussed in the main text; see Fig. 4.3e,f. Information processing in the system is facilitated by two distinct processes: polar ordering due to pairwise collisions and decision making of the individual signaling units, as specified by the excitable signaling field dynamics. Below the isotropic-to-polar transition at the critical density ($\rho_c = 1$), the disordering effect of the agent's angular diffusion dominates over their ordering alignment dynamics, such that in the absence of chemical signaling the system must relax towards a homogeneous disordered state. This relaxation process is expected to proceed at a rate λ. As an organizing factor, the signaling machinery counteracts the natural trend of the polar active-matter system towards the homogeneous state. We hypothesize that most of the information processing occurs through the signaling machinery, and we quantify its activity by the information processing

rate R. The latter is represented by the area fraction of the excitable system in the refractory state. Specifically, we define this state as exhibiting a super-threshold concentration in the chemical signaling field, $c > 1$. Taken together, we posit that the time evolution of the stored information content I can be approximated as given in Eq. (4.7). By means of this dynamic equation, and based on the assumption that information in the system is mainly processed by the signaling machinery, we are able to predict the temporal evolution of the total stored information. Starting from a value of the system's initial information content, and supplied with the time-dependent processing rates R, Eq. (4.7) allows for a prediction of the temporal dynamics of the stored information. The comparison between this prediction and the actual dynamics of the stored information content quantified by the file size of the lossless compressed data at a given time in Fig. 4.3e yields good agreement. This again validates the basic assumption of signaling-mediated information processing in the system. Based on the cluster classification and cluster number analysis, we can quantify the three main stages of the aggregation process described above and in the main text; see also Fig. 4.3 and Supplementary Movies 1 and 8[331]. In the following, we describe the basic modes of mass aggregation in terms of the efficiency of the processes. Consider a system of droplets of equal size, concentration n and diffusion coefficient $D \sim S^\gamma$, with a yet-to-be determined exponent γ relating the diffusion to the droplet sizes S. For diffusion-limited coalescence of droplets in two spatial dimensions, the time dependence of droplet sizes and numbers is given by[339]

$$S \sim t^z, \quad N_\mathrm{c} \sim t^{-z}, \tag{4.12}$$

where the exponent z can be determined from the hydrodynamic equations underlying the aggregation process at the corresponding stages. For instance, the probability of coalescence in a binary collision process is given by n^2, and thus, the mean-field equation for the droplet density n reads

$$\frac{\mathrm{d}n}{\mathrm{d}t} = -D(S)n^2 = -D_0 S^\gamma n^2 \,. \tag{4.13}$$

Substituting the expressions for S and n, one obtains for the exponent

$$z = \frac{1}{1-\gamma} \,. \tag{4.14}$$

For the case where diffusion does not depend on the cluster size, $\gamma = 0$, one obtains $N_\mathrm{c} \sim 1/t$. This behavior is similar to the interface-controlled Ostwald ripening for which the coarsening of droplets is independent of their diffusive motion. Additionally, our hydrodynamic model gives rise to directed motion of active droplets, which is guided by organizing spiral waves. Including the guided movement of active droplets towards the organizing vortices, one can estimate the cluster number dynamics by

$$N_\mathrm{c}(t) \sim \left(N_0 - \kappa t^2\right)/t \,, \quad \text{with } \kappa > 0 \,. \tag{4.15}$$

This estimate incorporates the directed ballistic motion of clusters towards a collective aggregation center $\sim N_0 - \kappa t^2$. Moreover, these clusters may still exhibit interface-driven coarsening, which is accounted for by an additional factor t^{-1}. Thus, the estimate captures the main behavior of the first two aggregation stages, which are dominated by Ostwald ripening and coordinated movement of droplets towards spiral waves as organizing centers. This becomes manifest in a good qualitative agreement between the estimate and the measured evolution of the cluster number as shown in Fig. 4.3a, with fit parameters $N_0 = 382,000$ and $\kappa = 0.15$. However, at longer times, vortex-vortex competition, which is not accounted for in the given estimate, becomes increasingly important. Therefore, the deviations between the estimated and measured dynamics of the cluster numbers grow as the aggregation process progresses.

4.6.5 DERIVATION OF THE HYDRODYNAMIC EQUATIONS THROUGH A BOLTZMANN-LIKE KINETIC APPROACH

In this section we show how the set of hydrodynamic equations,

$$\partial_t \rho(\boldsymbol{r},t) = -v_0 \boldsymbol{\nabla}\cdot\boldsymbol{p} + D_\rho\,\Delta\rho\,, \tag{4.16a}$$
$$\partial_t \boldsymbol{p}(\boldsymbol{r},t) = \sigma\,(\rho-1)\,\boldsymbol{p} - \delta\,|\boldsymbol{p}|^2\,\boldsymbol{p} + D_p\,\Delta\boldsymbol{p} - \chi\,\boldsymbol{p}\cdot\boldsymbol{\nabla}\boldsymbol{p} - Q(\rho)\boldsymbol{\nabla}\rho + \rho\,\omega\boldsymbol{\nabla}c\,, \tag{4.16b}$$
$$\partial_t c(\boldsymbol{r},t) = D_c\,\Delta c - \alpha\,c + \rho\,\beta\,\Theta\,(c-c_{\mathrm{th}})\,(1-s)\ , \tag{4.16c}$$
$$\partial_t s(\boldsymbol{r},t) = D_\rho\,\Delta s - \epsilon\,(s-c) - \bar{v}\,\boldsymbol{p}\cdot\boldsymbol{\nabla}s\,, \tag{4.16d}$$

can be derived from a Boltzmann-like approach for the probability density $P(\boldsymbol{r},\varphi,t)$ of finding a particle at position $\boldsymbol{r}$ with orientation φ at time t; the particle's orientation is signified by the unit vector $\boldsymbol{n} = (\cos\varphi,\sin\varphi)^T$. The equation accounts for center-of-mass diffusion, particle self-propulsion, rotational diffusion, alignment with the signaling field, and interactions between particles:

$$\partial_t P(\boldsymbol{r},\varphi,t) = D_\rho\partial_i\partial_i P - v_0\,\partial_i(n_i P) + \partial_\varphi\big[D_{\mathrm{R}}\partial_\varphi + \omega(c)\sin(\varphi-\varphi_c)\big]P + \text{interactions}\,. \tag{4.17}$$

The advection term together with the rotational diffusion describe the self-propelled motion of the particles combined with the angular noise as in the agent-based model. The fourth term corresponds to a probability flux directed towards orientations that are aligned with the local gradients of the signaling field c with sensitivity parameter $\omega(c)$ and $\varphi_c \equiv \tan^{-1}(\partial_y c/\partial_x c) = \mathrm{angle}\,(\nabla c)$. The interaction contributions will be discussed further below.

We follow the standard approach for deriving hydrodynamic equations from a Boltzmann-type of equation by expanding the probability density function in Fourier modes for the spatial orientation of the director $\boldsymbol{n}$ in two-dimensional space[198,199],

$$P(\boldsymbol{r},\varphi) = \sum_k P_k(\boldsymbol{r})\,e^{ik\varphi}\,, \tag{4.18}$$

whereby, for the sake of brevity, we suppress the time dependency here and in the following. The corresponding Fourier coefficients follow from the forward transform

$$P_k(\boldsymbol{r}) = \frac{1}{2\pi}\int_0^{2\pi}\mathrm{d}\varphi\,P(\boldsymbol{r},\varphi)\,e^{-ik\varphi}\,. \tag{4.19}$$

We define the particle density ρ and the density-weighted polar order $\boldsymbol{p}$ by relating them to the harmonics via the Fourier expansion, Eq. (4.18):

$$\rho(\boldsymbol{r}) \equiv \int_0^{2\pi}\mathrm{d}\varphi\,P(\boldsymbol{r},\varphi) = 2\pi P_0\,, \tag{4.20}$$

$$\begin{aligned}\boldsymbol{p}(\boldsymbol{r}) &\equiv \int_0^{2\pi}\mathrm{d}\varphi\,\boldsymbol{n}(\varphi)P(\boldsymbol{r},\varphi)\,,\\ &= \sum_k \frac{1}{2}\int_0^{2\pi}\mathrm{d}\varphi\left(e^{i\varphi}+e^{-i\varphi}, i\left(e^{-i\varphi}+e^{i\varphi}\right)\right)^T P_k(\boldsymbol{r})\,e^{ik\varphi}\,,\\ &= \pi\big(P_1+P_{-1}, i(P_1-P_{-1})\big)^T\,.\end{aligned} \tag{4.21}$$

To describe the intrinsic states of the communicating active matter, we introduce a probability density $P^s(s)$ of particles in a given signaling state s and assume that the total probability density $P_{\mathrm{tot}}(\boldsymbol{r},\varphi,s) = P^s(s)\,P(\boldsymbol{r},\varphi)$ factorizes in a part for the signaling state and the distribution for the agent's positions and orientations. Thus, the density-weighted signaling state of the agents is given

by

$$\bar{s} \equiv \int \mathrm{d}s \int_0^{2\pi} \mathrm{d}\varphi \, s \, P^s(s) \, P(\boldsymbol{r}, \varphi) \, . \tag{4.22}$$

In the following, the different contributions to the Boltzmann equation, Eq. (4.17), are analyzed separately. First, in order to derive expressions for the diffusive contributions in the hydrodynamic equations we use the projection onto the m-th harmonic,

$$\overline{(\dots)}^m = \frac{1}{2\pi} \int_0^{2\pi} \mathrm{d}\varphi \, e^{-im\varphi} \, (\dots) \, , \tag{4.23}$$

which gives the m-th Fourier coefficient to the expansion above, Eq. (4.18). Applying the projection operator, Eq. (4.23), onto the corresponding term in Eq. (4.17) one obtains

$$\partial_t \rho = D_\rho \Delta \rho \, , \tag{4.24}$$

for the dynamics of the density. One would obtain the same dynamics for the center-of-mass diffusion in the polar order field, but contributions from interaction kernels, representing elasticity of the polarity field, can lead to similar terms, which is why we assume a different coefficient D_p for the polar field. Continuing with the advective term, (i.e. $\sim v_0$), the projection onto the modes yields

$$\begin{aligned}
\partial_t P_m(\boldsymbol{r}) &= \overline{-v_0 \partial_i (n_i P(\boldsymbol{r}, \varphi))}^m \, , \\
&= -\frac{v_0}{2\pi} \int_0^{2\pi} d\varphi \sum_k P_k(\boldsymbol{r}) e^{ik\varphi} \left[\partial_x e^{-im\varphi} \frac{(e^{i\varphi} + e^{-i\varphi})}{2} + \partial_y e^{-im\varphi} \frac{(e^{i\varphi} - e^{-i\varphi})}{2i} \right] , \\
&= -\frac{v_0}{2} \left[\partial_x \sum_k P_k(\boldsymbol{r}) (\delta_{k,m-1} + \delta_{k,m+1}) + i \partial_y \sum_k P_k(\boldsymbol{r}) (\delta_{k,m+1} - \delta_{k,m-1}) \right] .
\end{aligned} \tag{4.25}$$

With the definitions, Eqs. (4.20) and (4.21), we obtain for the field variables

$$\partial_t \rho(\boldsymbol{r}) = 2\pi \partial_t P_0(\boldsymbol{r}) = -v_0 \partial_i p_i(\boldsymbol{r}) \, , \tag{4.26a}$$

$$\partial_t p_x(\boldsymbol{r}) = \pi \partial_t (P_1(\boldsymbol{r}) + P_{-1}(\boldsymbol{r})) = -\frac{v_0}{2} \partial_x \rho(\boldsymbol{r}) \, , \tag{4.26b}$$

$$\partial_t p_y(\boldsymbol{r}) = i\pi \partial_t (P_1(\boldsymbol{r}) - P_{-1}(\boldsymbol{r})) = -\frac{v_0}{2} \partial_y \rho(\boldsymbol{r}) \, . \tag{4.26c}$$

Since a Boltzmann-approach is by design a low-density approximation, these results must be interpreted as such and require for an extension to assure well-behavedness at higher densities. Notably, this applies to the coupling of the polarity field to density gradients, $\partial_t p_i \sim -\frac{1}{2} \, v_0 \, \partial_i \rho$. At low densities, this term accounts for an effective pressure, increasing with increasing particle densities. At higher densities, other cooperative effects emerging from anisotropic interactions can dominate the coupling of the polarity field to density gradients, counteracting the repulsion dominating at low densities. In addition, at a critical maximum density, which we set to $\rho = 2$, the effective pressure increases significantly due to the finite volumes of the agents. Therefore, steric interactions dominate the cooperative interactions for $\rho \to 2$. We account for these effects by extending the terms $\sim -\partial_i \rho$ by a density-dependent prefactor $Q(\rho)$ which is proportional to v_0 and has the following form:

$$Q(\rho) = \frac{v_0}{2} \Big[\exp(-32\rho) + \exp(16(\rho - 2)) \Big] \, . \tag{4.27}$$

The function $Q(\rho)$ captures the repulsion at low densities which decays for intermediate densities due to cooperative effects. Moreover, it limits the maximum density to values $\rho \approx 2$ taking into account the steric repulsion at dense packing of the agents. The presented results do not qualitatively depend on the particular choice of the function $Q(\rho)$. The scalar field corresponding to the agent's signaling

activity, Eq. (4.22) is directly associated with the agents. Hence, in the same way as the particles it is advected with the polar flow and exhibits center-of-mass diffusion. From the definition, Eq. (4.22), we obtain

$$\begin{aligned}\partial_t \bar{s} &= -v_0 \int \mathrm{d}\varphi\, \mathrm{d}s\, s \partial_i n_i P\,, \\ &= -v_0 \int \mathrm{d}\varphi\, \mathrm{d}s\, s \left[\partial_x \frac{e^{i\varphi}+e^{-i\varphi}}{2} + \partial_y \frac{e^{i\varphi}-e^{-i\varphi}}{2i}\right] \sum_k P^k P^s\,, \\ &= -2\pi v_0 \int \mathrm{d}s\, s \left[\frac{1}{2}\,\partial_x \left(P^\varphi_{-1} + P^\varphi_1\right) + \frac{1}{2i}\,\partial_y \left(P^\varphi_{-1} - P^\varphi_1\right)\right] P^s\,,\end{aligned}$$

and with the definition of the polarity field, Eq. (4.21),

$$\partial_t \bar{s} = -v_0 \partial_i \left(\frac{\bar{s}\, p_i}{\rho}\right)\,. \tag{4.28}$$

Thus, the complete diffusive and advective contributions to the dynamics of the density weighted signaling state $\bar{s} = \rho s$ are given by

$$\partial_t \bar{s} = D_\rho \Delta \bar{s} - v_0 \partial_i \left(\frac{\bar{s} p_i}{\rho}\right)\,. \tag{4.29}$$

Correspondingly to the agent-based model, we re-express the state field $\bar{s}$ in terms of the 'state concentration', i.e., the local state normalized by the particle density, s by replacing $s = \bar{s}/\rho$ in Eq. (4.29); one obtains

$$\partial_t s = D_\rho \Delta s - \frac{v_0 p_i}{\rho} \cdot (\partial_i s)\,, \tag{4.30}$$

where we neglected cross-gradient contributions in the density ρ and the field s.

Next, we turn to the contribution of the angular noise to the dynamics of the polar field. Fourier-expanding the corresponding term $\sim D_\mathrm{R}$ in Eq. (4.17) and projecting it onto the j^{th} harmonic according to Eq. (4.23), yields the equation

$$\partial_t P_j(\boldsymbol{r}) = -D_R j^2 P_j(\boldsymbol{r}) \tag{4.31}$$

and, thus, with the definition of the polar field, Eq. (4.21),

$$\partial_t \boldsymbol{p}(\boldsymbol{r}) = -2D_\mathrm{R}\, \boldsymbol{p}(\boldsymbol{r})\,. \tag{4.32}$$

Finally, regarding the alignment of the agents' orientation vectors with gradients of the signaling field c, we want to briefly highlight the origin of the corresponding terms, $\sim \omega$, in the Boltzmann equation (4.17) starting from the proposed underlying Langevin dynamics

$$\begin{aligned}\frac{\partial \boldsymbol{r}}{\partial t} &= v_0\, \boldsymbol{n}(\varphi)\,, \\ \frac{\partial \varphi}{\partial t} &= \xi(t) + \omega(c) \sin\left(\varphi - \varphi_c\right)\,,\end{aligned} \tag{4.33}$$

with the particle position vector $\boldsymbol{r}$ and the angle of the chemical gradient $\varphi_c = \mathrm{angle}(\nabla c)$. The chemotaxis contributes to the Boltzmann equation, Eq. (4.17), directly as the angular drift term

$$\partial_t P \sim -\partial_\varphi \left[\omega(c) \sin\left(\varphi - \varphi_c\right)\right] P\,. \tag{4.34}$$

Expanding the probability density in the Fourier harmonics as in Eq. (4.18), one obtains

$$\partial_t P_k = -\frac{\omega(c)}{2\pi}\int_0^{2\pi} \mathrm{d}\varphi\, e^{-ik\varphi}\partial_\varphi \left[\sin\left(\varphi-\varphi_c\right)\sum_{k'} P_{k'} e^{ik'\varphi}\right], \tag{4.35}$$

and after integration by parts

$$\begin{aligned}\partial_t P_k &= -\frac{ik\omega(c)}{2\pi}\sum_{k'}\int_0^{2\pi} \mathrm{d}\varphi\, \left[\cos(\varphi_c)\sin(\varphi)-\sin(\varphi_c)\cos(\varphi)\right] P_{k'} e^{i(k'-k)\varphi}\,,\\ &= -\frac{ik\omega(c)}{4\pi}\sum_{k'}\left[\cos(\varphi_c)\left(i\delta_{k,k'-1}-i\delta_{k,k'+1}\right)-\sin(\varphi_c)\left(\delta_{k,k'-1}+\delta_{k,k'+1}\right)\right] P_{k'}\,.\end{aligned} \tag{4.36}$$

Using the definitions, Eqs. (4.20),(4.21), and neglecting contributions of the second harmonics, the response of the dynamics of $\boldsymbol{p}$ to the signaling stimulus is given by

$$\partial_t p_i = \omega\,\rho\,\partial_i c\,, \tag{4.37}$$

where we chose a linear dependence of the alignment strength on the signaling amplitude c, namely $\omega(c) = 4\pi\,\omega c$. The contributions arising from particles' interactions can be motivated as done in Refs.[191,198,201]. As such, we include for completeness an elasticity like contribution

$$\partial_t \boldsymbol{p} \sim D_p \Delta \boldsymbol{p}\,, \tag{4.38}$$

and a self-propulsion

$$\partial_t \boldsymbol{p} \sim \chi\,\boldsymbol{p}\cdot\nabla\boldsymbol{p}\,, \tag{4.39}$$

in the model. Both terms may arise from anisotropic interactions, e.g., for elongated particles. They are not included in the agent-based model and we set the corresponding parameters D_p and χ to small values as the effects are not crucial for the reported behavior of signaling active matter. Altogether we obtain the set of hydrodynamic equations

$$\partial_t \rho(\boldsymbol{r},t) = -v_0 \boldsymbol{\nabla}\cdot\boldsymbol{p} + D_\rho\,\Delta\rho\,, \tag{4.40a}$$

$$\partial_t \boldsymbol{p}(\boldsymbol{r},t) = \sigma\,(\rho-1)\,\boldsymbol{p} - \delta\,|\boldsymbol{p}|^2\,\boldsymbol{p} + D_p\,\Delta\boldsymbol{p} - \chi\,\boldsymbol{p}\cdot\boldsymbol{\nabla}\boldsymbol{p} - Q(\rho)\boldsymbol{\nabla}\rho + \rho\,\omega\boldsymbol{\nabla}c\,, \tag{4.40b}$$

$$\partial_t c(\boldsymbol{r},t) = D_c\,\Delta c - \alpha\,c + \rho\,\beta\,\Theta\left(c-c_{\mathrm{th}}\right)(1-s)\,, \tag{4.40c}$$

$$\partial_t s(\boldsymbol{r},t) = D_\rho\,\Delta s - \epsilon\,(s-c) - \bar{v}\,\boldsymbol{p}\cdot\boldsymbol{\nabla}s\,, \tag{4.40d}$$

complementing the derived contributions from the Boltzmann equation, Eq. (4.17), with the interaction terms, Eqs. (4.38), (4.39), and the continuous versions of the equations for the signaling machinery, Eqs. (4.3), (4.5) in the main text.

4.6.6 REDUCED MODEL WITHOUT DECISION MAKING

To highlight the role of the individual decision making for the multi-scale aggregation process, for comparison we also investigate the behavior of a system lacking such a mechanism. In particular, we modify the source dynamics given in main text Eq. (4.3), such that it becomes independent of the agents' internal state,

$$\partial_t c(\boldsymbol{r},t) = D_c\Delta c - \alpha c + \beta\sum_{i=1}^{N} f(\boldsymbol{r},t)\,. \tag{4.41}$$

The polar agents with dynamics given by Eqs. (4.1), (4.2), and Eq. (4.41), are assumed to contribute as persistent sources of the signaling field. Similar to what has been reported in reference[322], we observe aster-like stationary cluster formation with interface controlled ripening, see Supplementary

Fig. 4.7a. Moreover, the interplay between self-propulsion and attraction towards a local aggregation center can give rise to short-lived ring-like structures and vortices which eventually tend to dissolve into a few aster-like aggregates as depicted in Supplementary Fig. 4.7b. Since in the modified model there is only local interactions mediated by the comparably slow diffusion of the signaling field, it does not exhibit a collective long-range organization of aggregation centers. In contrast to a system with active decision making, here the established smaller aggregates collide and merge upon random encounters.

4.6.7 MODEL PARAMETERS

The supplementary tables 4.1-4.3 provide an overview of the system parameters used in the numerical simulations shown in the main text as well as in the supplementary figures and movies. We measure densities in units of the critical density for the isotropic-polar transition. Time is given in units of the signal decay rate $[\alpha]$ and lengths are given in units of the resulting diffusion length $\sqrt{D_c/[\alpha]}$.

Parameter	Description	Value (continuum model)	Value (agent-based)
α	signal decay rate	10	0.9
β	signal production rate	40	2
a	threshold factor	0.9	0.9
b	constant threshold	0.05	0.05
ϵ	refractory rate	4	0.3
D_c	signal diffusion	1	0.9

Table 4.1: Parameters of the signaling system, Eqs. (4.16c), (4.16d), in the excitable regime used for the hydrodynamic- and the agent-based model, respectively.

Parameter	Description	Value
v_0	propulsion speed	0.2
D_{R}	rotational diffusion	0.05
r_c	interaction radius	2
r_p	particle radius	0.25
Γ	polar alignment factor	0.1

Table 4.2: Parameters of the agent-based model as detailed in section 4.6.1. The chemical susceptibility parameter in Fig. 4.1 is set to $\omega \in \{0.1, 0.4, 0.004, 0.2, 0.004\}$ for panels e-i, respectively.

		Value				
Parameter	Description	Default	Fig. 4.1j	Fig. 4.1k	Fig. 4.1l,n	Fig. 4.1m
v_0	motility	0.5	0.1	0.5	0.2	0.1
σ	polar persistence parameter	0.01	0.1	0.2	0.5	0.05
ω	signal susceptibility	0.1	0.8	0.3	0.8	0.4
D_ρ	translational diffusion	0.05				
D_p	elasticity parameter	0.1				
χ	convective derivative coefficient	0.1				
δ	magnitude of bulk order	1.0				
ρ_0	average density	0.6				

Table 4.3: Parameters of the hydrodynamic continuum model, described in section 4.6.2.

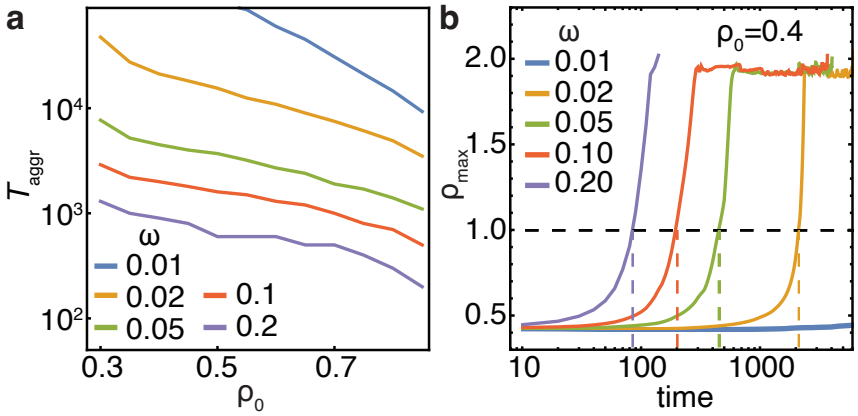

Figure 4.4: Signaling-enhanced aggregation capabilities. a, Aggregation times T_{aggr} of the hydrodynamic system, main text Eqs. (4.6), reaching the polar-order transition at $\rho = 1$ from a homogeneous initial density ρ_0. We observe faster aggregation for higher initial densities as well as larger signaling susceptibilities ω. b, Corresponding temporal evolution of the system's maximum density ρ_{max} evolving from a homogeneous initial density $\rho_0 = 0.4$ for different values of ω. We determine the aggregation times T_{aggr} (dashed colored lines) as the first times at which the critical density (dashed black line) is reached, $\rho_{\mathrm{max}} = \rho_c = 1$. Other parameters as given in section 4.6.7. This figure is reproduced from Ref.[3] under license [CC BY 4.0].

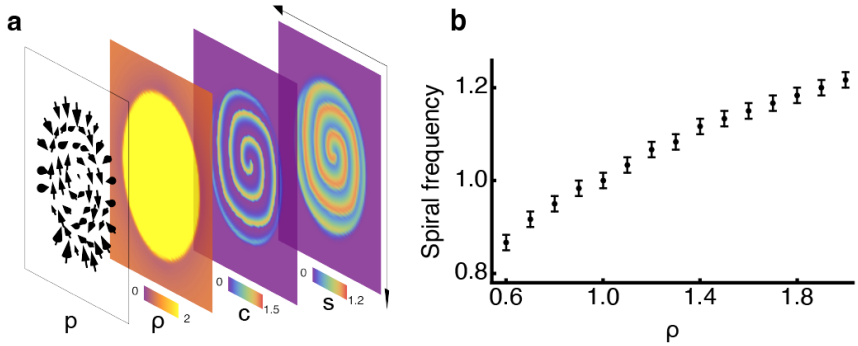

Figure 4.5: Spiral waves and vortex solution in the hydrodynamic model. a, Vortex solution with persistent spiral wave activity in the hydrodynamic model, see section 4.6.2. The composite image containing layers representing the orientation vector field $\boldsymbol{p}(\boldsymbol{r})$ (arrows), the local density profile $\rho(\boldsymbol{r})$, concentration of signaling molecules $c(\boldsymbol{r})$, and field of state $s(\boldsymbol{r})$. b, Dependence of spiral frequency on spatially homogeneous density values ρ. Error bars indicate error ranges arising from the numerical measurement of spiral frequencies. Parameters as stated in section 4.6.7. This figure is reproduced from Ref.[3] under license [CC BY 4.0].

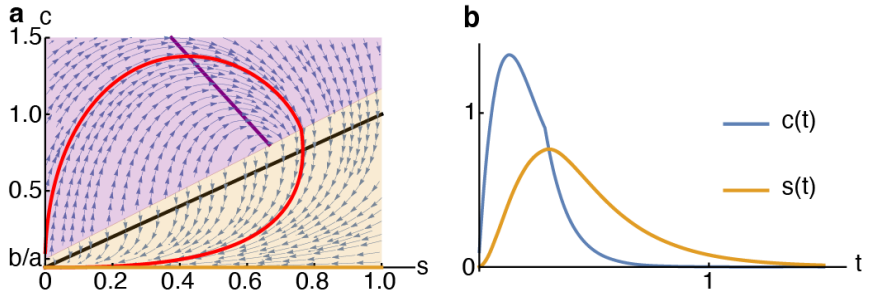

Figure 4.6: Excitable dynamics of the well-mixed signaling system. The agents serve both as a source of chemical signals and can adapt their internal state to the chemical environment. In this process, the release of the chemicals by the agents depends on the internal state of the agents and the state of the environment. The combination of these factors leads to a 'sense-and-response' system that exhibits excitable dynamics. a, Phase-space flow of the excitable system, main text Eqs. (4.3),(4.5). The black line indicates the nullcline $c = s$ of the agents' state kinetics, main text Eq. (4.5). Due to the discontinuous switch in the agents' signal relaying capability, there are two nullclines (violet and orange) originating from the signaling kinetics, main text Eq. (4.3), with $c = \beta/\alpha(1 - s)$ and $c = 0$, respectively. These nullclines are valid in the correspondingly colored areas $c \gtrless (s + b)/a$. The red trajectory highlights an excursion in phase space upon initial excitation. b, Dynamics of the chemical concentration c and the signaling state s corresponding to the red trajectory in a. Parameters as stated in section 4.6.7. Time is measured in the units of the decay rate $[\alpha]$. This figure is reproduced from Ref.[3] under license [CC BY 4.0].

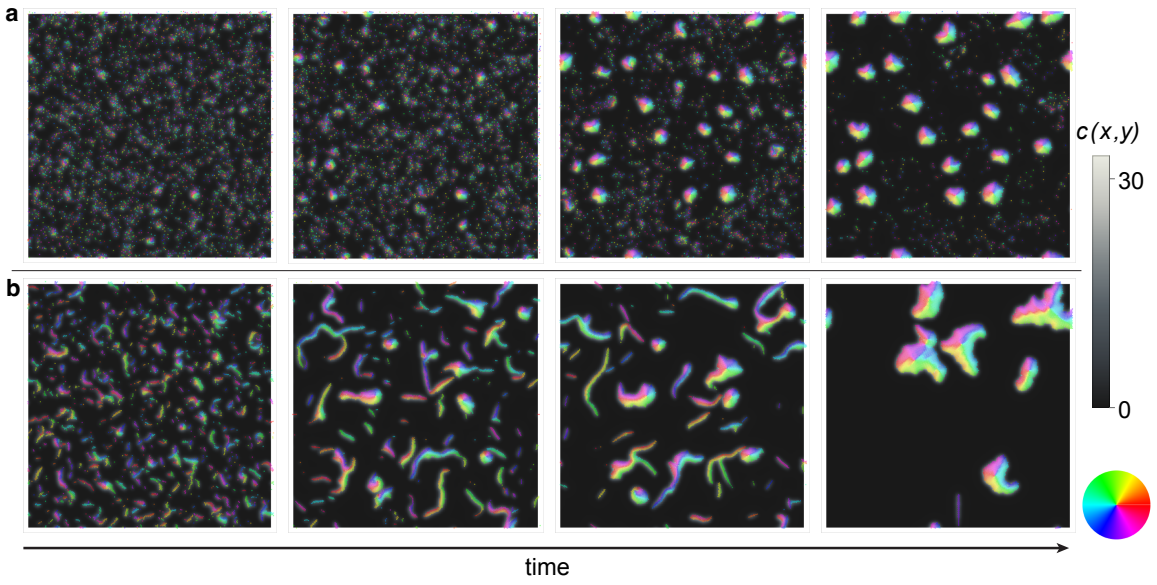

Figure 4.7: Time evolution of a reduced model, lacking the internal decision making machinery of the self-propelling agents, main text Eqs. (4.1), (4.2), and Eq. (4.41). The two parameter regimes shown in panels a and b illustrate localized cluster formation as a generic form of aggregation in the model. The clusters exhibit an interface-controlled coarsening behavior. a, Formation of localized clusters for small polar alignment $\Gamma = 0.01$. b, Cluster formation with intermediate transient solutions for stronger polar alignment, $\Gamma = 0.1$. Agent colors indicate the polar orientation and background colors represents concentrations of the communication field $c(\boldsymbol{r}, t)$, see Eq. (4.41). Parameters as in table 4.2 with $r_p = 0.5$, $\beta = 0.9$, and $\omega = 0.05$. This figure is reproduced from Ref.[3] under license [CC BY 4.0].

5

Acoustic signaling enables collective perception and control in active matter systems

Emergent cooperative functionality in active matter systems plays a crucial role in various applications of active swarms, ranging from pollutant foraging and collective threat detection to tissue embolization. In nature, animals like bats and whales use acoustic signals to communicate and enhance their evolutionary competitiveness. Here, we show that information exchange by acoustic waves between active agents creates a large variety of multifunctional structures. In our realization of collective swarms, each unit is equipped with an acoustic emitter and a detector. The swarmers respond to the resulting acoustic field by adjusting their emission frequency and migrating toward the strongest signal. We find self-organized structures with different morphology, including snake-like self-propelled entities, localized aggregates, and spinning rings. These collective swarms exhibit emergent functionalities, such as phenotype robustness, collective decision-making, and environmental sensing. For instance, the collectives show self-regeneration after strong distortion, allowing them to penetrate through narrow constrictions. Additionally, they exhibit a population-scale perception of reflecting objects and a collective response to acoustic control inputs. Our results provide insights into fundamental organization mechanisms in information-exchanging swarms. They may inspire design principles for technical implementations in the form of acoustically or electromagnetically communicating microrobotic swarms capable of performing complex tasks and concerting collective responses to external cues.

5

5.1 INTRODUCTION

What are the most distinct markers of living systems? What makes them so different from the inanimate world? These are their ability to move (locomotion), consume energy (metabolism), process information, and form multicellular aggregates. The onset of collective behavior among simple interacting units is a central paradigm in nonequilibrium physics and an opportunity for materials science and microrobotics[340–342]. Biological systems exhibit diverse signaling strategies and mutual synchronization, giving them an evolutionary advantage[343,344]. For instance, social amoeba use cell-to-cell signaling through the emission of cyclic adenosine monophosphate (cAMP) concentration waves and chemotaxis to aggregate under starvation[311], insects rely on sound to coordinate the formation of cohesive swarms[312,345], bats and whales use ultrasound sonar for communication, navigation, and hunting[346,347]. To what degree can one use simple information processing capabilities to design self-organized functional aggregates from simple building blocks or to create swarms of active agents performing elaborate tasks collectively[348]? Biological systems have mastered complex functionality and environmental adaptation through evolution and self-organization: the tendency of simple units (e.g., molecules, colloids, cells) to form hierarchical functional superstructures[349,350]. Out-of-equilibrium self-organization opens the way to sophisticated aggregated states with many levels of functionality akin to living systems[217,351]. Imagine synthetic bottom-up systems capable of communicating, making decisions, adapting, and even repairing damages in their collective structures. However, currently, these features are mostly lacking in simple microrobots[352,353], and enabling communication and self-organization in synthetic swarm-like systems is so far perceived as nothing more than science fiction[354,355].

Chemical signaling and emergent self-organization have been extensively studied in various biological and synthetic systems[41], such as social amoebas[45], chemically interacting colloidal particles[218], and pheromone-driven social insects[42]. While effective in facilitating coordinated behaviors, this form of communication is inherently limited by localized diffusive spreading of information and the relaying of signals by distributed agents[3]. As a result, information propagation is comparably slow and remains constrained to regions where agents are present. In contrast, signaling via acoustic and electromagnetic waves, readily accessible to technological systems like microrobots, offers greater versatility and range. Yet it remains largely underexplored in the context of collective behaviors and self-organization.

To examine the potential of acoustic signaling in technical systems, we enhance the communication capability of individual units (swarmers) through rapid signal exchange by propagating acoustic, electromagnetic, or surface waves. Each self-propelled swarmer is equipped with an “on-board” oscillator, broadcasting and detecting acoustic signals[356,357]. Synchronizing internal oscillator states

enhances the swarms' cohesiveness, multifunctionality, and robustness to heterogeneities or disorder. The self-organization of a collective swarm is guided by the following principles: the swarmers respond to the common acoustic field by synchronizing their broadcast frequencies and migrating towards the strongest signal.

Our computational studies reveal the spontaneous formation of a plethora of self-organized structures with different morphology, including snake-like self-propelled objects, localized aggregates, and closed, rotating rings. Importantly, these structures exhibit emergent functionalities like phenotype robustness, collective decision making, and environmental sensing. Some structures, like snakes, exhibit shape memory and self-regeneration: after a strong distortion, they are able to recover earlier phenotypes. Akin to an octopus escaping from a cage through a tiny hole, the snake swarm can squeeze through a narrow constriction and reassemble behind it. These results suggest new design principles and control strategies for multifunctional synthetic swarms which could be relevant for various applications, e.g., for pollutant foraging[358–360], threat detection[361], and tissue embolization[362,363].

Moreover, our approach enriches the traditional scope of active matter: the onset of collective behavior emerging in the system of interacting self-propelled particles[55,364]. In addition to alignment interactions in active systems[365], our agents communicate via acoustic waves and synchronize their intrinsic states. The long-range coupling brings this system closer to the celebrated Kuramoto model of globally coupled oscillators[366]. Notably, our agents dynamically reconfigure the coupling due to the self-organized motion. Contrary to "swarmalator models"[222,223], we disentangle the spatial orientation of agents from their internal communication state, making the system more suitable for synthetic implementations such as in microrobotic swarms.

5.2 MODEL DESCRIPTION

5.2.1 AGENT-BASED MODEL

In this study, we investigate the dynamics of self-propelled polar agents coupled through wave interactions, using acoustic waves as a concrete example. For simplicity, we assume that the swarmers move in a two-dimensional plane (their "habitat"), while sound wave propagation occurs in three spatial dimensions, leading to a realistic non-local acoustic coupling. Specifically, we consider a system of N acoustically interacting self-propelled particles (swarmers); see Fig. 5.1. The swarmers move persistently along their intrinsic orientation $\boldsymbol{n}_l = (\cos\varphi_l, \sin\varphi_l)^{\mathrm{T}}$ at a constant speed v_0 with two-dimensional orientation angle φ_l. Within an interaction radius r_c, they align their direction of motion with the one of their neighbors (Fig. 5.1a). A repulsive force f_{lj} ensures hard-core repulsion between agents when they come within a distance of two agent radii, r_p. The dynamics of the agent's orientation angle φ are governed by polar alignment with neighbors at a rate Γ, as well as by alignment with the amplitude of the common sound field, i.e., $\varphi_s = \mathrm{angle}(\nabla|u|)$, at a rate Ξ. The adaptation of orientation φ_l, Eq. (5.1b), is assumed to be error-prone. Therefore, a zero-mean Gaussian white noise ξ_l is added to the angular dynamics as a perturbation. In summary, the agents' position and orientation change according to

$$\frac{\mathrm{d}\boldsymbol{r}_l}{\mathrm{d}t} = v_0\boldsymbol{n}_l + \sum_{j[r_{lj}<2r_\mathrm{p}]} f_{lj}\,, \tag{5.1a}$$

$$\frac{\mathrm{d}\varphi_l}{\mathrm{d}t} = -\Gamma \sum_{j[r_{lj}<r_c]} \frac{\sin\left(\varphi_l - \varphi_j\right)}{|\boldsymbol{r}_l - \boldsymbol{r}_j|} + \Xi\sin\left(\varphi_s - \varphi_l\right) + \xi_l\,. \tag{5.1b}$$

We consider agents that are equipped with an internal oscillator continuously emitting sound waves like a loudspeaker. For simplicity, we model the oscillation using a generic form near a supercritical

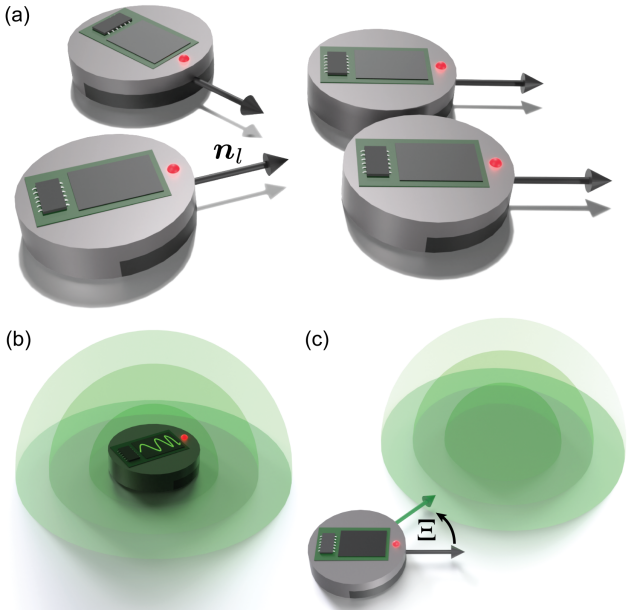

Figure 5.1: **Acoustically communicating active matter**. (a) Schematics of self-propelled swarmers with polar alignment. Arrows indicate the swarmers' direction of motion, $\boldsymbol{n}_l$. (b) Individual swarmers possess an internal oscillator controlling their acoustic emissions. In turn, their oscillatory states can synchronize via the acoustic field. (c) Swarmers align towards higher sound amplitudes with acoustic susceptibility Ξ. This figure is reproduced from Ref.[4] under license [CC BY 4.0].

Hopf bifurcation, represented by a Stuart-Landau oscillator[367,368],

$$\partial_t a_l(t) \quad = (1+i\omega)\, a_l - (1+ib)\, |a_l|^2 a_l + \lambda u(\boldsymbol{r}_l, t)\,. \tag{5.1c}$$

Here, ω and b describe the linear, respectively, non-linear coupling of frequencies and amplitudes, and λ determines the coupling rateto the acoustic field $u(\boldsymbol{r}, t)$. Thus, the intrinsic oscillator is affected by acoustic waves from other swarmers, creating acoustic feedback (Fig. 5.1b). Via emitting acoustic waves, the swarmers establish a dynamic signaling landscape (*soundscape*) to which they adapt their intrinsic oscillation state with respect to their individual baseline frequency ω. The dynamics of the common acoustic field $u(\boldsymbol{r}, t)$ generated by all constituting agents is given by

$$\frac{1}{c^2}\partial_t^2 u(\boldsymbol{r}, t) \quad = \nabla^2 u + \textstyle\sum_{j=1}^{N} w\,(\boldsymbol{r} - \boldsymbol{r}_j)\, a_j \delta(z)\,. \tag{5.1d}$$

The soundscape evolution is described by the wave equation in three spatial dimensions with the swarmers' oscillating membranes as sources $w(\boldsymbol{r})$ of the sound field, Eq. (5.1d). The function w specifies the shape of the agent (i.e., round). The speed of sound is denoted by a parameter c and is assumed to be large compared to the agent velocity v_0. The $\delta(z)$ function in Eq. (5.1d) stipulates that all agents are confined to the $z = 0$ plane. As stated above, in the presence of an established acoustic field, agents align their motion toward regions of higher acoustic field amplitudes with susceptibility Ξ (Fig. 5.1c). To integrate numerically the dynamics of the acoustically interacting self-propelled polar agents, we solve the discrete stochastic equations, Eqs. (5.1a), (5.1b), and the agents' oscillatory dynamics, Eq. (5.1c), with a forward Euler-Maruyama method at fixed time steps dt[369]. The resulting acoustic field is calculated from Eq. (5.1d) for the quasi-stationary case in the limit of large sound velocities $c \gg v_0$ using an inverse Fourier transform of the analytic expression

$$\tilde{u}_{\boldsymbol{k}} = \frac{\tilde{g}_{\boldsymbol{k}}}{2c^2\sqrt{k_x^2 + k_y^2}}\,, \tag{5.2}$$

with Fourier-transformed acoustic source contributions $\tilde{g}_{\boldsymbol{k}}$ and wave vector $\boldsymbol{k} = (k_x, k_y)^T$; see also appendix Section 5.6.1. We discretize the entire habitat domain into Fourier modes down to length scales of the order of a single agent diameter. Subsequently, we integrate the states of the intrinsic oscillators by incorporating the collectively established acoustic field, see appendix Section 5.6.3 for details on the numerical integration of the model equations.

5.2.2 CONTINUOUS FIELD EQUATIONS

We complement the agent-based discrete description of the system with corresponding continuous field equations. The phenomenological equations for the agent density $\rho(\boldsymbol{r}, t)$ and the particles' polar orientation field $\boldsymbol{p}(\boldsymbol{r}, t)$ in the two-dimensional habitat $\boldsymbol{r} \in \mathbb{R}^2$ read

$$\partial_t \rho(\boldsymbol{r}, t) = -v_0 \partial_i p_i + \mu \nabla^2_{\mathrm{2D}} \rho \,, \tag{5.3a}$$

$$\partial_t p_i(\boldsymbol{r}, t) = \sigma\,(\rho - 1)\, p_i - \delta p_j p_j p_i + \kappa \nabla^2_{\mathrm{2D}} p_i - \chi p_j \partial_j p_i - \frac{v_0}{2} P'(\rho) \partial_i \rho + \rho\, \Xi\, \partial_i |u|^2 \,, \tag{5.3b}$$

where the spatial derivatives ∂_i with $i \in \{x, y\}$ and the Laplacian ∇_{2D} refer to the two-dimensional habitat. Field theories with similar contributions have been developed for a range of active matter systems[176,189,370]. These theories are particularly relevant for studying biological and experimental polar and nematic active systems[53,365], such as microtubule-kinesin mixtures[371] and the actin motility assay[164]. Recently, in the latter case, a combination of computational and field-theoretical approaches has provided insights into the coexistence of nematic lanes and defects in the motility assay[372]. In addition to phenomenological models based on symmetry considerations, hydrodynamic field equations can be derived from Smoluchowski[196] and Fokker-Planck equations[194], or through the Boltzmann-Ginzburg-Landau framework[191,198–200]. The latter has been successfully applied, for instance, to inelastically aligning microtubule systems[198,201,202] and to actin dynamics in motility assays[203]. The approach can also be used to describe biopolymers systems driven by interactions mediated by molecular motors[373], as well as the collective behavior of chemotactic polar active agents[3], among others.

The rationale behind the above set of continuum equations is as follows: The dynamics of the density is described by a diffusion-advection equation, Eq. (5.3a), where alongside spatial diffusion with diffusion coefficient μ, the agents' self-propulsion induces an advection of density with velocity v_0 along the direction of polar orientation. The dynamics of the density-weighted polar orientation p_i is governed by a third-order polynomial in p_i, describing an isotropic to polar order transition at critical density $\rho_c \equiv 1$. For low densities, $\rho < \rho_c$, angular diffusion of agents dominates and the system favors the isotropic state. In contrast, in denser regions, $\rho > \rho_c$, an increased polar alignment between agents induces polar order. Additionally, we consider elastic contributions to the polar field ($\sim \kappa$), which originate from polar alignment of neighboring agents, and self-advection ($\sim \chi$) of the polar director along the direction of the agent motion p_i. Moreover, a pressure-like contribution ($\sim P'(\rho)$, with a prime denoting the derivative w.r.t. the density, appendix Sec. 5.6.3) implements the assumed finite volume of the agents and ensures a maximum density of swarmers. Finally, similar to chemotactic models[322], the polar orientation is coupled to gradients in the signaling field. Here, it is given by the acoustic field amplitudes $|u|^2$ and the acoustic susceptibility Ξ controls the agents' alignment strength.

The continuum equations for the acoustic field and the oscillatory states of the agents are obtained by coarse-graining their agent-based representations. Similar to the agent-based model, swarmers with density $\rho(\boldsymbol{r}, t)$ and state $a(\boldsymbol{r}, t)$ act as sources of the acoustic field. In the continuum description, the discrete contributions from individual agents become a continuous source term, weighted by the agent density field $\rho(\boldsymbol{r}, t)$. The rest of the wave equation, Eq. (5.1d), for the propagation of acoustic signals with sound velocity c remains unchanged. The oscillatory states of the agents are transformed into a continuous field, $a(\boldsymbol{r}, t)$. Coarse-graining also introduces a diffusion-like contribution to this field ($\sim \mu$), corresponding to the positional diffusion of agents. Additionally, since the oscillatory states are tied to the individual agents, the state field is advected with the agent velocity

($\sim v_0$), similar to the analysis performed in Ref.[3] for chemical agent states, with the limit cycle oscillations now distributed across the entire domain. As in the discrete model, the synchronization of oscillatory states is captured through coupling to the acoustic field ($\sim \lambda$). Altogether, the continuum representation of the equations reads

$$\frac{1}{c^2}\partial_t^2 u(\boldsymbol{r},t) = \nabla^2 u + a\,\rho\,\delta(z)\,, \tag{5.3c}$$

$$\partial_t a(\boldsymbol{r},t) = \mu\nabla_{2\mathrm{D}}^2 a + (1+i\omega)\,a - (1+ib)\,|a|^2 a - v_0\frac{p_j}{\rho}\partial_j a + \lambda\,u\,. \tag{5.3d}$$

For homogeneous densities, $\rho = \rho_0$, one can integrate Eq. (5.3c) in Fourier space which introduces a long-range coupling to the state field a. This transforms the system into a non-locally (acoustically) coupled version of the complex Ginzburg-Landau equation (CGLE)[368], as shown in appendix Sec. 5.6.2. The emergence of a non-local coupling of oscillators through the acoustic field underscores potential advantages that acoustic signaling offers to active matter systems. In the case of homogeneous density, $\rho = \rho_0$, we observe that acoustic interactions accelerate the coarsening of phase defects compared to the CGLE, indicating the long-range interaction between the emergent spiral cores, see appendix Fig. 5.8. Moreover, this coarsening process halts at a characteristic length scale, where acoustic interactions prevent further attractive forces between phase defects, highlighting the potential of long-range communication and synchronization between self-organizing collectives. These effects are crucial for understanding the emergence of the self-organized structures and their mutual interactions, which we will explore in the following sections.

5.3 SELF-ORGANIZED STATES

As described above, acoustic coupling between agents generates long-range interactions which may lead to intriguing forms of self-organization and novel functional structures. In this section, we examine the properties and distinct acoustic signatures of these emergent structures and determine the conditions under which they occur. We start by employing discrete agent-based simulations of Eqs. (5.1) and extend our analysis with large-scale numerical simulations of the continuous field equations, Eqs. (5.3), in the latter part of this section.

5.3.1 AGENT-BASED SIMULATIONS

Acoustic signaling enables the swarmers to communicate, navigate, and assemble. Through acoustic communication, the agents' oscillatory states can locally synchronize, enhancing local sound amplitudes. As agents move towards these high-amplitude regions, self-organized collective states with distinct properties emerge. In Fig. 5.2 we present the predominant collective solutions as a function of the agent's velocity v_0 and acoustic susceptibility Ξ (Fig. 5.2(a)) and describe their phenomenology as well as their acoustic emission in terms of signal amplitudes and frequencies as measured at a nearby fixed microphone position (Fig. 5.2(b-f)).

The simplest self-organized state is a polar aggregate (*blob*) in which swarmers are aligned towards a central pacemaker (white arrows, Fig. 5.2(b)). Since individual agents are oriented towards its center, they create an enclosed polar defect. Blob solutions predominantly occur for comparably small agent velocities and large sound susceptibilities; see Fig. 5.2(a). They emerge from a homogeneous distribution of swarmers through the initial formation of small aggregates. Then, the aggregating swarmers become tightly packed and synchronized (similar agent colors in Fig. 5.2(b), color-code indicates oscillatory phase of agents). Due to the alignment of agents towards larger signaling amplitudes, an almost circular region of synchronized agents develops (Fig. 5.2(b)). The entire blob contributes as a large collective source to the acoustic field and emits, almost isotropically, concentric sound waves into its surroundings. The aggregation, attraction, and mutual activation generate higher oscillation frequencies (frequency panel, Fig 5.2(b)) and amplitudes (signal panel) and, in

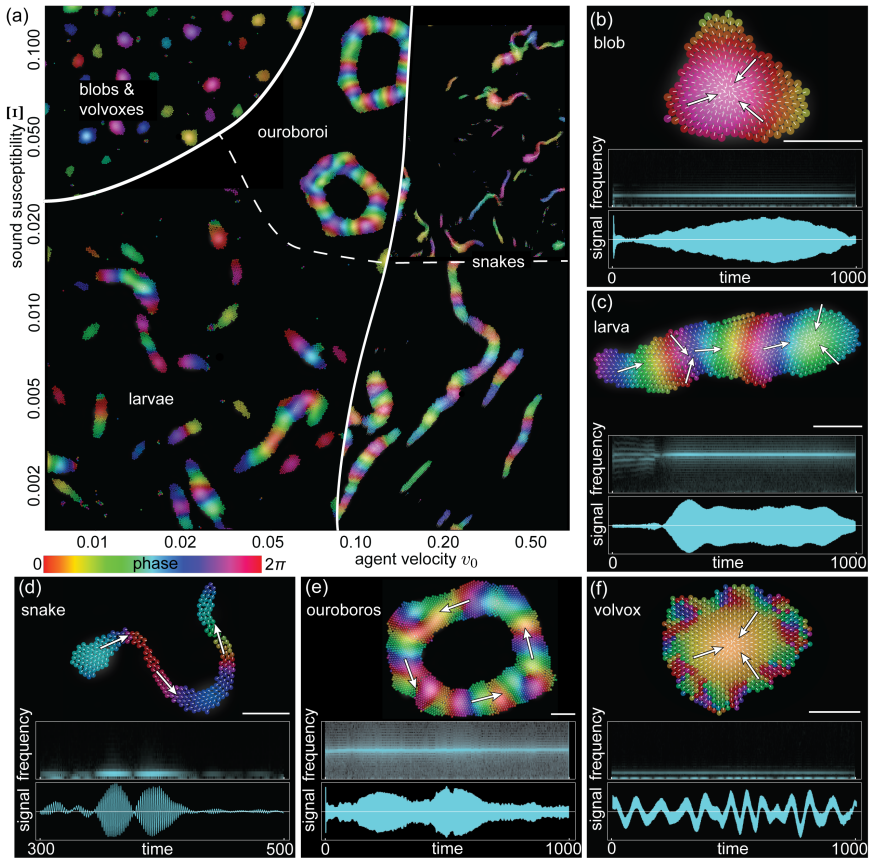

Figure 5.2: **Diversity of collective states.** (a) Phase diagram relating the most prominent collective states vs. agent's self-propulsion velocity v_0 and their susceptibility to align with acoustic signals Ξ. Representative solutions of the agent-based model, Eq. (5.1), are shown for the five qualitatively distinct phenotypes, with the color code indicating the agents' oscillatory phase. (b-f) Representative solutions with their acoustic signatures given by frequency distribution and the acoustic signal amplitude measured in the vicinity of the collective solutions. Agent color indicates its oscillator phase, white arrows highlight the local average agent orientation and white scale bars signify a length of 5 units. (b) Localized blob with central polar defect and target-wave pattern. (c) Larva. A polar wave-emitting defect is located in its head. (d) Rapidly moving snake; no internal polar defect. Phase waves propagate along its body. (e) Ouroborus, a closed larva-like ring structure. (f) Localized volvox with a synchronized center decorated by outer circular traveling phase waves or decoherent outer layers. Below each image (b-f) is the solution's acoustic signature: spectrogram as obtained from short-time discrete Fourier transform depicted over a frequency range $0-8$ Hz (uncoupled agent's free frequency ~ 0.07 Hz) and the normalized acoustic signal spatially adjacent to the respective solution. Parameters as given in Table 5.1. This figure is reproduced from Ref.[4] under license [CC BY 4.0].

turn, increasing sound intensities at the aggregate's center. This self-amplifying effect results in an emergent pacemaker—a region of agents with increased frequency, leading the phase dynamics—located in the blob's center. As a consequence of the increased collective sound amplitudes, the blob attracts an even growing number of nearby swarmers. In particular, we observe a dominant oscillatory mode in the blob that is at approximately 1.8 Hz; around 25-fold the frequency of the uncoupled individual agents' baseline (frequency panel in Fig. 5.2(b)). Additionally, a secondary, incoherent frequency mode at much lower frequencies is present. It represents the outer agents in the collective that are not fully synchronized with the center and experience weaker acoustic inputs. From the normalized signal amplitudes of the solution (lower panel in Fig. 5.2(b)) we see that amplitudes at a fixed microphone position are modulated over long time scales, representing the slow drifting motion of the blob solution. As a rather synchronized solution, blobs create a standing wave field around them and the modulation of the amplitude reflects the drift of the maximum position of the standing wave.

Another example of a self-organized, symmetry-broken state is an elongated, slowly migrating ag-

gregate that we term a *larva* (Fig. 5.2(c). Here, a broken symmetry in the position of the enclosed polar defect—resulting from an asymmetric aggregation process or the merging of two blobs—may cause the larva to move slowly but persistently. Larvae are observed for similarly low agent velocities as blobs but typically at weaker acoustic susceptibilities (Fig. 5.2(a)). In this parameter regime, agents experience weaker torques towards the phase-leader with the highest sound amplitudes and the colocalized polar defect. Thus, asymmetries around that polar defect may emerge more readily. As apparent from numerical simulations, the asymmetrically enclosed pacemaker in the larva emits phase waves, aligning all other swarmers in the aggregate towards it. Given these characteristics, the larva acts as a motile community that can absorb individual clusters and reintegrate them into its structure. Investigating its acoustic fingerprint, we observe that the aggregate displays high collective frequencies (Fig. 5.2(c), frequency panel). For the chosen parameters, these frequencies are approximately 80 times higher than the frequency of uncoupled individual agents. Such a significant frequency increase requires a comparably large amplitude of the collective acoustic field. Hence, we propose that phase differences between neighboring agents within the larva align with the acoustic wavelength, enabling all contributing agents to cooperatively reinforce one another. As a result, signal amplitudes increase and mutual phase velocities accelerate. Consistently, the acoustic amplitudes received from the larva (Fig. 5.2(c), signal panel) rise considerably as it approaches the microphone position. As it passes by, the sound amplitudes remain relatively stable, suggesting a nearly uniform coupling across the entire collective. However, a slight amplification occurs when the head of the structure is closest to the acoustic detector ($t \approx 350$). This highlights a key characteristic of the larva as its head houses the pacemaker, the region with highest frequency and amplitude (Fig. 5.2(c), signal panel). Compared to the blob solution discussed above, the larva completely passed the microphone position with its entire length in the time-frame shown, whereas the blob solution just slightly drifted into a minimum of the standing acoustic wave. This distinction highlights the persistent, directed motion of the larva solution and represents another significant difference in the solutions' acoustic signatures.

Rapidly moving *snakes* are yet another example of states with collective functionality (Fig. 5.2(d). They occur at large agent velocities where the directed propagation of agents gives rise to the collective, snake-like motion of these structures. Snakes lack an internal pacemaker such that phase waves of the oscillation typically propagate from head to tail. The resulting acoustic field aligns all agents in a common direction along the emerging center line as highlighted by the white arrows in Fig. 5.2(d). Somewhat similar collective snake-like states have been observed in active matter with vision cones[207]. In our study, the latter structures emerge via spontaneous symmetry breaking from the acoustic interactions and the self-organized information propagation through the phase waves. The mutual alignment of all the agents within a snake results in a collective propagation velocity of snakes that is comparable to the single swarmer speed v_0. Unlike individual agents, snakes exhibit significantly higher persistence of motion due to the coordinated alignment of neighboring agents. This enhanced coordination leads to a rapid collective propagation, which is reflected in the acoustic signal detected by a stationary microphone. The signal shows a brief duration and rapid modulation as the snake passes by. Additionally, because snakes lack an internal pacemaker and high self-sustained acoustic field amplitudes, the oscillation frequencies of the agents in the snakes are relatively low, comparable to those of uncoupled agents. This is evident from the signal and frequency panels shown in Fig. 5.2(d).

When increasing the sound susceptibility Ξ, larvae can transform into rotating ring-like entities (top center in Fig. 5.2(a)). Since this process involves the larvae curling into a circular shape and metaphorically "eating" their tails to form a continuous loop, we refer to these entities as *ouroboroi*, inspired by an ancient symbol (Fig. 5.2(e). These ouroboroi display periodic phase waves that propagate through the entire structure, as can be seen from the color-coded phases. Typically, these phase waves propagate in the direction opposite to the motion of agents, indicated by the white arrows. Since ouroboroi are essentially "closed-larvae" states, where rotation is limited due to mutual blocking of the agents, their acoustic signatures closely resemble those of larvae solutions. However, as ouroboroi are mainly localized at a given position, the emitted acoustic signal does not decay as strongly as for the passing larvae; see bottom panels in Fig. 5.2(e).

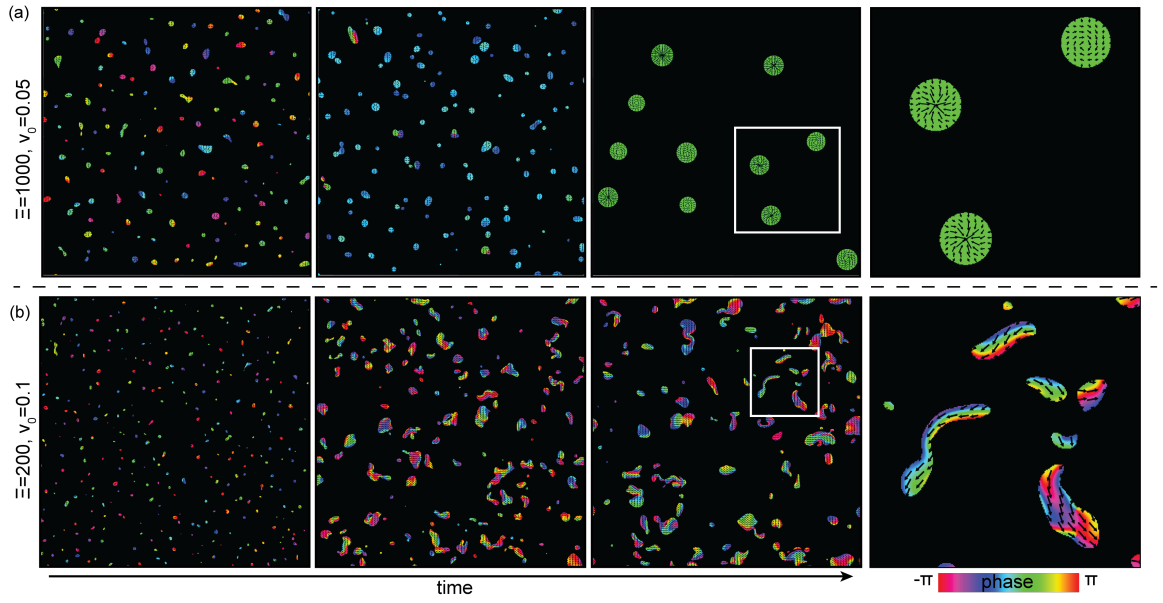

Figure 5.3: **Collective states in the continuum model.** Temporal evolution of the continuum field representation of acoustic active matter, Eqs. (5.3). Different types of solutions emerge from a disordered homogeneous state. (a) Prevalence of localized blobs for $v_0 = 0.05$ as shown in the zoom-in on the right side panel. (b) Snakes emerge upon initial blob formation and partially aggregate into larger blobs for $v_0 = 0.1$. Snake solutions in the continuum model are highlighted in the zoom-in (rightmost panel). The color indicates local oscillatory phases for densities $\rho > 1$. Arrows represent the polar orientation $\boldsymbol{p}(\boldsymbol{r}, t)$. The system size is set to $L = 200$, and zoom-ins detail the highlighted domains. Remaining parameters as given in Table 5.2. This figure is reproduced from Ref.[4] under license [CC BY 4.0].

Finally, if the structure size of blobs exceeds the range over which constituting agents are able to acoustically synchronize, the aggregates can become decorated by outer layers of agents with traveling, metachronal waves or desynchronized oscillations (*volvoxes*) (Fig. 5.2(f). Therefore, heterogeneous phase patterns or decorrelated oscillations surround the central phase-synchronized region. This situation is reminiscent of the "chimera states" occurring in coupled oscillator systems[374]. The coexistence of synchronized and desynchronized swarmers is also reflected in the agents' frequency distribution, where we observe a constant part with increased frequencies, about 10-fold that of free agents, and an irregular fraction of agents with lower frequencies (frequency panel in Fig. 5.2(f)). In the example shown in Fig. 5.2(f), featuring metachronal waves, the emitted waves interfere with the center synchronized oscillations and lead to a strong modulation of the acoustic signal.

Altogether, we observe multiple emergent collective states in the system of acoustically coupled swarmers. Blobs and volvoxes arise predominantly for small agent velocities and when the sound-mediated attraction is strong (Fig. 5.2(a)). For weaker acoustic susceptibility/larger agent velocities, aggregates can become asymmetric, leading to the formation of larvae or ouroboroi solutions. Increasing the agent velocities further, the collectives lose any internal polar defects, and snake solutions become predominant. The collective solutions not only feature phenomenological differences in terms of their polar defect localization or collective propagation velocity but also exhibit distinct acoustic signatures. The acoustic coupling induces different collective frequency distributions with varying mean and spread and distinguishable dynamics of acoustic amplitudes. Thereby, the acoustic system gives rise to cognitive flock configurations through spontaneous symmetry breaking and self-organized frequency distribution of agents via acoustic coupling. Similar solutions so far required externally imposed, symmetry breaking vision cones for mutual interactions[208].

5.3.2 CONTINUUM EQUATIONS

In this section, we explore the collective dynamics in the continuum model, given by Eqs. (5.3). We begin by comparing the emerging structures with those found in the agent-based model. Then, we

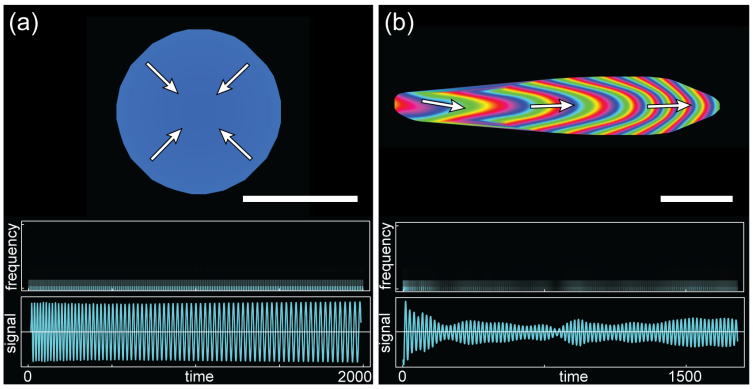

Figure 5.4: Acoustic signatures of aggregates in continuous field description. (a) Representation of a blob solution. Densities $\rho > 1$ are color-coded by their oscillatory phase (see color bar, Fig. 5.3). The swarmers are oriented towards a central polar defect; white arrows indicate the average polar direction. (b) Snake-like solution. Phase waves propagate from head to tail through the structure. The resulting average polar orientation (white arrows) of agents leads to a net motion of the entire aggregate. White bars represent a length of 10 units and spectrograms show a frequency range from $0 - 4$ Hz. This figure is reproduced from Ref.[4] under license [CC BY 4.0].

leverage the continuum field equations to study the behavior of acoustic active matter at large time and length scales, a regime beyond the reach of the agent-based simulations.

As for the agent-based description, we observe a rich phenomenology due to the acoustic coupling of swarmers (Fig. 5.3). Upon formation of small clusters, we observe coarsening behavior with the swarmers merging into larger aggregates. In particular, as in the agent-based model, the system dynamics strongly depends on the susceptibility parameter Ξ and the swarmer velocity v_0. Namely, at low self-propulsion velocities, $v_0 = 0.05$, we see the formation of multiple small blobs which subsequently coarsen to fewer larger ones (Fig. 5.3(a)); see zoom-in in the rightmost panel. Here, an aster-like polar orientation of the swarmer matter towards a central defect is prevalent. In addition to what has been observed for the discrete system, the field equations also exhibit vortex-type blob solutions with chiral motion around the central defect. At larger velocities, $v_0 = 0.1$, and weaker signal susceptibility, $\Xi = 200$, we observe a prevalence of snake-type structures (Fig. 5.3(b)); see zoom-in for details. As for the agent-based case, these structures are highly motile and free of internal pace-making polar defects. They typically collide and aggregate into larger structures, but occasionally also split such that new smaller snakes emerge.

In summary, the continuum model captures two distinct collective phenomena also observed in the agent-based model: blobs (Fig. 5.3(a)) and snake-like aggregates (Fig. 5.3(b)). Similar to the agent-based model, blobs in the continuum model also exhibit a high degree of synchronization, as evidenced by the uniform phase color in Fig. 5.4(a). As swarmers are aligned to the blob's center, the collective has an almost vanishing net motion. Combined with the stable synchronization of the oscillatory matter within, the amplitude of the emitted signal shows only slight modulation (see signal panel). Oscillation frequencies of the swarmer matter are slightly increased compared to the uncoupled case, i.e., without the input from the collective acoustic field. In contrast, snake solutions (Fig. 5.4(b)) are characterized by stronger fluctuations in their acoustic signals (signal panel in Fig. 5.4(b)). Compared to blob solutions, the snakes exhibit slighly lower oscillation frequencies (frequency panel) due to the lack of a phase leader with increased collective stimulus.

Notably, we do not observe larva-type structures in the continuum model. We rationalize this as follows: In the agent-based model, the net motion of larvae results from short-range repulsion between individual agents and the asymmetrical pushing of agents around the enclosed defect. In contrast, in the field theory, the finite size of the swarmers is represented by gradients in the swarmer density, which show only slight variation within the aggregates. Thus, swarmers are mainly advected in the direction of their self-propulsion —towards the $+1$ polar defect— implying a lack in persistent net motion of defect-enclosing structures. Being caused by a high-density effect, the net motion of larvae is not captured by the gradient expansion which is the basis for the continuum model.

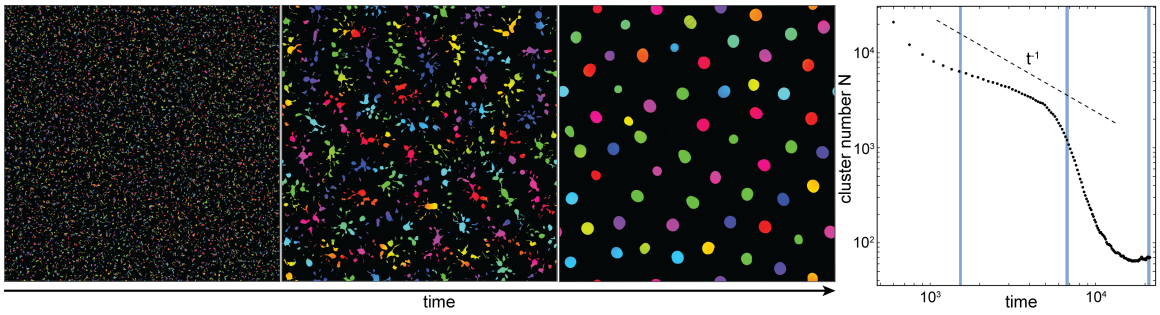

Figure 5.5: Large scale dynamics of acoustic active matter. Upon emergence of clusters, the aggregates coarsen mediated by acoustic interactions (rightmost panel). Vertical blue lines indicate the time points of the snapshots (left). Densities are shown for $\rho(\boldsymbol{r}, t) > 1$ and color code represents oscillatory phase $a(\boldsymbol{r}, t)$ (color scale as in Fig. 5.3). System length $L = 2000$. Parameters as stated in Table 5.2. This figure is reproduced from Ref.[4] under license [CC BY 4.0].

Having established the phenomenological relation between the emergent behavior in the agent-based model and the continuous field representation, we next discuss the large-scale dynamics (Fig. 5.5). We observe that the acoustic coupling not only enables the formation of aggregates in the system but it also yields coarsening dynamics that is much faster than typical Cahn-Hilliard-like Ostwald ripening. Small aggregates interact via emission of acoustic waves and synchronize their collective oscillations with neighboring aggregates through the acoustic soundscape. This leads to the formation of large-scale synchronization patterns which overspan multiple clusters (phase colors in snapshot $t = 2000$, Fig. 5.5).

This large-scale synchronization between clusters promotes their merging and speeds up aggregation into fewer larger structures. Compared to local diffusive interface-mediated ripening, which would induce a coarsening dynamics for which the cluster number scales as $N \sim t^{-1}$, the acoustic synchronization yields an accelerated coarsening. Reminiscent of the defect coarsening discussed for the non-locally (acoustically) coupled complex Ginzburg-Landau subsystem (appendix Sec. 5.6.2), the cluster number saturates for large times and coarsening is halted at a particular structure distance. As for the defect coarsening in the non-locally coupled complex Ginzburg-Landau equation, this inter-cluster distance may be selected by the wavelength of the established acoustic wave field.

Overall, the continuum field equations are a complementary way of assessing the relevance of acoustic interaction in active matter. They reveal a phenomenology that closely parallels the agent-based model, which enables us to draw broader conclusions about the role of acoustic coupling in the large-scale dynamics of the system. Specifically, we find that acoustic waves facilitate nonlocal phase synchronization and mutual attraction between aggregates, which in turn regulate the length scales of emergent structures and their interactions. By mediating these long-range effects, acoustic coupling plays a crucial role in shaping the collective behavior and spatial organization of the system.

The field equations examined in this study provide valuable insights into the large-scale dynamics of acoustic active matter. Beyond this preliminary investigation, they open up a wide range of potential applications, including wave-coupled swarming systems in heterogeneous media and general acoustically coupled active media, along with various others. While the field equations qualitatively capture some key solutions including their acoustic signatures, they fail to represent others such as the larva solutions. This limitation arises because the continuous model, based on a gradient expansion, does not account properly for high density effects that drive the net motion of the larvae. In the following, we aim to explore potential applications of the emergent collective solutions which involve a tractable number of agents. To better incorporate potential small-number effects and gain more accurate insights, we turn again to the agent-based model.

5.4 COLLECTIVE FUNCTIONS

The wide spectrum of self-assembled states (Fig. 5.2) provides the opportunity to tailor these states for specific functions. As we have demonstrated, acoustic active matter generates self-organized collective states with distinct acoustic signatures. By leveraging this self-organized behavior, we next show how to harness the emergent collective functionality for a range of practical applications.

In general, individual agents in active matter systems are small in comparison to the collective structures and, as in our case, have limited processing capabilities. Furthermore, they can only access local information. Therefore, potential applications rely on cooperation and require a collectively synchronized behavior. This synchronization can be achieved through acoustic interactions. Importantly, since the systems' dynamics is relying on self-organization it offers inherent robustness of the emergent collective states against perturbations such as environmental changes or failure of individual swarmers. For collectives of identical swarmers, self-organization yields a behavioral specification —that is, a kind of phenotypic state— by which agents develop different oscillation frequencies and exhibit self-organized motion due to their acoustic coupling. As this specification is emergent, individual swarmers can be seamlessly replaced without compromising the functionality of the group.

With regard to potential applications, emergent collectives must possess the ability to identify where their action is needed, move accordingly, and assess the effectiveness of their action. This crucially requires adaptability to their environment and a dynamic, coordinated response to external cues. Additionally, although self-organization drives these emergent structures, external control may still be necessary to harness and direct the collective's functionality. This raises key questions: how can collectives adapt to changing conditions, and how can they be externally controlled? Acoustic signaling, in principle, provides a mechanism that enables both these crucial elements. Environmental changes can be detected through the reflection of collectively emitted acoustic signals from passive objects. A collective response to external stimuli is achieved by modulating the oscillatory behavior of the swarmers, where changes of the oscillations and the mutual interactions between swarmers enables the coordination of collective behavior. In the following, we will address these questions by investigating the self-organization capabilities that emerge at the collective level, including the collective perception of the structures and their response to external control inputs.

5.4.1 COLLECTIVE SENSING

A key capability of systems that use (acoustic) waves for communication is their ability to emit and detect signals. Beyond transmitting signals between agents, these active systems can also acquire information about their surroundings through the reflections of the acoustic waves off various objects. However, this requires a collective response of the system, since a single agent on its own cannot generate a significant response due to its relatively weak emission amplitudes. When agents are organized in collective states, as discussed above, they are able to synchronize and emit acoustic waves in unison, substantially boosting the amplitudes of the waves. This coordination results in emergent cooperative sensing, where the enhanced signal strength and coordinated emissions enable more effective detection and interpretation of signals reflected from invading objects.

As an illustration of such a sense-and-response capability, we consider the response of a propagating larva and a localized blob to an invading object (Fig. 5.6). As the external object descends toward the habitat, the acoustic waves emitted by the collective state get reflected at the object. This, in turn, is perceived by the collective as it results in a change in their oscillatory states. In particular, we model the spherical waves reflected at the object as quasi-planar and with a homogeneous phase. This approximation is valid for objects with sufficiently large distance (height above the habitat). Then, the additional reflective input to Eq. (5.1d) is given by

$$u_{\text{refl}}(\boldsymbol{r}, t) = A_{\text{refl}} \langle a_l \rangle_N \, e^{2i\omega d/c} \,. \tag{5.4}$$

For the assumed spherical wave solution in three-dimensional space that decays inversely proportional to the distance, the sound amplitude depends on the distance d as $A_{\text{refl}} = 1/(2d)$. If there is a

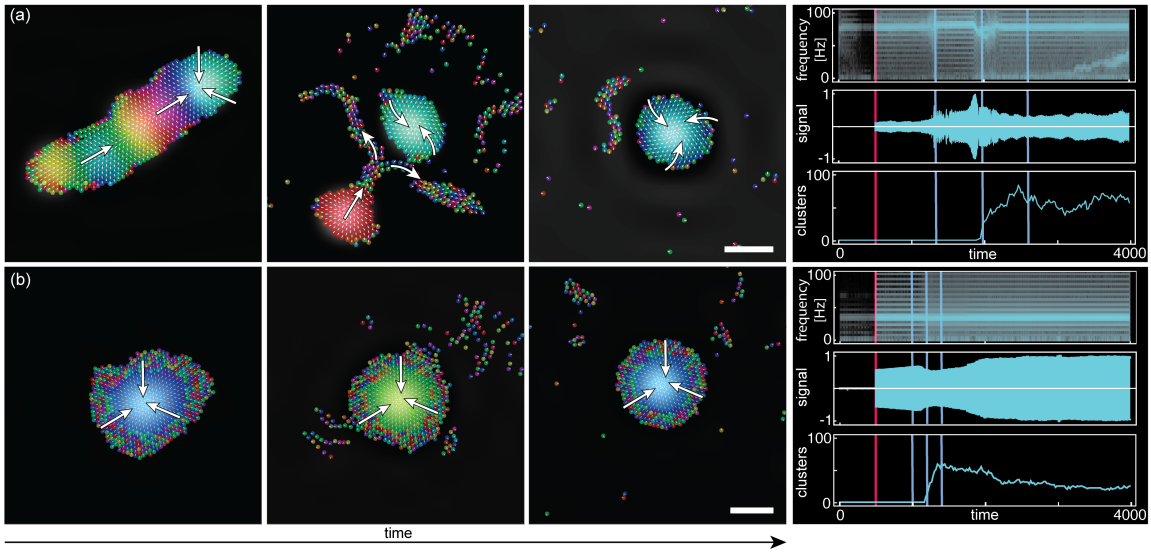

Figure 5.6: Collective sensing of approaching objects. (a) A sequence of snapshots illustrating the phenotype change of a traveling collective solution (larva) in response to an approaching object ("intruder" / "threat") above the habitat; the acoustic signals are reflected at the external object. The temporal evolution of sound frequencies, amplitudes, and the number of individual clusters in the entire simulation domain $L = 50$ are displayed in the rightmost panel. The vertical red line marks the instance when an intruder is introduced. Blue lines indicate times corresponding to the snapshots. The oscillation amplitude is measured in dimensionless units of Eq. (5.1d). (b) A sequence of snapshots illustrating the response of a localized collective solution (blob) on an approaching intruder. Disks represent individual agents, and the RGB color map shows the relative phases; see Fig. 5.2. White arrows indicate the agent's polar orientation and white bars represent a length of 5 units. This figure is reproduced from Ref.[4] under license [CC BY 4.0].

non-vanishing contribution $\langle a_l \rangle_N$ averaged over all the N acoustic oscillators, the agents receive a reflected phase-shifted acoustic feedback signal. The strength of the reflected signal not only depends on the distance of the reflective object but is significantly determined by the degree of synchronization in the emitting collective. The more agents emit signals in unison, the stronger the reflected signal will be. Thus, the system shows a cooperative exploration of the surroundings.

In our simulations we observe that upon detecting the reflected waves (left panel in Fig. 5.6(a), left blue indicator in right panel), a larva solution undergoes a dramatic transformation of its morphology ('metamorphoses', center), disassembling into a blob and expelling peripheral swarmers (right panel in timeseries). The ejection of agents (center blue time marker) is evidenced by the strong increase in the number of clusters in the entire simulation domain ('clusters' panel). Right before this event, the signal amplitudes increase significantly ('signal' panel) as more and more agents of the larva start to synchronize their oscillatory state. Apparently, at some point, local synchronizations within the larva become too strong. The larva destabilizes and starts to metamorph into an intermediate state in which its head and tail form two separate blob-like structures. One of them further emits agents into the surrounding and eventually decays. This event corresponds to a dip in the aggregate's oscillation frequency, as emitted swarmers decouple from the center aggregate. The other developing blob remains spatially localized and shows a slight vorticity. While the swarmers within the remaining blob display synchronized oscillations, the expelled swarmers have decoherent phases. Finally, some of the dispersed agents aggregate into a secondary snake-like structure (second growing mode in 'frequency' panel) which is spatially captured in a high-amplitude acoustic wave ring emitted by the blob (Fig. 5.6(a), last snapshot).

Like larvae, blobs, and volvoxes can also detect and respond to approaching objects via reflected signals (Fig. 5.6(b)). Once the reflective object is introduced above the habitat (red marker in right panel), the blob's acoustic signature is changed: The amplitude of acoustic emission increases significantly given the additional input through reflection at the intruder. As the reflective object gets closer to the habitat, the volvox sheds peripheral, desynchronized agents, reducing its overall size

(clusters panel). Thereby, the aggregate takes a more circular shape, as agents further away from the synchronized center can no longer be attracted. At this point, the volvox has reached its carrying capacity. The ejection of excess swarmers also leads to a slight reduction of the dominant oscillation frequency (frequency panel) and a dip in the signal amplitude (signal panel).

In both these cases, the collective states responded to the reflective object by altering their collective behavior. The observed self-organized responses to intruders, along with the resulting behavioral changes, can be linked to specific collective functions. For instance, the morphological transition from a larva to a blob corresponds to an externally induced localization of the aggregate. Similarly, the volvox's response can be seen as a self-organized, coordinated dispersion of agents in reaction to the intruder. Since we did not specifically design the system with this functionality in mind, the observed behavior is emergent, demonstrating that minimal physical interactions between agents can give rise to a higher-order collective functionality. Again we have observed a correspondence between the emergent behavior of the aggregates and their collective acoustic signatures. Through acoustic coupling, the agents emit distinct state information into their surroundings, suggesting a rudimentary form of inter-collective communication.

5.4.2 COOPERATIVE FUNCTIONALITY

Next, we explore two other types of targeted behavior examining how systems can: (i) navigate through narrow constrictions and subsequently restore their original shape; (ii) regenerate both their shape and functionality after experiencing significant distortion.

Figure 5.7(a) shows a time series (t_1, t_2, t_3) of a snake-like collective state navigating through a narrow constriction in a wall (gray). Upon colliding with the wall, the snake's shape becomes significantly distorted, suggesting that only a fraction of the agents might eventually pass through the constriction (t_2). However, after the majority of the agents successfully traversed the slit, the snake nearly regains its original shape and resumes its movement, pulling the temporarily clustered agents with it (t_3). The rightmost panel in Fig. 5.7(a) shows the dependence of the agents' passing fraction on the snake length and the slit width. We observe that the passing fraction decreases significantly as slit width narrows or snake length increases. For increasingly narrow constrictions, the snake must greatly reduce its width to fit through, and due to the finite size of the swarmers, more agents are left behind at the constriction. Similarly, longer snakes with more swarmers also leave behind a growing number of agents at the slit. These left-behind agents then occasionally form a stable, localized cluster, preventing them from being pulled through with the snake, which further reduces the passing fraction. Despite these limitations, we find that snakes are often able to pass through constrictions much narrower than their initial diameter without leaving any constituting swarmers behind.

Moreover, we observe that the collective states shown in Fig. 5.2 exhibit shape memory and self-healing capabilities, enabling them to recover both their morphology and functionality even after experiencing strong perturbations. For instance, if the pacemaking defect in a larva's head is destroyed (Fig. 5.7(b), t_1), the larva initially ejects some agents (t_2). It then recovers by regrowing a body part that contains a new pacemaker and eventually re-absorbs the ejected agents (t_3).

To quantitatively assess how the larva recovers its characteristic behavior upon the perturbation, we investigate the dependence of the aggregate's velocity on the position of the included polar defect (Fig. 5.7(b), right panel). We find that the collective propagation of larvae is determined by the spatial offset of the polar defect with respect to the center of mass of the aggregate. As agents are oriented around the enclosed polar defect, asymmetries of the defect position control the collective velocity. Thus, measuring the collective velocity of various larva solutions in dependence of their defect offset (black dots, Fig. 5.7(b), right), we observe an approximately linear behavior up to a saturation value of about $20\,\%$ of the single swarmer's velocity (gray line). The linear dependence of the collective velocity on the defect localization gives a quantifiable measure for the larva phenotype. Since the motion of all larvae is driven by the same underlying mechanism, we expect that the velocity to defect offset ratio for each larva will follow the trend shown by the black dotted line in Fig. 5.7(b). For the larva depicted in the time series (Fig. 5.7(b)), the strong perturbation causes its

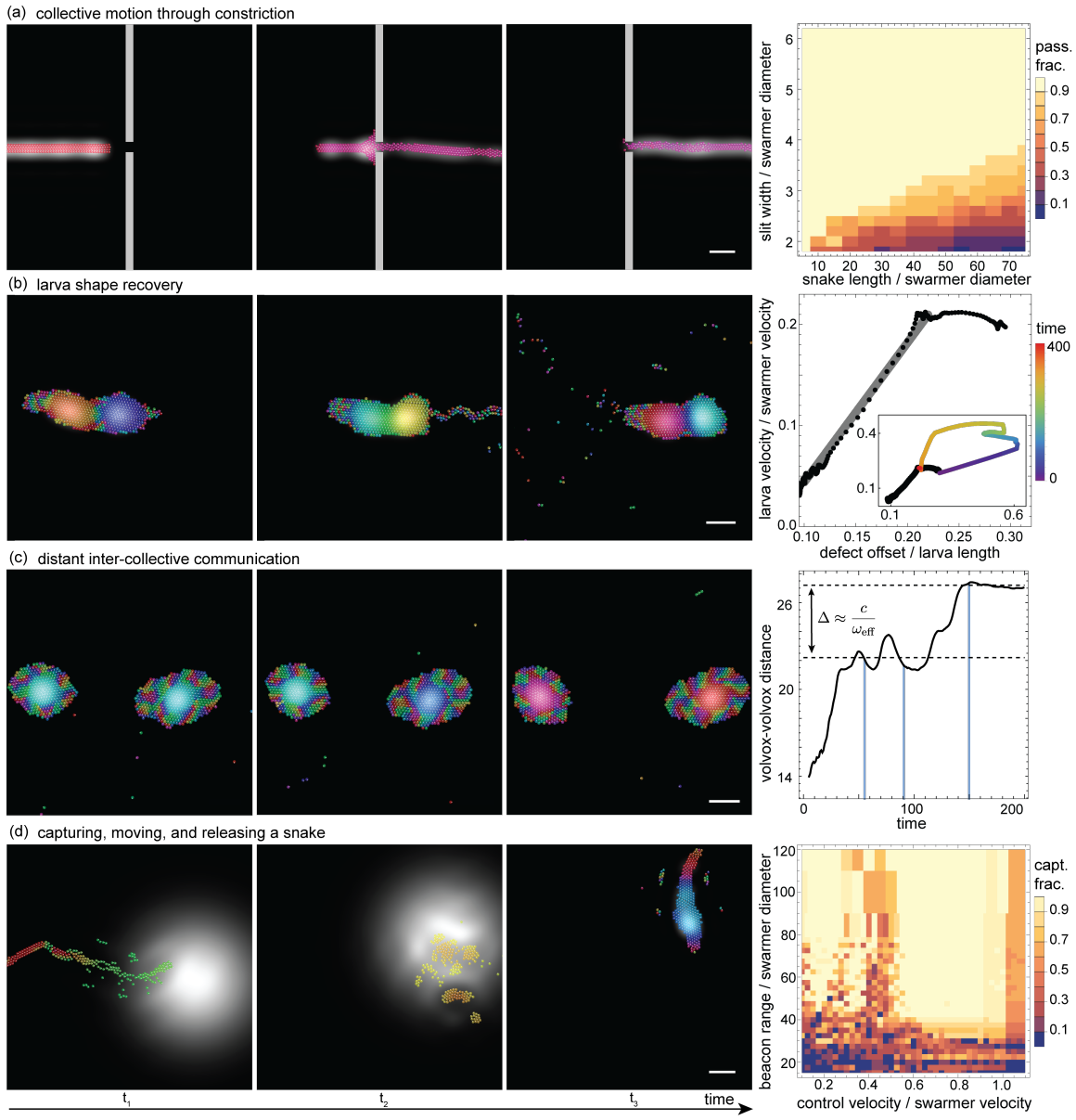

Figure 5.7: **Illustrations of emergent functionalities.** (a) A stable snake propagates through a narrow constriction (gray). The rightmost panel shows the dependence of the passing fraction of agents on slit width and snake length. (b) A larva regrows cut-off head. Larvae exhibit a saturating linear dependence of collective velocity on enclosed polar defect position (right panel). Upon recovery, the larva eventually returns to the projected dependence of the collective velocity of larvae states (colored trace in inset). (c) Distant acoustic communication. Two volvoxes interact via emitted acoustic waves and assume stable inter-cluster distance, an integer multiple of standing acoustic wave length Δ. Blue lines indicate the times of the snapshots. (d) Capture, transport, and release of a snake by the acoustic beam (snake-in-the-egg). The applied control protocol is stable for sufficiently large beacon sizes up to control velocities equal to the individual agent velocity. The right panel indicates the fraction of successfully captured agents. Agent color code shows oscillatory phase, see Fig. 5.2, and background shows normalized acoustic field amplitudes $|u|^2$ in gray scale. White bars indicate 5 length units. Parameters are given in Table 5.1. This figure is reproduced from Ref.[4] under license [CC BY 4.0].

polar defect to be abruptly removed. In such cases where there is no enclosed polar defect, we define the defect position as being located at the outer boundary of the aggregate. Consequently, the defect offset is taken as the maximum distance from the boundary to the center of mass of the solution. We observe that upon the strong perturbation, the aggregate leaves the characteristic linear dependence

of larva velocity on defect position (trajectory, purple, inset Fig. 5.7(b)). It has lost its characteristic larva behavior and has transitioned to another phenotype with large defect offset up to 60% of the larva's total length and velocities up to over 40% of the individual agents. In response, the solution quickly regrows its head by developing a new enclosed polar defect. By doing so it regains the larva phenotype and returns to the characteristic velocity behavior of larvae (trajectory, red).

In summary, we have demonstrated that, for specific swarmer characteristics and system parameters, the emergent collective states are resilient to perturbations, exhibiting a form of phenotype memory by recovering after external disruptions. This reveals a mechanism for stable, emergent functionality that is robust against swarmer replacement and can adapt to environmental changes, ensuring robustness and flexibility in collective behavior.

5.4.3 COMMUNICATION

In the previous examples, we observed that the different types of collective states exhibit distinct acoustic signatures. As a consequence, each aggregate emits unique waves into their surroundings, enabling the potential for inter-collective communication. An elementary example of this communication is the distance regulation of two volvox solutions (Fig. 5.7(c)). Each volvox emits acoustic waves into its surrounding with individual signature similar to Fig. 5.2(f). The interference of these emissions creates a standing wave field between the two aggregates, controlling their mutual distance. As shown in the rightmost panel in Fig. 5.7(c), the inter-volvox distance oscillates about metastable distances that depend on the wavelength of the emitted acoustic signals. Given the mutual acoustic input, the solutions have an effective average frequency ω_{eff}, such that the standing wavelength can be approximated as

$$\Delta \approx \frac{c}{\omega_{\text{eff}}} \approx 5\,. \tag{5.5}$$

Thus, the dynamics of the inter-volvox distance depend on the length scale of the acoustic waves of the two aggregates, enabling them to measure their distance by means of the emitted wave strength and signal frequencies.

Beyond this very basic form of interaction studied here, acoustic communication facilitates far more complex interactions, ranging from the recognition of specific signals with orchestrated responses up to the development of intricate languages. The acoustic coupling enables the exchange of information between individuals and collectives. As such it can mediate synchronization between communities depending on inherent properties and shared or distinct external stimuli.

5.4.4 POSITION CONTROL

Given the system's use of acoustic communication between agents, it is also responsive to external acoustic stimuli. As we have seen for the response to reflected signals (Sec. 5.4.1), additional inputs can give rise to significant changes in the observed behavior of the collectives. This external control over emergent structures has potential applications, such as manipulating the positioning, orientation, or even the exhibited phenotypes of the agents. In this section, we will explore how external acoustic signals can be used to control the spatial positioning of the agents.

Specifically, we study a scenario where we superimpose a bell-shaped acoustic signal with frequency ω_c at position $\boldsymbol{r}_c(t)$ onto the acoustic field generated by the agents:

$$u_c(\boldsymbol{r}, t) = A_c e^{-(\boldsymbol{r}-\boldsymbol{r}_c(t))^2/(2\sigma_c^2)} e^{i\omega_c t}\,, \tag{5.6}$$

that is, we add this field as a source term to the dynamics of the acoustic field, Eq. (5.1d). To be specific, we select a control frequency of $\omega_c = 2\omega_0$, which is twice the frequency of the free agents. This value is chosen because it closely matches the frequencies observed in snakes, which are typically elevated by up to an order of magnitude compared to those of free agents. However,

it is important to note that this particular choice is not essential, and position control can still be effective with other frequency choices.

For capturing agents and controlling their position, the control signal, with amplitude A_c and range σ_c is moved along the protocol position

$$\boldsymbol{r}_c(t) = \begin{cases} (2/3\,L, 1/4\,L)^T & ,t < 800\,, \\ (2/3\,L, 1/4\,L + v_c t)^T & ,800 \leq t \leq \frac{L}{2v_c}\,, \\ (2/3 L, 3/4 L)^T & ,t > \frac{L}{2v_c}\,. \end{cases} \tag{5.7}$$

Using the focused acoustic beam, we aim to capture snakes and then transport them to a desired position to subsequently release them (Fig. 5.7(d). Capturing the snake at $\boldsymbol{r}_c = (2/3\,L, 1/4\,L)^T$, we shift the target position by half system length $L = 100$ with velocity v_c. For the snake solution in Fig. 5.7(d), the applied control first leads to the disintegration of the snake and the capture of all its agents inside the beam (*snake-in-the-egg*, t_2). Moving the beam toward the target position can successfully transport the contained agents to the desired location. Once the beam is switched off, the agents escape the temporary confinement and readily reassemble into a snake (t_3).

Even though this generic, open-loop control scheme does not require detailed knowledge of the controlled collective, it is successful over a broad range of control parameters. Indeed, it is effective as long as the beacon range is large enough to capture all the constituting agents and the protocol velocity does not exceed the free agent's velocity; see rightmost panel in Fig. 5.7(d). However, we also observe failure of the applied scheme, predominantly when enforcing a stronger mismatch between the control velocity and the agents' free velocity. This failure occurs because the agent's orientation rather than positioning is directly impacted by the control. For the results shown in Fig. 5.7(d), the selected control amplitudes $A_c \sim 100$ are in the same order as the acoustic field amplitudes induced by the snake. Larger amplitude signals or more elaborate closed-loop control schemes could be applied to implement a more reliable position control. As the applied control initially causes the snake to transform into a blob, this generic control scheme is also effective for blob or volvox solutions (not shown here), and we anticipate potential applicability beyond the example studied in this work.

5.5 DISCUSSION AND OUTLOOK

Unlike systems at thermal equilibrium, active matter has the unique ability to form complex structures. This capacity arises from the constant input of energy at the level of individual agents, allowing the system to self-organize into dynamic, adaptable patterns. Myosin motors have been shown to generate force through the conversion of chemical energy, enabling actin filaments in actin motility assays to form self-organized, coexisting polar density waves and nematic lanes[163,164]. Colloidal Janus particles represent another example of self-organizing active matter, as they harvest chemical energy to exhibit self-propelled motion[375], chemotaxis[376], and dynamically aggregate into clusters[221,377]. Similarly, mixtures of actin and microtubules can self-organize into polar aster-like defects[378] and active foam structures[373,379]. These studies, along with many others, highlight the remarkable self-organization capabilities inherent to active matter systems[54,56]. Continuously driven out of equilibrium, these systems transform energy to enable the formation of collective structures and self-organized patterns. The building blocks of these structures are encoded in the microscopic interactions between their constituent agents. However, to go beyond self-organisation into complex structures and achieve even higher-order organization that can perform specific tasks or respond to environmental changes, an additional mechanism for coordination or interaction among agents is needed. In essence, to achieve functionality, an efficient means of communication is necessary that supports both collective decision-making among agents and interaction with the environment.

Several experiments have explored the potential of chemical signaling for the development of higher-order organization into functional structures: It has been demonstrated that self-avoidance in self-propelled Janus particles arises from information stored within a surrounding chemical field[219]. Active droploids, which are aggregates of colloidal particles, exhibit self-organized polarity and co-

herent self-propulsion[380]. Additionally, there is a growing interest in the possibility of extracting work from active matter systems. For instance, when agents collectively assemble, asymmetries in their orientation and positioning can generate net rotational motion of the emergent structures[381]. Passive gear-like objects, designed with chiral shapes, can act as nuclei for this aggregation and thereby promote the breaking of rotational symmetry and inducing effective rotation as a collective phenomenon[382]. Similarly, collective activity can be harnessed for driving of active droplets[383], and cargo transport[384]. While such systems with chemical signaling in active matter have been well studied in recent years[3,216,220,385,386], they rely on the diffusion of chemical species, resulting in relatively slow information exchange. In contrast, wave-type signaling, such as via acoustic or electromagnetic waves, offers faster communication and can readily be implemented in various synthetic or micro-robotic systems. Despite its potential advantages, this form of signaling has remained largely unstudied, and its role in driving emergent functional behaviors is still mostly unexplored.

In this work, we proposed and analyzed a first theoretical model of acoustically coupled active agents, termed swarmers. These polar agents, which self-propel in a two-dimensional habitat, are equipped with internal oscillators that continuously emit acoustic waves into their surroundings. Propagating through the three-dimensional space, these waves enable long-distance communication among individual agents and facilitating non-local interactions between the emergent collectives of swarmers they form. We have coupled this long-distance information transfer to the motility of the agents by assuming that the swarmers align towards regions with higher signal amplitudes, typically where agents' oscillations are highly synchronized. We discuss the main results and their broader implications in the following sections.

5.5.1 EMERGENT COLLECTIVE STATES: BEHAVIORAL AND ACOUSTIC PHENOTYPES

Numerical simulations of this agent-based model reveal a rich diversity of emergent collective states driven by the intricate interplay of self-propulsion, mechanical alignment, and acoustic signaling. We observe the formation of localized *blobs*, in which swarmers cluster around a highly synchronized central region containing a polar defect. Additionally, we identify *larva* solutions, which move slowly and exhibit an asymmetrical arrangement of agents around a polar defect. Yet another collective structure we observe are fast-moving *snakes*, which consist of a cohesive group of swarmers that are well aligned and move coherently in a common direction. These snake solutions bear a strong resemblance to structures in polar active matter with vision cone alignment[207]. There, a non-reciprocal interaction between agents is globally imposed by varying vision cones that control the mutual alignment interaction[207,208]. In contrast, our model features emergent symmetry breaking, with a self-organizing pacemaker acting as a phase leader. It guides the propagation of phase waves through the structure and thereby controls directed information transport. Finally, acoustic active matter exhibits *volvox* structures with synchronized central region and an outer layer of incoherently oscillating swarmers, and ring-like *ouroboros* structures. The volvox solutions resemble chimera states in networks of non-locally coupled oscillators characterized by the coexistence of synchronized and incoherently oscillating agents[374,387]. In contrast to static networks of oscillators, volvoxes are a spatially organized chimera structures with a dynamic exchange of interaction partners due to the self-propulsion of agents. Their synchronized center and the incoherently oscillating outer layers reflect two opposed regimes of acoustic signaling. These could be further linked to different behavioral modes to gain higher order functionality. As the incoherence in the agents identifies the positioning within the outer layer of the aggregate, agents could develop properties important for a specific physical interaction. For instance, they could develop into a static shell, further protecting the aggregate.

Taken together, acoustic active matter is characterized by a rich variety of phenotypes, each exhibiting distinct morphology and mesoscopic behavior. The occurrence of the different phenotypes is closely influenced by the chosen values of microscopic agent parameters. Our analysis shows that slow, highly susceptible swarmers form localized blobs, while fast, persistent agents generate snake-like structures. The other solutions arise in intermediate regimes. This suggests that manipulating these microscopic parameters allows for a control of the emergent phenotypes. In this

study, we focused on emergent functionality based on basic alignment with acoustic amplitude gradients. However, designing more complex functional structures will increasingly require incorporating higher-order interactions between microscopic agent parameters and the information derived from the signaling field.

The emergent structures not only show distinct behavioral phenotypes but also produce specific acoustic emission characteristics. Each collective state generates different frequency distributions and emission amplitudes, making structures distinguishable based on their acoustic signatures. Through the emission of these distinctive signals, the collectives can communicate with one another, allowing them to identify the type and potentially also the current state of the surrounding solutions. As a result, the collectives can develop varied behavioral responses to the different acoustic interactions they encounter.

5.5.2 FIELD THEORY OF ACOUSTIC ACTIVE MATTER

Beyond exploring emergent structures, we also investigated how the aggregation process continues on larger time- and length scales. To access these, we proposed complementary continuous field equations as a coarse-grained version of the agent-based model. Similar to known hydrodynamic field equations for polar active matter[176,189,196,198,199], our model includes polar alignment interactions of swarmers by a density-dependent isotropic-to-polar order transition and the alignment with gradients in the acoustic signaling amplitude. This field-based approach successfully reproduces the blobs and snake solutions as two central collective states of the system. Thereby, the model captures the essentials of the structures' phenotypical and acoustic signatures. Over longer time scales, we have observed rapid coarsening of aggregates, much faster than classical Ostwald-ripening or cluster aggregation in motility-induced phase separation. Ultimately, clustering stabilizes at a length scale that is influenced by the acoustic wavelength. We find that different clusters interact with each other via the acoustic field and extract distance and positional information from it. This highlights once again the significant role of wave-like coupling in cluster aggregation and long-distance information transfer. The hydrodynamic field theory serves as an effective tool to study acoustic coupling in very large systems, and may be valuable for future studies of systems with large agent numbers. Our study demonstrates that information can be propagated efficiently over large distances. While we focused on system sizes where wave absorption could be neglected, absorption characteristics can vary across different media. Future studies with specific settings may need to consider such additional factors like wave absorption and boundary reflections.

5.5.3 ADAPTIVE RESPONSES AND INTERACTIONS WITH THE ENVIRONMENT

For the emergence of collective functional structures, adaptability to environmental changes is crucial as it enables the collectives to locate target positions and to organize and monitor their function. It is widely recognized as critical for the functioning of biological systems[388], spanning from complex animals such as social insects[215] to microscopic organisms like bacteria[389]. However, despite its importance, few studies have investigated the capabilities of synthetic active matter systems to respond to environmental changes. For instance, active colloids can form swirl-like structures and adapt their self-propulsion in response to external changes[390]. More broadly, colloidal and de-mixed droplet systems can measure and respond to changes in their chemical or optical surroundings, and adapt their self-propulsion accordingly[219,381,391]. These initial implementations of environmental sensing in synthetic systems already demonstrate its potential impact on the systems' collective behavior. Unlike these previous studies that rely on individual agents to sense environmental cues, our results demonstrate a collective form of environmental sensing in acoustic active matter that emerges as a cooperative function through acoustic synchronization within the collectives. In our model, the environmental sensing is achieved through the acoustic field. Agents emit synchronized waves and detect reflections from objects in their surroundings. Thereby, the swarmers gain a cooperative increase in the strength of environmental coupling by collectively emitting stronger signals. We have examined how blob and larva structures respond to an approaching reflective object above

their habitat. The reflected signals trigger phenotype changes in the solutions and lead to cluster localization or dispersal of agents. This demonstrates that collectives can sense and react to external stimuli using the acoustic field. Similarly, inter-cluster communication is facilitated by the acoustic signals. We observed that two volvox-like aggregates could maintain a stable distance by sensing and responding to each other's acoustic emissions, essentially measuring their separation through these interactions.

Our study also reveals that different collective functions require distinct behaviors of the individual swarmers. In a system of identical units, the swarmers must adapt and differentiate their behaviors in response to the acoustic input they receive from their surrounding. As this behavioral differentiation is self-organized and agents are functionally identical, the system can compensate for agent failures and dynamically adapt to imposed perturbations. As a result, the collective states acquire a high level of robustness. For example, snake structures can collectively navigate through constrictions narrower than their original diameter, and larva structures can recover their polar defect, demonstrating their resilience.

Finally, we presented that acoustic waves can be used to externally control the system. For instance, snake structures can be captured and relocated via acoustic signals, resuming their behavior once released at the desired position. Altogether, this enables external supervision and control of the active matter system through the measurement and application of acoustic signals.

In conclusion, we have shown that wave coupling between self-propelled active agents yields various distinct functional structures with emergent capabilities. The emission and detection of acoustic signals by the swarmers enable a fast information exchange over large distances. Through the acoustic field, aggregates communicate characteristic acoustic signals and gain information about their environment via a collective sonar-like mechanism.

5.5.4 TOWARDS A CYBERNETICS OF ACTIVE MATTER

We believe that the present study takes an important step towards a new form of active matter that is able to organize into collective states that can be regarded as phenotypes, which exhibit higher-level features (functions) that allow them to respond in an adaptive way to changes in the environment. In the proposed framework of acoustic active matter, the system acquires emergent functionality without external supervision, relying solely on microscopic interaction rules at the level of individual swarmers. Similar to neural networks, collective functionality arises from the interaction among units, with each performing only simple computational steps. This approach keeps individual agents simple and their computational energy consumption minimal, as each swarmer processes only a small portion of the information available to the entire cluster.

Our minimal model for wave interaction already demonstrates the rich collective behavior achievable through acoustic coupling. This model offers insights into the fundamental principles of wave-type interactions and the collective organization of oscillatory self-propelled units, as well as the emergence of collective sensing. It serves as a foundation for exploring more complex interactions and microscopic behaviors, guiding the development of functional active matter systems towards more specific and advanced applications.

The potential applications for unsupervised functional active matter systems are diverse. Once this form of communication is integrated into synthetic systems, it could enable tasks in environments that are otherwise inaccessible or hazardous. The robustness and adaptability of these structures suggest significant potential for real-world applications in environments where external supervision is impractical. For example, following the presented principles, ensembles of acoustically communicating agents may develop a more evolved cooperative sonar, where phase differences in reflected signals can be evaluated by the collective, yielding insights into the nature of the reflective objects and triggering appropriate behavioral responses. The wave-like coupling has been motivated by acoustic waves and could be used by naval drones or robots in a mechanically coupled medium[392–394]. One can expect similar behavior from electromagnetically communicating agents.

From a broader perspective, future studies should extend beyond the microscale energy conversion—that defines the field of active matter—to explore the ability of agents to perceive and respond to

their environment. Through communication, these agents can then form collectives that exhibit cooperative behavior, make collective decisions, and actively reshape their surroundings. Investigating such functional synthetic active matter lays the groundwork for a cybernetics of active systems, which focuses on designing and controlling synthetic systems to achieve specific objectives.

5.6 APPENDIX

5.6.1 QUASISTATIC SOLUTION OF THE WAVE EQUATION

The system of acoustic active matter introduces a wave-like coupling between self-propelled oscillators. In the model, the swarmers, confined to their two-dimensional habitat, emit waves into the surrounding three-dimensional medium. Typically, the acoustic wavelengths are much larger than the size of the individual agents, and the speed of sound significantly exceeds the self-propulsion velocities of the swarmers. In this section, we explain how we take advantage of these scale differences to incorporate acoustic coupling by employing a quasi-static solution to the three-dimensional wave equation with the agents as acoustic sources. The dynamics of the sound field $u(\boldsymbol{r}, t)$ in three spatial dimensions, $\boldsymbol{r} = (x, y, z)^T \in \mathbb{R}^3$, is modeled using the wave equation

$$\frac{1}{c^2}\partial_t^2 u(\boldsymbol{r}, t) = \nabla^2 u + \sum_j w(\boldsymbol{r} - \boldsymbol{r}_j, t) a_j(t) \delta(z)\,, \tag{5.8}$$

with the speed of sound c and active agents as sources confined to the two-dimensional plane at $z = 0$. As detailed in the main text, the agents' source contribution $a_j(t)$ is weighted by a Gaussian kernel $w(\boldsymbol{r}, t)$, representing the agent's size. Assuming a fast sound dynamics as wave propagation is fast compared to the agent velocity, i.e., $c \ll v_0$, we consider the quasi-stationary case,

$$c^2 \nabla^2 u(\boldsymbol{r}) + g\delta(z) = 0\,. \tag{5.9}$$

with general source contributions $g\delta(z)$. It can be solved using a separation ansatz for the in-plane solution in the two-dimensional habitat and the perpendicular out-of-plane direction, $u(\boldsymbol{r}) = u_{x,y}(x, y)Z(z)$. Assuming periodic boundary conditions within the habitat, we apply a Fourier transform in (x, y)-plane with two-dimensional wave vector $\boldsymbol{k} = (k_x, k_y)^T$. Then, outside the habitat plane ($z \neq 0$) in the absence of additional sources, the stationary wave equation reads

$$0 = c^2 \left(-k_x^2 - k_y^2 + \partial_z^2\right) \tilde{u}_{\boldsymbol{k}} Z(z)\,, \tag{5.10}$$

with Fourier transform $\tilde{u}_{\boldsymbol{k}} \equiv \mathcal{F}\left[u_{x,y}(x, y)\right](\boldsymbol{k})$. Next, we aim to find the corresponding out-of-plane bulk solution $Z(z)$. For non-vanishing in-plane wave vectors, $k = |\boldsymbol{k}| = \left(k_x^2 + k_y^2\right)^{1/2} \neq 0$, the equation reads

$$\partial_z^2 Z(z) = \left(k_x^2 + k_y^2\right) Z(z)\,, \tag{5.11}$$

and one can find the solution

$$Z(z) = e^{-k|z|}\,, \tag{5.12}$$

which fulfills the boundary conditions of vanishing contributions at $z \to \pm\infty$. Waves emitted from the two-dimensional habitat exponentially decay in the bulk depending on their wave length $1/k$. Accordingly for the homogeneous emission from the bulk, $k = 0$, the equation reduces to

$$\partial_z^2 Z(z) = 0\,, \tag{5.13}$$

with the solution

$$Z_0(z) = \alpha + \beta|z|\,. \tag{5.14}$$

As we neglect absorption in the medium, which is valid for sufficiently small systems, the decay of waves away from the habitat is only caused by interference effects between the waves emitted at different position within the two-dimensional plane. The waves will overlay and eventually average out at some height above the habitat. Homogeneous oscillations on the other hand, will never average out as they have a net contribution over the whole domain. Next, we consider the sources at $z = 0$, such that the full solution to the wave equation has to fulfill

$$c^2\left(\partial_z^2 - k^2\right)\tilde{u}_{\boldsymbol{k}} Z(z) + \tilde{g}_{\boldsymbol{k}}\delta(z) = 0\,. \tag{5.15}$$

We integrate this equation over a small interval around the habitat $z \in (-\epsilon, \epsilon)$ and subsequently consider the limit $\epsilon \to 0$. As, the integral

$$\lim_{\epsilon\to 0}\int_{-\epsilon}^{\epsilon} Z(z)k^2 \mathrm{d}z = 0 \tag{5.16}$$

vanishes in the limit, we remain with the terms

$$\lim_{\epsilon\to 0} c^2\partial_z\tilde{u}_{\boldsymbol{k}} Z(z)\Big|_{-\epsilon}^{\epsilon} + \tilde{g}_{\boldsymbol{k}} = 0\,. \tag{5.17}$$

Evaluating the limit, we obtain for $k \neq 0$,

$$-2c^2\tilde{u}_{\boldsymbol{k}} k Z(z) + \tilde{g}_{\boldsymbol{k}} = 0\,, \tag{5.18}$$

which is solved by

$$\tilde{u}_{\boldsymbol{k}} Z(z) = \frac{\tilde{g}_{\boldsymbol{k}}}{2kc^2}\,. \tag{5.19}$$

For vanishing wave vectors, $k = 0$, evaluation of the limit in equation, Eq. (5.17), yields

$$2c^2\tilde{u}_0\beta + \tilde{g}_0 = 0\,, \tag{5.20}$$

with the solution

$$\tilde{u}_0 Z_0(z) = \tilde{u}_0\left(\alpha - \frac{\tilde{g}_0|z|}{2c^2\tilde{u}_0}\right)\,. \tag{5.21}$$

Finally, as argued before, we neglect any homogeneous contributions to the acoustic field, $\tilde{u}_0 = 0$ as these would represent global offsets and therefore just shift the baseline of the acoustic field. Consequently, for a given Fourier representation of the sources, $\tilde{g}_{\boldsymbol{k}}$, the acoustic field at the habitat, $z = 0$, is given by

$$\tilde{u}_{\boldsymbol{k}} = \frac{\tilde{g}_{\boldsymbol{k}}}{2c^2\sqrt{k_x^2 + k_y^2}}\,. \tag{5.22}$$

Under negligence of damping, we solve the three-dimensional quasi-static wave equation for acoustic emitters confined to a two-dimensional plane. The resulting acoustic field gives rise to a non-local acoustic coupling that scales as $1/k$ in Fourier space. To understand the impact of this non-local coupling on structure formation, we study a minimal version of the acoustic active matter. Namely, for homogeneous agent densities, the system simplifies to a non-locally coupled complex Ginzburg-Landau equation, see appendix Sec. 5.6.2.

5.6.2 NON-LOCALLY COUPLED COMPLEX GINZBURG LANDAU EQUATION

In the main text, we discuss how for constant densities, $\rho \equiv \rho_0$, the system of acoustic active matter, Eq. (5.1), can be described by a non-locally coupled version of the complex Ginzburg Landau equation (CGLE). Indeed, for homogeneous densities and without swarmer motility, $\rho(x, y) = \rho_0$, $v_0 = 0$, the system reduces to

$$\partial_t a = \mu \nabla_{2D} a + (1 + i\omega)\, a - (1 + ib)\, |a|^2 a + \lambda u|_{z=0} \tag{5.23}$$

$$\frac{1}{c^2}\partial_t^2 u = \nabla^2 u + \rho_0 a \delta(z)\,. \tag{5.24}$$

Assuming large wave propagation velocities $c \gg 1$, one can consider the quasi-static wave equation, namely the Poisson equation,

$$\nabla^2 u = -\rho_0 a \delta(z)\,, \tag{5.25}$$

with solutions given by Eq. (5.22), see appendix Sec. 5.6.1. Inserting this solution into Eq. (5.23), we consider plain wave solutions,

$$a(x, t) = a_0 \exp\{i\Omega t + ikx\}\,. \tag{5.26}$$

Plugging this ansatz into Eq. (5.23) yields a dispersion relation $\Omega(k)$,

$$i\Omega = (1 + i\omega) - (1 + ib)\, a_0^2 + \frac{\lambda\rho_0}{2|k|} - \mu k^2\,. \tag{5.27}$$

From it, one can see that the coupling of the oscillatory medium mediated by the acoustic field induces non-local interactions ($\sim 1/|k|$) which scale with the wavelength of the considered wave. Solving this equation, the amplitude and, respectively, the phase of the plane-wave solutions read

$$a_0 = 1 + \frac{\lambda\rho_0}{2|k|} - \mu k^2 \tag{5.28}$$

$$\Omega = \omega - b a_0^2\,. \tag{5.29}$$

As for the classical CGLE, the frequency of the acoustic wave has a non-linear relationship with the amplitude as $\Omega \sim b a_0^2$. The non-local acoustic coupling reflects itself in an additional contribution ($\sim \lambda$) which modulates the plane wave amplitude. Considering the group velocity within the plain wave solution, one gets

$$v_g = \frac{\partial\Omega}{\partial k} = 2ba_0 \left[\frac{\lambda\rho_0 k}{2|k|^3} - 2\mu k\right]\,. \tag{5.30}$$

As such, the acoustic coupling induces a divergence of the group velocity for long wavelength modes, $k \to 0$. As discussed in appendix Sec. 5.6.1, this is due to the fact that waves overlay and propagate through the three-dimensional environment. They eventually anihilate over length scales at which positive and negative contributions vanish on average. For larger wavelength, $k \to 0$, this length scale over which waves negatively interfere becomes larger and larger. Thus, interactions become increasingly strong for larger wavelength of the acoustic signals. This non-local coupling on large length scales has a significant impact on the system's coarsening dynamics, as we will see below. We measure the number of phase defects in the non-locally coupled CGLE, Eq. (5.23), for a constant homogeneous agent density $\rho_0 = 0.6$ over time (Fig. 5.8). Without the long-range acoustic coupling, $\lambda = 0$, we observe slow defect coarsening due to the exponentially decaying interaction between defects[368,395]. In contrast, enabling the acoustic coupling yields a significantly faster merging of defects as regions synchronize via the acoustic field. The final number of defects, N_{defect}, saturates according to the CGLE screening length, $L_{\text{screening}} \sim 1/bk_0$, with the wavenumber selected by the defects k_0. The explicit relationship can be obtained from the asymptotic linear stability of the planar waves emitted by the topological defects[368]. Then, one can find that the defect number

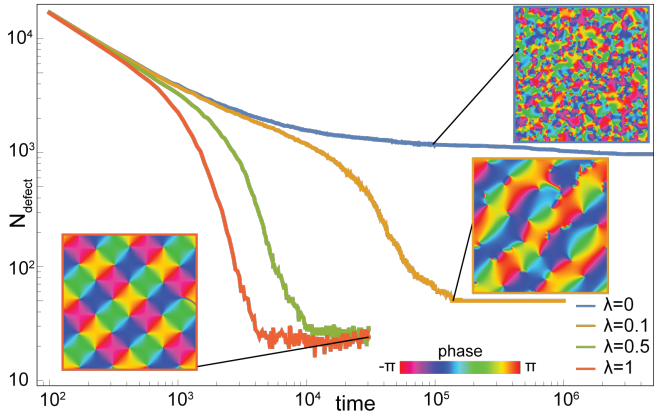

Figure 5.8: Temporal evolution of number N_{defect} of phase defects. The non-local coupling $\lambda > 0$ accelerates defect coarsening significantly until a final length scale is reached. Measured numbers correspond to a box with side length $L = 1000$ with periodic boundary conditions. System parameters as in Table 5.2. This figure is reproduced from Ref.[4] under license [CC BY 4.0].

$N_{\text{defect}} \sim L^2/L^2_{\text{screening}}$, where L represents the system size[368]. For conciseness, we will not perform the calculations explicitly here. The study of this minimal system for acoustically non-locally coupled oscillators emphasizes the significance of the long-range interaction for the coarsening of defects on a large scale.

5.6.3 DETAILS ON NUMERICAL SIMULATIONS

AGENT-BASED SIMULATIONS

In this section, we give the details of the applied numeric integration scheme for the dynamics of the N acoustically interacting active agents in a two-dimensional domain $(x, y) \in [0, L] \times [0, L]$ with periodic boundary conditions. In the agent-based simulations, we directly solve the equations (5.1) for the agents' positions $\boldsymbol{r}_l$, orientation angles φ_l, and oscillatory states a_l applying a forward Euler-Maruyama scheme with fixed time step dt. Agents interact through a hard-sphere interaction rule f_{lj}, causing overlapping agents to shift in the direction of their distance vector equally until a distance of $2\,r_{\text{p}}$ is restored. Further, agents exhibit polar alignment with neighboring agents within an interaction radius of $r_c = 4\,r_{\text{p}}$. We assume a stochastic reorientation of individual agents by adding a zero-mean Gaussian white noise with amplitude ξ_l to the dynamics of the orientation angle. For the direct agent-agent interactions, neighborhoods are tracked using regular linked cell lists with periodic wrapping. To implement the acoustic interactions between swarmers, we compute the instantaneous quasi-stationary acoustic field in Fourier space as detailed in section 5.2.1. Each agent contributes as a source according to its real unbinned position with its current oscillator state a_l, extended as a Gaussian contribution with width $\sigma = 2\,r_{\text{p}}$. Namely, the source contribution of agents to the acoustic field is modeled as

$$w(\boldsymbol{r}) = \exp\left\{-\boldsymbol{r}^2/2\sigma\right\}\,, \quad \text{with } \sigma = 2\,r_{\text{p}}\,. \tag{5.31}$$

Depending on the size of the studied system, we resolve the acoustic field with 128 up to 512 Fourier modes per spatial direction. Derivatives of the acoustic field amplitudes with which the swarmers align their direction of self-propagation are computed in Fourier space. If not stated otherwise, the swarmers are initially uniformly distributed in the two-dimensional domain, avoiding overlaps between swarmers when drawing random positions. Their orientation angles are picked from a uniform distribution, $\varphi_l \in [0, 2\pi]$ and oscillatory states are set to the stable amplitude $|a| = 1$ with uniformly distributed phases $[0, 2\pi]$.

Parameter	Description	Fig. 5.2	Fig. 5.6(a)	Fig. 5.6(b)	Fig. 5.7(a)	Fig. 5.7(b)	Fig. 5.7(c)	Fig. 5.7(d)
v_0	agent velocity	various	0.1	0.1	0.2	0.1	0.2	0.1
D_R	angular noise	0.02	0.02	0.01	0.01	0.02	0.01	0.01
r_p	particle radius	0.25						
r_c	interaction radius	$4\,r_\mathrm{p}$						
Γ	polar alignment factor	0.1	0.1	0.2	0.2	0.1	0.2	0.2
Ξ	sound susceptibility	various	0.05	0.1	0.01	0.05	0.2	0.05
ω	free oscillator frequency	0.5	0.1	0.5	0.5	0.1	0.5	0.5
b	nonlinear frequency coupling	0.5	0.05	0.05	0.5	0.05	0.05	0.05
λ	acoustic coupling	0.1	0.1	0.02	0.00001	0.1	0.01	0.1
c	sound speed	20	5	50	50	50	50	50

Table 5.1: Parameters used for the agent-based model, Eqs. (5.1).

CONTINUUM FIELD EQUATIONS

In this appendix section, we give details on the numerical solution of the continuum field model for acoustic active matter, Eqs. (5.3). We consider the equations on a 2D square domain, $\boldsymbol{r} = (x, y)^T \in [0, L] \times [0, L]$. The pressure-like contribution to the polar field dynamics

$$P'(\rho) = \exp\left(-32\rho\right) + \exp\left(16(\rho - 2)\right) \,, \tag{5.32}$$

implements the minimal and maximal agent densities at the values zero and two, respectively. We numerically solve the equations for the swarmer density $\rho(\boldsymbol{r}, t)$, oscillator state $a(\boldsymbol{r}, t)$, and polar orientation $\boldsymbol{p}(\boldsymbol{r}, t)$ in Fourier space by applying pseudo-spectral methods with typical resolutions of 256 to 8192 modes per dimension, depending on system size. The critical computations and particularly the fast Fourier transform are parallelized running on the GPU using CUDA. We implement differential operators using their respective Fourier kernels, and nonlinearities in the dynamics are computed in real space. The temporal integration is implemented using exponential time differencing (ETD2), realizing a semi-implicit solving of the linear contributions to the dynamics. As for the agent-based simulations, we employ the stationary solutions for the acoustic field u, Eq. (5.2), with continuous sources $g(\boldsymbol{r}, t) = \rho(\boldsymbol{r}, t)\, a(\boldsymbol{r}, t)$. The system is typically initialized with a homogeneous density of 0.6, well below the isotropic to polar order transition at $\rho = 1$, perturbed with a zero-mean Gaussian white noise of small amplitude. We initialize the polar order field as well as the swarmer's complex oscillatory state with zero-mean Gaussian white noise around vanishing values.

5.6.4 MODEL PARAMETERS

The system parameters used for the numerical simulations of the agent-based model, Eq. (5.1) are given in Table 5.1. For the numerical simulations of the continuous field equations, Eqs. (5.3), we used the parameter values detailed in Table 5.2.

Parameter	Description	Fig. 5.3	Fig. 5.4	Fig. 5.5	Fig. 5.8
v_0	agent velocity	various	0.02 (a), 0.1 (b)	0.04	0
μ	density diffusion	0.05	0.05 (a), 0.02 (b)	0.02	0
σ	polar order transition factor	1	1	1	n.a.
δ	polar order magnitude parameter	1	1	1	n.a.
κ	polar elasticity	0.05	0.05	0.05	n.a.
χ	polar self-advection	0.05	0.05	0.05	n.a.
Ξ	sound susceptibility	various	5000 (a), 100 (b)	100	n.a.
ω	oscillation frequency	0.5	0.5	0.5	0.5
b	nonlinear frequency coupling	0.05	0.05	0.05	0.05
λ	acoustic coupling	1 (a), 0.001 (b)	1000 (a), 0.001 (b)	1	various
c	sound speed	50	50 (a), 20 (b)	50	50

Table 5.2: Parameters used for numerical simulations of the continuous field equations, Eqs. (5.3).

6

Conclusion

In this thesis, we explored two different classes of systems in which non-local interactions play a crucial role in facilitating self-organization and creating emergent, structured behavior. The first part was concerned with protein demixing and pattern formation in static and dynamic geometries, as discussed in Chapters 2 and 3, respectively. The second part, Chapters 4 and 5, focused on self-propelled active matter, where long-range communication between active agents enables collective dynamics.

In Chapter 2, we analyzed protein pattern dynamics in fixed geometries. Here, spatial variations of the confinement break translational invariance, introducing spatially heterogeneous conditions on the enclosed reaction-diffusion dynamics. The behavior of individual proteins is determined by their immediate surroundings and sampling an entire geometry would take a long time for single proteins. However, as a collective effect, protein patterns can almost immediately 'sense' geometric properties such as bulk-to-boundary ratios and the spatial confinement through reactive surface interactions and concentration gradients. The spatial heterogeneity imposed by the geometric deformation rather provides static spatial information than a dynamic non-local coupling. Nevertheless, this system yields interesting findings on its own and it could be extended to mechano-chemically coupled systems involving non-local geometric coupling. Here, Chapter 2 sets the stage for the study of dynamically modulated membrane surfaces discussed in Chapter 3. For this system, we observed that the dynamic interplay between phase separation of proteins and protein density-dependent membrane deformations directly induces an effective mechanical non-local coupling between the protein density patterns.

The second class of systems discussed in this thesis, self-propelled active matter, was addressed in Chapters 4 and 5, where we investigated the fundamental role of long-range communication in enabling emergent collective behaviors. Similar to isolated proteins, individual agents have only access to local information of the system and collecting information on the larger scales would require a significant amount of sampling, and becomes unfeasible given large system sizes or dynamic changes of the environment. However, as a collective, the active agents can communicate information about states of the system at different positions and thereby develop distinct collective behavior. The nature of this communication is a central theme in these chapters. In Chapter 4, we focused on chemical communication as a mechanism for self-organization within active matter. Chemical signaling allows agents to collectively coordinate their behaviors and develop organized spatial patterns. Moving beyond self-organization, Chapter 5 explored how acoustic coupling enables active agents to respond collectively to external stimuli. Implementing this mode of communication, we observed the emergence of collective functionality such as collective perception and cooperative behavioral adaptation, highlighting the rich dynamics that can arise through non-local interactions.

6.1 GEOMETRIC EFFECTS ON PROTEIN PATTERN FORMATION

GEOMETRY-INDUCED PATTERN SELECTION

Summary In Chapter 2, we developed a minimal framework to study the effects of spatially modulated confinements on protein pattern formation in systems with bulk-boundary coupling. To analyze the behavior of such systems, we assumed a deformed tubular geometry and derived an effective one-dimensional equation by dimensional reduction. The dimensionally reduced equations incorporate the geometric effects such as the spatially varying bulk volume and the surface area via effective advective terms.

Geometric modulations break the system's translational symmetry, leading to spatial variations in local bulk-to-boundary ratios and effective reactive rates. Using the reduced equation, we performed a perturbative linear stability analysis, treating geometric deformations as weak deviations from the dynamics in an undeformed tube. Our study analytically predicts the geometrically controlled wavelength and localization of the emergent patterns. The predictions align very well with the results of full three-dimensional numerical simulations.

Additionally, we investigated the long-term dynamics of a two-component mass-conserving reaction-diffusion system[24,25]. Considering the dynamics within an undeformed tube, we observed

coarsening behavior in which diffusive mass flux increases the mass in larger high-density domains at the expense of smaller ones. The pattern length scale increases successively until a single high-density domain survives. However, we show that in spatially modulated geometries, deformations can interrupt this coarsening process. The strength of coarsening decreases with increasing distance between high-density plateaus, while the system's tendency for interface minimization depends only on local interactions between the solution and the geometric modulation. Using our analysis, we identified a critical deformation strength at which these competing effects balance, halting coarsening and thereby controlling the final pattern length scale.

Discussion In this study, we identified spatially varying bulk-boundary ratios and locally available mass as key factors driving geometrically induced pattern formation in bulk-boundary systems. The system's tendency to minimize interfaces emerges as the primary mechanism behind pattern motion in spatially varying geometries. Notably, this diffusive interface minimization can counteract mass transfer during coarsening dynamics, particularly when changes in the mass of localized solutions, such as mesas, require adjustments of interface lengths. The study of geometrically interrupted coarsening in the reduced system presented here provides valuable insights into the broader principles underlying the interaction between geometry and interface dynamics. Overall, we demonstrate that spatially modulated confinements can control pattern length scales and arrest coarsening, offering a geometric means of regulating emergent patterns in reaction-diffusion systems.

Building on our study of static tubular geometries, future work could explore dynamic confinements, such as dynamic surface deformations governed by the Canham-Helfrich free energy, as demonstrated in Chapter 3 for a two-dimensional membrane manifold. Extending the current framework in this direction would enable investigations of minimal models for mechano-chemically coupled bulk-boundary systems. Even in the absence of dynamic modulations, the interplay between interface minimization and geometric modulation gives rise to non-trivial motion and pattern localization. Introducing an energetic contribution from an enclosing elastic membrane could further generate intricate feedback mechanisms. This extended framework could serve as a minimal setting to study processes relevant to cellular organization and experimental systems, like Min-protein-enclosing vesicles, which exhibit a beating behavior driven by enclosed Min protein oscillations[231]. Such investigations may provide valuable insights into pattern localization and the mechanisms underlying length scale selection in biological systems, including cellular patterning.

Furthermore, incorporating flow contributions resulting from membrane contractions could address phenomena observed in various biological systems, such as the vein network of *Physarum polycephalum*[240]. These flows can facilitate rapid bulk transport of species, significantly influencing pattern formation. For instance, in a minimal two-component mass-conserving reaction-diffusion system, it has been shown that a constant flow in planar geometries can induce pattern formation and cause patterns to move against the flow direction[52]. Exploring such effects in an interplay with dynamic membrane contractions presents an intriguing research question.

For all these proposed extensions, the reduced description presented here could be applied, along with perturbative approaches, to gain analytical insights into the underlying mechanisms. Additionally, when the system permits a one-dimensional reduction, the derived dimensionally reduced equations also provide an efficient basis for numerical simulations. This may be particularly advantageous compared to solving full three-dimensional bulk-boundary reaction-diffusion system, especially in scenarios involving dynamic variations of the enclosing surface.

MECHANICALLY COUPLED PROTEIN PATTERNS

Summary In Chapter 3, we studied the mechanical coupling between proteins embedded in a dynamic membrane surface. In our model system, proteins are assumed to exhibit Flory-Huggins phase-separation dynamics, allowing them to demix. In the presented setting, the proteins interact with membrane dynamics by inducing a spontaneous curvature which is incorporated in form of a Canham-Helfrich term in an effective free energy.

A linear stability analysis of the fully mixed state, complemented by numerical simulations, revealed a transition in the type of instability exhibited by the system. Specifically, the system transitions from an unbounded Cahn-Hilliard-type instability to a finite-wavelength, conserved Turing instability. Our results demonstrate that the mechanical coupling of protein densities via membrane deformations yields an effective surface tension, which quantifies the energetic cost associated with unfavorable protein concentrations during expansions or contractions of the local membrane surface area.

For intermediate ranges of the protein-induced spontaneous curvature, we observed the emergence of a finite pattern wavelength in the system's long-term dynamics. To investigate this arrested coarsening behavior, we analyzed the effective free energy and expanded it to quadratic order in both the membrane height and protein density fields. This approach led to an effective equation incorporating a non-local coupling term, which represents the influence of membrane deformations on protein densities. The resulting non-local coupling introduces a characteristic length scale into the system, thereby interrupting coarsening dynamics. Based on this analysis, we derived an expression for the length scale selected by the geometric interactions which we validated by numerical simulations.

Discussion Altogether, we find that the effective mechanical coupling through membrane deformations leads to a pattern wavelength selection, that depends on the mechanical properties of the membrane and the protein-induced curvature.

Interactions between phase-separating proteins that are mediated by deformations of membranes can serve as a minimal setting for the formation of patters with distinct length scales. Remarkably, the geometric regulation of length scales is possible even in such minimal systems that relax to thermodynamic equilibrium. In cellular contexts, these fundamental mechanisms are likely to occur but may be further influenced by active processes, such as active protein reactions or active transport[71,73]. Therefore, combining protein-induced membrane deformations with active reactions represents a promising approach to explore the effects of deformation-mediated mechanical coupling in (weakly) actively driven systems.

Certain proteins, such as BAR domains, exhibit anisotropic shapes, which can induce anisotropic deformations in the membrane surfaces to which they are bound[227,276]. These anisotropic membrane deformations may, in turn, promote deformation-mediated nematic alignment of proteins, thereby potentially amplifying the induced membrane deformations[396,397]. A deeper understanding of these systems could provide valuable insights into processes such as FtsZ ring formation at cellular division sites and related biological phenomena[398–400].

PERSPECTIVES

The presented discussion of coupled phase-separation or reaction-diffusion dynamics with fixed and dynamic geometric confinements reveals the intricate feedback between mechanical aspects of the geometry and biochemical pattern formation. Our findings show that the behavior of pattern forming systems can be effectively controlled by geometric cues as spatial deformations significantly influence pattern length scales and dynamics. As a result, we have seen that for dynamic geometries, a mutual feedback emerges: protein patterns can induce deformations in the system's geometry. Thereby the patterns remodel the domain they are confined in and consequently adapt to these changes. For instance, in lipid vesicle-enclosed MinDE protein systems, protein-induced membrane curvature leads to substantial shape changes of the enclosing vesicles[231]. Similarly, in starfish oocytes, protein-induced control of actin cytoskeleton contractions generates surface contraction waves that organize meiotic cell division through dynamic feedback between protein patterns and deformations[5,52]. For such experimental systems one could imagine a scenario in which a dynamic geometric confinement interacts with the embedded protein reaction network. Multiple of these mechano-chemically interacting units could then interact mechanically with each other by exerting deforming forces on their neighbors and thereby effecting their internal protein pattern dynamics. This would allow for a mechanical communication between the units mediated through deformations. It is reminiscent

of the mechano-sensitive behavior of cells in tissues which diversify also on the basis of mechanical cues and interactions[401,402].

Beyond these exemplary systems, the interplay between patterns and geometry represents a fundamental mechanism in biological organization. Developing a mechanistic understanding of this feedback is essential for unraveling the complexity of cellular systems and for exploring key design principles for constructing artificial cells.

6.2 TOWARDS FUNCTIONAL ACTIVE MATTER

CHEMICAL ACTIVE MATTER

Summary In our study on chemically communicating active matter, Chapter 4, we developed a model of self-propelled, chemotactic active agents equipped with an excitable internal state. When these agents detect chemical signals, they can either amplify and relay the signals by emitting additional signaling molecules or remain inactive. This non-linear relaying mechanism implements a minimal form of signal processing. Despite the fact that the chemical signals only diffuse, the agents' relaying behavior gives rise to trigger wave propagation, enabling relatively rapid signal transport throughout the entire population. The resulting form of non-local communication facilitates the system's self-organization into various collective dynamic states, each characterized by distinct behavioral properties.

These states play specific roles within the hierarchical self-organization process: At the first level, through local chemical interactions, the agents form smaller active droplets exhibiting collective motion. These droplets subsequently aggregate into few vortex state, localized structures that continuously emit chemical signals via internal spiral wave activity. The vortices thereby act as self-organized aggregation centers. The emitted signals from these centers organize further aggregation as active droplets merge into directed streams, converging toward a central vortex. This mechanism results in a remarkably rapid aggregation process, enabled by the long-range communication.

To quantify the emergent order within the system, we analyzed the information content associated with the different states observed throughout the aggregation process. We established a qualitative link between the system's organization, changes in information content, and the agents' signal processing capabilities. Through this analysis, we identified the individual agents' processing of the chemical signals as the fundamental driving mechanism behind the observed self-organization.

Discussion Communicating active matter represents a novel class of systems where the internal degrees of freedom of active agents enable complex, non-trivial interactions between individual units. Our analysis of a chemically interacting system reveals that such a communication yields relaying of signals through agents functioning as excitable nodes. This results in a trigger wave propagation of signals with amplitudes and velocities persistent over large distances. For effective communication, it is crucial that local information is either spread across space or retained over time, allowing agents to acquire collective information. For example, an established chemical field can act as a form of collective memory.

To access this shared pool of information, the agents could directly change their self-propulsion behavior in response to the measured chemical field, such as by chemotactic alignment. In our model, however, also the agents' internal states are coupled to the chemical field. This coupling enables non-trivial communication and is essential for achieving long-range signal transport.

The observed self-organization capabilities of this system surpass those seen in purely chemotactic models, such as the renowned Keller-Segel model[167] or in synthetic experimental systems like chemotactic Janus particles sensing fuel gradients[376]. Introducing internal degrees of freedom to synthetic systems could therefore unlock new behaviors. For instance, internal chemical reactions could be implemented in a system of active droplets enclosing Belousov-Zhabotinsky reaction[403] or Min protein enclosing vesicles[231]. These systems could then implement long-range chemical signaling serving as a communication strategy between the individual units. Such strategies hold promise for artificial systems requiring efficient long-range coupling and coordination.

The aggregation process studied in Chapter 4 bears a strong resemblance to the behavior observed in *Dictyostelium discoideum*, where cyclic AMP serves as a signaling molecule to organize aggregation[43,45]. This parallel suggests that the biological system may have gained an evolutionary advantage by employing a similar chemical communication technique to spread signals effectively over large distances.

Beyond this specific biological context, our study highlights the critical role of communication in facilitating self-organization among active agents. We demonstrate how the emergent order in the system arises from the signal-processing capabilities of individual agents. These findings, along with the identified minimal motifs for communicating active matter, have broad implications for synthetic systems and provide insights into the functioning of chemically communicating biological systems. This may prove particularly significant for the development of functional active matter.

ACOUSTICALLY COUPLED ACTIVE MATTER

Summary In Chapter 5, we introduced a model for acoustic active matter composed of self-propelled agents capable of acoustic signaling. Each agent possesses an internal oscillatory degree of freedom, periodically emitting acoustic waves into its environment. These acoustic signals, in turn, serve as inputs that feed back into the agents' internal oscillators, creating a coupling mechanism dependent on the agents' positions within the collectively established acoustic field. Through this position-dependent acoustic coupling, the agents form a motile network of oscillators that can synchronize both their spatial positioning and oscillatory states.

Using numerical simulations of an agent-based model and phenomenological hydrodynamic field equations, we observed a range of emergent collective states. These include localized, fully synchronized 'blob' solutions; slowly propagating 'larvae', exhibiting enclosed target patterns of oscillations; and rapidly moving 'snakes' that feature phase waves propagating from head to tail through the structure. Each of these states displays distinct synchronization patterns, leading to the emission of characteristic acoustic signals that convey information about the structure's state and location. These emitted signals enable the structures to communicate collectively and interact dynamically with their environment.

Thus, the acoustic interactions not only enhance the ability of a few agents to self-organize and aggregate into coherent collectives but also facilitate a form of collective communication that results in emergent functionality. For example, we observed inter-cluster communication, whereby clusters maintain a stable distance from each other through their acoustic signaling. Within the collective structures, identical agents differentiate their behavior by adapting their internal oscillators in response to inputs from the collective acoustic field. This self-organized differentiation produces phenotypic states that are highly robust to perturbations. Following strong disturbances, the structures exhibit remarkable resilience, rearranging their internal order to recover their phenotypic organization. Moreover, the collective dynamics are not limited to emitting waves but also include responses to incoming acoustic signals. For instance, aggregates demonstrated a collective response to waves reflected from passive objects, undergoing significant changes in phenotype such as induce localization of a propagating solution or dispersal of agents from an aggregate into the surrounding environment.

Finally, we explored the controllability of the system through external acoustic inputs. By applying external stimuli, we effectively guided the spatial positioning of aggregates, demonstrating the potential for external control over the collective behavior.

Discussion In this work, we presented a model for acoustic interactions in active matter systems. The physical coupling by acoustic signals enables agents to communicate over large distances, even across regions only sparsely populated with agents. In contrast to the chemical communication studied in Chapter 4 which requires signal relaying already over comparably short distances, acoustic signals typically allow for much larger communication ranges.

A key feature of communicating active matter lies in an additional internal degree of freedom that is not directly tied to the agent's self-propulsion. This freedom enables emergent properties within

the collective that do not fully result from their propulsion behavior alone.

Considering technical implementations of active matter in the field of robotics, acoustic or electromagnetic wave-like communication may have broader applicability compared to chemical diffusion, which can be heavily influenced by flows and turbulence within the medium or other environmental factors. This is particularly relevant for underwater swarm robotics, where acoustic interactions promise significant advantages[404]. Establishing functional active matter systems and artificial swarms is an open field in robotics, highlighting the importance of understanding the underlying mechanisms behind acoustic coupling for designing such systems.

Future studies could explore behavioral switches in agents driven by their internal states, or investigate interactions between multiple agent populations, gradually increasing system complexity. Tasks such as cargo pick up and transport could be implemented by detection through a collective sonar functionality and propagation towards an acoustic beacon identifying a target position for drop off. Clearly, for real-world applications, self-organization capabilities and interaction rules will need to have significantly greater complexity than presented in this initial study. We rather provide a starting point focusing on key ingredients in communicating active matter that already lead to emergent functionality.

In particular, we identified key advantages of acoustic communication, such as the ability of agents to synchronize and communicate effectively over long distances. We further showed that collectives can develop a form of cooperative sonar, where agents emit acoustic waves, collectively perceive reflections, and adapt their collective behavior in response to the reflected signals.

For unsupervised functional active matter, relying on self-organized behavior represents a promising approach. If desired behaviors emerge naturally from simple interaction rules, they can arise reliably, independent of external supervision. In Chapter 5, we presented a first exploration of how unsupervised self-organization can be realized in acoustically active matter systems.

PERSPECTIVE

After decades of theoretical, numerical, and experimental research on the self-organization of active matter systems, increasing attention is being directed toward practical applications that make use of the collective behavior of active matter. Promising areas of application include medical technologies[405] and environmental monitoring tasks[406]. Rapid advancements are also occurring in the development of technological implementations, particularly in the field of artificial robotic swarms[407–409], with a focus on establishing systems for tasks such as artificial pollination[410,411] or active monitoring[412].

To fully unlock the potential of active matter systems in practical applications, it is essential to make use of their collective effects. For instance, these effects could be realized through collective structure formation or by enabling the spread and exchange of information over large distances among numerous agents in a collective. For such applications, the systems could rely on cooperative functionalities that are self-organized and emerge from principle behavioral rules. This may be particularly beneficial for scenarios involving small robots or agents, which are often constrained by limited memory and processing power. In such cases, collective signal and information processing becomes critical, as in the absence of external supervision and control of each individual units, the system must respond self-organized as a unified whole. Another key advantage of self-organized systems lies in their ability to adapt dynamically to environmental changes and to compensate for agent failure. This adaptability arises through the self-organized specification of agents within the collective which is a fundamental mechanism in emergent behavior. Even though agents may be identical, they can take on different roles within the system. This self-organization ensures that the collective remains functional, resilient, and capable of fulfilling tasks even when direct control or supervision is unfeasible.

Our studies represent a step toward understanding emergent collective behavior, particularly the processes underlying collective decision-making and the emergence of cooperative perception. To develop functional active matter systems capable of performing real-world tasks, such as those outlined above, it is clear that more sophisticated behavioral routines and interaction mechanisms will be required.

6.2.1 CLOSING

Overall, this thesis demonstrates how non-local interactions, whether mediated through geometric deformations or by means of communication, are essential drivers of self-organization and emergent behavior in both biological and general active matter systems. Our findings reveal principles of collective dynamics and offer insights into the mechanisms by which systems ranging from proteins to active agents, overcome local information constraints to exhibit complex, coordinated behaviors at larger scales.

We discussed relevant subjects such as the impact of geometric deformations and mechanical coupling on confined pattern-forming systems which is applicable to cellular organization processes and biological structure formation. We studied the role of long-range communication for collectives of active agents by which they gain access to information about distant positions and can collectively organize. These insights address general questions surrounding collective perception, the emergence of shared decision-making, and the development of cooperative functionalities. Importantly, our study of elementary communication mechanisms also has potential implications for technological applications, such as the design of unsupervised robotic swarms. Our work points toward a future 'cybernetics of active matter', where emergent cooperativity serves as the foundation for collective functionality.

By connecting ideas from biology and physics, this thesis provides a deeper understanding of self-organizing systems and yields principles and potential concepts for bio-inspired technologies and adaptive active materials. Moving forward, further exploring the balance between local and non-local interactions could help address challenges in areas such as synthetic biology, swarm robotics, and material science. Ultimately, this work contributes to the broader vision of harnessing emergent behaviors to design systems capable of robust, adaptable, and intelligent collective dynamics

BIBLIOGRAPHY

[1] Alexander Ziepke, Michael Reichert, Luca Stadtmüller, and Erwin Frey. Geometric control of protein pattern formation in bulk-boundary systems. in preparation.

[2] Antonia Winter, Yuhao Liu, Alexander Ziepke, George Dadunashvili, and Erwin Frey. Phase Separation on Deformable Membranes: interplay of mechanical coupling and dynamic surface geometry. *arXiv*, 2024, 2409.16049.

[3] Alexander Ziepke, Ivan Maryshev, Igor S Aranson, and Erwin Frey. Multi-scale organization in communicating active matter. *Nature Communications*, 13(1):6727, 2022.

[4] Alexander Ziepke, Ivan Maryshev, Igor S Aranson, and Erwin Frey. Acoustic signaling enables collective perception and control in active matter systems. *arXiv*, 2024, 2410.02940.

[5] Jinghui Liu, Tom Burkart, Alexander Ziepke, John Reinhard, Yu-Chen Chao, Tzer Han Tan, S Zachary Swartz, Erwin Frey, and Nikta Fakhri. Light-induced cortical excitability reveals programmable shape dynamics in starfish oocytes. *arXiv*, 2024, 2409.08651.

[6] Martin Howard, Andrew D. Rutenberg, and Simon de Vet. Dynamic Compartmentalization of Bacteria: Accurate Division in E. Coli. *Physical Review Letters*, 87(27):278102, 2001.

[7] Hans Meinhardt and Piet A. J. de Boer. Pattern formation in Escherichia coli: A model for the pole-to-pole oscillations of Min proteins and the localization of the division site. *Proceedings of the National Academy of Science*, 98(25):14202–14207, 2001.

[8] Tom Burkart, Manon C. Wigbers, Laeschkir Würthner, and Erwin Frey. Control of protein-based pattern formation via guiding cues. *Nature Reviews Physics*, 4(8):511–527, 2022.

[9] A. J. Koch and H. Meinhardt. Biological pattern formation: from basic mechanisms to complex structures. *Reviews of Modern Physics*, 66(4):1481–1507, 1994.

[10] Victor Hatini and Stephen DiNardo. Divide and conquer: pattern formation in Drosophila embryonic epidermis. *Trends in Genetics*, 17(10):574–579, 2001.

[11] Karsten Kruse and Frank Jülicher. Oscillations in cell biology. *Current Opinion in Cell Biology*, 17(1):20–26, 2005.

[12] Manon C. Wigbers, Fridtjof Brauns, Tobias Hermann, and Erwin Frey. Pattern localization to a domain edge. *Physical Review E*, 101(2):022414, 2020, 1908.07309.

[13] Noo Li Jeon, Stephan K. W. Dertinger, Daniel T. Chiu, Insung S. Choi, Abraham D. Stroock, and George M. Whitesides. Generation of Solution and Surface Gradients Using Microfluidic Systems. *Langmuir*, 16(22):8311–8316, 2000.

[14] Jörg Lahann, Mercedes Balcells, Hang Lu, Teresa Rodon, Klavs F. Jensen, and Robert Langer. Reactive Polymer Coatings: A First Step toward Surface Engineering of Microfluidic Devices. *Analytical Chemistry*, 75(9):2117–2122, 2003.

[15] Thomas Gervais and Klavs F. Jensen. Mass transport and surface reactions in microfluidic systems. *Chemical Engineering Science*, 61(4):1102–1121, 2006.

[16] Joseph D. Kirtland, Gregory J. McGraw, and Abraham D. Stroock. Mass transfer to reactive boundaries from steady three-dimensional flows in microchannels. *Physics of Fluids*, 18(7):073602, 2006.

[17] Dominik Thalmeier, Jacob Halatek, and Erwin Frey. Geometry-induced protein pattern formation. *Proceedings of the National Academy of Sciences*, 113(3):548–553, 2016.

[18] Raphaela Geßele, Jacob Halatek, Laeschkir Würthner, and Erwin Frey. Geometric cues stabilise long-axis polarisation of PAR protein patterns in C. elegans. *Nature Communications*, 11(1):539, 2020.

[19] Jakob Schweizer, Martin Loose, Mike Bonny, Karsten Kruse, Ingolf Mönch, and Petra Schwille. Geometry sensing by self-organized protein patterns. *Proceedings of the National Academy of Sciences*, 109(38):15283–15288, 2012.

[20] Katja Zieske and Petra Schwille. Reconstitution of Pole-to-Pole Oscillations of Min Proteins in Microengineered Polydimethylsiloxane Compartments. *Angewandte Chemie International Edition*, 52(1):459–462, 2013.

[21] Katja Zieske and Petra Schwille. Reconstitution of self-organizing protein gradients as spatial cues in cell-free systems. *eLife*, 3:e03949, 2014.

[22] G. Chacón-Acosta, M. Núñez-López, and I. Pineda. Turing instability conditions in confined systems with an effective position-dependent diffusion coefficient. *The Journal of Chemical Physics*, 152(2):024101, 2020.

[23] John R. Frank, Jemal Guven, Mehran Kardar, and Henry Shackleton. Pinning of diffusional patterns by non-uniform curvature. *EPL*, 127(4):48001, 2019, 1901.09900.

[24] Fridtjof Brauns, Henrik Weyer, Jacob Halatek, Junghoon Yoon, and Erwin Frey. Wavelength Selection by Interrupted Coarsening in Reaction-Diffusion Systems. *Physical Review Letters*, 126(10):104101, 2021, 2005.01495.

[25] Henrik Weyer, Fridtjof Brauns, and Erwin Frey. Coarsening and wavelength selection far from equilibrium: A unifying framework based on singular perturbation theory. *Physical Review E*, 108(6):064202, 2023, 2203.03892.

[26] Clifford P. Brangwynne, Christian R. Eckmann, David S. Courson, Agata Rybarska, Carsten Hoege, Jöbin Gharakhani, Frank Jülicher, and Anthony A. Hyman. Germline P Granules Are Liquid Droplets That Localize by Controlled Dissolution/Condensation. *Science*, 324(5935):1729–1732, 2009.

[27] Anthony A. Hyman, Christoph A. Weber, and Frank Jülicher. Liquid-Liquid Phase Separation in Biology. *Annual Review of Cell and Developmental Biology*, 30(1):39–58, 2014.

[28] Karin John and Markus Bär. Travelling lipid domains in a dynamic model for protein-induced pattern formation in biomembranes. *Physical Biology*, 2(2):123, 2005.

[29] Sarah L. Veatch and Sarah L. Keller. Separation of Liquid Phases in Giant Vesicles of Ternary Mixtures of Phospholipids and Cholesterol. *Biophysical Journal*, 85(5):3074–3083, 2003.

[30] Jay T. Groves. Bending Mechanics and Molecular Organization in Biological Membranes. *Physical Chemistry*, 58(1):697–717, 2007.

[31] Sergio Alonso and Markus Bär. Phase separation and bistability in a three-dimensional model for protein domain formation at biomembranes. *Physical Biology*, 7(4):046012, 2010.

[32] Michael Heinrich, Aiwei Tian, Cinzia Esposito, and Tobias Baumgart. Dynamic sorting of lipids and proteins in membrane tubes with a moving phase boundary. *Proceedings of the National Academy of Sciences*, 107(16):7208–7213, 2010.

[33] Sarah A. Shelby, Ivan Castello-Serrano, Kathleen C. Wisser, Ilya Levental, and Sarah L. Veatch. Membrane phase separation drives responsive assembly of receptor signaling domains. *Nature Chemical Biology*, 19(6):750–758, 2023.

[34] Qiwei Yu and Andrej Košmrlj. Pattern formation of phase-separated lipid domains in bilayer membranes. *arXiv*, 2023, 2309.05160.

[35] Arijit Mahapatra, David Saintillan, and Padmini Rangamani. Curvature-driven feedback on aggregation–diffusion of proteins in lipid bilayers. *Soft Matter*, 17(36):8373–8386, 2021.

[36] M. C. Cross and P. C. Hohenberg. Pattern formation outside of equilibrium. *Reviews of Modern Physics*, 65(3):851–1112, 1993.

[37] Tobias Frohoff-Hülsmann and Uwe Thiele. Nonreciprocal Cahn-Hilliard Model Emerges as a Universal Amplitude Equation. *Physical Review Letters*, 131(10):107201, 2023.

[38] D E Ingber. The mechanochemical basis of cell and tissue regulation. *Mechanics & chemistry of biosystems : MCB*, 1(1):53–68, 2004.

[39] Mingxing Lei, Hans I-Chen Harn, Qiwei Li, Jingwei Jiang, Wang Wu, Wei Zhou, Tin-Xin Jiang, Mengyue Wang, Jinwei Zhang, Yung-Chih Lai, Wen-Tau Juan, Randall Bruce Widelitz, Li Yang, Zhong-Ze Gu, and Cheng-Ming Chuong. The mechano-chemical circuit drives skin organoid self-organization. *Proceedings of the National Academy of Sciences*, 120(36):e2221982120, 2023.

[40] Gholson J Lyon and Tom W Muir. Chemical Signaling among Bacteria and Its Inhibition. *Chemistry & Biology*, 10(11):1007–1021, 2003.

[41] Michiko E. Taga and Bonnie L. Bassler. Chemical communication among bacteria. *P Natl Acad Sci*, 100:14549–14554, 2003.

[42] Tomer J. Czaczkes, Christoph Grüter, and Francis L.W. Ratnieks. Trail Pheromones: An Integrative View of Their Role in Colony Organization. *Annual Review of Entomology*, 60(1):1–19, 2015.

[43] D. Dormann, B. Vasiev, and C. J. Weijer. Propagating waves control Dictyostelium discoideum morphogenesis. *Biophysical Chemistry*, 72(1-2):21–35, 1998.

[44] Richard H. Kessin. Dictyostelium: Evolution, Cell Biology, and the Development of Multicellularity. *Developmental and Cell Biology Series*, 38, 2001.

[45] G. Singer, T. Araki, and C. J. Weijer. Oscillatory cAMP cell-cell signalling persists during multicellular Dictyostelium development. *Communications Biology*, 2:139, 2019.

[46] P. W. Anderson. More Is Different. *Science*, 177(4047):393–396, 1972.

[47] Steven Strogatz, Sara Walker, Julia M. Yeomans, Corina Tarnita, Elsa Arcaute, Manlio De Domenico, Oriol Artime, and Kwang-Il Goh. Fifty years of 'More is different'. *Nature Reviews Physics*, 4(8):508–510, 2022.

[48] David M. Raskin and Piet A. J. de Boer. MinDE-Dependent Pole-to-Pole Oscillation of Division Inhibitor MinC in Escherichia coli. *Journal of Bacteriology*, 181(20):6419–6424, 1999.

[49] Elizabeth Harry, Leigh Monahan, and Lyndal Thompson. Bacterial Cell Division: The Mechanism and Its Precison. *International Review of Cytology*, 253:27–94, 2006.

[50] Sophie G. Martin and Robert A. Arkowitz. Cell polarization in budding and fission yeasts. *FEMS Microbiology Reviews*, 38(2):228–253, 2014.

[51] Beatrice Ramm, Tamara Heermann, and Petra Schwille. The E. coli MinCDE system in the regulation of protein patterns and gradients. *Cellular and Molecular Life Sciences*, 76(21):4245–4273, 2019.

[52] Manon C. Wigbers, Tzer Han Tan, Fridtjof Brauns, Jinghui Liu, S. Zachary Swartz, Erwin Frey, and Nikta Fakhri. A hierarchy of protein patterns robustly decodes cell shape information. *Nature Physics*, 17(5):578–584, 2021.

[53] M. C. Marchetti, J. F. Joanny, S. Ramaswamy, T. B. Liverpool, J. Prost, Madan Rao, and R.A. Simha. Hydrodynamics of soft active matter. *Reviews of Modern Physics*, 85(3):1143–1189, 2013.

[54] Daniel Needleman and Zvonimir Dogic. Active matter at the interface between materials science and cell biology. *Nature Reviews Materials*, 2(9):17048, 2017.

[55] Igor S Aranson. Bacterial active matter. *Reports on Progress in Physics*, 85(7):076601, 2022.

[56] Mark J. Bowick, Nikta Fakhri, M. Cristina Marchetti, and Sriram Ramaswamy. Symmetry, Thermodynamics, and Topology in Active Matter. *Physical Review X*, 12(1):010501, 2022.

[57] Anthony A Hyman and Eric Karsenti. Morphogenetic Properties of Microtubules and Mitotic Spindle Assembly. *Cell*, 84(3):401–410, 1996.

[58] Christopher B. O'Connell and Alexey L. Khodjakov. Cooperative mechanisms of mitotic spindle formation. *Journal of Cell Science*, 120(10):1717–1722, 2007.

[59] Alex Mogilner and Erin Craig. Towards a quantitative understanding of mitotic spindle assembly and mechanics. *Journal of Cell Science*, 123(20):3435–3445, 2010.

[60] Cornelis J. Weijer. Collective cell migration in development. *Journal of Cell Science*, 122(18):3215–3223, 2009.

[61] Yilin Wu. Collective motion of bacteria in two dimensions. *Quantitative Biology*, 3(4):199–205, 2015.

[62] Charlène Guillot and Thomas Lecuit. Mechanics of Epithelial Tissue Homeostasis and Morphogenesis. *Science*, 340(6137):1185–1189, 2013.

[63] Andreas Buttenschön and Leah Edelstein-Keshet. Bridging from single to collective cell migration: A review of models and links to experiments. *PLoS Computational Biology*, 16(12):e1008411, 2020, 2011.10873.

[64] Masao Doi. *Soft Matter Physics*. Oxford University Press, 2013.

[65] Simon Alberti. Phase separation in biology. *Current Biology*, 27(20):R1097–R1102, 2017.

[66] Brian G. O'Flynn and Tanja Mittag. The role of liquid–liquid phase separation in regulating enzyme activity. *Current Opinion in Cell Biology*, 69:70–79, 2021.

[67] Manoël Prouteau and Robbie Loewith. Regulation of Cellular Metabolism through Phase Separation of Enzymes. *Biomolecules*, 8(4):160, 2018.

[68] Haneul Yoo, Catherine Triandafillou, and D. Allan Drummond. Cellular sensing by phase separation: Using the process, not just the products. *Journal of Biological Chemistry*, 294(18):7151–7159, 2019.

[69] Xing Liu, Xu Liu, Haowei Wang, Zhen Dou, Ke Ruan, Donald L. Hill, Lin Li, Yunyu Shi, and Xuebiao Yao. Phase separation drives decision making in cell division. *Journal of Biological Chemistry*, 295(39):13419–13431, 2020.

[70] P. W. Voorhees. The theory of Ostwald ripening. *Journal of Statistical Physics*, 38(1-2):231–252, 1985.

[71] Frank Jülicher and Christoph A. Weber. Droplet Physics and Intracellular Phase Separation. *Annual Review of Condensed Matter Physics*, 15(1):237–261, 2023.

[72] Daniel S. W. Lee, Chang-Hyun Choi, David W. Sanders, Lien Beckers, Joshua A. Riback, Clifford P. Brangwynne, and Ned S. Wingreen. Size distributions of intracellular condensates reflect competition between coalescence and nucleation. *Nature Physics*, 19(4):586–596, 2023.

[73] Jan Kirschbaum and David Zwicker. Controlling biomolecular condensates via chemical reactions. *Journal of the Royal Society Interface*, 18(179):20210255, 2021, 2103.02921.

[74] David Zwicker. The intertwined physics of active chemical reactions and phase separation. *Current Opinion in Colloid & Interface Science*, 61:101606, 2022, 2202.13646.

[75] Johannes Söding, David Zwicker, Salma Sohrabi-Jahromi, Marc Boehning, and Jan Kirschbaum. Mechanisms for Active Regulation of Biomolecular Condensates. *Trends in Cell Biology*, 30(1):4–14, 2020.

[76] Fong Liu and Nigel Goldenfeld. Dynamics of phase separation in block copolymer melts. *Physical Review A*, 39(9):4805–4810, 1989.

[77] István Lengyel and Irving R Epstein. A chemical approach to designing Turing patterns in reaction-diffusion systems. *Proceedings of the National Academy of Sciences*, 89(9):3977–3979, 1992.

[78] Irving R. Epstein and Kenneth Showalter. Nonlinear Chemical Dynamics: Oscillations, Patterns, and Chaos. *The Journal of Physical Chemistry*, 100(31):13132–13147, 1996.

[79] Shigeru Kondo and Takashi Miura. Reaction-Diffusion Model as a Framework for Understanding Biological Pattern Formation. *Science*, 329(5999):1616–1620, 2010.

[80] J. Halatek, F. Brauns, and E. Frey. Self-organization principles of intracellular pattern formation. *Philosophical Transactions of the Royal Society B: Biological Sciences*, 373(1747):20170107, 2018, 1802.07169.

[81] John J Tyson and Paul C Fife. Target patterns in a realistic model of the Belousov–Zhabotinskii reaction. *The Journal of Chemical Physics*, 73(5):2224–2237, 1980.

[82] Vladimir K Vanag. Waves and patterns in reaction–diffusion systems. Belousov–Zhabotinsky reaction in water-in-oil microemulsions. *Physics-Uspekhi*, 47(9):923–941, 2004.

[83] M. Bär, M. Eiswirth, H. Rotermund, and G. Ertl. Solitary-wave phenomena in an excitable surface reaction. *Physical Review Letters*, 69(6):945–948, 1992.

[84] S Nettesheim, A von Oertzen, H H Rotermund, and G Ertl. Reaction diffusion patterns in the catalytic CO-oxidation on Pt(110): Front propagation and spiral waves. *The Journal of Chemical Physics*, 98(12):9977–9985, 1993.

[85] Irving R. Epstein and Bing Xu. Reaction–diffusion processes at the nano- and microscales. *Nature Nanotechnology*, 11(4):312–319, 2016.

[86] Martin Howard. A Mechanism for Polar Protein Localization in Bacteria. *Journal of Molecular Biology*, 335(2):655–663, 2004.

[87] Leah Edelstein-Keshet, William R. Holmes, Mark Zajac, and Meghan Dutot. From simple to detailed models for cell polarization. *Philosophical Transactions of the Royal Society B: Biological Sciences*, 368(1629):20130003, 2013.

[88] J. Halatek and E. Frey. Rethinking pattern formation in reaction–diffusion systems. *Nature Physics*, 14(5):507–514, 2018.

[89] Alan Mathison Turing. The chemical basis of morphogenesis. *Philosophical Transactions of the Royal Society of London. Series B, Biological Sciences*, 237(641):37–72, 1952.

[90] Rashmi C. Desai and Raymond Kapral. *Dynamics of Self-Organized and Self-Assembled Structures*. Cambridge University Press, Cambridge, 2009.

[91] M. Otsuji, S. Ishihara, C. Co, K. Kaibuchi, A. Mochizuki, and S. Kuroda. A mass conserved reaction-diffusion system captures properties of cell polarity. *PLoS Computational Biology*, 3(6):e108, 2007.

[92] Yoichiro Mori, Alexandra Jilkine, and Leah Edelstein-Keshet. Wave-Pinning and Cell Polarity from a Bistable Reaction-Diffusion System. *Biophysical Journal*, 94(9):3684–3697, 2008.

[93] A. B. Goryachev and A. V. Pokhilko. Dynamics of Cdc42 network embodies a Turing-type mechanism of yeast cell polarity. *FEBS Letters*, 582(10):1437–43, 2008.

[94] Fridtjof Brauns, Jacob Halatek, and Erwin Frey. Phase-Space Geometry of Mass-Conserving Reaction-Diffusion Dynamics. *Physical Review X*, 10(4):041036, 2020, 1812.08684.

[95] Erwin Frey, Jacob Halatek, Simon Kretschmer, and Petra Schwille. Protein Pattern Formation. In P. Bassereau and P. Sens, editors, *Physics of Biological Membranes*, pages 229–260. Springer International Publishing, Cham, 2018.

[96] Tina Freisinger, Ben Klünder, Jared Johnson, Nikola Müller, Garwin Pichler, Gisela Beck, Michael Costanzo, Charles Boone, Richard A. Cerione, Erwin Frey, and Roland Wedlich-Söldner. Establishment of a robust single axis of cell polarity by coupling multiple positive feedback loops. *Nature Communications*, 4(1):1807, 2013.

[97] B. Klünder, T. Freisinger, R. Wedlich-Soldner, and E. Frey. GDI-mediated cell polarization in yeast provides precise spatial and temporal control of Cdc42 signaling. *PLoS Computational Biology*, 9(12):e1003396, 2013.

[98] Martin Loose, Karsten Kruse, and Petra Schwille. Protein Self-Organization: Lessons from the Min System. *Annual Review of Biophysics*, 40(1):315–336, 2011.

[99] J. Denk, S. Kretschmer, J. Halatek, C. Hartl, P. Schwille, and E. Frey. MinE conformational switching confers robustness on self-organized Min protein patterns. *Proceedings of the National Academy of Science*, 115(18):4553–4558, 2018.

[100] Ziyuan Ren, Henrik Weyer, Laeschkir Würthner, Dongyang Li, Cindy Sou, Daniel Villarreal, Erwin Frey, and Suckjoon Jun. Robust and resource-optimal dynamic pattern formation of Min proteins in vivo. *bioRxiv*, 2023. 2023.08.15.553443.

[101] Zonglin Hu and Joe Lutkenhaus. Topological regulation of cell division in Escherichia coli involves rapid pole to pole oscillation of the division inhibitor MinC under the control of MinD and MinE. *Molecular Microbiology*, 34(1):82–90, 1999.

[102] Martin Loose, Elisabeth Fischer-Friedrich, Jonas Ries, Karsten Kruse, and Petra Schwille. Spatial Regulators for Bacterial Cell Division Self-Organize into Surface Waves in Vitro. *Science*, 320(5877):789–792, 2008.

[103] Petra Schwille. Giant Unilamellar Vesicles: From Minimal Membrane Systems to Minimal Cells? In P. Luisi and P. Stano, editors, *The Minimal Cell*, pages 231–253. Springer Netherlands, Dordrecht, 2011.

[104] Thomas Litschel and Petra Schwille. Protein Reconstitution Inside Giant Unilamellar Vesicles. *Annual Review of Biophysics*, 50(1):1–24, 2021.

[105] Haiyang Jia and Petra Schwille. Bottom-up synthetic biology: reconstitution in space and time. *Current Opinion in Biotechnology*, 60:179–187, 2019.

[106] Ariadna Martos, Mercedes Jiménez, Germán Rivas, and Petra Schwille. Towards a bottom-up reconstitution of bacterial cell division. *Trends in Cell Biology*, 22(12):634–643, 2012.

[107] William M. Bement, Marcin Leda, Alison M. Moe, Angela M. Kita, Matthew E. Larson, Adriana E. Golding, Courtney Pfeuti, Kuan-Chung Su, Ann L. Miller, Andrew B. Goryachev, and George von Dassow. Activator–inhibitor coupling between Rho signalling and actin assembly makes the cell cortex an excitable medium. *Nature Cell Biology*, 17(11):1471–1483, 2015.

[108] Johanna Bischof, Christoph A. Brand, Kálmán Somogyi, Imre Májer, Sarah Thome, Masashi Mori, Ulrich S. Schwarz, and Péter Lénárt. A cdk1 gradient guides surface contraction waves in oocytes. *Nature Communications*, 8(1):849, 2017.

[109] Eduardo Moreno and Sergio Alonso. Mass-Conservation Increases Robustness in Stochastic Reaction-Diffusion Models of Cell Crawling. *Frontiers in Physics*, 10:881885, 2022.

[110] W. W. Mullins and R. F. Sekerka. Morphological Stability of a Particle Growing by Diffusion or Heat Flow. *Journal of Applied Physics*, 34(2):323–329, 1963.

[111] W. W. Mullins and R. F. Sekerka. Stability of a Planar Interface During Solidification of a Dilute Binary Alloy. *Journal of Applied Physics*, 35(2):444–451, 1964.

[112] A. Arneodo, J. Elezgaray, J. Pearson, and T. Russo. Instabilities of front patterns in reaction-diffusion systems. *Physica D: Nonlinear Phenomena*, 49(1-2):141–160, 1991.

[113] István Lengyel and Irving R Epstein. Diffusion-induced instability in chemically reacting systems: Steady-state multiplicity, oscillation, and chaos. *Chaos: An Interdisciplinary Journal of Nonlinear Science*, 1(1):69–76, 1991.

[114] Wim van Saarloos. Three basic issues concerning interface dynamics in nonequilibrium pattern formation. *Physics Reports*, 301(1-3):9–43, 1998.

[115] Zsuzsanna Nagy-Ungvarai, Janos Ungvarai, Stefan C Müller, and Benno Hess. The role of curvature and pulse width for transition to unstable wave fronts in the Belousov–Zhabotinsky reaction. *The Journal of Chemical Physics*, 97(2):1004–1009, 1992.

[116] Anatol M Zhabotinsky, Milos Dolnik, and Irving R Epstein. Pattern formation arising from wave instability in a simple reaction-diffusion system. *The Journal of Chemical Physics*, 103(23):10306–10314, 1995.

[117] Zs. Nagy-Ungvarai and S.C. Müller. Characterization of Wave Front Instabilities in the Belousov-Zhabotinsky Reaction: An Overview. *International Journal of Bifurcation and Chaos*, 4(05):1257–1264, 1994.

[118] G. Bordyugov and H. Engel. Anomalous pulse interaction in dissipative media. *Chaos*, 18(2):026104, 2008.

[119] Grigory Bordyugov, Nils Fischer, Harald Engel, Niklas Manz, and Oliver Steinbock. Anomalous dispersion in the Belousov–Zhabotinsky reaction: Experiments and modeling. *Physica D: Nonlinear Phenomena*, 239(11):766–775, 2010.

[120] Brent T. Ginn, Bettina Steinbock, Murat Kahveci, and Oliver Steinbock. Microfluidic Systems for the Belousov–Zhabotinsky Reaction. *The Journal of Physical Chemistry A*, 108(8):1325–1332, 2004.

[121] Masanobu Tanaka, Akihiro Isomura, Marcel Hörning, Hiroyuki Kitahata, Konstantin Agladze, and Kenichi Yoshikawa. Unpinning of a spiral wave anchored around a circular obstacle by an external wave train: Common aspects of a chemical reaction and cardiomyocyte tissue. *Chaos: An Interdisciplinary Journal of Nonlinear Science*, 19(4):043114, 2009.

[122] Zsuzsanna Nagy-Ungvarai, Janos Ungvarai, and Stefan C Müller. Complexity in spiral wave dynamics. *Chaos: An Interdisciplinary Journal of Nonlinear Science*, 3(1):15–19, 1993.

[123] P. Politi and C. Misbah. When does coarsening occur in the dynamics of one-dimensional fronts? *Physical Review Letters*, 92(9):090601, 2004.

[124] P. Politi and C. Misbah. Nonlinear dynamics in one dimension: a criterion for coarsening and its temporal law. *Physical Review E*, 73(3):036133, 2006.

[125] T. Kolokolnikov, T. Erneux, and J. Wei. Mesa-type patterns in the one-dimensional Brusselator and their stability. *Physica D: Nonlinear Phenomena*, 214(1):63–77, 2006.

[126] M. Nicoli, C. Misbah, and P. Politi. Coarsening dynamics in one dimension: the phase diffusion equation and its numerical implementation. *Physical Review E*, 87(6):063302, 2013.

[127] Shuichi Jimbo and Yoshihisa Morita. Lyapunov function and spectrum comparison for a reaction–diffusion system with mass conservation. *Journal of Differential Equations*, 255(7):1657–1683, 2013.

[128] Yoshihisa Morita and Toshiyuki Ogawa. Stability and bifurcation of nonconstant solutions to a reaction–diffusion system with conservation of mass. *Nonlinearity*, 23(6):1387–1411, 2010.

[129] Joshua F Robinson, Thomas Machon, and Thomas Speck. Universal limiting behaviour of reaction-diffusion systems with conservation laws. *arXiv*, 2024, 2406.02409.

[130] G. Danker, O. Pierre-Louis, K. Kassner, and C. Misbah. Interrupted coarsening of anisotropic step meander. *Physical Review E*, 68(2):020601, 2003.

[131] Wonhwa Cho and Robert V. Stahelin. Membrane-Protein Interactions in Cell Signaling and Membrane Trafficking. *Annual Review of Biophysics and Biomolecular Structure*, 34(1):119–151, 2005.

[132] Martin Loose, Elisabeth Fischer-Friedrich, Christoph Herold, Karsten Kruse, and Petra Schwille. Min protein patterns emerge from rapid rebinding and membrane interaction of MinE. *Nature Structural & Molecular Biology*, 18(5):577–583, 2011.

[133] Adrián Merino-Salomón, Leon Babl, and Petra Schwille. Self-organized protein patterns: The MinCDE and ParABS systems. *Current Opinion in Cell Biology*, 72:106–115, 2021.

[134] Frédéric Paquin-Lefebvre, Bin Xu, Kelsey L. DiPietro, Alan E. Lindsay, and Alexandra Jilkine. Pattern formation in a coupled membrane-bulk reaction-diffusion model for intracellular polarization and oscillations. *Journal of Theoretical Biology*, 497:110242, 2020.

[135] Kumaran S. Ramamurthi, Sigolene Lecuyer, Howard A. Stone, and Richard Losick. Geometric Cue for Protein Localization in a Bacterium. *Science*, 323(5919):1354–1357, 2009.

[136] Bruno Antonny. Mechanisms of Membrane Curvature Sensing. *Annual Review of Biochemistry*, 80(1):101–123, 2011.

[137] Andriy Goychuk and Erwin Frey. Protein Recruitment through Indirect Mechanochemical Interactions. *Physical Review Letters*, 123(17):178101, 2019.

[138] Brian J. Peter, Helen M. Kent, Ian G. Mills, Yvonne Vallis, P. Jonathan G. Butler, Philip R. Evans, and Harvey T. McMahon. BAR Domains as Sensors of Membrane Curvature: The Amphiphysin BAR Structure. *Science*, 303(5657):495–499, 2004.

[139] Carsten Mim and Vinzenz M. Unger. Membrane curvature and its generation by BAR proteins. *Trends in Biochemical Sciences*, 37(12):526–533, 2012.

[140] Kumaran S. Ramamurthi and Richard Losick. Negative membrane curvature as a cue for subcellular localization of a bacterial protein. *Proceedings of the National Academy of Sciences*, 106(32):13541–13545, 2009.

[141] Rok Lenarcic, Sven Halbedel, Loek Visser, Michael Shaw, Ling Juan Wu, Jeff Errington, Davide Marenduzzo, and Leendert W Hamoen. Localisation of DivIVA by targeting to negatively curved membranes. *The EMBO Journal*, 28(15):2272–2282, 2009.

[142] Jacob Halatek and Erwin Frey. Highly Canalized MinD Transfer and MinE Sequestration Explain the Origin of Robust MinCDE-Protein Dynamics. *Cell Reports*, 1(6):741–752, 2012.

[143] Jeremy Nance. PAR proteins and the establishment of cell polarity during C. elegans development. *BioEssays*, 27(2):126–135, 2005.

[144] Carsten Hoege and Anthony A. Hyman. Principles of PAR polarity in Caenorhabditis elegans embryos. *Nature Reviews Molecular Cell Biology*, 14(5):315–322, 2013.

[145] Henrik Weyer, Tobias A Roth, and Erwin Frey. Deciphering the Interface Laws of Turing Mixtures and Foams. *arXiv*, 2024, 2409.20070.

[146] Fabai Wu, Jacob Halatek, Matthias Reiter, Enzo Kingma, Erwin Frey, and Cees Dekker. Multistability and dynamic transitions of intracellular Min protein patterns. *Molecular Systems Biology*, 12(6):MSB156724, 2016.

[147] Amit R. Singh, Travis Leadbetter, and Brian A. Camley. Sensing the shape of a cell with reaction diffusion and energy minimization. *Proceedings of the National Academy of Sciences*, 119(31):e2121302119, 2022, 2111.08496.

[148] M. H. Jacobs. *Diffusion Processes*. Springer Berlin Heidelberg, Berlin, Heidelberg, 1935.

[149] Robert Zwanzig. Diffusion past an entropy barrier. *The Journal of Physical Chemistry*, 96(10):3926–3930, 1992.

[150] S. Martens, G. Schmid, L. Schimansky-Geier, and P. Hanggi. Entropic particle transport: higher-order corrections to the Fick-Jacobs diffusion equation. *Physical Review E*, 83(5 Pt 1):051135, 2011.

[151] Shneior Lifson and Julius L Jackson. On the Self-Diffusion of Ions in a Polyelectrolyte Solution. *The Journal of Chemical Physics*, 36(9):2410–2414, 1962.

[152] P. Kalinay and J. K. Percus. Extended Fick-Jacobs equation: Variational approach. *Physical Review E*, 72(6):061203, 2005.

[153] P. S. Burada, G. Schmid, D. Reguera, J. M. Rubi, and P. Hanggi. Biased diffusion in confined media: test of the Fick-Jacobs approximation and validity criteria. *Physical Review E*, 75(5 Pt 1):051111, 2007.

[154] Alexander M. Berezhkovskii, Leonardo Dagdug, and Sergey M. Bezrukov. Range of applicability of modified Fick-Jacobs equation in two dimensions. *The Journal of Chemical Physics*, 143(16):164102, 2015.

[155] Jakob Löber, Markus Bär, and Harald Engel. Front propagation in one-dimensional spatially periodic bistable media. *Physical Review E*, 86(6):066210, 2012.

[156] S. Martens, J. Lober, and H. Engel. Front propagation in channels with spatially modulated cross section. *Physical Review E*, 91(2):022902, 2015.

[157] A. Ziepke, S. Martens, and H. Engel. Wave propagation in spatially modulated tubes. *The Journal of Chemical Physics*, 145(9):094108, 2016.

[158] Sriram Ramaswamy. Active matter. *Journal of Statistical Mechanics: Theory and Experiment*, 2017(5), 2017.

[159] Walter F. Paxton, Ayusman Sen, and Thomas E. Mallouk. Motility of Catalytic Nanoparticles through Self-Generated Forces. *Chemistry – A European Journal*, 11(22):6462–6470, 2005.

[160] Daniel L. Blair, T. Neicu, and A. Kudrolli. Vortices in vibrated granular rods. *Physical Review E*, 67(3):031303, 2003.

[161] Igor S. Aranson and Lev S. Tsimring. Model of coarsening and vortex formation in vibrated granular rods. *Physical Review E*, 67(2):021305, 2003.

[162] Dmitri Volfson, Arshad Kudrolli, and Lev S. Tsimring. Anisotropy-driven dynamics in vibrated granular rods. *Physical Review E*, 70(5):051312, 2004.

[163] V. Schaller, C. Weber, C. Semmrich, E. Frey, and A. R. Bausch. Polar patterns of driven filaments. *Nature*, 467(7311):73–7, 2010.

[164] L. Huber, R. Suzuki, T. Krüger, E. Frey, and A. R. Bausch. Emergence of coexisting ordered states in active matter systems. *Science*, 361(6399):255–258, 2018.

[165] Evelyn F. Keller and Lee A. Segel. Initiation of slime mold aggregation viewed as an instability. *Journal of Theoretical Biology*, 26(3):399–415, 1970.

[166] Tamás Vicsek, András Czirók, Eshel Ben-Jacob, Inon Cohen, and Ofer Shochet. Novel Type of Phase Transition in a System of Self-Driven Particles. *Physical Review Letters*, 75(6):1226–1229, 08 1995.

[167] Evelyn F. Keller and Lee A. Segel. Model for chemotaxis. *Journal of Theoretical Biology*, 30(2):225–234, 1971.

[168] Jeremy P. Moore and Thierry Emonet. Physics of bacterial chemotaxis. *Current Biology*, 34(20):R972–R977, 2024.

[169] Zahra Mokhtari, Robert I A Patterson, and Felix Höfling. Spontaneous trail formation in populations of auto-chemotactic walkers. *New Journal of Physics*, 24(1):013012, 2022.

[170] Andrea Cavagna and Irene Giardina. Bird Flocks as Condensed Matter. *Condensed Matter Physics*, 5(1):183–207, 2014.

[171] Stefano Marras and Paolo Domenici. Schooling Fish Under Attack Are Not All Equal: Some Lead, Others Follow. *PLoS ONE*, 8(6):e65784, 2013.

[172] Daniel S Calovi, Ugo Lopez, Sandrine Ngo, Clément Sire, Hugues Chaté, and Guy Theraulaz. Swarming, schooling, milling: phase diagram of a data-driven fish school model. *New Journal of Physics*, 16(1):015026, 2014, 1308.2889.

[173] Markus Bär, Robert Großmann, Sebastian Heidenreich, and Fernando Peruani. Self-Propelled Rods: Insights and Perspectives for Active Matter. *Annual Review of Condensed Matter Physics*, 11(1):441–466, 2020.

[174] Roland G. Winkler and Gerhard Gompper. Hydrodynamics in Motile Active Matter. In W. Andreoni and S. Yip, editors, *Handbook of Materials Modeling*, pages 1471–1491. Springer, Cham, 2020.

[175] Andreas Zöttl and Holger Stark. Modeling Active Colloids: From Active Brownian Particles to Hydrodynamic and Chemical Fields. *Annual Review of Condensed Matter Physics*, 14(1):109–127, 2022.

[176] J. Toner and Y. Tu. Long-Range Order in a Two-Dimensional Dynamical XY Model: How Birds Fly Together. *Physical Review Letters*, 75(23):4326–4329, 1995.

[177] Benoît Mahault, Francesco Ginelli, and Hugues Chaté. Quantitative Assessment of the Toner and Tu Theory of Polar Flocks. *Physical Review Letters*, 123(21):218001, 2019.

[178] J. Tailleur and M. E. Cates. Statistical mechanics of interacting run-and-tumble bacteria. *Physical Review Letters*, 100(21):218103, 2008.

[179] Yaouen Fily and M. Cristina Marchetti. Athermal Phase Separation of Self-Propelled Particles with No Alignment. *Physical Review Letters*, 108(23):235702, 2012.

[180] Michael E. Cates and Julien Tailleur. Motility-Induced Phase Separation. *Annual Review of Condensed Matter Physics*, 6(1):1–26, 2014.

[181] H. H. Wensink and H. Löwen. Aggregation of self-propelled colloidal rods near confining walls. *Physical Review E*, 78(3):031409, 2008.

[182] A. Kaiser, H. H. Wensink, and H. Löwen. How to Capture Active Particles. *Physical Review Letters*, 108(26):268307, 2012.

[183] Jens Elgeti and Gerhard Gompper. Wall accumulation of self-propelled spheres. *Europhysics Letters*, 101(4):48003, 2013.

[184] F. D. C. Farrell, M. C. Marchetti, D. Marenduzzo, and J. Tailleur. Pattern Formation in Self-Propelled Particles with Density-Dependent Motility. *Physical Review Letters*, 108(24):248101, 2012.

[185] J. Stenhammar, A. Tiribocchi, R. J. Allen, D. Marenduzzo, and M. E. Cates. Continuum theory of phase separation kinetics for active Brownian particles. *Physical Review Letters*, 111(14):145702, 2013.

[186] Gabriel S. Redner, Michael F. Hagan, and Aparna Baskaran. Structure and Dynamics of a Phase-Separating Active Colloidal Fluid. *Physical Review Letters*, 110(5):055701, 2013.

[187] Alexandre P. Solon, Joakim Stenhammar, Michael E. Cates, Yariv Kafri, and Julien Tailleur. Generalized thermodynamics of phase equilibria in scalar active matter. *Physical Review E*, 97(2):020602, 2018.

[188] John Toner, Yuhai Tu, and Sriram Ramaswamy. Hydrodynamics and phases of flocks. *Annals of Physics*, 318(1):170–244, 2005.

[189] F. Jülicher, S. W. Grill, and G. Salbreux. Hydrodynamic theory of active matter. *Reports on Progress in Physics*, 81(7):076601, 2018.

[190] R. Aditi Simha and Sriram Ramaswamy. Hydrodynamic Fluctuations and Instabilities in Ordered Suspensions of Self-Propelled Particles. *Physical Review Letters*, 89(5):058101, 2002.

[191] Anton Peshkov, Igor S Aranson, Eric Bertin, Hugues Chaté, and Francesco Ginelli. Nonlinear field equations for aligning self-propelled rods. *Physical Review Letters*, 109(26):268701, 2012.

[192] Eric Bertin, Hugues Chaté, Francesco Ginelli, Shradha Mishra, Anton Peshkov, and Sriram Ramaswamy. Mesoscopic theory for fluctuating active nematics. *New Journal of Physics*, 15(8):085032, 2013.

[193] A. Peshkov, E. Bertin, F. Ginelli, and H. Chaté. Boltzmann-Ginzburg-Landau approach for continuous descriptions of generic Vicsek-like models. *The European Physical Journal Special Topics*, 223(7):1315–1344, 2014.

[194] Pawel Romanczuk and Lutz Schimansky-Geier. Mean-field theory of collective motion due to velocity alignment. *Ecological Complexity*, 10:83–92, 2012.

[195] Thomas Ihle. Kinetic theory of flocking: Derivation of hydrodynamic equations. *Physical Review E*, 83(3):030901, 2011.

[196] A. Baskaran and M. C. Marchetti. Hydrodynamics of self-propelled hard rods. *Physical Review E*, 77(1):011920, 2008.

[197] Anton Peshkov, Sandrine Ngo, Eric Bertin, Hugues Chaté, and Francesco Ginelli. Continuous Theory of Active Matter Systems with Metric-Free Interactions. *Physical Review Letters*, 109(9):098101, 2012.

[198] Igor S Aranson and Lev S Tsimring. Pattern formation of microtubules and motors: Inelastic interaction of polar rods. *Phys. Rev. E*, 71(5):050901(R), 2005.

[199] E. Bertin, M. Droz, and G. Gregoire. Boltzmann and hydrodynamic description for self-propelled particles. *Phys Rev E*, 74(2):022101, 2006.

[200] Eric Bertin, Michel Droz, and Guillaume Grégoire. Hydrodynamic equations for self-propelled particles: microscopic derivation and stability analysis. *Journal of Physics A*, 42(44):445001, 2009.

[201] Ivan Maryshev, Davide Marenduzzo, Andrew B. Goryachev, and Alexander Morozov. Kinetic theory of pattern formation in mixtures of microtubules and molecular motors. *Physical Review E*, 97(2):022412, 2018.

[202] Ivan Maryshev, Andrew B. Goryachev, Davide Marenduzzo, and Alexander Morozov. Dry active turbulence in a model for microtubule–motor mixtures. *Soft Matter*, 15:6038, 2019.

[203] J. Denk, L. Huber, E. Reithmann, and E. Frey. Active Curved Polymers Form Vortex Patterns on Membranes. *Physical Review Letters*, 116(17):178301, 2016.

[204] Ran Ni, Martien A. Cohen Stuart, and Peter G. Bolhuis. Tunable Long Range Forces Mediated by Self-Propelled Colloidal Hard Spheres. *Physical Review Letters*, 114(1):018302, 2015.

[205] Iain D. Couzin, Jens Krause, Richard James, Graeme D. Ruxton, and Nigel R. Franks. Collective Memory and Spatial Sorting in Animal Groups. *Journal of Theoretical Biology*, 218(1):1–11, 2002.

[206] Chad M. Topaz and Andrea L. Bertozzi. Swarming Patterns in a Two-Dimensional Kinematic Model for Biological Groups. *SIAM Journal on Applied Mathematics*, 65(1):152–174, 2004.

[207] Rajendra Singh Negi, Roland G. Winkler, and Gerhard Gompper. Collective behavior of self-steering active particles with velocity alignment and visual perception. *Physical Review Research*, 6(1):013118, 2024.

[208] Lucas Barberis and Fernando Peruani. Large-Scale Patterns in a Minimal Cognitive Flocking Model: Incidental Leaders, Nematic Patterns, and Aggregates. *Physical Review Letters*, 117(24):248001, 2016.

[209] O. Dauchot and H. Lowen. Chemical Physics of Active Matter. *Journal of Chemical Physics*, 151(11):114901, 2019.

[210] Clifford S. Patlak. Random walk with persistence and external bias. *The bulletin of mathematical biophysics*, 15(3):311–338, 1953.

[211] J. J. Tyson and J. D. Murray. Cyclic AMP waves during aggregation of Dictyostelium amoebae. *Development*, 106(3):421–6, 1989.

[212] Loling Song, Sharvari M. Nadkarni, Hendrik U. Bödeker, Carsten Beta, Albert Bae, Carl Franck, Wouter-Jan Rappel, William F. Loomis, and Eberhard Bodenschatz. Dictyostelium discoideum chemotaxis: Threshold for directed motion. *European Journal of Cell Biology*, 85(9):981–989, 2006.

[213] H. Levine, I. Aranson, L. Tsimring, and T. V. Truong. Positive genetic feedback governs cAMP spiral wave formation in Dictyostelium. *Proceedings of the National Academy of Science*, 93(13):6382–6386, 1996.

[214] Duncan E. Jackson and Francis L.W. Ratnieks. Communication in ants. *Current Biology*, 16(15):R570–R574, 2006.

[215] Claire Detrain and Jean-Louis Deneubourg. Collective Decision-Making and Foraging Patterns in Ants and Honeybees. *Advances in Insect Physiology*, 35:123–173, 2008.

[216] Benno Liebchen and Hartmut Löwen. Synthetic Chemotaxis and Collective Behavior in Active Matter. *Accounts of Chemical Research*, 51(12):2982–2990, 2018.

[217] Alexandra V. Zampetaki, Benno Liebchen, Alexei V. Ivlev, and Hartmut Löwen. Collective self-optimization of communicating active particles. *Proceedings of the National Academy of Science*, 118(49):e2111142118, 2021.

[218] Alicia Altemose, María Antonieta Sánchez-Farŕan, Wentao Duan, Steve Schulz, Ali Borhan, Vincent H Crespi, and Ayusman Sen. Chemically controlled spatiotemporal oscillations of colloidal assemblies. *Angewandte Chemie Internationale Edition*, 56(27):7817–7821, 2017.

[219] Babak Vajdi Hokmabad, Jaime Agudo-Canalejo, Suropriya Saha, Ramin Golestanian, and Corinna C. Maass. Chemotactic self-caging in active emulsions. *Proceedings of the National Academy of Sciences*, 119(24):e2122269119, 2022.

[220] I. Theurkauff, C. Cottin-Bizonne, J. Palacci, C. Ybert, and L. Bocquet. Dynamic clustering in active colloidal suspensions with chemical signaling. *Physical Review Letters*, 108(26):268303, 2012.

[221] Ivo Buttinoni, Julian Bialké, Felix Kümmel, Hartmut Löwen, Clemens Bechinger, and Thomas Speck. Dynamical Clustering and Phase Separation in Suspensions of Self-Propelled Colloidal Particles. *Physical Review Letters*, 110(23):238301, 2013.

[222] Kevin P O'Keeffe, Hyunsuk Hong, and Steven H Strogatz. Oscillators that sync and swarm. *Nature Communications*, 8(1):1504, 2017.

[223] Steven Ceron, Kevin O'Keeffe, and Kirstin Petersen. Diverse behaviors in non-uniform chiral and non-chiral swarmalators. *Nature Communications*, 14(1):940, 2023.

[224] Michael Riedl, Isabelle Mayer, Jack Merrin, Michael Sixt, and Björn Hof. Synchronization in collectively moving inanimate and living active matter. *Nature Communications*, 14(1):5633, 2023.

[225] P. Girard, J. Prost, and P. Bassereau. Passive or Active Fluctuations in Membranes Containing Proteins. *Physical Review Letters*, 94(8):088102, 2005.

[226] Cem Yolcu, Robert C. Haussman, and Markus Deserno. The Effective Field Theory approach towards membrane-mediated interactions between particles. *Advances in Colloid and Interface Science*, 208:89–109, 2014.

[227] Mijo Simunovic, Emma Evergren, Ivan Golushko, Coline Prévost, Henri-François Renard, Ludger Johannes, Harvey T. McMahon, Vladimir Lorman, Gregory A. Voth, and Patricia Bassereau. How curvature-generating proteins build scaffolds on membrane nanotubes. *Proceedings of the National Academy of Sciences*, 113(40):11226–11231, 2016.

[228] Katja Zieske and Petra Schwille. Reconstituting geometry-modulated protein patterns in membrane compartments. In Jennifer Ross and Wallace F. Marshall, editors, *Methods in Cell Biology*, volume 128, pages 149–163. Academic Press, 01 2015.

[229] J. Prost, Frank Jülicher, and J. F. Joanny. Active gel physics. *Nature Physics*, 11:111–117, 2015.

[230] Thomas Litschel, Michael M. Norton, Vardges Tserunyan, and Seth Fraden. Engineering reaction–diffusion networks with properties of neural tissue. *Lab on a Chip*, 18(5):714–722, 2017.

[231] Thomas Litschel, Beatrice Ramm, Roel Maas, Michael Heymann, and Petra Schwille. Beating Vesicles: Encapsulated Protein Oscillations Cause Dynamic Membrane Deformations. *Angewandte Chemie International Edition*, 57(50):16286–16290, 2018.

[232] P. Sekhar Burada, Peter Hänggi, Fabio Marchesoni, Gerhard Schmid, and Peter Talkner. Diffusion in Confined Geometries. *ChemPhysChem*, 10(1):45–54, 2009.

[233] Ivan Santamaría-Holek, Zbigniew J. Grzywna, and J. Miguel Rubi. A non-equilibrium thermodynamics model for combined adsorption and diffusion processes in micro- and nanopores. *Journal of Non-Equilibrium Thermodynamics*, 37(3):273–290, 2012.

[234] S. Martens, A. V. Straube, G. Schmid, L. Schimansky-Geier, and P. Hänggi. Hydrodynamically Enforced Entropic Trapping of Brownian Particles. *Physical Review Letters*, 110(1):010601, 2013.

[235] Naohisa Ogawa. Diffusion in a curved tube. *Physics Letters A*, 377(38):2465–2471, 2013.

[236] John J. Tyson and James P. Keener. Singular perturbation theory of traveling waves in excitable media (a review). *Physica D: Nonlinear Phenomena*, 32(3):327–361, 1988.

[237] Daniel M. Davis and Stefanie Sowinski. Membrane nanotubes: dynamic long-distance connections between animal cells. *Nature Reviews Molecular Cell Biology*, 9(6):431–436, 2008.

[238] Haleh Alimohamadi, Ben Ovryn, and Padmini Rangamani. Modeling membrane nanotube morphology: the role of heterogeneity in composition and material properties. *Scientific Reports*, 10(1):2527, 2020.

[239] Markus Radszuweit, Sergio Alonso, Harald Engel, and Markus Bär. Intracellular Mechanochemical Waves in an Active Poroelastic Model. *Physical Review Letters*, 110(13):138102, 2013.

[240] Sophie Marbach and Karen Alim. Active control of dispersion within a channel with flow and pulsating walls. *Physical Review Fluids*, 4(11):114202, 2019.

[241] Henrik Strahl and Leendert W Hamoen. Finding the corners in a cell. *Current Opinion in Microbiology*, 15(6):731–736, 2012.

[242] Peter Gross, K. Vijay Kumar, Nathan W. Goehring, Justin S. Bois, Carsten Hoege, Frank Jülicher, and Stephan W. Grill. Guiding self-organized pattern formation in cell polarity establishment. *Nature Physics*, 15(3):293–300, 2019.

[243] R.G. Plaza, F. Sánchez-Garduño, P. Padilla, R.A. Barrio, and P.K. Maini. The Effect of Growth and Curvature on Pattern Formation. *Journal of Dynamics and Differential Equations*, 16(4):1093–1121, 2004.

[244] Laeschkir Würthner, Andriy Goychuk, and Erwin Frey. Geometry-induced patterns through mechanochemical coupling. *Physical Review E*, 108(1):014404, 2023.

[245] Manon C. Wigbers, Fridtjof Brauns, Ching Yee Leung, and Erwin Frey. Flow Induced Symmetry Breaking in a Conceptual Polarity Model. *Cells*, 9(6):1524, 2020.

[246] Wolfram Research, Inc. Mathematica, Version 14.1. Champaign, IL, 2024.

[247] Tosio Kato. *Perturbation theory for linear operators*. Springer, 1966.

[248] Amitabha Bose. A Geometric Approach to Singularly Perturbed Nonlocal Reaction-Diffusion Equations. *SIAM Journal on Mathematical Analysis*, 31(2):431–454, 2000.

[249] S. Alonso, J. Löber, M. Bär, and H. Engel. Wave propagation in heterogeneous bistable and excitable media. *The European Physical Journal Special Topics*, 187(1):31–40, 2010.

[250] Paul C. Bressloff. Cellular diffusion processes in singularly perturbed domains. *Journal of Mathematical Biology*, 89(6):58, 2024.

[251] COMSOL Multiphysics® v. 6.2. www.comsol.com. COMSOL AB, Stockholm, Sweden.

[252] Jian-Geng Chiou, Samuel A. Ramirez, Timothy C. Elston, Thomas P. Witelski, David G. Schaeffer, and Daniel J. Lew. Principles that govern competition or co-existence in Rho-GTPase driven polarization. *PLoS Computational Biology*, 14(4):e1006095, 2018.

[253] I Prigogine and R Lefever. Symmetry Breaking Instabilities in Dissipative Systems. II. *The Journal of Chemical Physics*, 48(4):1695–1700, 1968.

[254] G. Nicolis and I. Prigogine. *Self-Organization in Nonequilibrium Systems: From Dissipative Structures to Order Through Fluctuations*. A Wiley-Interscience publication. Wiley, 1977.

[255] Kai Simons and Derek Toomre. Lipid rafts and signal transduction. *Nature Reviews Molecular Cell Biology*, 1(1):31–39, 2000.

[256] Marten Postma, Jeroen Roelofs, Joachim Goedhart, Harriët M. Loovers, Antonie J. W. G. Visser, and Peter J. M. Van Haastert. Sensitization of Dictyostelium chemotaxis by phosphoinositide-3-kinase-mediated self-organizing signalling patches. *Journal of Cell Science*, 117(14):2925–2935, 2004.

[257] Elina Ikonen. Roles of lipid rafts in membrane transport. *Current Opinion in Cell Biology*, 13(4):470–477, 2001.

[258] S Leibler. Curvature instability in membranes. *Journal de Physique*, 47(3):507–516, 1986.

[259] Khashayar Farsad and Pietro De Camilli. Mechanisms of membrane deformation. *Current Opinion in Cell Biology*, 15(4):372–381, 2003.

[260] Coline Prévost, Hongxia Zhao, John Manzi, Emmanuel Lemichez, Pekka Lappalainen, Andrew Callan-Jones, and Patricia Bassereau. IRSp53 senses negative membrane curvature and phase separates along membrane tubules. *Nature Communications*, 6(1):8529, 2015.

[261] Raghuveer Parthasarathy, Cheng-han Yu, and Jay T. Groves. Curvature-Modulated Phase Separation in Lipid Bilayer Membranes. *Langmuir*, 22(11):5095–5099, 2006.

[262] Frederick A. Heberle and Gerald W. Feigenson. Phase Separation in Lipid Membranes. *Cold Spring Harbor Perspectives in Biology*, 3(4):a004630, 2011.

[263] Giulio Vandin, Davide Marenduzzo, Andrew B. Goryachev, and Enzo Orlandini. Curvature-driven positioning of Turing patterns in phase-separating curved membranes. *Soft Matter*, 12(17):3888–3896, 2016.

[264] Andrew Callan-Jones, Benoit Sorre, and Patricia Bassereau. Curvature-Driven Lipid Sorting in Biomembranes. *Cold Spring Harbor Perspectives in Biology*, 3(2):a004648, 2011.

[265] Aurélien Roux, Damien Cuvelier, Pierre Nassoy, Jacques Prost, Patricia Bassereau, and Bruno Goud. Role of curvature and phase transition in lipid sorting and fission of membrane tubules. *The EMBO Journal*, 24(8):1537–1545, 2005.

[266] Stefan Semrau and Thomas Schmidt. Membrane heterogeneity – from lipid domains to curvature effects. *Soft Matter*, 5(17):3174–3186, 2009.

[267] Timon Idema, Stefan Semrau, Cornelis Storm, and Thomas Schmidt. Membrane Mediated Sorting. *Physical Review Letters*, 104(19):198102, 2010.

[268] Udo Seifert. Curvature-induced lateral phase segregation in two-component vesicles. *Physical Review Letters*, 70(9):1335–1338, 1993.

[269] Maxim O. Lavrentovich, Eric M. Horsley, Asja Radja, Alison M. Sweeney, and Randall D. Kamien. First-order patterning transitions on a sphere as a route to cell morphology. *Proceedings of the National Academy of Sciences*, 113(19):5189–5194, 2016.

[270] Jaime Agudo-Canalejo and Ramin Golestanian. Pattern formation by curvature-inducing proteins on spherical membranes. *New Journal of Physics*, 19(12):125013, 2017.

[271] R. E. Magi and J. P. Keener. Modelling A Biological Membrane as a Two Phase Viscous Fluid with Curvature Elasticity. *SIAM Journal on Applied Mathematics*, 77(1):128–153, 2017.

[272] Paul J Flory. Thermodynamics of High Polymer Solutions. *The Journal of Chemical Physics*, 9(8):660–660, 1941.

[273] Maurice L Huggins. Solutions of Long Chain Compounds. *The Journal of Chemical Physics*, 9(5):440–440, 1941.

[274] P.B. Canham. The minimum energy of bending as a possible explanation of the biconcave shape of the human red blood cell. *Journal of Theoretical Biology*, 26(1):61–81, 1970.

[275] W Helfrich. Elastic Properties of Lipid Bilayers: Theory and Possible Experiments. *Zeitschrift für Naturforschung C*, 28(11-12):693–703, 1973.

[276] Juha Saarikangas, Hongxia Zhao, Anette Pykäläinen, Pasi Laurinmäki, Pieta K. Mattila, Paavo K.J. Kinnunen, Sarah J. Butcher, and Pekka Lappalainen. Molecular Mechanisms of Membrane Deformation by I-BAR Domain Proteins. *Current Biology*, 19(2):95–107, 2009.

[277] Marijn G. J. Ford, Ian G. Mills, Brian J. Peter, Yvonne Vallis, Gerrit J. K. Praefcke, Philip R. Evans, and Harvey T. McMahon. Curvature of clathrin-coated pits driven by epsin. *Nature*, 419(6905):361–366, 2002.

[278] Wanda Kukulski, Martin Schorb, Marko Kaksonen, and John A.G. Briggs. Plasma Membrane Reshaping during Endocytosis Is Revealed by Time-Resolved Electron Tomography. *Cell*, 150(3):508–520, 2012.

[279] Simon Christ, Thomas Litschel, Petra Schwille, and Reinhard Lipowsky. Active shape oscillations of giant vesicles with cyclic closure and opening of membrane necks. *Soft Matter*, 17(2):319–330, 2020.

[280] Tobias Frohoff-Hülsmann, Uwe Thiele, and Len M. Pismen. Non-reciprocity induces resonances ina two-field CahnHilliard model. *Philosophical Transactions of the Royal Society A*, 381(2245):20220087, 2023, 2211.08320.

[281] W. T. Góźdź. The Interface Width of Separated Two-Component Lipid Membranes. *The Journal of Physical Chemistry B*, 110(43):21981–21986, 2006.

[282] Markus Deserno. Fluid lipid membranes: From differential geometry to curvature stresses. *Chemistry and Physics of Lipids*, 185:11–45, 2015.

[283] Erwin Frey and David R Nelson. Dynamics of flat membranes and flickering in red blood cells. *Journal de Physique I*, 1(12):1715–1757, 1991.

[284] Guillaume Salbreux and Frank Jülicher. Mechanics of active surfaces. *Physical Review E*, 96(3):032404, 2017.

[285] S.R. De Groot and P. Mazur. *Non-equilibrium thermodynamics*. Dover Publications, Inc., New York, 1984.

[286] John W Cahn and John E Hilliard. Free Energy of a Nonuniform System. I. Interfacial Free Energy. *The Journal of Chemical Physics*, 28(2):258–267, 1958.

[287] John W Cahn. On spinodal decomposition. *Acta Metallurgica*, 9(9):795–801, 1961.

[288] Delia Bucher, Felix Frey, Kem A. Sochacki, Susann Kummer, Jan-Philip Bergeest, William J. Godinez, Hans-Georg Kräusslich, Karl Rohr, Justin W. Taraska, Ulrich S. Schwarz, and Steeve Boulant. Clathrin-adaptor ratio and membrane tension regulate the flat-to-curved transition of the clathrin coat during endocytosis. *Nature Communications*, 9(1):1109, 2018.

[289] Philip W. Fowler, Jean Hélie, Anna Duncan, Matthieu Chavent, Heidi Koldsø, and Mark S. P. Sansom. Membrane stiffness is modified by integral membrane proteins. *Soft Matter*, 12(37):7792–7803, 2016.

[290] François Quemeneur, Jon K. Sigurdsson, Marianne Renner, Paul J. Atzberger, Patricia Bassereau, and David Lacoste. Shape matters in protein mobility within membranes. *Proceedings of the National Academy of Sciences*, 111(14):5083–5087, 2014.

[291] Tobias Baumgart, Samuel T. Hess, and Watt W. Webb. Imaging coexisting fluid domains in biomembrane models coupling curvature and line tension. *Nature*, 425(6960):821–824, 2003.

[292] Ron Milo and Rob Phillips. *Cell Biology by the numbers*. Garland Science, 2015.

[293] Zhong-can Ou-Yang and Wolfgang Helfrich. Bending energy of vesicle membranes: General expressions for the first, second, and third variation of the shape energy and applications to spheres and cylinders. *Physical Review A*, 39(10):5280–5288, 1989.

[294] I.M. Lifshitz and V.V. Slyozov. The kinetics of precipitation from supersaturated solid solutions. *Journal of Physics and Chemistry of Solids*, 19(1-2):35–50, 1961.

[295] Carl Wagner. Theorie der Alterung von Niederschlägen durch Umlösen (Ostwald-Reifung). *Zeitschrift für Elektrochemie*, 65(7-8):581–591, 09 1961.

[296] P. C. Matthews and S. M. Cox. Pattern formation with a conservation law. *Nonlinearity*, 13(4):1293–1320, 2000.

[297] Reinhard Lipowsky. Remodeling of Membrane Shape and Topology by Curvature Elasticity and Membrane Tension. *Advanced Biology*, 6(1):e2101020, 2022.

[298] D. Schüler, S. Alonso, A. Torcini, and M. Bär. Spatio-temporal dynamics induced by competing instabilities in two asymmetrically coupled nonlinear evolution equations. *Chaos: An Interdisciplinary Journal of Nonlinear Science*, 24(4):043142, 2014.

[299] Suropriya Saha, Jaime Agudo-Canalejo, and Ramin Golestanian. Scalar Active Mixtures: The Nonreciprocal Cahn-Hilliard Model. *Physical Review X*, 10(4):041009, 2020.

[300] Fridtjof Brauns and M. Cristina Marchetti. Nonreciprocal Pattern Formation of Conserved Fields. *Physical Review X*, 14(2):021014, 2024.

[301] Fabian Bergmann and Walter Zimmermann. On system-spanning demixing properties of cell polarization. *PLoS ONE*, 14(6):e0218328, 2019.

[302] A. Sokolov, I. S. Aranson, J. O. Kessler, and R. E. Goldstein. Concentration dependence of the collective dynamics of swimming bacteria. *Phys Rev Lett*, 98(15):158102, 2007.

[303] A. Decoene, A. Lorz, S. Martin, B. Maury, and M. Tang. Simulation of self-propelled chemotactic bacteria in a stokes flow. *ESAIM: Proceedings*, 30:104–123, 2010.

[304] T. Sanchez, D. T. Chen, S. J. DeCamp, M. Heymann, and Z. Dogic. Spontaneous motion in hierarchically assembled active matter. *Nature*, 491(7424):431–4, 2012.

[305] A. Doostmohammadi, J. Ignes-Mullol, J. M. Yeomans, and F. Sagues. Active nematics. *Nature Communications*, 9(1):3246, 2018.

[306] Iain D Couzin and Jens Krause. Self-Organization and Collective Behavior in Vertebrates. *Advances in the Study of Behavior*, 32(Auk.1021985):1–75, 2003.

[307] J. R. Howse, R. A. Jones, A. J. Ryan, T. Gough, R. Vafabakhsh, and R. Golestanian. Self-motile colloidal particles: from directed propulsion to random walk. *Physical Review Letters*, 99(4):048102, 2007.

[308] Xi Chen, Yankai Xu, Chao Zhou, Kai Lou, Yixin Peng, H. P. Zhang, and Wei Wang. Unraveling the physiochemical nature of colloidal motion waves among silver colloids. *Science Advances*, 8(eabn9130), 2022.

[309] Stefano Palagi and Peer Fischer. Bioinspired microrobots. *Nature Review Materials*, 3:113–124, 2018.

[310] Michael Rubenstein, Christian Ahler, and Radhika Nagpal. Kilobot: A Low Cost Scalable Robot System for Collective Behaviors. *2012 IEEE International Conference on Robotics and Automation*, pages 3293–3298, 2012.

[311] Carole A Parent and Peter N Devreotes. A cell's sense of direction. *Science*, 284(5415):765–770, 1999.

[312] Dan Gorbonos, Reuven Ianconescu, James G Puckett, Rui Ni, Nicholas T Ouellette, and Nir S Gov. Long-range acoustic interactions in insect swarms: an adaptive gravity model. *New Journal of Physics*, 18(7):073042, 2016.

[313] Beatrice Ramm, Andriy Goychuk, Alena Khmelinskaia, Philipp Blumhardt, Hiromune Eto, Kristina A Ganzinger, Erwin Frey, and Petra Schwille. A diffusiophoretic mechanism for ATP-driven transport without motor proteins. *Nature Physics*, pages 1–9, 2021.

[314] C. Zhou, N. J. Suematsu, Y. Peng, Q. Wang, X. Chen, Y. Gao, and W. Wang. Coordinating an Ensemble of Chemical Micromotors via Spontaneous Synchronization. *ACS Nano*, 14(5):5360–5370, 2020.

[315] R. K. Katzschmann, J. DelPreto, R. MacCurdy, and D. Rus. Exploration of underwater life with an acoustically controlled soft robotic fish. *Science Robotics*, 3(16), 2018.

[316] S. Li, R. Batra, D. Brown, H. D. Chang, N. Ranganathan, C. Hoberman, D. Rus, and H. Lipson. Particle robotics based on statistical mechanics of loosely coupled components. *Nature*, 567(7748):361–365, 2019.

[317] C. M. Waters and B. L. Bassler. Quorum sensing: cell-to-cell communication in bacteria. *Annual Review of Cell and Developmental Biology*, 21(1):319–46, 2005.

[318] Z. T. Liu, Y. Shi, Y. Zhao, H. Chaté, X. Q. Shi, and T. H. Zhang. Activity waves and freestanding vortices in populations of subcritical Quincke rollers. *Proceedings of the National Academy of Science*, 118(40):e2104724118, 2021.

[319] Benno Liebchen, Michael E. Cates, and Davide Marenduzzo. Pattern formation in chemically interacting active rotors with self-propulsion. *Soft Matter*, 12(35):7259–7264, 2016.

[320] Suropriya Saha, Ramin Golestanian, and Sriram Ramaswamy. Clusters, asters, and collective oscillations in chemotactic colloids. *Physical Review E*, 89(6):062316, 2014.

[321] Elena Sesé-Sansa, Demian Levis, and Ignacio Pagonabarraga. Phase separation of self-propelled disks with ferromagnetic and nematic alignment. *Physical Review E*, 104(5):054611, 2021.

[322] P. Romanczuk, U. Erdmann, H. Engel, and L. Schimansky-Geier. Beyond the Keller-Segel model. *European Physics Journal*, 157(1):61–77, 2008.

[323] Tobias Bäuerle, Andreas Fischer, Thomas Speck, and Clemens Bechinger. Self-organization of active particles by quorum sensing rules. *Nature Communications*, 9(1):3232, 2018.

[324] M. R. Parsek and E. P. Greenberg. Acyl-homoserine lactone quorum sensing in gram-negative bacteria: a signaling mechanism involved in associations with higher organisms. *Proceedings of the National Academy of Science*, 97(16):8789–93, 2000.

[325] B. Sager and D. Kaiser. Intercellular C-signaling and the traveling waves of Myxococcus. *Genes and Development*, 8(23):2793–804, 1994.

[326] Otto H Schmitt. A thermionic trigger. *Journal of Scientific Instruments*, 15:24, 1938.

[327] Wouter-Jan Rappel, Alastair Nicol, Armand Sarkissian, Herbert Levine, and William F Loomis. Self-organized vortex state in two-dimensional Dictyostelium dynamics. *Physical Review Letters*, 83:1247, 1999.

[328] Herbert Levine, Wouter-Jan Rappel, and Inon Cohen. Self-organization in systems of self-propelled particles. *Physical Review E*, 63(1):017101, 2000.

[329] Marcel Meyer, Lutz Schimansky-Geier, and Pawel Romanczuk. Active Brownian agents with concentration-dependent chemotactic sensitivity. *Physical Review E*, 89(2):022711, 2014.

[330] Michael P. Brenner, Leonid S. Levitov, and Elena O. Budrene. Physical Mechanisms for Chemotactic Pattern Formation by Bacteria. *Biophysical Journal*, 74(4):1677–1693, 1998.

[331] Supplementary Material to Alexander Ziepke, Ivan Maryshev, Igor S. Aranson, and Erwin Frey, 'Multi-scale organization in communicating active matter', *Nat. Commun.* **13**, 6727 (2022) is available at doi:10.1038/s41467-022-34484-2.

[332] I. S. Aranson, H. Levine, and L. Tsimring. Spiral competition in three-component excitable media. *Physical Review Letters*, 76(7):1170–1173, 1996.

[333] Alan J. Bray, Satya N. Majumdar, and Grégory Schehr. Persistence and first-passage properties in nonequilibrium systems. *Advances in Physics*, 62(3):225–361, 2013.

[334] Ram Avinery, Micha Kornreich, and Roy Beck. Universal and Accessible Entropy Estimation Using a Compression Algorithm. *Physical Review Letters*, 123(17):178102, 2019.

[335] Stefano Martiniani, Paul M Chaikin, and Dov Levine. Quantifying hidden order out of equilibrium. *Physical Review X*, 9:11031, 2019.

[336] J. Ziv and A. Lempel. A universal algorithm for sequential data compression. *IEEE Transactions on Information Theory*, 23(3):337–343, 1977.

[337] Shashi Thutupalli and Stephan Herminghaus. Tuning active emulsion dynamics via surfactants and topology. *European Physiscs Journal E*, 36:1–10, 2013.

[338] G. Guennebaud, B. Jacob, and et al. Eigen v3, 2010.

[339] Paul Meakin. Diffusion-limited droplet coalescence. *Physica A*, 165(1):1–18, 1990.

[340] Shucong Li, Michael M. Lerch, James T. Waters, Bolei Deng, Reese S. Martens, Yuxing Yao, Do Yoon Kim, Katia Bertoldi, Alison Grinthal, Anna C. Balazs, and Joanna Aizenberg. Self-regulated non-reciprocal motions in single-material microstructures. *Nature*, 605(7908):76–83, 2022.

[341] Gaurav Gardi, Steven Ceron, Wendong Wang, Kirstin Petersen, and Metin Sitti. Microrobot collectives with reconfigurable morphologies, behaviors, and functions. *Nature Communications*, 13(1):2239, 2022.

[342] Hillel Ori, Marc Duque, Rebecca Frank Hayward, Colin Scheibner, He Tian, Gloria Ortiz, Vincenzo Vitelli, and Adam E. Cohen. Observation of topological action potentials in engineered tissues. *Nature Physics*, 19(2):290–296, 2023.

[343] Gillian Sales. *Ultrasonic communication by animals*. Springer Science & Business Media, 2012.

[344] Couzin and D. Iain. Synchronization: The Key to Effective Communication in Animal Collectives. *Trends in Cognitive Sciences*, 22(10):844–846, 2018.

[345] Michael Sinhuber, Kasper van der Vaart, Yenchia Feng, Andrew M Reynolds, and Nicholas T Ouellette. An equation of state for insect swarms. *Scientific Reports*, 11(1):3773, 2021.

[346] Lance G. Barrett-Lennard, John K.B. Ford, and Kathy A. Heise. The mixed blessing of echolocation: differences in sonar use by fish-eating and mammal-eating killer whales. *Animal Behavior*, 51(3):553–565, 1996.

[347] Arjan Boonman, Brock Fenton, and Yossi Yovel. The benefits of insect-swarm hunting to echolocating bats, and its influence on the evolution of bat echolocation signals. *PLoS Computational Biology*, 15(12):e1006873, 2019.

[348] G. C. H. E. de Croon, J. J. G. Dupeyroux, S. B. Fuller, and J. A. R. Marshall. Insect-inspired AI for autonomous robots. *Science Robotics*, 7(67):eabl6334, 2022.

[349] George M. Whitesides and Bartosz Grzybowski. Self-Assembly at All Scales. *Science*, 295(5564):2418–2421, 2002.

[350] Wei Wang, Wentao Duan, Suzanne Ahmed, Ayusman Sen, and Thomas E. Mallouk. From One to Many: Dynamic Assembly and Collective Behavior of Self-Propelled Colloidal Motors. *Accounts of Chemical Research*, 48(7):1938–1946, 2015.

[351] George M. Whitesides and George W. Crabtree. Don't Forget Long-Term Fundamental Research in Energy. *Science*, 315(5813):796–798, 2007.

[352] Xiaoguang Dong and Metin Sitti. Controlling two-dimensional collective formation and cooperative behavior of magnetic microrobot swarms. *International Journal of Robotic Research*, 39(5):617–638, 2020.

[353] Lidong Yang, Jiangfan Yu, Shihao Yang, Ben Wang, Bradley J Nelson, and Li Zhang. A Survey on Swarm Microrobotics. *IEEE Transactions on Robotics*, 38(3):1531–1551, 2022.

[354] Frank Schätzing. *The Swarm: A Novel*. HarperCollins, 2009.

[355] Michael Crichton. *Prey*. HarperCollins, 2013.

[356] S H Strogatz and I Stewart. Coupled oscillators and biological synchronization. *Scientific American*, 269(6):102–9, 1993.

[357] M. Rosenblum, A. Pikovsky, J. Kurths, C. Schäfer, and P.A. Tass. Chapter 9, Phase synchronization: From theory to data analysis. In F. Moss and S. Gielen, editors, *Neuro-Informatics and Neural Modelling*, volume 4 of *Handbook of Biological Physics*, pages 279–321. North-Holland, 2001.

[358] Jinrun Liu, Hong Chen, Xiaojie Shi, Saraf Nawar, Jörg G Werner, Gaoshan Huang, Miaomiao Ye, David A Weitz, Alexander A Solovev, and Yongfeng Mei. Hydrogel microcapsules with photocatalytic nanoparticles for removal of organic pollutants. *Environmental Science Nano*, 7(2):656–664, 2020.

[359] Xiaocong Chang, Yiwen Feng, Bin Guo, Dekai Zhou, and Longqiu Li. Nature-inspired micro/nanomotors. *Nanoscale*, 14(2):219–238, 2022.

[360] Mario Urso, Martina Ussia, and Martin Pumera. Smart micro- and nanorobots for water purification. *Nature Review Bioengineering*, 1(4):236–251, 2023.

[361] Huosheng Hu, John Oyekan, and Dongbing Gu. A school of robotic fish for pollution detection in port. In Y. Liu and D. Sun, editors, *Biologically Inspired Robotics*, pages 85–104. CRC Press, 2011.

[362] Junhui Law, Xian Wang, Mengxi Luo, Liming Xin, Xingzhou Du, Wenkun Dou, Tiancong Wang, Guanqiao Shan, Yibin Wang, Peng Song, Xi Huang, Jiangfan Yu, and Yu Sun. Microrobotic swarms for selective embolization. *Science Advances*, 8(29):eabm5752, 2022.

[363] Cagatay M. Oral and Martin Pumera. In vivo applications of micro/nanorobots. *Nanoscale*, 15(19):8491–8507, 2023.

[364] Gerhard Gompper, Roland G Winkler, Thomas Speck, Alexandre Solon, Cesare Nardini, Fernando Peruani, Hartmut Löwen, Ramin Golestanian, U Benjamin Kaupp, Luis Alvarez, Thomas Kirboe, Eric Lauga, Wilson C K Poon, Antonio DeSimone, Santiago Muios-Landin, Alexander Fischer, Nicola A Sker, Frank Cichos, Raymond Kapral, Pierre Gaspard, Marisol Ripoll, Francesc Sagues, Amin Doostmohammadi, Julia M Yeomans, Igor S Aranson, Clemens Bechinger, Holger Stark, Charlotte K Hemelrijk, Franois J Nedelec, Trinish Sarkar, Thibault Aryaksama, Mathilde Lacroix, Guillaume Duclos, Victor Yashunsky, Pascal Silberzan, Marino Arroyo, and Sohan Kale. The 2020 motile active matter roadmap. *Journal of Physics*, 32(19):193001, 2020.

[365] Hugues Chaté. Dry Aligning Dilute Active Matter. *Annual Reviews of Condensed Matter Physics*, 11(1):189–212, 2020.

[366] Juan A. Acebrón, L. L. Bonilla, Conrad J. Pérez Vicente, Félix Ritort, and Renato Spigler. The Kuramoto model: A simple paradigm for synchronization phenomena. *Reviews of Modern Physics*, 77(1):137–185, 2005.

[367] Strogatz and H. Steven. *Nonlinear Dynamics and Chaos with Student Solutions Manual*. CRC Press, 2018.

[368] Igor S Aranson and Lorenz Kramer. The world of the complex Ginzburg-Landau equation. *Rev Mod Phys*, 74(1):99–143, 2002.

[369] Peter E. Kloeden and Eckhard Platen. Stochastic Differential Equations. In *Numerical Solution of Stochastic Differential Equations. Applications of Mathematics*, volume 23, pages 103–160. Springer, Berlin, Heidelberg, 1992.

[370] M. Reza Shaebani, Adam Wysocki, Roland G. Winkler, Gerhard Gompper, and Heiko Rieger. Computational models for active matter. *Nature Review Physics*, 2(4):181–199, 2020.

[371] Mattia Serra, Linnea Lemma, Luca Giomi, Zvonimir Dogic, and L. Mahadevan. Defect-mediated dynamics of coherent structures in active nematics. *Nature Physics*, 19(9):1355–1361, 2023.

[372] Timo Krüger, Ivan Maryshev, and Erwin Frey. Hierarchical defect-induced condensation in active nematics. *Soft Matter*, 19(46):8954–8964, 2023.

[373] Filippo De Luca, Ivan Maryshev, and Erwin Frey. Supramolecular Assemblies in Active Motor-Filament Systems: Micelles, Bilayers, and Foams. *Physical Review X*, 14(3):031031, 2024.

[374] Daniel M Abrams and Steven H Strogatz. Chimera states for coupled oscillators. *Physical Review Letters*, 93(17):174102, 2004.

[375] J. R. Gomez-Solano, A. Blokhuis, and C. Bechinger. Dynamics of Self-Propelled Janus Particles in Viscoelastic Fluids. *Physical Review Letters*, 116(13):138301, 2016.

[376] Mihail N. Popescu, William E. Uspal, Clemens Bechinger, and Peer Fischer. Chemotaxis of Active Janus Nanoparticles. *Nano Letters*, 18(9):5345–5349, 2018.

[377] Ran Niu, Thomas Palberg, and Thomas Speck. Self-Assembly of Colloidal Molecules due to Self-Generated Flow. *Physical Review Letters*, 119(2):028001, 2017.

[378] John Berezney, Bruce L. Goode, Seth Fraden, and Zvonimir Dogic. Extensile to contractile transition in active microtubule–actin composites generates layered asters with programmable lifetimes. *Proceedings of the National Academy of Sciences*, 119(5):e2115895119, 2022.

[379] Bezia Lemma, Noah P. Mitchell, Radhika Subramanian, Daniel J. Needleman, and Zvonimir Dogic. Active Microphase Separation in Mixtures of Microtubules and Tip-Accumulating Molecular Motors. *Physical Review X*, 12(3):031006, 2022.

[380] Jens Grauer, Falko Schmidt, Jesús Pineda, Benjamin Midtvedt, Hartmut Löwen, Giovanni Volpe, and Benno Liebchen. Active droploids. *Nature Communications*, 12(1):6005, 2021.

[381] Antoine Aubret, Quentin Martinet, and Jeremie Palacci. Metamachines of pluripotent colloids. *Nature Communications*, 12(1):6398, 2021.

[382] Claudio Maggi, Juliane Simmchen, Filippo Saglimbeni, Jaideep Katuri, Michele Dipalo, Francesco De Angelis, Samuel Sanchez, and Roberto Di Leonardo. Self-Assembly of Micromachining Systems Powered by Janus Micromotors. *Small*, 12(4):446–451, 2016.

[383] D. P. Singh, A. Domínguez, U. Choudhury, S. N. Kottapalli, M. N. Popescu, S. Dietrich, and P. Fischer. Interface-mediated spontaneous symmetry breaking and mutual communication between drops containing chemically active particles. *Nature Communications*, 11(1):2210, 2020.

[384] Ahmet F. Demirörs, Mehmet Tolga Akan, Erik Poloni, and André R. Studart. Active cargo transport with Janus colloidal shuttles using electric and magnetic fields. *Soft Matter*, 14(23):4741–4749, 2018.

[385] Chenyu Jin, Carsten Krüger, and Corinna C. Maass. Chemotaxis and autochemotaxis of self-propelling droplet swimmers. *Proceedings of the National Academy of Sciences*, 114(20):5089–5094, 2017.

[386] Holger Stark. Artificial Chemotaxis of Self-Phoretic Active Colloids: Collective Behavior. *Accounts of Chemical Research*, 51(11):2681–2688, 2018.

[387] Yoshiki Kuramoto and Dorjsuren Battogtokh. Coexistence of Coherence and Incoherence in Nonlocally Coupled Phase Oscillators. *arXiv*, 2002, cond-mat/0210694.

[388] Simon Garnier, Jacques Gautrais, and Guy Theraulaz. The biological principles of swarm intelligence. *Swarm Intelligence*, 1(1):3–31, 2007.

[389] Eshel Ben-Jacob and Herbert Levine. Self-engineering capabilities of bacteria. *Journal of the Royal Society Interface*, 3(6):197–214, 2006.

[390] Tobias Bäuerle, Robert C. Löffler, and Clemens Bechinger. Formation of stable and responsive collective states in suspensions of active colloids. *Nature Communications*, 11(1):2547, 2020.

[391] Gianni Jacucci, Davide Breoni, Sandrine Heijnen, José Palomo, Philip Jones, Hartmut Löwen, Giorgio Volpe, and Sylvain Gigan. Patchy energy landscapes promote stability of small groups of active particles. *Communications Physics*, 7(1):245, 2024.

[392] Paul Baconnier, Dor Shohat, and Olivier Dauchot. Discontinuous Tension-Controlled Transition between Collective Actuations in Active Solids. *Physical Review Letters*, 130(2):028201, 2023.

[393] Haoran Xu, Yulu Huang, Rui Zhang, and Yilin Wu. Autonomous waves and global motion modes in living active solids. *Nature Physics*, 19(1):46–51, 2023.

[394] Federico Pratissoli, Andreagiovanni Reina, Yuri Kaszubowski Lopes, Carlo Pinciroli, Genki Miyauchi, Lorenzo Sabattini, and Roderich Groß. Coherent movement of error-prone individuals through mechanical coupling. *Nature Communications*, 14(1):4063, 2023.

[395] Carolina Brito, Igor S Aranson, and Hugues Chaté. Vortex glass and vortex liquid in oscillatory media. *Physical Review Letters*, 90(6):068301, 2003.

[396] Hiroshi Noguchi. Shape deformation of lipid membranes by banana-shaped protein rods: Comparison with isotropic inclusions and membrane rupture. *Physical Review E*, 93(5):052404, 00 2016.

[397] Nikhil Walani, Jennifer Torres, and Ashutosh Agrawal. Anisotropic spontaneous curvatures in lipid membranes. *Physical Review E*, 89(6):062715, 2014.

[398] Alfonso Paez, Pedro Tarazona, Pablo Mateos-Gil, and Marisela Vélez. Self-organization of curved living polymers : FtsZ protein filaments. *Soft Matter*, 5(13):2625–2637, 2009.

[399] Elisabeth Fischer-Friedrich and Nir Gov. Modeling FtsZ ring formation in the bacterial cell—anisotropic aggregation via mutual interactions of polymer rods. *Physical Biology*, 8(2):026007, 2011.

[400] Diego A. Ramirez-Diaz, Adrián Merino-Salomón, Fabian Meyer, Michael Heymann, Germán Rivas, Marc Bramkamp, and Petra Schwille. FtsZ induces membrane deformations via torsional stress upon GTP hydrolysis. *Nature Communications*, 12(1):3310, 2021.

[401] Benoit Ladoux and Alice Nicolas. Physically based principles of cell adhesion mechanosensitivity in tissues. *Reports on Progress in Physics*, 75(11):116601, 2012.

[402] Vesa P. Hytönen and Bernhard Wehrle-Haller. Mechanosensing in cell–matrix adhesions – Converting tension into chemical signals. *Experimental Cell Research*, 343(1):35–41, 2016.

[403] Kristian Torbensen, Federico Rossi, Sandra Ristori, and Ali Abou-Hassan. Chemical communication and dynamics of droplet emulsions in networks of Belousov–Zhabotinsky micro-oscillators produced by microfluidics. *Lab on a Chip*, 17(7):1179–1189, 2017.

[404] Jack Connor, Benjamin Champion, and Matthew A. Joordens. Current Algorithms, Communication Methods and Designs for Underwater Swarm Robotics: A Review. *IEEE Sensors Journal*, 21(1):153–169, 2021.

[405] Arijit Ghosh, Weinan Xu, Neha Gupta, and David H. Gracias. Active matter therapeutics. *Nano Today*, 31:100836, 2020.

[406] Danesh Tarapore, Roderich Groß, and Klaus-Peter Zauner. Sparse Robot Swarms: Moving Swarms to Real-World Applications. *Frontiers in Robotics and AI*, 7:83, 2020.

[407] Frederick Ducatelle, Gianni A. Di Caro, Carlo Pinciroli, and Luca M. Gambardella. Self-organized cooperation between robotic swarms. *Swarm Intelligence*, 5(2):73, 2011.

[408] Belkacem Khaldi and Foudil Cherif. An Overview of Swarm Robotics: Swarm Intelligence Applied to Multi-robotics. *International Journal of Computer Applications*, 126(2):31–37, 2015.

[409] Mohamed Abdelkader, Samet Güler, Hassan Jaleel, and Jeff S. Shamma. Aerial Swarms: Recent Applications and Challenges. *Current Robotics Reports*, 2(3):309–320, 2021.

[410] João Tomás Castro, Isabel Pinheiro, Miguel Nakajima Marques, Pedro Moura, and Filipe Neves dos Santos. Pollinationbots - A Swarm Robotic System for Tree Pollination. In *Progress in Artificial Intelligence*, volume 14969 of *Lecture Notes in Computer Science*, pages 90–101. Springer Nature Switzerland, 2025.

[411] Ranjan Sapkota, Matthew D Whiting, Dawood Ahmed, and Manoj Karkee. Robotics for crop pollination: recent advances and future direction. *TechRxiv*, 2024. techrxiv.172840753.37656156.

[412] Dario Albani, Joris IJsselmuiden, Ramon Haken, and Vito Trianni. Monitoring and Mapping with Robot Swarms for Agricultural Applications. *2017 14th IEEE International Conference on Advanced Video and Signal Based Surveillance (AVSS)*, pages 1–6, 2017.

Acknowledgements & Danksagung

First and foremost I would like to express my deepest gratitude to Erwin for giving me the opportunity to become part of his fantastic group at LMU. Before joining, a former PhD student of his told me, “It’s different, but certainly a worthy experience.” Looking back, I can confidently say this is true. I thank Erwin for being always supportive and I especially appreciate his critical thinking and ability to ask the right questions. I very much enjoyed working in this open and creative environment.

I extend my heartfelt thanks to Prof. Igor Aranson with whom I had the pleasure to collaborate on two active matter projects. Receiving direct input and engaging in regular discussions with one of the leading experts in the field is the best thing you can hope for. Also I want to thank him for hosting me on two occasions at Penn State University. I am especially grateful for the warm hospitality he, his wife Olya, and his group showed me during my two visits. Thank you for always being open and supportive.

I am also deeply thankful to Prof. Nikta Fakhri for hosting me during my one-month stay at MIT in Boston. This collaboration, particularly with Jinghui Liu, was an enriching experience, and I am very grateful for the opportunity to work with her group.

I want to thank Prof. Harald Engel and the people from his group in Berlin, particularly Steffen, Jan, Dirk, and Arash for introducing me to the fascinating world of nonlinear dynamics, active matter, and biological physics during my Bachelor’s and Master’s studies. Their support and inspiration played a big role in my decision to pursue a PhD.

I would like to express my appreciation to the many people I had the pleasure of sharing my time with at the chair in Munich:
David, who was my first contact via phone. Thanks for setting up my contract and getting me excited to move to Munich and start my PhD and for always being friendly and entertaining.
Felix, for socially integrating me into the group and attempting (unsuccessfully though) to get me excited about trains.
I’d like to thank the squash squad (Fede, David, Vanja, Flo, Tom, George (I appreciated your historic squash play)) for enjoyable and exhausting sport nights.
I want to thank my office mates Federico, Grześ, Fridtjof, Onurcan (for at least two days), and Ruslan for scientific discussions, fun chats, and an extensive collection of memes. I am very sorry, I cannot thank all of you explicitly, but I am really grateful that I met you all and I connect at least one special memory with each one of you [1]: Grześ, David M., Federica, Tom Bu., Bene, Felix, Raphaela, Christoph, Julian S., Andriy, Onurcan, Carsten, Jonas, Silke, Flo R., Filippo, Sevi, Flo G., James, Bea, Federico, Linus, Ruslan, Philipp, Tom Br., Mingqi, Joris, Boris, Vanja, Ching Yee, Aida, Fridtjof, Schugga, Moritz, Jan, David Br., Isabella, Alina, Timo, Julian K., Davide, George, Frigo, Lucas, Henrik, Julian K., Manon, Patrick, Leschi (in randomized order and after randomly removing one name - if that was your name, I am sorry and would still like to thank you!)

A very special thanks to Tom who shared much of this PhD journey with me. Our parallel paths sometimes caused confusion — not only for Erwin. I appreciate your constant availability, support, and entertaining spirit. I particularly want to thank you for motivating me to join you in Boston to work on the starfish oocyte project. I really enjoyed the time we had there.

I want to thank George. When working together on Lavalamp and phasefields we regularly discussed arising problems and updated each other about the latest findings. This was very motivating and one of the greatest experiences during my PhD. Not to mention the many nights we had sittings in coffee room and Tumult and particular shots in multiples of four. I really loved working together with you and am happy that I found a friend in you.

[1] ‘Is it just one memory? I thought it were two.’

I am also thankful to Divya and Linus for their work on the Lavalamp solver project and for their friendliness. Hanging around with you is always fun. I want to thank the Master and Intern students I had the pleasure to co supervise during my time at the Chair: Michael Reichert, Luca Stadtmüller, Andreas Tsevas, Simon Bauer, Yuhao Liu, Antonia Winter, and Divya Ranjan. Working together with you, discussing the latest results and learning about your viewpoints on the problems was simply great.

I extend my gratitude to the professors at the chair and visiting ones, whose contributions brought diversity of thought and perspective: Particularly, Martin, Chase[2], and Steffen[3].

I would like to thank all the people, I had wonderful and inspiring schools and conferences with. Again I want to thank Erwin, for generously supporting my participation in these events, enabling me to broaden my perspectives, connect with researchers, and create unforgettable memories.

I would like to thank QBM[4] for all the support during my PhD. Special thanks go to Markus and Beate for holding this interdisciplinary group together and navigating us even through challenging COVID times.

My appreciation also goes to CeNS and especially Susanne Hennig for flawlessly organizing events and conferences and for providing guidance on administrative processes. Thanks as well to Alex, Tamara, Emily, and Judith. Organizing Science Rocks! with you over the years has been so much fun.

With all of you — colleagues, collaborators, friends — I connect important memories that are a large part of the PhD experience. I am incredibly grateful for this.

Ich möchte diese Möglichkeit nutzen, mich auch muttersprachlich bei meiner Familie und meinen Freunden zu bedanken. Ich danke euch allen sehr dafür, dass ihr mich immer bei all meinen Vorhaben unterstützt habt. Ich freue mich sehr, dass auch nach dem Umzug nach München unsere Verbindungen bestehen geblieben sind und wir gelernt haben mit dem Abstand umzugehen. Ich danke euch für euer Verständnis. Ohne euch, wäre das alles nicht möglich gewesen.

Insbesondere möchte ich meinen Eltern danken. Danke, dass ihr mich stets unterstützt und mir auch den nötigen Freiraum gegeben habt, mich zu entwickeln. Allein die unzähligen Stunden, in denen ihr mich zum Tennis- oder Gitarrenunterricht gebracht habt, und in denen ihr einfach für mich da wart als ich euch gebraucht habe. Auf euch ist immer Verlass und dafür bin ich euch sehr dankbar. Insbesondere möchte ich meinem Vater für die zahlreichen kreativen Sachaufgaben und die Diskussionen über philosophische Fragestellungen in meiner Kindheit danken; ich bin mir sicher, dass sie mein Interesse an Mathematik und dem Lösen komplexer Probleme gefördert haben.

Ich möchte mich auch bei meinen Großeltern bedanken. Sie waren immer für mich da und haben mich in allem einfach bedingungslos unterstützt. Für die Werte, die sie mir vorgelebt und vermittelt haben, bin ich sehr dankbar. Es macht mich sehr traurig, dass drei von ihnen diese Zeilen nicht mehr lesen können, aber ich hoffe, dass sie wussten, wie dankbar ich ihnen bin.

Zu guter Letzt, möchte ich mich bei meiner Frau Lisa bedanken. Wir sind schon so viele Jahre zusammen und haben dabei vieles erlebt und durchgestanden. Danke, dass du meinen langen Bildungsweg ab dem Studium mit mir gegangen bist. Ich danke dir dafür, dass du immer für mich da bist, mich unterstützt und ich mich darauf verlassen kann, dass wir gemeinsam alles bewältigen können. Ich bin sehr dankbar dafür, mein Leben mit dir zu verbringen. Außerdem kann man sagen, dass wir es letztendlich auch der Physik zu verdanken haben, dass wir uns das ‘I do’ nach der APS-Tagung in Vegas gegeben haben (Also noch einmal ein weiterer Dank an Erwin!). Sonst wäre es aber sicherlich auch woanders passiert.

[2] If you read this, please pay your coffee debts.
[3] aka Prof. Headshot
[4] now QMB